List of Contributors

I. Ando, *Department of Chemistry and Materials Science, International Research Center of Macromolecular Science, Tokyo Institute of Technology, Ookayama, Meguro-ku, Tokyo, Japan*

Q. Chen, *Analytical Center and The Key Laboratory of Education Ministry for Optical and Magnetic Resonance Spectroscopy, East China Normal University, Shanghai 200062, P. R. China*

H. Duddeck, *Hannover University, Institute of Organic Chemistry, Schneiderberg 1B, D-30167 Hannover, Germany*

H. Kimura, *Department of Chemistry and Materials Science, International Research Center of Macromolecular Science, Tokyo Institute of Technology, Ookayama, Meguro-ku, Tokyo, Japan*

S. Kuroki, *Department of Chemistry and Materials Science, International Research Center of Macromolecular Science, Tokyo Institute of Technology, Ookayama, Meguro-ku, Tokyo, Japan*

H. Kurosu, *Department of Human Life and Environment, Nara Women's University, Kitauoya-Nishimachi, Nara 630-8506, Japan*

D.-K. Lee, *Biophysics Research Division, Department of Chemistry, and Macromolecular Science and Engineering, University of Michigan, Ann Arbor, MI 48109-1055, USA*

A. Ramamoorthy, *Biophysics Research Division, Department of Chemistry, and Macromolecular Science and Engineering, University of Michigan, Ann Arbor, MI 48109-1055, USA*

U. Sternberg, *Institute of Instrumental Analysis, Forschungszentrum Karlsruhe, Hermann-von-Helmholtz-Platz 1, Postfach 3640, D-76021 Karlsruhe, Germany*

A. S. Ulrich, *Institute of Instrumental Analysis, Forschungszentrum Karlsruhe, Hermann-von-Helmholtz-Platz 1, Postfach 3640, D-76021 Karlsruhe, Germany; Institute of Organic Chemistry, University of Karlsruhe, Fritz-Haber-Weg 6, 76131 Karlsruhe, Germany*

Y. Wei, *Biophysics Research Division, Department of Chemistry, and Macromolecular Science and Engineering, University of Michigan, Ann Arbor, MI 48109-1055, USA*

R. Witter, *Institute of Instrumental Analysis, Forschungszentrum Karlsruhe, Hermann-von-Helmholtz-Platz 1, Postfach 3640, D-76021 Karlsruhe, Germany*

Preface

Volume 52 of Annual Reports on NMR is devoted to Advances in Solid-State NMR Studies of Materials and Polymers and is dedicated to my longstanding co-worker, Professor Isao Ando of Tokyo Institute of Technology who is planning to retire early in 2005.

The volume opens with an account of PISEMA Solid-State NMR Spectroscopy by A. Ramamoorthy, Y. Wei and D.-K. Lee, this is followed by a review of 3D Structure Elucidation Using NMR Chemical Shifts by U. Sternberg, R. Witter and A. S. Ulrich, next comes an account of ^{77}Se NMR Spectroscopy and Its Applications in Chemistry by H. Duddeck, the following report is on Structural Studies of Polymer Blends by Solid State NMR from H. Kurosu and Q. Chen, finally there is a discussion of the Structural Characterization of Silicon-based Polymer Materials by Solid-State NMR Spectroscopy from S. Kuroki, H. Kimura and I. Ando.

It is my considerable pleasure to offer my thanks to the authors for their very timely accounts and to the production team for the effort involved in the appearance of this volume.

Royal Society of Chemistry
Burlington House
London
UK

G. A. WEBB
November 2003

Contents

Structural Studies of Polymer Blends by Solid-State NMR
HIROMICHI KUROSU and QUN CHEN

Structural Characterization of Si-based Polymer Materials by Solid-State NMR Spectroscopy
SHIGEKI KUROKI, HIDEAKI KIMURA and ISAO ANDO

PISEMA Solid-State NMR Spectroscopy

A. RAMAMOORTHY, YUFENG WEI* AND DONG-KUK LEE

Biophysics Research Division, Department of Chemistry, and Macromolecular Science and Engineering, University of Michigan, Ann Arbor, MI 48109-1055, USA; E-mail: ramamoor@umich.edu (AR)
**Present address: Laboratory of Molecular Biophysics, The Rockefeller University, 1230 York Ave., New York, NY 10021*

Gone are the days when solid-state NMR spectroscopy was considered to be untouchable-like as it provided unappealing spectral lines due to poor resolution and sensitivity. Introduction of a number of powerful concepts dramatically increased the resolution and sensitivity of the spectroscopy and paved numerous avenues for researchers from all walks of science. Now, the new era is harvesting the valuable technique's applications on chemical, material, biological, and pharmaceutical systems in all types of non-isotropic phases such as single crystal, liquid crystal, fibre, powder, and amorphous. One of the most powerful solid-state NMR techniques is PISEMA, which provides very high resolution of the correlation and the precise measurement of chemical shift and heteronuclear dipolar coupling interactions. It is a combination of polarization inversion, that doubles the sensitivity, and spin exchange at the magic angle (SEMA) among dipolar coupled heteronuclear spins. The SEMA pulse sequence suppresses dipole–dipole interaction among

ANNUAL REPORTS ON NMR SPECTROSCOPY
VOLUME 52 ISSN 0066 4103
DOI 10.1016/S0066-4103(04)52001-X

protons and simultaneously generates a doubly rotating frame to have no role for chemical shifts of ^{1}H and S nuclei (such as ^{13}C and ^{15}N). The PISEMA pulse sequence has a high dipolar scaling factor, and the dipolar resolution in the PISEMA spectrum is up to 10 times higher than in spectra obtained by the conventional separated-local-field method. A 2D PISEMA spectrum can be viewed as an image that could be used to determine the secondary structure and topology of aligned molecules. In fact, this was the first solid-state NMR technique that rendered complete resolution and partial assignment of resonances, and the structure and the topology of uniformly labeled membrane proteins. Fascinated by the efficiency of PISEMA, a family of multi-dimensional pulse sequences has been designed to further increase the resolution and applied to study the structure of biological solids, particularly membrane-associated peptides and proteins which are increasingly important, but notorious in general to investigate. In this review, the pulse sequence, line-narrowing mechanism, experimental set-up, applications and limits of 2D PISEMA and related techniques, and different types of PISEMA spectra are discussed. Multi-dimensional solid-state NMR experiments designed based on 2D PISEMA and their applications are reviewed. A new one-dimensional ^{1}H-detected PISEMA pulse sequence to enhance the sensitivity of the experiment is also presented.

1. INTRODUCTION

Ever since the very first attempt of NMR spectroscopy in solid-state,[1] poor sensitivity and poor resolution have been the most *depressing* aspects of solid-state NMR spectroscopy. In spite of these devastating problems, the ability of nuclear spins to dance for various rhythms of RF pulses provided nearly complete information about molecules in solid-state that are otherwise not possible to obtain using other physical techniques.[2–4] In addition, fortunately, tireless efforts of fearless scientists (*kudos* to solid spectroscopists) contributing a plethora of powerful techniques dramatically shaped up solid-state NMR spectroscopy as the unique tool for amazing applications into such diverse realms as analytical chemistry, bioengineering, material sciences, polymer chemistry, structural genomics, nanotechnology, quantum computing, and microimaging. Studies have shown that solid-state NMR spectroscopy is the most valuable technique to provide the structural and functional aspects of many important solid-state systems with no long-range order such as glass, resins, amorphous catalysts, polymers, cellulose, coals, silicates, and a variety of biological solids (viruses, fibril forming molecules like amyloid proteins, silk, collagen, cell walls, molecules embedded in the cell membrane like lipids, cholesterol, proteins, and carbohydrates, and so on). The ever increasing broad-spectrum of developments and applications continues to glorify the intrinsic beauty and wealth of solid-state NMR spectroscopy.[5–10]

Line narrowing has been the *mantra* to increase the resolution and sensitivity of solid-state NMR experiments.[2] In this context, multiple rf pulse sequences and magic angle spinning (MAS) combined with multiple frequency dimensions have been useful to measure NMR parameters, such as chemical shift and dipolar couplings.[2–4] The *local-field*[11] (*IS* dipolar coupling) 'seen' by *S* spins was measured by the first 2D solid-state NMR technique namely separated-local-field (SLF) spectroscopy.[12] This method separates the chemical shift and the local-field, heteronuclear dipolar interactions, in two different frequency dimensions and enables the simultaneous measurement of these two parameters which are essential in determining the structure and dynamics of molecules using NMR spectroscopy. Therefore, the inception of 2D SLF triggered and accelerated the applications of solid-state NMR experiment to investigate non-isotropic systems such as single crystal, liquid crystal, fibre, powder, amorphous, and aligned samples.[3,5,10,13]

A basic 2D SLF pulse sequence is given in Fig. 1. In this method, after the preparation of ^{1}H magnetization using a 90° pulse, the transverse *I*-spin (typically a high γ and highly abundant nuclei such as ^{1}H and ^{19}F) magnetization is coherently transferred to the less sensitive *S* nuclei (such as ^{15}N, ^{13}C) via *I*–*S* dipolar coupling using a cross-polarization (CP) pulse sequences in order to increase the sensitivity of the experiment;[14] instead of the standard CP sequence, there are other pulse sequences that have been proven to be more efficient can be used.[15–18] During the variable time period t_1, the transverse *S*-spin magnetization is allowed to evolve under the chemical shift of *S*, *I*–*S* dipolar coupling, and *I*–*I* dipolar couplings. Since the chemical shift of *S* nuclei is unnecessary in the dipolar coupling dimension (i.e., during t_1 or in the indirect frequency dimension, ω_1), a π-pulse is used to refocus the interaction prior to acquisition of the *S*-spin magnetization under *I*-spin decoupling. The π-pulse is able to refocus the evolution of the magnetization under the chemical shift alone because of the commuting nature of

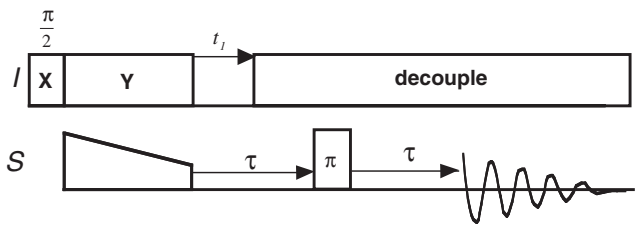

Fig. 1. A two-dimensional pulse sequence for separated-local-field spectroscopy. The pulse sequence correlates the chemical shift of a low-sensitive nuclei *S* (e.g., ^{15}N or ^{13}C) with the dipolar coupling between *S* and the abundant nuclei *I* (e.g., ^{1}H or ^{19}F). During the delays before ($\tau - t_1$) and after (τ) the π-pulse, *I* spins are decoupled from *S* spins by continuous rf irradiation on *S* spins. The details of this pulse sequence are discussed in the text.

the chemical shift and the heteronuclear dipolar coupling Hamiltonians.[19] A constant time period 2τ with I-spin decoupling for $2\tau-t_1$ is used for all t_1 experiments in order to avoid the differing T_2 effects on different experiments. (Incidentally, this was the first constant-time NMR experiment, which has later become the key concept in the development of new solution and solid-state NMR techniques.) The resultant frequency domain 2D spectrum consists of S nuclear chemical shift in ω_2 (or the direct dimension) and the I–S dipolar coupling in the ω_1 dimension. The chemical shift dimension is intrinsically high resolution as I–S interactions are completely decoupled during the acquisition in t_2. However, the unwanted very strong I–I dipolar couplings broaden the spectral lines in the ω_1 dimension, which reduces the accuracy of the measured I–S dipolar coupling values. Therefore, in order to measure I–S dipolar couplings accurately using an SLF experiment, it is important to suppress I–I dipolar couplings from the SLF spectrum.

We would like to mention here that the standard CP experiment itself offers a way to measure local fields in semi-solids or partially aligned systems (such as bicelles and lamellar phase bilayers at a high temperature) or in solids (for example, ferrocene) where I–I couplings are weak.[20] In such systems, a CP experiment (with a variable contact time) could be better than the above-mentioned standard SLF method as CP is a rotating frame experiment and retains the S-spin magnetization for a longer time and to some extent the spin-lock reduces the homonuclear dipolar couplings among I spins; off-resonance spin-lock was shown to suppress I–I dipolar couplings.[21] For the sake of completeness, it may be noted that this SLF experiment is similar to the 2D heteronuclear J-resolved method used in liquid NMR as the spin part (i.e., I_zS_z) of the heteronuclear J and dipole–dipole coupling Hamiltonians are identical. Since J_{IS} coupling is a weaker interaction than the dipolar-coupling (D_{IS}), it is not observed in an SLF spectrum. Although SLF is the simplest 2D solid-state NMR experiment, it is more difficult to perform than a 2D J-resolved experiment.

Heteronuclear dipolar coupling measured from 2D SLF experiments is the key parameter in the structural and motional studies of aligned and powder samples.[5,13] Since accurate measurement of this parameter is essential to precisely determine an interatomic distance, or the orientation of a chemical bond relative to the magnetic field direction ($\vec{B}_0$ parallel to the z-axis of the laboratory frame) in aligned samples, and it heavily relies on the resolution in the dipolar coupling dimension, it is essential to narrow I–S dipolar coupling spectral lines in a 2D SLF spectrum. This is accomplished by suppressing I–I dipole–dipole interactions in the t_1 period. Accordingly, the 2D SLF method has been modified using various multiple pulse sequences (shown in Fig. 2(A)) that were designed based on the average Hamiltonian theory.[3,4,12,22] In the t_1 period of the modified pulse sequence, the S-spin magnetization evolves only under heteronuclear dipolar couplings in a plane perpendicular to the

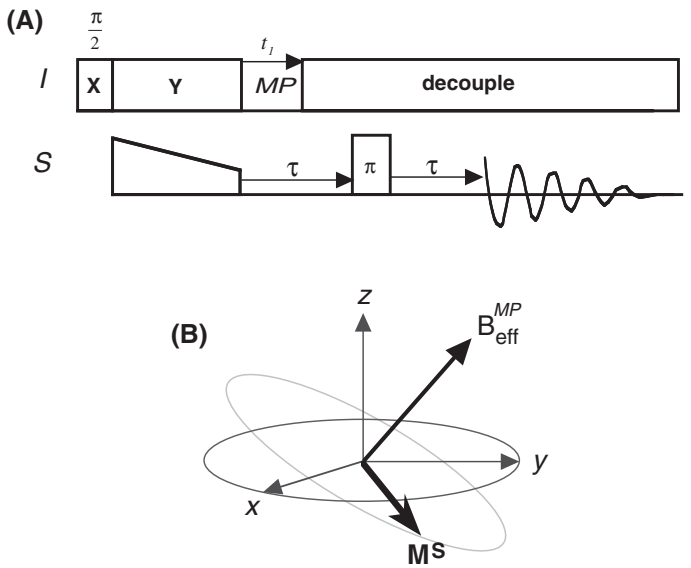

Fig. 2. A 2D SLF pulse sequence (A) with *S*-spin magnetization evolution (B) subject only to heteronuclear dipolar couplings in the t_1 period and detection of chemical shift spectrum in the t_2 period. Various multiple pulse (MP) sequences can be used to suppress dipolar coupling among *I* spins in the laboratory frame during the t_1 period, which enables line-narrowing in the *I*–*S* dipolar coupling dimension (i.e., the ω_1 frequency dimension of the 2D spectrum). This experiment under MAS can be used for separating *I*–*S* dipolar sideband patterns by isotropic chemical shifts; the π-pulse and the start of the acquisition need to be synchronized with rotational echoes. Other aspects of this pulse sequence are similar to the SLF sequence in Fig. 1.

effective field direction of the multiple pulse sequence as shown in Fig. 2(B); for example, the effective field direction of WAHUHA is the (111) axis. Such SLF sequences have been applied to single crystalline, polycrystalline, amorphous, and aligned materials in the presence and absence of MAS.[3,4] Because of the *inhomogeneous* nature of the *S*-spin chemical shift and the *I*–*S* dipolar coupling, the 2D SLF spectrum under MAS consists of a set of rotational sidebands spaced at the spinning frequency in each frequency dimension.[3,4,22]

While the multiple pulse sequences (such as WAHUHA,[23] MREV-8,[24] and Lee-Goldburg (LG)[25]) used in SLF methods are specifically designed to suppress homonuclear *I*–*I* dipolar couplings, they also have the undesirable side effect of significantly scaling down the magnitude of *I*–*S* dipolar couplings. These pulse sequences differ in many aspects: extent of line-narrowing, duration for which they need to be applied, rf power requirement, dependence on the resonance offset and rf field inhomogeneity, and the scaling factor (varies from 0–1; larger the scaling factor larger is the measured dipolar coupling).[2–4] In general, the best SLF sequence should provide the narrowest

dipolar coupling spectral lines, which increase the sensitivity and resolution of the experiment and also increase the accuracy of the measured dipolar couplings. It should also have the highest scaling factor in order to resolve as many dipolar coupling lines as possible, which would allow the measurement of dipolar couplings for chemically equivalent sites. In addition, particularly for biological applications, the best SLF sequence should be efficient even with the use of low rf power as the samples are heat sensitive and the sequence should be tolerant to pulse imperfections (such as offset and rf field inhomogeneity). One such recently developed technique is PISEMA (which stands for the polarization inversion spin exchange at the magic angle) that has been well utilized in solid-state NMR applications.[26]

Among all SLF pulse sequences, PISEMA provides the narrowest dipolar coupling spectral lines and has the most favorable scaling factor (0.82). This is reflected in the steadily increasing applications of PISEMA, particularly in the structural studies of biological solids.[5] A family of 3D and 4D pulse sequences designed using the SEMA sequence has been proposed to further enhance the resolution in the spectral lines and also to assign the resolved resonances from uniformly labeled proteins.[27–31] A 2D PISEMA spectrum of an aligned helical membrane protein contains certain wheel-like patterns of peaks and has been shown to provide the topology of the helix in membranes.[32,33] The purpose of this review is to provide the details and applications of the 2D PISEMA and related solid-state NMR pulse sequences. The intrinsic beauty and complications of 2D PISEMA spectra of several membrane-associated proteins are discussed. In addition to the summary of the literature on PISEMA, a new one-dimensional ^{1}H-detected PISEMA pulse sequence to enhance the sensitivity of the experiment is also presented.

2. PULSE SEQUENCE

2.1. Spin exchange at the magic angle

Line widths in the heteronuclear dipolar coupling dimension of a two-dimensional SLF spectrum highly depend on the efficacy of the line-narrowing pulse sequence used in the t_1 period. It is possible to improve the line-narrowing efficiency using super cycles of a multiple pulse sequence such as BR-24,[34] BR-52,[34] and FFLG.[35,36] However, the main disadvantage for most of these sequences is that a supercycle increases the dwell time in t_1 and therefore shortens the spectral width in the dipolar-coupling dimension of a 2D SLF spectrum. Therefore, SLF methods using supercycles like BR-24 and BR-52 are not common. Irrespective of the drawbacks of supercycles, the longest duration for which the magnetization can be retained in t_1 is restricted by T_2, as most SLF experiments are laboratory frame experiments. On the other hand, this limitation can be removed if the activities in t_1 are

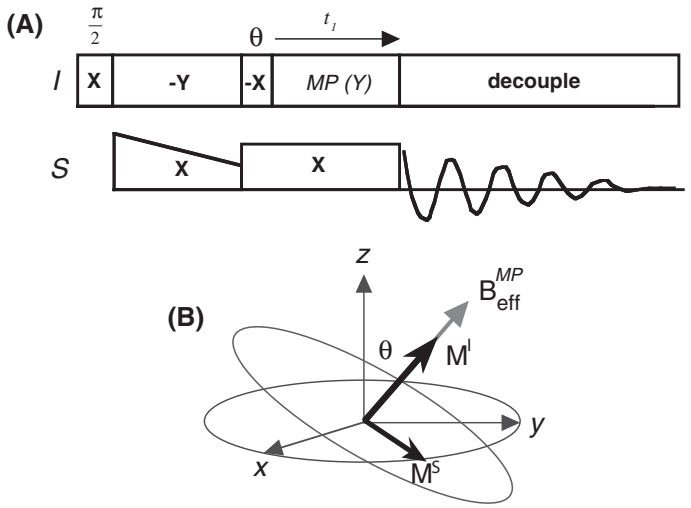

Fig. 3. A 2D SLF pulse sequence (A) that uses a multiple pulse sequence to lock *I*-spins along its effective field direction and a continuous rf field to lock *S*-spins in the transverse plane during the t_1 period (B). The *I*-spin-lock suppresses *I*–*I* dipolar couplings and the *I*-spin chemical shift while the *S*-spin-lock suppresses the *S*-spin chemical shift. See the text for more details on the pulse sequence.

carried out in the rotating frame where $T_{1\rho}$ (longer than T_2 due to the spin-lock) defines the decay of the magnetization. This is achieved by simultaneously spin-locking the magnetization of *I* and *S* spins during t_1 as shown in the pulse sequence given in Fig. 3(A). While the *S* spin magnetization can be spin-locked using a continuous rf field, *I* spins need to be spin-locked using a multiple pulse sequence along its effective field direction (as shown in Fig. 3(B)) in order to suppress *I*–*I* dipolar couplings. (One example is to use windowless isotropic mixing (WIM-12 or WIM-24) sequence[37] that retains the complete spin part of the heteronuclear dipolar coupling Hamiltonian in t_1; such an experiment is not preferred for reasons mentioned later in this review.) For example, transverse magnetization of *I* spins can be flipped and locked along the effective field direction of a multiple pulse sequence, which is the magic angle for many sequences such as LG, FFLG, and WAHUHA. When the effective field strengths of the spin-locks in both rf channels are the same (or when the Hartmann-Hahn condition is satisfied, $B_{\mathrm{eff},I} = B_{\mathrm{rf},S}$), the exchange of magnetization among *S* and *I* nuclei occurs via the *I*–*S* dipolar coupling (known as SEMA, the spin exchange at the magic angle), which is scaled by $\sin\theta_m$ (θ_m is the magic angle) (Fig. 4).[26] Since this method eliminates the long 2τ delay that is used to refocus chemical shifts, it reduces the loss of magnetization and increases the signal intensity compared to other SLF experiments. The SEMA sequence also increases the decay time from

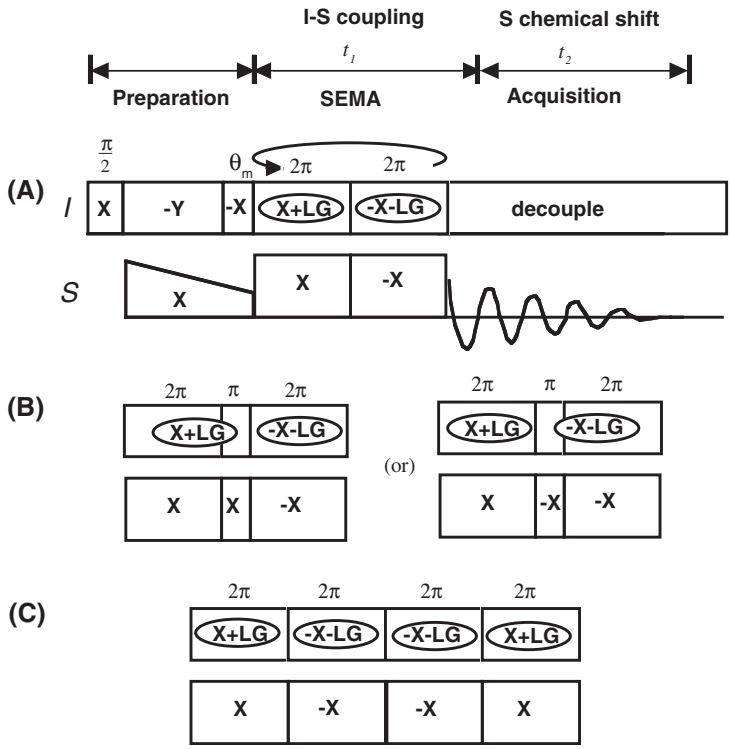

Fig. 4. Pulse sequences for 2D PISEMA experiments on static or slow-spinning samples. It has been shown that the use of ramped rf pulses for *S*-spin-lock during the t_1 period makes the pulse more tolerant to experimental errors. The original PISEMA sequence (A) does not suppress the effects of phase transients. Incorporation of the modified SEMA sequences, (B) and (C), in the t_1 period of the PISEMA sequence (A) have been shown to suppress the effects of phase transients.

T_2 (laboratory frame) to $T_{1\rho}$ (rotating frame), and suppresses the chemical shifts of *I* and *S* nuclei.

For a two spin system, the ω_1 dimension of the 2D PISEMA spectrum contains a doublet with the splitting corresponding to the *I*–*S* dipolar coupling scaled by 0.82. In the presence of more protons, unlike other SLF methods, the SEMA sequence suppresses the line broadening due to weak *I*–*S* dipolar couplings between *S* and other neighbouring *I* spins. This is because the different rotating frame heteronuclear dipolar coupling Hamiltonians do not commute and therefore the weak dipolar couplings from the neighbouring protons are truncated by the much larger dipolar coupling Hamiltonian of the directly bonded heteronuclei. Thus a very high resolution of dipolar spectral lines is achieved in the 2D PISEMA spectrum.[38] On the other hand, care must be taken in analyzing the dipolar coupling spectra of PISEMA for many-spin system as the modulation of dipolar couplings can mislead

the interpretation of the measured values.[39] The multiplet pattern observed in the dipolar-coupling spectrum depends on the relative magnitudes of *I*–*S* dipolar couplings, and it may be difficult to measure weaker *I*–*S* dipolar couplings using the PISEMA sequence. For example, in the case of an IS_2 spin system, the dipolar-coupling spectrum obtained from PISEMA shows a doublet with a splitting of $1.63(D_{IS1}^2 + D_{IS2}^2)^{1/2}$; this effect is unlike the 4 lines pattern observed in other SLF experiments. On the other hand, when one of the *I*–*S* couplings is very weak (for example, $D_{IS1}^2 \gg D_{IS2}^2$), in the PISEMA spectrum, the weak dipolar coupling (i.e., D_{IS2}^2) perturbs the frequency separation between the two peaks in the doublet by $0.82(D_{IS2}^2/2D_{IS1})$ without inducing any further splitting (or broadening) of the doublet; whereas in a regular SLF spectrum, the weak dipolar coupling broadens the doublet. While this is a disadvantage of PISEMA in measuring weak *I*–*S* dipolar couplings, it has been highly useful in measuring strong ^{1}H–^{15}N and ^{1}H–^{13}C dipolar couplings from proteins.

As discussed later, the application of the SEMA sequence is not limited to the 2D PISEMA experiment, but it can be used to design a variety of sophisticated pulse sequences.[27–30] For example, the selective transfer of magnetization between strongly coupled heteronuclei by SEMA is the key feature of the sequence that can be utilized in experiments such as HETCOR,[27] ^{1}H-detected experiments,[40] and experiments to selectively measure relaxation parameters of a proton bonded to *S* nuclei.

2.2. Polarization inversion

In a CP experiment, under the Harman-Hahn match, the transverse *I*-spin magnetization is transferred to *S* nuclei via *I*–*S* dipolar couplings. The magnitude of the transferred *S*-spin magnetization oscillates but steadily increases as a function of the contact time and reaches a steady state.[19,20] This can be thought as the flow of heat energy from a hot reservoir to a cold reservoir. At the steady state, the *I* and *S* spin reservoirs are in thermal equilibrium and they no longer exchange magnetization. On the other hand, if the temperature of one of the reservoirs is altered, they will exchange the magnetization again until they reach an equilibrium. For example, after CP, reversal of the phase of the spin-lock on the ^{1}H channel, while keeping the phase of the spin-lock on the *S*-spin channel the same, would inverse the spin temperature of protons and thus the temperature difference between the two reservoirs becomes the maximum. Therefore, the magnitude of the exchange of magnetization (or the heat energy) becomes a maximum after CP. This process can be exactly described using the density matrix analysis. The density matrix after the contact time is $aI_x + bS_x$ when an *x*-phase spin-lock is used on both rf channels during cross-polarization. Since both *I* and *S* nuclei are in thermal equilibrium after CP, the extent of transverse magnetization of *I* and *S* spins would be the same (or $a = b$). This symmetric

representation of the density matrix would have a constant of motion under the *I*–*S* dipolar coupling Hamiltonian ($\sim I_yS_y+I_zS_z$) under the spin-lock as given by the following equations.

$$I_x \longrightarrow \frac{1}{2}I_x(1+\cos\omega_{IS}t)+\frac{1}{2}S_x(1-\cos\omega_{IS}t)+\left(I_yS_z-I_zS_y\right)\sin\omega_{IS}t \quad (1)$$

$$S_x \longrightarrow \frac{1}{2}I_x(1-\cos\omega_{IS}t)+\frac{1}{2}S_x(1+\cos\omega_{IS}t)-\left(I_yS_z-I_zS_y\right)\sin\omega_{IS}t \quad (2)$$

$$I_x+S_x \longrightarrow I_x+S_x \quad (3)$$

$$I_x-S_x \longrightarrow I_x\cos\omega_{IS}t-S_x\cos\omega_{IS}t+2\left(I_yS_z-I_zS_y\right)\sin\omega_{IS}t \quad (4)$$

Where $\omega_{IS}=-[(\mu_0\hbar/4\pi)(\gamma_I\gamma_s/r_{IS}^3)]\cdot(1/2)(3\cos^2\theta_{IS}-1)$. On the other hand, the reversal of the *I* spin-lock phase after the CP would change the density matrix to aI_x–bS_x, i.e., the polarization inversion of the *S*-spin magnetization, which would further evolve under the heteronuclear dipolar coupling. Since the extent of magnetization participating in the exchange is two times (it is $a+b=2b=2a$ after the CP) larger than the amount of *S*-spin magnetization alone (i.e., *b*), the sensitivity is expected to increase by a factor of two. This fact that the polarization inversion (PI) after CP increases the sensitivity of the spin exchange by a factor of two has been experimentally demonstrated.[38,41] CP–PI was first used to separate morphologically distinct environments, or differently substituted carbons, and to study the relative molecular mobility of individual functional groups.[42a] Since the spin-lock reduces the dipolar couplings among *I* spins, CP–PI has been used as an SLF experiment.[38,41,42b] The oscillation of the *S*-spin magnetization due to the evolution under the *I*–*S* dipolar coupling after cross-polarization in a CP–PI experiment is, however, damped by the unsuppressed coupling among *I* spins and couplings of remote *I* spins with the *S* spin. This has been clearly demonstrated on a single crystal sample of a peptide.[38] Therefore, implementing the PI process in the SEMA experiment (i.e., PISEMA[26]) would increase the sensitivity by a factor of two and retains the line-narrowing efficiency of SEMA.

2.3. PISEMA

A two-dimensional PISEMA pulse sequence that combines CP, PI, and SEMA is given in Fig. 4(A).[26] After CP, the transverse *I*-spin magnetization is flipped to the magic angle by a 35.3° pulse and locked by the flip-flop Lee-Goldburg (FFLG;[35] it has also been referred to as FSLG or FSLG-2 in the literature;[36a] we prefer to use FFLG as both the phase and the frequency of the rf field are altered to invert the effective field direction after each cycle the sequence, i.e., a 2π duration; the phase modulated version, PMLG, can also be used[36b]) pulse sequence along the magic angle. LG sequence is an rf irradiation applied at an off-resonance frequency, Δ, to establish an

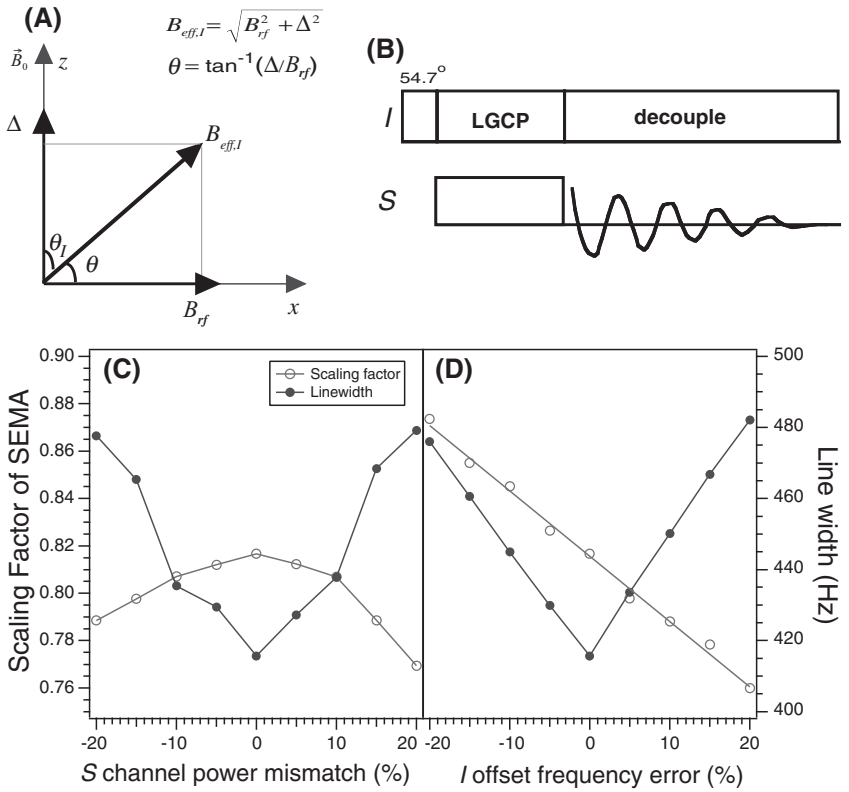

Fig. 5. (A) Vector picture describing the relationship between the rf field strength and offset frequency in off-resonance experiments such as LGCP and PISEMA. (B) A simple pulse sequence (called LGCP or FFLGCP) to set-up the Lee-Goldburg condition. As explained in the text, this sequence can be used to determine the *S*-spin-lock field strength ($B_{rf,S}$) that matches $B_{eff,I}$ for the effective spin exchange between *I* and *S* spins. Performing LGCP as a 2D experiment by incrementing the contact time, this pulse sequence can also be used to measure the scaling factor of the LG or FFLG spin-lock sequence. (C and D) Evaluation of the effects of rf power mismatch on *S*-spin channel ($\omega_{eff,I} - \omega_{rf,S}$) and offset frequency errors (deviation from the offset frequency value, Δ, needed to set $B_{eff,I}$ at the magic angle) on the scaling factor of the SEMA sequence and the line width of dipolar coupling lines in the 2D PISEMA spectrum. (C) The scaling factor (open circles) and line width (close circles) are plotted against the rf power mismatch which is expressed as the percentage of the perfectly matched rf power on the *S*-spin channel. (D) The scaling factor (open circles) and line width (close circles) as functions of an error in the *I*-spin offset frequency which is expressed as the percentage of the *I*-spin offset frequency value without error.

effective field, $B_{eff,I}$, at the magic angle relative to $\vec{B}_0$ (Fig. 5(A)). The efficiency of the LG sequence is improved by the implementation of the (phase- and frequency-switched) FFLG pulse sequence where the direction of the effective field is inverted after each 2π rotation. In Fig. 4(A), X+LG means an X-phase

S-spin-lock and an rf irradiation of *I*-spins at an offset Δ, while –X-LG means a –X-phase *S*-spin-lock and an rf irradiation of *I*-spins at an offset $-\Delta$. The phase of the first cycle of FFLG in t_1 has to be inverted relative to the *I*-spin-lock phase in CP for polarization inversion as discussed in Section 2.2. The rf field strength of the spin-lock applied to *S*-spins ($B_{\mathrm{rf},S}$) is matched to the effective FFLG field strength ($B_{\mathrm{eff},I}$) and needs to be phase alternated synchronously with the phase and frequency alternation of the FFLG pulse sequence. This procedure enables the coherent exchange of magnetization via the *I*–*S* dipolar coupling and the oscillating frequency is given by[38]

$$\Omega = \frac{\gamma_I \gamma_s h}{r_{IS}^3}\{3\cos^2\theta - 1\}\sin(\theta_I)\sin(\theta_S) = \kappa\frac{\gamma_I \gamma_s h}{r_{IS}^3}\{3\cos^2\theta - 1\} \tag{5}$$

where the angles θ_I and θ_S define the directions of the effective spin locking fields for *I* and *S* nuclei, respectively, relative to $\vec{B}_0$ (see Fig. 5(A)). As mentioned earlier, the FFLG sequence suppresses *I*–*I* dipolar couplings and scales the *I*–*S* dipolar coupling by a factor $\kappa = \sin(\theta_I)\sin(\theta_S) = \sin(54.7^\circ)\sin(90^\circ) = 0.82$. Modified versions of the SEMA sequence are shown in Fig. 4(B–D) and they are discussed below.

Line-narrowing efficiency of several 2D SLF methods was examined by performing experiments on a [$^{13}C_\alpha$, ^{15}N]-labeled *N*-acetyl, D,L-valine single crystal at an arbitrary orientation with respect to $\vec{B}_0$. All these experiments were performed on a Chemagnetics/Varian Infinity 400 MHz solid-state NMR spectrometer at room temperature under identical conditions using a home-built (4-mm solenoid coil) probe. Line widths of ^1H–^{15}N and ^1H–^{13}C dipolar coupling spectral lines were measured at different rf field strengths, ν_{rf}, in the ^1H channel) and the results are summarized in Table 1. These results suggest that 2D PISEMA provided the narrowest dipolar coupling lines irrespective of the rf field strength used in the experiments. These results also suggest that the spin-lock SLF experiments, in general, provide better resolution than other SLF experiments.

2.4. FFLG is the natural choice for PISEMA

PISEMA pulse sequences, similar to the one shown in Fig. 4(A), can also be designed using other multiple pulse sequences (as shown in Fig. 3(A)). However, FFLG was specifically chosen because, unlike most other multiple pulse sequences, FFLG is tolerant to resonance offset, rf field inhomogeneity, and other experimental errors, and easy to implement in an experiment. A systematic examination of various forms of rotating frame SLF experiments on a single crystal peptide sample revealed FFLG is better than other pulse sequences like CP–PI, LG, and WIM-24 (also see our recent experimental results in Table 1).[38] WIM-24[37] is relatively difficult to

Table 1. Spectral parameters measured from 2D SLF spectra of a single-crystal sample of [^{13}Cα, ^{15}N]-labeled *N*-acetyl-D,L-valine at an arbitrary orientation with respect to the external magnetic field

Experiment	Line width of ^{1}H–^{15}N dipolar lines (Hz) $\nu_{rf} = 85$ kHz	$\nu_{rf} = 50$ kHz	Line width of ^{1}H–^{13}C dipolar lines (Hz) $\nu_{rf} = 65$ kHz
SLF	1530	1530	1860
WAHUHA-4-SLF	728	1040	960
MREV-8-SLF	505	910	628
BR-24-SLF	420	–	–
LG–SLF	630	667	705
FFLG–SLF	514	550	630
WIM-24-SLF[a]	412	–	–
LG–PISEMA[a]	320	354	375
FFLG–PISEMA[a]	172	185	220

[a]Rotating frame experiments where a multiple pulse spin-lock was used in the t_1 period.

implement, but efficient in suppressing ^{1}H–^{1}H dipolar couplings, and was found to be not suitable as the dwell time in t_1 was too long especially when low rf power is used.[38] However, the isotropic structure of the heteronuclear dipolar coupling Hamiltonian provided by the WIM sequence[37] could be important in the development of pulse sequences for other applications in solid-state NMR spectroscopy. Most multiple pulse sequences, except LG and FFLG, consist of a series of rf pulses with specific width and phase whose accuracy determines the efficiency of the entire pulse sequence.[2–4,23,24,34] Therefore, they are less tolerant to experimental errors and tedious to set-up experimentally.

In addition to the simple form of the FFLG sequence, it is efficient in suppressing ^{1}H–^{1}H dipolar couplings even when it is applied with a low rf field strength (see Table 1). This is mainly because the effective field strength of LG, $B_{\mathrm{eff},I} = \sqrt{B_{\mathrm{rf}}^2 + \Delta^2}$, appears to be larger even when the rf power is small, as it is given by the combination of the rf field strength and the frequency offset as defined in Fig. 5(A). Therefore, this unique property of LG dramatically reduces the rf power requirement to achieve the same level of line narrowing as by other multiple pulse sequences, and is of significant importance in studying biological solids.[43] Since rf power is proportional to B_1^2, any power loss due to the nature of the sample demands more rf power to generate the same rf field strength. In addition to being technically demanding, the use of high rf power leads to significant heat dissipation in the sample. In particular, a hydrated phospholipid bilayer sample containing a membrane-associated protein is power lossy due to the high water content, and at the same time, the dissipated heat dehydrates the bilayer and can denature the sample. These concerns are especially important for long-duration solid-state NMR experiments (typically a few days) as most biological samples are not

abundantly available and extensive signal averaging is unavoidable. Also, the benefit of higher magnetic fields to increase the S/N and resolution comes with the price of requiring higher rf power for solid-state NMR experiments. Therefore, any pulse sequence that requires high rf power tends to be not suitable for practical applications.

3. EXPERIMENTAL PROCEDURE TO OPTIMIZE THE PERFORMANCE OF PISEMA

Implementation of the 2D PISEMA pulse sequence on any spectrometer (commercial or home-built) is relatively easy unlike other experiments containing multiple pulse sequences such as WAHUHA,[23] MREV,[24] BR,[34] and WIM.[37] Even a quick and careless run of the PISEMA experiment provides dipolar lines narrower than those obtained using other SLF experiments.[38] However, the scaling factor and efficiency of such uncalibrated PISEMA experiment could be different from the ideal one. Use of an inaccurate scaling factor increases the error in the measured dipolar coupling values from the PISEMA spectrum. Therefore, even though FFLG and PISEMA are, to a large extent, tolerant to experimental imperfections, we recommend the following steps to implement the most efficient PISEMA experiment.

1. *Optimize the phase and amplitude of rf pulses.* Several tune-up pulse sequences used to set-up the ^{1}H CRAMPS experiment[44] can be performed using the ^{1}H resonance of liquid water. On the other hand, typically a sample labeled with S nuclei (^{15}N, ^{13}C, or other isotopes of low sensitive nuclei) is needed to optimize rf pulses on the S-spin channel. For example, a single crystal of ^{15}N-labeled peptide (a model peptide like N-acetylated amino acid or a short peptide) is used for experiments on ^{15}N-labeled proteins and peptides. Particularly, the phase and shape of rf pulses used in the t_1 period of 2D PISEMA need to be examined. A test pulse sequence consisting of a series of pulses, with no delay in between them, applied at on-resonance and off-resonance frequency that satisfies the LG condition can be used to examine the amplitude of the pulse.[38] The I-spin rf power amplifier needs to be tuned to provide the same amplitude at on- and off-resonances. Length of rf pulses used in the PISEMA sequence at on- and off-resonance frequencies need to be determined. This procedure makes sure that FFLG suppresses I–I dipole–dipole couplings efficiently and the FFLG spin-lock during t_1 is efficient. It is important to note that the 2π pulse duration is determined based on the effective field strength ($B_{\mathrm{eff},I} = \sqrt{B_{\mathrm{rf}}^2 + \Delta^2} = \sqrt{3/2}B_{\mathrm{rf}}$) of FFLG in PISEMA and not directly from the strength of the rf field (B_{rf}) applied on I-spin

channel. For example, an rf field strength of 41.7 kHz and an offset of, $\Delta = B_{rf}/\sqrt{2}$, 29.5 kHz used to set the LG condition ($B_{eff} = 51.0$ kHz). Therefore, the 2π pulse width, $\tau = \sqrt{2/3}\,(2\pi/B_{rf})$, is 19.6 μs.

2. *Synchronization of the phase and frequency jumps*. Since all commercial spectrometers now have fast phase and frequency switching capabilities, the short delays (< 300 ns) needed to switch the phase and frequency for the FFLG sequence can be calibrated and accordingly the timings of pulses in the pulse program can be adjusted. Power reflections from the probe, as observed on an oscilloscope with an in-line directional coupler, can be minimized under high-power rf irradiations by careful adjustment of the probe tuning for both on- and off-resonance frequencies.[38]
3. *Optimization of SEMA*. The rf power and the offset frequency, required to satisfy the LG condition in the FFLG sequence and to match the rf power on the *S*-spin channel during t_1, need to be determined. This can be done using the standard CP sequence but replacing the initial 90° pulse and the *I*-spin-lock by a 54.7° pulse to flip the *I*-spin magnetization to the magic angle followed by an off-resonance spin-lock that satisfies the LG condition as shown in Fig. 5(B). Using this LGCP pulse sequence on a standard solid-state sample, measure the magnitude of the *S*-spin magnetization under *I*-spin decoupling as a function of the *S*-spin-lock field strength. Maximum magnetization transfer from *I* to *S* nuclei is observed when the effective field of the *I* spin-lock ($B_{eff,I}$) matches the rf power of the *S*-spin-lock ($B_{rf,S}$).[38] After optimizing the LGCP condition, similar test experiment can be performed using the pulse sequence (called FFLGCP) where the spin-lock (on both channels) in the LGCP sequence can be replaced by the SEMA sequence. Optimize the rf power of the pulses in SEMA to minimize the effects of phase transients by maximizing the efficiency of the spin exchange. In addition, the width and phase of 2π-pulses in the FFLG sequence can be confirmed by this test experiment.

   A quick 2D experiment can be performed, assuming that the S/N of the 1D LGCP or FFLGCP spectrum is sufficient enough, by recording the *S*-spin signal under proton decoupling (t_2) while incrementing the spin-lock time (t_1). The oscillation of the *S*-spin magnetization with a frequency corresponding to the scaled *I*–*S* dipolar coupling as a function of the mixing time (or called 'dipolar oscillations') in t_1 can be processed to measure the efficiency of the SEMA sequence. Since the spin-lock by SEMA in FFLGCP (or LG in LGCP) suppresses weak *I*–*S* dipolar couplings (due to the non-commuting nature of the Hamiltonians for the dipolar coupling between *S* and *I* spins) and spin diffusion among protons, the cross-polarized *S*-spin magnetization is much weaker than that observed in a

regular CP experiment. The match of effective fields on I and S channels (i.e., $B_{\mathrm{eff},I} = B_{\mathrm{rf},S}$) is critical for the spin exchange via the I–S dipolar coupling in SEMA. It is also useful to understand the effects of rf power mismatch during the t_1 period of the 2D PISEMA experiment is important as the rf power is usually calibrated from crystalline standard samples whose rf power requirements can significantly differ from those of the hydrated lipid bilayer samples, which are power lossy. The frequency offset (Δ) used to set up FFLG sequence is also error-pro due to the fact that the offset frequency is determined by the mis-calibrated rf field strength on the I-spin channel. Therefore, effect of these experimental errors on the performance of the SEMA sequence was examined using SIMPSON[45] simulations.

The test system used for simulations included directly bonded ^{1}H and ^{15}N nuclei with the N–H bond length of 1.07 Å, and two remote protons that are weakly coupled to the ^{15}N-bonded proton with dipolar couplings of 4 and 5 kHz at different orientations. The powder patterns of ^{1}H–^{15}N dipolar coupling were then simulated to evaluate the effects of rf power mismatch and offset error on scaling factor of SEMA (Fig. 5(C)) and line width of dipolar spectral lines (Fig. 5(D)). In general, mismatch increases the line width and decreases the scaling factor as shown in Fig. 5(C). Simulations suggest that a 10% rf power mismatch changes the scaling factor to about 0.805 and increases the line width by about 20 Hz. A 20% rf power mismatch changes the scaling factor to about 0.77 and increases the line width by about 70 Hz. The simulations show that the scaling factor is linearly dependent on the ^{1}H offset frequency error. A decrease in the offset value (from the correct value) increases the scaling factor of the SEMA sequence and vice versa (Fig. 5(D)). On the other hand, the profile of the line width vs. ^{1}H offset frequency error appears as a V shape, with the smallest line width corresponds to no error in the offset (Fig. 5(D)). These results are in complete agreement with an experimental study which showed that the mismatch in rf fields up to 12 kHz in the PISEMA experiment had little effect on the observed ^{1}H–^{13}C dipolar splitting as the mismatch was suppressed by the inversion of the effective fields in t_1, but the dipolar coupling values, however, depended on the proton resonance offset.[39]

4. *Efficiency of spin-locks*. Examine the efficiency of t_1 spin-locks on I and S rf channels using pulse sequences discussed elsewhere.[38] The longest time for which the magnetization can be spin-locked on both channels depends on the strength of the rf power, stability of rf amplifiers, rf field inhomogeneity, effects of phase transients, span of the chemical shift, $T_{1\rho}$ of the nuclei (assuming no spin-lock on the other channel), and the quality of the probe. In addition, on the I-spin channel, it also depends on the degree of suppression of the I–I dipolar

couplings. However, in general, longer the retention of the magnetization better is the quality of spin locking. For example, our experiments on a single crystal of NAVL showed that a 10-ms spin-lock of the ^{15}N magnetization with phase-alternated rf spin-lock (the pulse sequence is similar to the PISEMA but there are no pulses during t_1 in the ^{1}H channel) resulted in the loss of only about 7% of the initial magnetization; use of ramped spin-lock pulses significantly reduced the loss of magnetization especially at higher rf field strengths (>65 kHz). This compares to a loss of roughly 9% of the magnetization with spin locking with continuous irradiation under the same condition. Continuous and FFLG spin-locking resulted in loses of 13 and 22%, respectively, over 10 ms.

5. *Suppress the effects of phase transients*. Since high rf power ($\sim$1kW) is essential for the phase-alternated spin-lock pulses on the *S* channel, the effect of phase transients needs to be minimized in order to retain the magnetization for a long time during the t_1 period. Phase transients shift the magnetization away from the effective field (or the spin-lock) direction and the cumulative effect forces the magnetization to oscillate as a function of t_1.[46] These false oscillations appear like extra dipolar coupling frequencies in the final 2D PISEMA spectrum. It has been successfully demonstrated that these effects can be suppressed using 3π–2π (or 2π–3π) FFLG cycles (see Fig. 4(B)) instead of 2π–2π.[46] The extra π pulse refocuses the transverse magnetization along the spin-lock direction, which dephases due to phase transients, while the modified PISEMA retains all the benefits of the unmodified PISEMA. On the other hand, decreasing the rate of the reversal of the effective field direction reduces the effects of transients.[38,47] For example, reversal of $B_{\mathrm{eff},I}$ *only* after the odd-numbered 2π pulses (t_1 dwell can still be 4π duration) (Fig. 4(C)) would significantly reduces the number of phase transients and their overall effect. While our experiments on a single crystal of NAVL suggested that the latter approach is not as significant as the former approach, the shorter dwell time of the latter approach would be attractive for low rf power experiments. It is also possible to overcome the effects of phase transients using supercycles of FFLG. Ramped pulses for *S*-spin-lock can be used to reduce the overall rf power in t_1, which could reduce phase transient effects.[48]
6. *Measure the scaling factor*. Chemical shift scaling (0.58 in an ideal case) of the LG and FFLG sequences can be measured by monitoring the ^{1}H resonance frequency of water as a function of the irradiation frequency as demonstrated elsewhere.[38] Even though this scaling factor (0.58)[49] is not directly needed for PISEMA experiments, it is essential for other PISEMA related experiments such as a 2D HETCOR experiment that uses FFLG to measure chemical shifts *I* nuclei and

SEMA to transfer *I*-spin magnetization to *S* nuclei.[27,40] In addition, this measurement also makes sure that the FFLG (rf amplitudes at two different offsets, phase, and 2π duration) in PISEMA is implemented correctly. The scaling of the heteronuclear dipolar coupling in PISEMA (0.82 in an ideal case) can be determined by measuring the *I*–*S* dipolar coupling using the same experiment suggested in step 3 (i.e., LGCP or FFLGCP experiment shown in Fig. 5(B)) on a sample for which the *I*–*S* dipolar coupling is already known from other experiments. It has been experimentally shown that the change in the scaling factor due to the mismatch in the effective fields on the *I* and *S* channels could be avoided using ramped amplitude pulses in t_1.[48]

4. APPLICATIONS OF PISEMA

Since the size and phase of the sample do not pose difficulties to the applications of solid-state NMR, it has now become one of the most important methods to study biological systems including membrane proteins. NMR parameters such as chemical shifts of ^{15}N, ^{13}C, ^{31}P, and ^{1}H nuclei, hetero- and homo-nuclear dipolar couplings, quadrupolar couplings of ^{14}N and ^{2}H nuclei, and relaxation parameters measured from solid-state NMR experiments have been commonly used in the structural studies of non-isotropic biological systems.[5,8,10] Since the discovery of PISEMA, a number of studies utilizing the high-resolution rendered by this technique have been reported.[27–33,50–53] Excellent performance of PISEMA triggered the development of several higher dimensional solid-state NMR methods to achieve higher resolution spectra and assign resonances from uniformly ^{15}N labeled proteins.[27–33] In fact, PISEMA has become the unique experiment to determine the topology of aligned molecules. Particularly, solid-state NMR experimental studies on uniaxially oriented bilayers are well-suited for the structure determination of membrane proteins as the unique orientation of the membrane protein relative to the membrane normal is preserved.[54] Some of these applications are discussed below.

4.1. PISEMA provides chemical shift and dipolar coupling tensors

Anisotropic nuclear spin interactions, such as chemical shift anisotropy (CSA) and heteronuclear dipolar coupling, are highly valuable in understanding the nature of chemical bonding, structure, dynamics, and function of chemical and biological molecules. For example, chemical shifts of ^{1}H, ^{15}N, and ^{13}C nuclei are routinely used in the structural and motional studies of proteins using solution and solid-state NMR methods.[5,10] Spectra of aligned solid-state

samples, such as membrane proteins embedded in phospholipid bilayers or bicelles and magnetically aligned biological systems, are interpreted using CSA tensors.[32,33,52–58] Relaxation studies to investigate the dynamics of globular proteins using solution NMR spectroscopy rely on the availability of CSA tensors.[55] In fact, the accuracy with which most NMR experimental data are analyzed is limited by the availability and accuracy of CSA tensors. Therefore, precise measurement of CSA tensors is important for the applications of NMR methods.

The anisotropic heteronuclear dipole–dipole interaction is a function of not only the distance between two nuclei but also the orientation of the internuclear vector with respect to $\vec{B}_0$. Therefore, the dipolar coupling values directly provide geometrical parameters that can be translated into molecular conformations. For example, ^{1}H–^{15}N, ^{13}C–^{15}N, and ^{1}H–^{13}C dipolar couplings are commonly used to determine the relative orientations of the chemical bonds, which are converted into the conformation and/or the topology of molecules using NMR methods.[5,10,54]

Until the discovery of 2D spectroscopy, a CSA tensor was determined *only* from experiments using large single crystals.[2–4,59,60] The tensors (both the magnitudes and the orientation of the principal components) determined from single crystals are highly accurate, but it is not easy to obtain a large single crystal for most biological systems of interest. In contrast, the magnitudes of a CSA tensor can directly be measured from a one-dimensional static powder pattern or MAS spinning side bands, but it is not possible to determine the orientation of the tensor in the molecular frame.[3,4] The introduction of 2D SLF experiments enabled the characterization of chemical shift and heteronuclear dipolar coupling tensors in the molecular frame from powder samples without the need for single crystals.[13b] Since then, a number of solid-state NMR studies characterizing CSA tensors have been reported in the literature.[55,61–71] The accuracy of the measured CSA tensor values mainly depends on the resolution in the dipolar-coupling dimension of the 2D SLF spectrum and therefore PISEMA has become the natural choice for the accurate measurement of CSA tensors.[46,50,61,62,70]

4.1.1. *PISEMA of static powder samples*

Two-dimensional PISEMA spectra experimentally obtained from powder samples are analyzed by comparison with simulations to determine Euler angles that define the orientation of the CSA tensor in the molecular frame, while the magnitudes of the CSA tensor is measured from a 1D chemical shift powder pattern. Some examples of PISEMA spectra of powder samples simulated using SIMPSON program[45] are shown in Fig. 6. PISEMA spectra correlating the ^{15}N chemical shift and the ^{1}H–^{15}N dipolar coupling interactions associated with an amide site of a peptide (Fig. 6(A))[61] and with the N_{π}–H bond of the imidazole ring in histidine (Fig. 6(B))[62] were simulated.

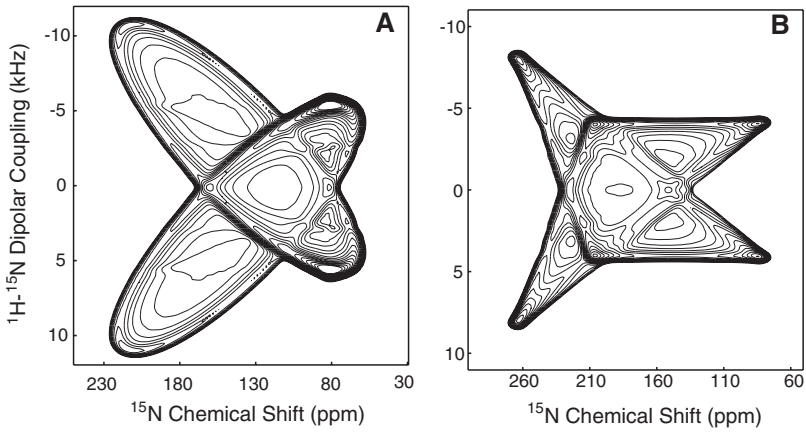

Fig. 6. Simulated 2D PISEMA spectra of powder samples. Correlation of ^{1}H–^{15}N dipolar coupling and ^{15}N chemical shift interactions associated with an amide N–H bond (A) and the histidine side chain Nπ–H bond (B). For the amide N–H bond, the simulations were performed using ^{15}N CSA principal values of $\delta_{33} = 64$, $\delta_{22} = 77$, and $\delta_{11} = 217$ ppm, an N–H bond length of 1.07 Å, and the Euler angles ($\alpha = 0^{\circ}$ and $\beta = 17^{\circ}$) to define the relative orientations of the chemical shift and dipolar coupling tensors. For the histidine side chain Nπ–H bond, the following parameters were used in the simulations: ^{15}N CSA principal values of $\delta_{33} = 77$, $\delta_{22} = 203$, and $\delta_{11} = 260$ ppm, an Nπ–H bond length of 1.06 Å, and Euler angles ($\alpha = 0^{\circ}$ and $\beta = 5^{\circ}$).

The appearance of the spectra highly depends on the relative orientation of the two tensors. 3D experiments constituting the SEMA sequence[27] have been used to determine the ^{1}H CSA, ^{15}N CSA, and ^{1}H–^{15}N dipolar coupling tensors in the molecular frame.[61,62] Interestingly, a 2D SLF spectrum correlating the ^{1}H CSA and the ^{1}H–^{15}N dipolar coupling can be obtained from the 3D spectrum which is otherwise difficult to obtain as the detection of protons has always proven to be difficult in solids. For the first time, this enabled the determination of amide-^{1}H CSA tensor from polycrystalline samples.[61] Further details on the measurement of CSA tensors and their importances can be found in the published papers.[27,50,61,62]

4.1.2. *PISEMA of slow-spinning powder samples*

Application of the PISEMA sequence was also extended beyond static samples. A two-dimensional experiment, PISEMAMAS, was successfully demonstrated on powder samples of peptides under a slow-spinning MAS condition.[46] During the SEMA sequence, the *I*–S dipolar coupling Hamiltonian does not commute as the sample rotates and therefore the line broadening due to this interaction is *homogeneous* (no *hole-burning* is possible[3]) like the broadening due to homonuclear dipolar coupling; it should be noted that under very high spinning speeds, the *I*–*I* dipolar couplings can

be averaged by MAS. This is unlike the *inhomogeneous* (*hole-burning* is possible[3]) line broadening, and high-resolution spinning sidebands, observed in the ω_1 dimension of other SLF experiments under MAS, where at any time of the sample rotation the *I–S* dipolar coupling Hamiltonian mutually commutes. It would be interesting to investigate the dipolar coupling line shapes obtained from SEMA type experiments under MAS for various spinning speeds.

A 3D experiment (PISEMAMAT)[50] was designed to take advantage of high-resolution dipolar couplings from PISEMA[46] and the capability to resolve isotropic chemical shift frequencies from magic angle turning (MAT).[72] The combined 2D PISEMA and 2D MAT pulse sequence (3D PISEMAMAT)[50] provided two-dimensional anisotropic chemical shift/heteronuclear dipolar coupling spectra for each resolved isotropic resonance in a powder sample. For example, it has been shown that the 3D pulse sequence correlates the heteronuclear ^{1}H–^{15}N dipolar coupling and isotropic and anisotropic ^{15}N chemical shifts interactions, and enables both the magnitudes and orientations of the principal elements of the ^{15}N CSA tensor to be determined relative to the ^{1}H–^{15}N dipolar coupling interaction, and thereby the orientations of the individual chemical shift tensors in the molecular frame can be measured. The use of this 3D pulse sequence eliminates the need for site-specific labeling to observe PISEMA powder patterns as long as the ^{15}N isotropic chemical shifts are resolved in the MAS spectrum of the sample.[50]

4.1.3. *PISEMA of fast-spinning powder samples*

In order to increase the sensitivity and resolution, and to reduce the experimental time, of PISEMAMAS technique, it is essential to perform the experiment with fast spinning speeds. While the PISEMA pulse sequence has been successfully used under slow spinning conditions, unfortunately, it cannot be used at high spinning speeds as the heteronuclear dipolar couplings are suppressed. However, changing the *S*-spin-lock rf field strength (in SEMA) to satisfy the Hartmann-Hahn condition, $B_{\mathrm{eff},I} = B_{\mathrm{eff},S} \pm n\nu_{\mathrm{rot}}$ with $n = \pm 1$, can recover the *I–S* dipolar coupling under fast MAS. In addition, the phase alternation and the amplitude modulation (toggling between $n = 1$ and $n = -1$ spinning sidebands) of the *S*-spin-lock pulses must be synchronized to avoid the cancellation of recoupled *I–S* dipolar coupling as shown in Fig. 7. The recovered *I–S* dipolar coupling under this modified SEMA sequence is given by $D_{IS}\cos\theta_m$, while the original PISEMA provides $2D_{IS}\sin\theta_m$ from static or slow spinning samples. Our experimental results on powder samples of peptides demonstrate that this modified PISEMA pulse sequence is efficient in suppressing dipolar couplings among protons and also provide high resolution spectra lines (unpublished results).

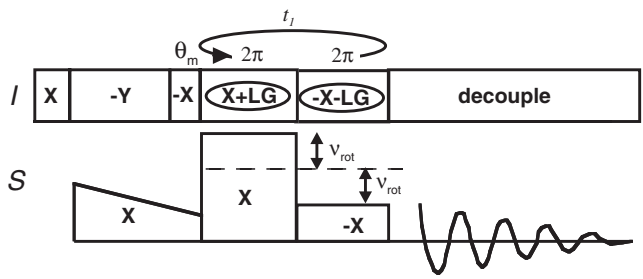

Fig. 7. A PISEMA pulse sequence for studies under a fast magic angle spinning condition. The modified SEMA pulse sequence in the t_1 period recovers *I*–*S* dipolar couplings under MAS. Unlike other SLF pulse sequences, this pulse sequence does not require the synchronization of the t_1 period with the spinning speed of the rotor.

4.2. 3D experiment on static samples

As mentioned above, multi-dimensional NMR experiments can significantly improve resolution even in solid-state by spreading resonances along multiple frequency axes, and by segregating the spectral parameters associated with each of the operative spin interactions by placing them along a unique frequency axis. Therefore, the SEMA sequence was incorporated into three- or four-dimensional experiments to achieve higher spectral resolution, separation, and correlation of spin parameters.[27–31] A three-dimensional experiment designed from 2D PISEMA and 2D HETCOR pulse sequences, which separates and correlates the chemical shifts of *I* and *S* nuclei and *I*–*S* dipole–dipole interactions, was reported for high-resolution studies on solids.[27] In this 3D sequence, during t_1, *I*–*I* dipolar couplings are suppressed by the FFLG sequence while *S* spins are continuously irradiated to remove the *I*–*S* dipolar coupling, leaving the *I*-spin magnetization to evolve under the sole influence of its chemical shift that is scaled by 0.58. During the period t_2, like in PISEMA, the SEMA sequence suppresses the *I*–*I* dipolar couplings and chemical shifts of *I* and *S* nuclei, while the in-phase coherence transfer between *I* and *S* spins are still in effect, which is displayed as *I*–*S* dipolar couplings in the 3D spectrum.[27] Finally, high-resolution chemical shifts of *S* nuclei are recorded during acquisition in the t_3 period.

The efficiency of the 3D pulse sequence has been successfully examined on polycrystalline and single crystal samples of peptides.[27] The powder pattern obtained from a polycrystalline sample comprises all frequencies available to the ^{1}H chemical shift, ^{1}H–^{15}N dipolar coupling, and ^{15}N chemical shift interactions with the amide group of the peptide, while the single crystal sample gave multiple resonance peaks each with the three frequencies that fall within the ranges observed in the 3D powder pattern. The 3D powder spectrum of an amide site showed a low-intensity 'hole', which was

rationalized as a consequence of none of the principal elements of the CSA tensor being collinear with the heteronuclear dipolar coupling vector.[61] The experimental ^{15}N chemical shift/^{1}H–^{15}N dipolar coupling, ^{1}H chemical shift/^{15}N chemical shift, and ^{1}H chemical shift/^{1}H–^{15}N dipolar coupling 2D spectra were simulated, and the principal values of the chemical shift tensors were measured, and the orientations of both ^{1}H and ^{15}N CSA tensors relative to the N–H bond vector were also determined. The 3D experiment was also used to obtain the magnitudes and orientations of the principal elements of ^{1}H and ^{15}N CSA tensors in the side chains of tryptophan and histidine from polycrystalline samples.[62] There are no low intensity 'holes' in the 3D spectra for these systems as the ^{1}H and ^{15}N chemical shift tensors are collinear with the N–H bond in both of these aromatic rings.

4.3. PISEMA of aligned molecules

Unlike polycrystalline or amorphous solids, oriented systems (such as liquid crystal, single crystal, and magnetically or mechanically aligned molecules) provide high-resolution spectral lines as a result of the orientational dependence of an anisotropic spin interaction.[8,10,54] Because of the high resolution, uniaxially aligned lipid bilayers have been used as model systems to study biological cell membranes. NMR parameters, particularly chemical shifts and dipolar couplings, have been routinely measured using 2D SLF experiments on oriented lipid bilayer samples in order to determine the secondary structure, dynamics, and topology of membrane-associated peptides and proteins.[5,10,54] For a membrane protein that is immobilized in phospholipid bilayers, the analysis of orientational dependence of spectral frequencies is particularly straight forward, as shown in the case of bacteriaphage fd coat protein in which each amide N–H spin pair has a single orientation and a maximum order parameter of 1.[53] In samples with axial rotational diffusion faster than the NMR time scale, an anisotropic interaction is motionally averaged to an isotropic value, as in the N- and C-terminal residues of a membrane-bound peptide aligned in oriented bilayers. If the motional averaging falls within the NMR time scale, or if multiple conformations are present, the linewidths will be substantially broadened, and the orientation of the site cannot be precisely assessed. However, crucial information about the secondary structure and dynamics can be obtained for sites with limited motional averaging due to either local segmental or global motions. In solid-state NMR of membrane associated proteins or peptides uniaxially oriented in lipid bilayers, three-dimensional structural coordinates are directly determined from the NMR data (for example, the orientational dependence of ^{15}N chemical shifts and ^{1}H–^{15}N dipolar couplings obtained from PISEMA experiments) relative to the lipid bilayer normal, which is set parallel to $\vec{B}_0$. The structure of a membrane peptide from solid-state NMR

data should be viewed as a supramolecular assembly with the peptide fixed within the lipid bilayer. As a result, the structure itself inherently contains information on the dynamics and the orientation of the peptide. Since a membrane protein has a unique orientation relative to the membrane normal, solid-state NMR experimental studies on uniaxially oriented bilayers, which preserve the directionality of the protein structure, are well suited for the structure determination of membrane proteins.

4.3.1. *CP on aligned samples can be tricky*

Enhanced sensitivity and lower rf power requirements (on the ^{1}H channel) of PISEMA experiment are highly suitable for such studies on hydrated lipid bilayer samples compared to other SLF methods. Experimental procedures outlined in Section 3 are strongly recommended to set-up the 2D PISEMA experiments on lipid bilayers. In addition, since the sensitivity of this experiment highly depends on the efficiency of the preparation period (or CP[14–18]) of the pulse sequence, it is important to optimize the contact time of CP to maximize the *S*-spin magnetization transferred from protons. The CP efficiency depends on the strength of the *I–S* and *I–I* dipolar couplings, which are determined by the solid-nature of the sample.[18] Since hydrated bilayers are semi(or non-rigid)-solids, the presence of molecular motions (in unfrozen solids) partially averages the dipolar couplings. As a result, unlike in rigid solids, the magnitude of the *S*-spin magnetization oscillates as a function of the contact time, due to the *I–S* dipolar coupling, and it may take unusually long time to reach the steady state. Therefore, care must be taken in setting-up the contact time of CP. For example, in most membrane bilayers containing proteins, a contact time of < 100 μs is sufficient to obtain a maximum signal intensity than a long mixing time ($\sim$ milliseconds).[18,53] It is also better to avoid a long mixing time as it increases the heat dissipation in the sample. On the other hand, when no information on the heteronuclear dipolar couplings of the sample is known, a long contact time might guarantee at least a moderate signal intensity where as a short contact time could fall in the trough of the dipolar oscillations resulting in poor signal intensity. Based on our experiments on mechanically aligned bilayers containing ^{15}N-labeled peptides, ramp-CP provided was found to be better than CPMOIST[16] and standard CP[14] sequences.

4.3.2. *Higher-resolution through higher-dimension*

Multi-dimensional experiments based on the PISEMA sequence also dramatically enhanced the resolution of peaks and enabled the measurement of multiple NMR parameters.[52,53] These parameters are orientation dependent and have been shown to be useful in determining the orientation of the peptide plane with respect to $\vec{B}_0$. Chemical shift and dipolar coupling

tensors determined from 2D and 3D PISEMA experiments[46,50,61,62] on multilamellar vesicles or powder samples of peptides were used to interpret the spectra of aligned samples. For example, phospholipid bilayers containing an antimicrobial peptide, magainin-2 with ^{15}N labels at Phe_{16} and Val_{17}, was prepared on glass plates and mechanically aligned with the bilayer normal parallel to the external magnetic field. Using a flat-coil probe, the ^{1}H chemical shift, ^{1}H–^{15}N dipolar coupling, and ^{15}N chemical shift parameters were accurately measured from a single 3D experiment at room temperature.[51] The spectral parameters were subsequently analyzed using the graphical restriction plot method,[54] which generated four possible peptide plane orientations with respect to $\vec{B}_0$. The 16 possible combinations of the Phe_{16} and Val_{17} peptide planes were further reduced to two low energy helical structures with dihedral angles (ϕ, ψ) of (-130°, -73°) and (-147°, -43°).[51] This application demonstrated that the direct measurement of three spectral parameters for each amide nitrogen site is sufficient to fully determine the orientation of a peptide plane in an oriented bilayer sample.

4.3.3. *Resonance assignment is the bottleneck*

The high-resolution and the high scaling factor of 2D PISEMA, for the first time, enabled the use of the dipolar dimension to resolve resonances from non-selectively or uniformly labeled proteins.[52,53] Three-Dimensional experiments[27] were used to enhance the resolution of resonances from uniformly ^{15}N-labeled peptides and proteins embedded in lipid bilayers. This was successfully demonstrated on aligned samples containing uniformly ^{15}N-labeled membrane-associated peptides and proteins.[52,53] Two-dimensional PISEMA spectra of some of these systems showed limited resolution due to a small frequency dispersion of resonances from α-helices oriented on the surface of the bilayer in both ^{15}N chemical shift and ^{1}H–^{15}N dipolar coupling dimensions.[53] However, when an additional ^{1}H chemical shift dimension was invoked, the 3D ^{1}H chemical shift/^{1}H–^{15}N dipolar coupling/^{15}N chemical shift spectra of these systems considerably increased the resolution of peaks.[53]

Even though accurate measurement of structural parameters was possible by the use of aligned samples and PISEMA experiments, the unavailability of a resonance assignment protocol hampered the applications of solid-state NMR spectroscopy to study uniformly labeled proteins. Structure determination mainly depended on synthetic peptides labeled with ^{15}N and/or ^{13}C isotope at a single-site.[5] While this procedure is simple and the data is straight-forward to interpret, it is extremely slow, expensive, unexciting, and limited to small synthetic peptides. This limit was removed by the introduction of SEMA based 3D and 4D experiments. Initial demonstration of resonance assignment using the 3D experiment was performed on a uniformly labeled bacteriophage fd coat protein in aligned samples. There are two Leu residues in the protein and the 3D experiment enabled the identification and

assignment of these residues in magnetically aligned sample.[52] For example, the two Leu residues, due to their distinct peptide plane orientations, display completely different resonance positions in all three spectral frequencies of the 3D spectrum. In a subsequent study, resonances from a uniformly ^{15}N-labeled fd coat protein orientated in phospholipid bilayers have been completely resolved using a SEMA related 3D technique.[53] Leu_{41} is located in the hydrophobic transmembrane helix of the protein, nearly parallel to B_0, and therefore the peak is located in the downfield region with a large ^{1}H–^{15}N dipolar splitting of the 2D PISEMA spectrum. On the other hand, Leu_{14} is located in the amphipathic in-plane helix of the protein, nearly perpendicular to B_0, and therefore the peak is located in the upfield region with a small ^{1}H–^{15}N dipolar splitting of the 2D PISEMA spectrum.

The capability to resolve resonances from a uniformly labeled protein using PISEMA related experiments necessitated the systematic development of new pulse sequences for resonance assignment. Subsequently, multi-dimensional experiments based on SEMA were developed to assign the resolved resonances from uniformly labeled proteins.[28–31] The general resonance assignment strategies based on the longitudinal exchange of magnetization among either amide-^{15}N or amide-^{1}H nuclei have been successfully demonstrated on several systems. In a 3D method called PSEUDO (proton spin exchange unraveled by dilute-spin observation),[29] the ^{1}H chemical shift evolution periods (t_1 and t_2) are separated by the ^{1}H homonuclear spin exchange mixing time (t_m). The SEMA sequence then transfers the ^{1}H magnetization to directly bonded ^{15}N spins through the ^{1}H–^{15}N dipolar coupling, which enables the detection of ^{15}N signals during the acquisition time, t_3. This 3D PSEUDO pulse sequence has been successfully demonstrated on single crystals of peptides.[29] A 4D experiment was also developed to correlate the ^{1}H chemical shift, ^{1}H–^{15}N dipolar coupling, and the ^{15}N chemical shift with the exchange of ^{15}N magnetization.[28] The 4D pulse sequence offers many benefits, including the high spectral resolution, various ways to sort, resolve, and measure spectral parameters, and to assign resonances among nearby nuclear sites through dilute *S*-spin exchange. These resonance assignment experiments have been used to study peptides embedded in lipid bilayers. The required mixing time for these experiments depends on the magnitude of the dipole–dipole interaction and it is much longer for ^{15}N (few seconds) than for ^{1}H (fraction of a millisecond).

The methodology discussed above has been used in the resonance assignment and to determine the backbone conformation of a uniformly ^{15}N-labeled M2 transmembrane peptide of nicotinic acetylcholine receptor (AChR), one of the major excitatory neurotransmitters in the brain.[73] By comparing with spectra from selectively and specifically ^{15}N-labeled M2 peptides and using the sequential (i to i+1) cross peaks in the spin exchange spectra, all the ^{15}N resonances from the M2 peptide were assigned,

and the backbone connectivity was traced. The ^{15}N chemical shift and ^{1}H–^{15}N dipolar coupling frequencies measured from 2D and 3D spectra provided orientational constraints that were used to determine the backbone conformation of the AChR M2 peptide. The structure of the peptide in lipid bilayers is similar to the structure independently determined using solution NMR experiments on detergent micelles.[74] However, only solid-state NMR experiments provided the global orientation of the M2 peptide in the membrane, which is a crucial in determining the architecture of the ion channel. Using solid-state NMR orientational constraints, the structure of the AChR M2 peptide was determined to be a transmembrane, amphipathic α-helix with its long helical axis tilted 12° away from the lipid bilayer normal.[74] Besides the helix tilt information, the helix rotation information of the peptide could also be derived from solid-state NMR data.

The long ^{15}N mixing time (close to T_1) reduces the sensitivity of the multidimensional experiment due to T_1 relaxation.[28] Flipping the ^{1}H magnetization to the z-axis before the long ^{15}N spin-exchange time allowed the recovery of ^{1}H magnetization before the next scan without the need for a recycle delay of the experiment and substantially shortened the experimental time.[73] On the other hand, in the 3D PSEUDO experiment, reducing the mixing time can overcome the loss of ^{1}H magnetization due to dipolar couplings with neighbouring protons in the mixing period, whereas the selective transfer of amide-^{1}H magnetization to amide-^{15}N reduces the sensitivity.[40] These complications mandate rapid development of ^{1}H-detected solid-state NMR experiments, which are discussed in Section 5, and the use of higher magnetic fields. Meanwhile, wheel like patterns observed in PISEMA and HETCOR spectra of uniformly labeled helical proteins can be used to qualitatively determine the secondary structure and topology even without completing the assignment of resonances.[32,33]

Triple-resonance ($^{1}H/^{15}N/^{13}C$) experiments using PISEMA were also developed for the structural studies of aligned, uniformly ^{15}N- and ^{13}C-labeled peptides.[30,31] Using homonuclear and heteronuclear decoupling techniques, 2D $^{13}C/^{15}N$ chemical shift correlation spectra have been obtained for sequential assignment of resonances from uniformly labeled peptides.[31] Chemical shifts of amide-^{1}H, amide-^{15}N, $^{13}C'$, and $^{13}C_{\alpha}$, and heteronuclear (^{1}H–^{15}N, ^{1}H–$^{13}C_{\alpha}$, $^{13}C_{\alpha}$–^{15}N, $^{13}C'$–^{15}N) dipolar couplings measured from these experiments were used as orientational constraints to accurately determine the peptide plane conformation. Based on the experimental results, it was suggested that a 3D triple resonance experiment could resolve signal from more than 100 residues.[31] However, the application of the triple-resonance experiment depends on the efficiency of $^{13}C/^{15}N$ cross polarization as the sequential assignment requires cross-peaks that connect amide-^{15}N and $^{13}C'$. Therefore, lack of broadband $^{13}C/^{15}N$ cross polarization sequences to cover the large span of $^{13}C'$CSA could limit the applications of this technique.

4.4. Structural images in the PISEMA spectrum

Structure determination of proteins using solid-state NMR spectroscopy involves several steps: (a) obtaining high resolution spectra to resolve resonances from individual sites; (b) resonance assignment; (c) measurement of spectral parameters for all sites of the protein; (d) conversion of NMR parameters to structural constraints, and orientations of peptide planes for aligned samples; (e) linkage of individual peptide planes to determine the backbone conformation of an aligned protein; (f) molecular dynamics simulations using NMR constraints to obtain the three-dimensional structure. As discussed in the previous section, resonance assignment is the most difficult step in the structural studies of membrane proteins using solid-state NMR spectroscopy. This difficulty in aligned solids is mainly because, unlike in liquid-state NMR or MAS studies, there is no direct correlation between the measured value of an NMR parameter (for example, chemical shift) and the amino acid type or the secondary structure. On the other hand, since a measured spectral parameter directly depends on the projection of a chemical bond (or a chemical group or a segment of the protein) on the reference axis, a correlation between the spectral parameters and the topology of the protein can be established. For example, if the lipid bilayer normal is parallel to $\vec{B}_0$, the chemical shift frequency of amide-^{15}N nuclei from a transmembrane helix fall in the low field region while the nuclei from a helix located on the surface of the membrane fall in the high-field region. Therefore, resonances from differently oriented segments of a protein can be isolated and assigned. In addition, an image of the segment can also be obtained without having to assign the individual resonances in a multi-dimensional solid-state NMR experiment as discussed below.

4.4.1. *PISEMA images of aligned peptides*

The two-dimensional ^{1}H–^{15}N dipolar coupling/^{15}N chemical shift PISEMA spectrum of uniformly ^{15}N-labeled α-helical peptides in uniaxially oriented lipid bilayer shows a characteristic 'wheel-like' pattern of resonances (or images) reflecting helical wheel projections of residues from both transmembrane and in-plane helices.[32,33] This intrinsic beauty of the 2D PISEMA spectrum provides indices of secondary structure and topology of membrane peptides embedded in lipid bilayers. Such pattern has been referred to as PISA (polarity index slant angle) wheel.[32,33] PISA wheels arise from the facts that the orientations of chemical shift and dipolar interaction tensors are different from each other and the tensor elements are not aligned parallel to the helical axis. The center of the PISA wheel uniquely reflects the specific tilt or slant angle, τ, of the helical axis with respect to the bilayer normal. PISA wheel patterns can be obtained by calculating ^{15}N chemical shift and the ^{1}H–^{15}N dipolar coupling values for different tilt angles of a helix.

The chemical shift of *S*-spin, δ_S, and the *I*–*S* dipolar coupling, D_{IS}, tensors in the laboratory frame (where $\vec{B}_0$ is along the z-axis) are defined by the following equations.[33]

$$\delta_I = \delta_{33}x^2 + \delta_{22}y^2 + \delta_{11}z^2 \tag{6a}$$

$$D_{IS} = \frac{D_{||}}{2}\left[3(x\cos\alpha\sin\beta + y\sin\alpha\sin\beta + z\cos\beta)^2 - 1\right] \tag{6b}$$

where δ_{ii} are the principal components of the CSA tensor (defined as; $\delta_{11} \geq \delta_{22} \geq \delta_{33}$; δ_{33} is the most shielding and δ_{11} is the least shielding elements), and $D_{||}$ is the value of D_{IS} when the rotation axis of the dipolar coupling tensor is collinear with $\vec{B}_0$. The polar angles (α, β) describing the rotation axis of dipolar coupling tensor in the CSA principal axis system give the relative orientations of the two tensors; β is the angle between the *I*–*S* bond and δ_{11}, and α is the angle between δ_{33} axis and the projection of the *I*–*S* bond on the δ_{22}–δ_{33} plane. Since an ideal α-helical structure ($\phi = -65^\circ$ and $\psi = -40^\circ$) is a repeat of a single peptide plane, the following standard parameters can be used in the calculations: $r_{N\text{–}C_\alpha} = 1.458$ Å, $r_{C_\alpha\text{–}C'} = 1.525$ Å, $r_{C'\text{–}N} = 1.329$ Å, $r_{C'\text{–}O} = 1.231$ Å, $r_{N\text{–}H} = 1.07$ Å, $\angle(C'\text{–}N\text{–}C_\alpha) = 121.7^\circ$, $\angle(N\text{–}C_\alpha\text{–}C') = 111.2^\circ$, $\angle(C_\alpha\text{–}C'\text{–}N) = 116.2^\circ$, $\angle(N\text{–}C'\text{–}O) = 123.0^\circ$, and $\angle(C'\text{–}N\text{–}H) = 123^\circ$; and $\alpha = 0^\circ$ and $\beta = 17^\circ$ for the relative orientation of the dipolar and chemical shift tensors.[55,62,63] The coordinates of the N–H bond can be derived as

$$\begin{pmatrix} x \\ y \\ z \end{pmatrix} = \begin{pmatrix} -0.828 & 0.558 & -0.047 \\ 0.554 & 0.803 & -0.220 \\ -0.088 & -0.206 & -0.975 \end{pmatrix} \begin{pmatrix} \cos\rho\sin\tau \\ \sin\rho\sin\tau \\ \cos\tau \end{pmatrix} \tag{7}$$

Using Eq. (7), Eq. (6) can be written as

$$\begin{aligned} \delta_S(\rho,\tau) = {} & \delta_{11}(-0.088\cos\rho\sin\tau + 0.206\sin\rho\sin\tau - 0.975\cos\tau)^2 \\ & + \delta_{22}(0.554\cos\rho\sin\tau + 0.803\sin\rho\sin\tau - 0.220\cos\tau)^2 \\ & + \delta_{33}(-0.828\cos\rho\sin\tau + 0.558\sin\rho\sin\tau - 0.047\cos\tau)^2 \end{aligned} \tag{8a}$$

$$D_{IS}(\rho,\tau) = \frac{D_{||}}{2}\left[3(-0.326\cos\rho\sin\tau - 0.034\sin\rho\sin\tau - 0.946\cos\tau)^2 - 1\right] \tag{8b}$$

Thus, for a given tilt angle τ, the PISA wheel can be generated by rotating the helix about its axis by a rotation angle ρ (from 0 to 360°), while calculating the dipolar coupling and the chemical shift parameters. To examine the behavior of the PISA wheel as the helix tilt changes, the centre of the wheel is

defined as the average (or the isotropic) value of the chemical shift, δ_{iso}, and dipolar tensor, D_{iso}, about the helix axis

$$\delta_{iso}(\tau) = \frac{1}{2\pi}\int_0^{2\pi} \delta(\rho,\tau)\,d\rho = (0.500\delta_{33} + 0.476\delta_{22})\sin^2\tau + 0.950\delta_{11}\cos^2\tau \quad (9a)$$

$$D_{iso}(\tau) = \frac{1}{2\pi}\int_0^{2\pi} D(\rho,\tau)\,d\rho = D_{||}\left(0.081\sin^2\tau + 1.34\cos^2\tau - 0.500\right) \quad (9b)$$

Figure 8 depicts PISA wheels in which the helix tilt angle τ varies from 15 to 90°. The magnitudes of the principal components of the *S*-spin CSA tensor ($\delta_{33} = 64$, $\delta_{22} = 77$, and $\delta_{11} = 217$ ppm) and the angles defining the relative orientations of the dipolar and chemical shift tensors ($\alpha = 0°$ and $\beta = 17°$) were used in the simulations of PISA wheels presented in Fig. 8. The centers of the wheels as a function of helix tilt angle from both the peaks of the dipolar-coupling doublet are also shown as dashed lines in Fig. 8. The centers of the chemical shift and dipolar coupling tensors intersect at the isotropic values of the ^{15}N chemical shift (119.3 ppm) and the ^{1}H–^{15}N dipolar coupling (0 Hz). The PISA wheel patterns can also be used to determine β-strand structures in lipid bilayers as the loop-like shapes of these β-strand resonances are very different from the wheel-like patterns of α-helices.[75] It is clear from the

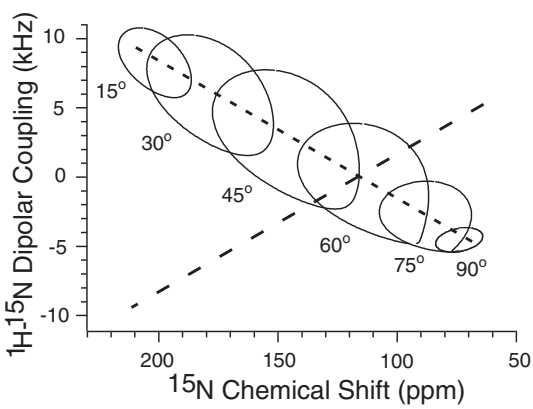

Fig. 8. PISA wheel patterns for the helix tilt (τ) varying from 15 to 90° simulated using Eq. (8) in the text. The chemical shift tensor values of $\delta_{33} = 64$, $\delta_{22} = 77$, and $\delta_{11} = 217$ ppm, an N–H bond length of 1.07 Å, and the relative orientations of the dipolar and chemical shift tensors of $\alpha = 0°$, $\beta = 17°$ were used in the simulations. Variation of the PISA wheel with respect to the tilt angle of the helix is shown for one peak of the dipolar-coupling doublet as the spectrum is symmetric with respect to the zero frequency. The centers (shown in dashed lines) of the wheels as a function of the helix tilt angle for both dipolar transitions are linear and intersect at the isotropic ^{15}N chemical shift frequency (119.3 ppm) and 0 Hz ^{1}H–^{15}N dipolar coupling [Eq. (9)].

simulated spectra (Fig. 8) that the patterns in the 2D PISEMA spectrum are extremely sensitive to the tilt, rotation, and twist of α-helices or β-strands of proteins embedded in the cell membrane.

PISA wheel patterns can also be easily generated using the simulation program SIMPSON[45] together with the visualization program SIMMOL[76] (Fig. 9); the combination of SIMPSON and SIMMOL programs has been used to simulate solid-state NMR experiments.[77] First an ideal α-helical peptide ($\phi = -65°$, $\psi = -40°$) with different tilt angles is built using the SIMMOL program, and then the PISA wheel patterns are calculated using SIMPSON. The simulated PISA wheel patterns are shown in Fig. 9(A). Similarly, an ideal β-strand peptide ($\phi = -135°$, $\psi = 140°$ or $\phi = -140°$, $\psi = 135°$) can also be simulated and the results are shown in Figs. 9(B) and (C). The resolution of resonance peaks in these PISEMA spectra depends on the tilt of the α-helix or the β-strand as the tilt introduces variations in the orientations of the NH vectors at different amide sites relative to $\vec{B}_0$. For orientations closer to $\vec{B}_0$ (or 0–10° tilts from the bilayer normal), all peaks in the 2D spectra are not well resolved and located in the low field region (near the δ_{11} value of ^{15}N CSA) with a large dipolar coupling value (~10 kHz). As the tilt angle increases the resolution of resonances increases. A tilt angle of >45° for an α-helix or >35° for a β-strand, orientations of some amide NH bonds are close to the magic angle (54.7°) with respect to $\vec{B}_0$ and therefore the peaks are located near the isotropic values of the tensors. The sign inversion of the ^{1}H–^{15}N dipolar coupling for NH vectors oriented at angles >54.7° results in the reflection of all or a portion of the PISEMA spectrum through the 0-kHz axis. Therefore, the pattern of resonances in the PISEMA spectrum can be used to qualitatively predict the types of secondary structures and their tilts for a membrane protein with respect to the bilayer normal. As an example, the 2D PISEMA spectrum of uniaxially aligned bilayers containing fd bacteriophage pVIII coat protein is shown in Fig. 10(A).[78] The spectrum shows two PISA wheels, corresponding to a transmembrane helix with a tilt angle of 30° and an in-plane helix with a tilt angle of 87° (Fig. 10(B–D)).

In general, 2D correlations of any two distinct, non-collinear, anisotropic spin interactions provide molecular images, like PISA wheels in the PISEMA spectrum. For proteins, spectra obtained from suitable combinations of CSA tensors of amide-^{1}H, amide-^{15}N, carbonyl carbon (^{13}C′) and $^{13}C_{\alpha}$, and heteronuclear dipolar couplings (such as ^{1}H–^{15}N, ^{1}H–$^{13}C_{\alpha}$, and ^{13}C′–^{15}N) could be used. For example, the correlation of the chemical shifts of amide-^{1}H and amide-^{15}N has been shown to provide pattern of resonances that depend on the secondary structure and topology of the peptide.[75] Some more examples of such correlation spectra are $^{13}C'_i$–$^{15}N_{i+1}$ dipolar coupling and $^{13}C'_i$ chemical shift (Fig. 11) and $^{1}H_{\alpha}$–$^{13}C_{\alpha}$ dipolar coupling and $^{13}C_{\alpha}$ chemical shift (Fig. 12) as shown for an ideal α-helix. However, small spans of the ^{13}C–^{15}N dipolar coupling (~1 kHz) and the $^{13}C_{\alpha}$ CSA (~30 ppm) tensors

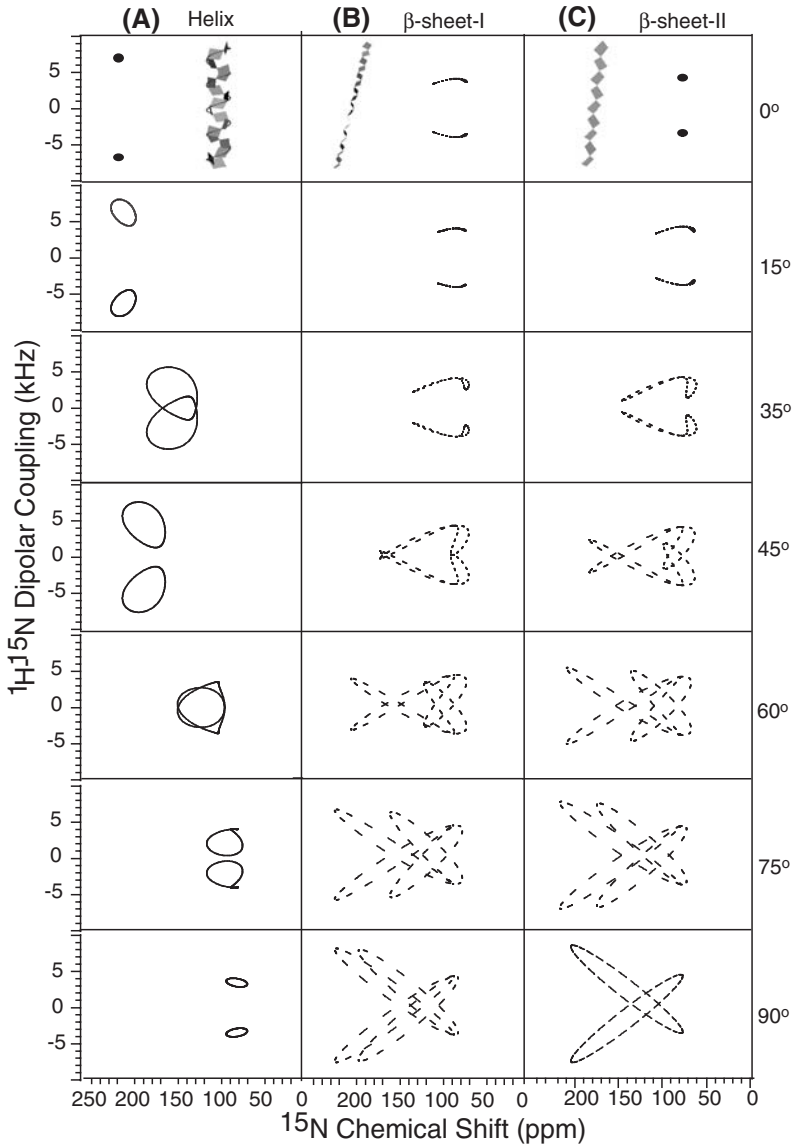

Fig. 9. Two-dimensional PISEMA spectra of a SIMMOL-generated 300-residue polyalanine containing PISA wheels simulated using the SIMPSON program: (A) an ideal α-helical peptide ($\phi = -65°$, $\psi = -40°$), (B) an ideal β-strand-I peptide ($\phi = -135°$, $\psi = 140°$), and (C) another ideal β-strand-II peptide ($\phi = -140°$, $\psi = 135°$) at different tilt angles. The spectra correlate the ^{15}N chemical shift/^{1}H–^{15}N dipolar coupling frequencies of the amide-NH bond. The chemical shift tensor values of $\delta_{33} = 64$, $\delta_{22} = 77$, and $\delta_{11} = 217$ ppm, an N–H bond length of 1.07 Å, and the relative orientations of the dipolar and chemical shift tensors of $\alpha = 0°$, $\beta = 17°$ were used in the simulations.

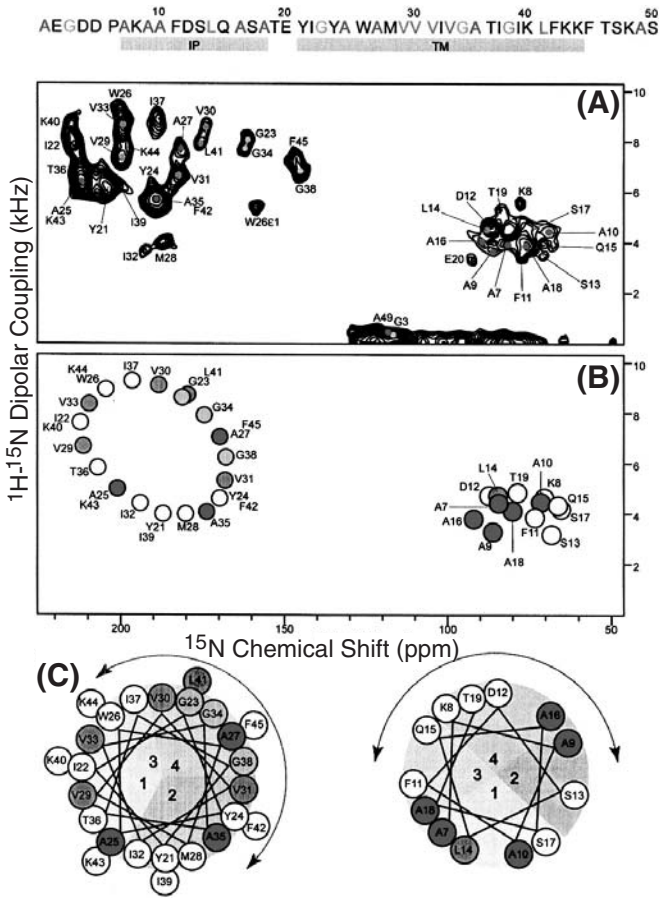

Fig. 10. (A) Two-dimensional experimental ^{15}N chemical shift/^{1}H–^{15}N dipolar coupling PISEMA spectrum of a uniformly ^{15}N-labeled fd coat protein in aligned lipid bilayers.[78] The amino acid sequence of the protein is shown at the top. The protein consists of two helices and the corresponding residues are indicated as IP (in-plane) and TM (transmembrane). (B) Pisa wheel PISEMA spectrum calculated from a protein model with the IP helix nearly parallel to the membrane surface (tilted by 87° from the bilayer normal or $\vec{B}_0$), and the TM helix crossing the membrane with a 30° tilt from the bilayer normal.[78] The PISA wheel (B) and helical wheel (C) rotations are set to match the resonances from Ala, Gly, Leu, and Val residues of the protein in the experimental PISEMA spectrum (A). (C) Helical wheel representations of the protein in-plane and transmembrane helices.[78] (D) The structure of the fd coat protein determined using solid-state NMR studies (PDB ID: 1MZT). (E) Simulated 2D PISEMA spectrum of the protein from its structure given in (D). PISA wheel patterns (similar to (B)) for ideal α-helices with tilt angles of 30° and 87° are also shown in (E).

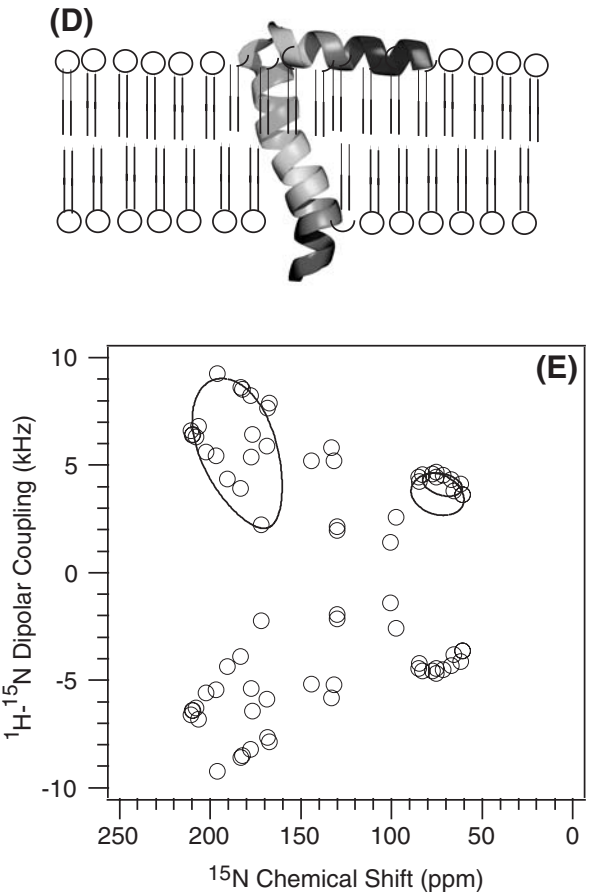

Fig. 10. Continued.

limit the applications of the related PISA wheel spectra. However, inclusion of these interactions to the conventional 2D ^{1}H–^{15}N dipolar coupling/^{15}N chemical shift PISEMA spectra would greatly increase the resolution, especially the ^{13}C′ spins which have a large CSA span.[66] In addition, a combination of PISEMA and HETCOR spectra of nuclei in the peptide plane will be powerful in obtaining high resolution structures of membrane proteins from uniaxially oriented samples.

4.4.2. *PISEMA images of membrane proteins*

While the PISA wheel patterns offer high throughput structure and topology for small helical proteins, extending the applications of PISEMA technique to analyze the structure of large membrane proteins will be of

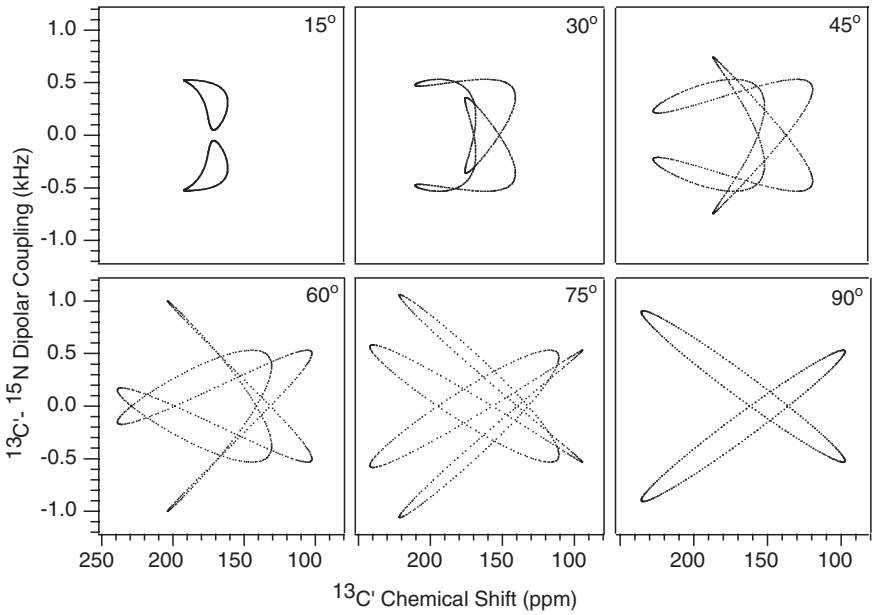

Fig. 11. Two-dimensional spectra correlating the $^{13}C'_i$–$^{15}N_{i+1}$ dipolar coupling and the $^{13}C'_i$ chemical shift interactions of an ideal α-helix with various tilt angles. The spectra were simulated using the following parameters: $\delta_{33} = 94$, $\delta_{22} = 173.8$, and $\delta_{11} = 242.2$ ppm, a C′–N bond length of 1.329 Å, and Euler angles ($\alpha = 90°$, $\beta = 43°$) that define the relative orientations of the dipolar and ^{13}C′chemical shift tensors; where δ_{11} lies in the peptide plane and makes 43° with respect to the C′–N bond vector and δ_{33} is perpendicular to the peptide plane.[66]

considerable interest in the field of structural genomics. In this context, to understand the applications and limitations of the 2D PISEMA technique, 2D PISEMA spectra of a few large membrane proteins were simulated and the results are discussed below. The selected examples represent typical folds of secondary structures of proteins observed in membranes: α-helical bundles and β-strand barrels. Most membrane-associated proteins adopt α-helical conformations as the backbone amides of these α-helices are all locally complemented by hydrogen bonds, so that non-polar side chains exclusively form the interface to the non-polar membrane interior. For membrane proteins comprised of β-strands, on the other hand, the backbone amide groups cannot be complemented by itself and therefore, a barrel of β-strand has to be formed so that all backbone amides are fully complemented by hydrogen bonds with its outer surface coated with non-polar side chains.[79]

The simulated 2D PISEMA spectra and crystal structures of KcsA (PDB ID: 1BL8)[80] and CLC chloride channels from *E. coli* (PDB ID: 1KPK)[81] are shown in Fig. 13. The molecules are oriented with the average orientation of

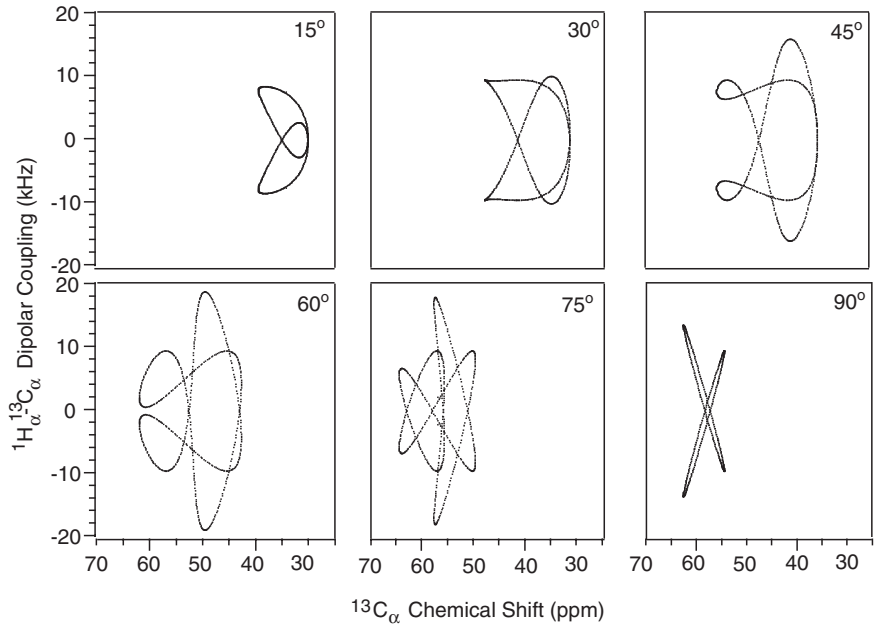

Fig. 12. Two-dimensional correlation of the $^{13}C_{\alpha}$–$^{1}H_{\alpha}$ dipolar coupling and the $^{13}C_{\alpha}$ chemical shift interaction for an ideal α-helix with various tilt angles. The spectra were simulated using $^{13}C_{\alpha}$ chemical shift tensor principal values of $\delta_{33} = 30$, $\delta_{22} = 55.7$, and $\delta_{11} = 64.3$ ppm, a C_{α}–H_{α} bond length of 1.09 Å, and the relative orientations of the dipolar and chemical shift tensors of $\alpha = 0°$, $\beta = 90°$.

all transmembrane α-helices along the *z*-axis, i.e., parallel to $\vec{B}_0$ (or the bilayer normal). The spectra correlate amide-^{15}N chemical shifts and ^{1}H–^{15}N dipolar couplings assuming that the protein is uniformly ^{15}N labeled and only the amide-^{15}N resonances are considered. A simple PISA wheel pattern of resonance in Fig. 13(B) suggests that the topology of most helices in the protein is similar, which can be seen from the crystal structure of the protein in Fig. 13(A). The absence of resonances in the high-field region of the PISEMA spectrum in Fig. 13(B) clearly suggests that there are no helices oriented on the bilayer surface (perpendicular to the bilayer normal). On the other hand, the PISEMA spectrum in Fig. 13(D) is more complicated as the resonances spread over the entire frequency ranges of CSA and dipolar coupling tensors (like in a powder pattern as shown in Fig. 6(A)). Nevertheless, the occurrence of most resonances in the low-field region of the spectrum suggests that the protein consists of transmembrane helices with various tilt angles.

Simulations of 2D PISEMA spectra can also be applied to more complex systems such as bacteriorhodopsin. It is a small integral membrane protein belonging to the family of rhodopsins and the simplest known light-driven

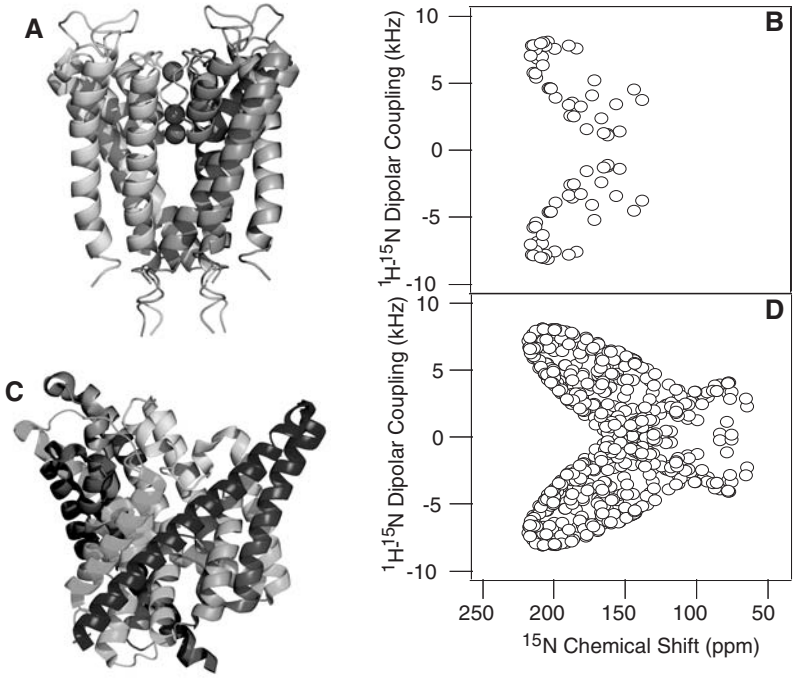

Fig. 13. Structures and simulated 2D ^{1}H–^{15}N dipolar coupling/^{15}N chemical shift PISEMA spectra of ion channel proteins: (A) crystal structure and (B) simulated PISEMA spectrum of a 10.2 kDa KcsA monomer (97 residues), a K^+ channel of *S. lividans* (PDB ID: 1BL8); (C) crystal structure and (D) simulated PISEMA spectrum of a monomeric 50.3 kDa (473 residues) CLC chloride channel from *E. coli* (PDB ID: 1KPK).

proton (H^+) pump. The simulated PISEMA spectrum for bacteriorhodopsin (PDB ID: 1C3W)[82] is shown in Fig. 14(B) along with its crystal structure in Fig. 14(A). The spectrum indicates that all helices in the protein are transmembrane, which is in complete agreement with the crystal structure of the protein (Fig. 14 (A)). These simulated spectra from helical transmembrane proteins are of high resolution although considerable overlap remains in the most crowded regions, which could be alleviated by an additional ^{1}H chemical shift dimension, or using amino acid specific labeling, as discussed previously. For example, there are 21 alanine residues in bacteriorhodopsin and the simulated PISEMA spectrum of Ala-only ^{15}N-labeled bacteriorhodopsin (Fig. 14(C)) shows well-resolved resonances.

Compared to the high occurrence of α-helical membrane proteins, β-barrel proteins are relatively rare due to the high entropy cost of translocating all β-strands that form the barrel into the membrane at once. At present,

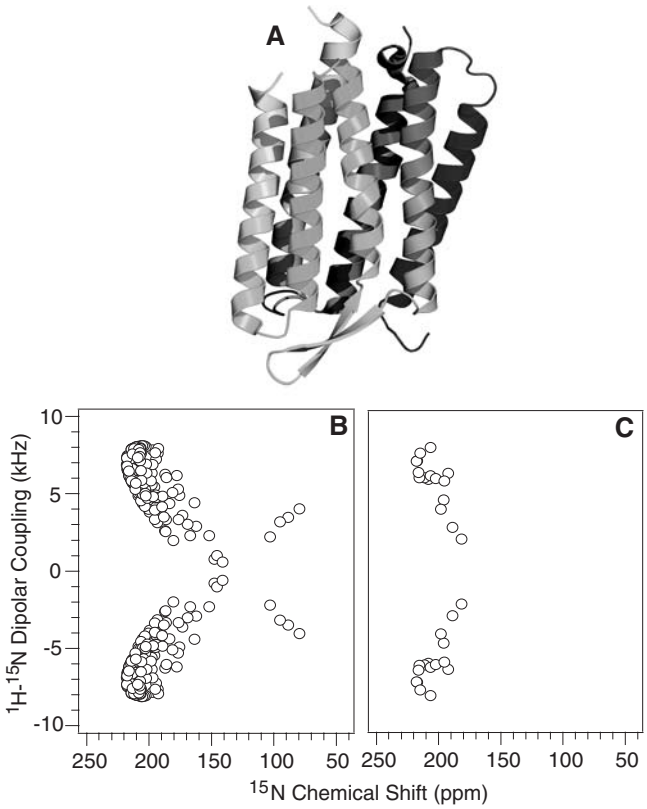

Fig. 14. (A) Crystal structure and simulated 2D ^{1}H–^{15}N dipolar coupling/^{15}N chemical shift PISEMA spectra [(B) all residues and (C) alanine residues only] of a 24.3 kDa (222 residues) bacteriorhodopsin (PDB ID: 1C3W).

transmembrane β-barrel proteins have been found exclusively in the outer membrane of gram-negative prokaryotes, including bacterial porins and outer membrane proteins *A* and *X*. The integral outer membrane protein *X* (Omp*X*) from *Escherichia coli* belongs to a family of highly conserved bacterial proteins that promote bacterial adhesion to and entry into mammalian cells. Moreover, these proteins have a role in the resistance against attack by the human complement system. Omp*X* is the smallest transmembrane β-barrel protein, consisting of an eight-stranded antiparallel all-next-neighbour β-barrel with a shear number $S = 8$ (the shear numbers S is derived by running from a given strand to the left along the hydrogen bonds once around the barrel and counting the residue number to the point of return to the same strand). The structure shows two girdles of aromatic amino acid residues and a ribbon of non-polar residues that attach to the membrane interior. The core of the barrel consists of an extended hydrogen-bonding

network of highly conserved residues (PDB ID: 1QJ8).[83] Omp*X* thus resembles an inverse micelle. The outer membrane protein *A* (Omp*A*) from *E. coli* is an abundant protein required for bacterial conjugation and for maintaining the structural stability of the outer membrane. It is also a receptor utilized by bacteriophage and colicines. The membrane domain of Omp*A* consists of an eight-stranded all-next-neighbour antiparallel β-barrel with short turns at the periplasmic barrel end and long flexible loops at the external end and shear number $S = 10$ (PDB ID: 1QJP).[84] Since both proteins share the same structural characteristics as eight-stranded antiparallel β-barrel, their corresponding simulated PISEMA patterns are similar (Fig. 15). The larger shear number *S* in Omp*A* results in a slightly larger barrel radius (7.9 vs. 7.2 Å) and tilt angle (43° vs. 37°) compared to Omp*X*.

As seen in the simulated spectra of the membrane proteins, the increase in the size of the protein as well as the inclusion of the different types of secondary structures complicates the interpretation of the 2D PISEMA spectra, which appear more like powder patterns. This is due to the fact

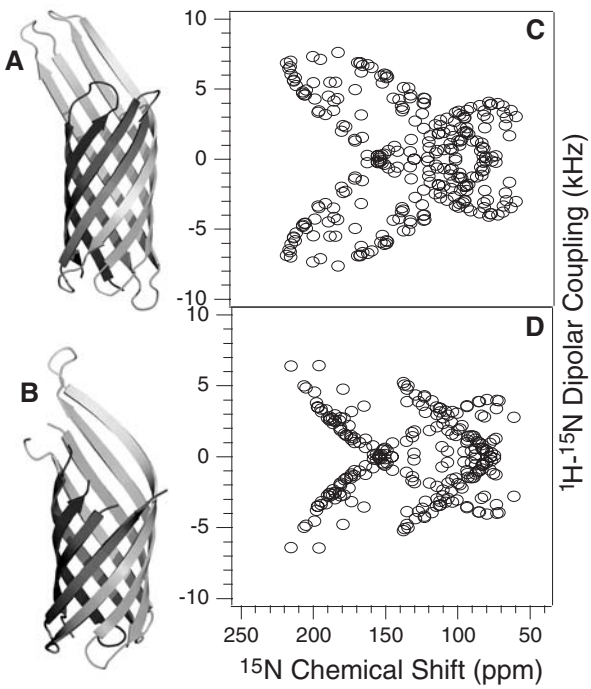

Fig. 15. Crystal structures and 2D ^{1}H–^{15}N dipolar coupling/^{15}N chemical shift PISEMA spectra of outer membrane proteins: (A) crystal structure and (B) simulated PISEMA spectrum of a 16.3 kDa (148 residues) outer membrane protein *X* (PDB ID: 1QJ8); (C) crystal structure and (D) simulated PISEMA spectrum of a 18.7 kDa (171 residues) outer membrane protein *A* (PDB ID: 1QJP).

that α-helices or β-strands found in these proteins are at different slant angles, and these conformations may be far from ideal structures (e.g., bending and kinking deviate from the ideal structure). In all simulated spectra, typical line widths observed in solid-state NMR studies on oriented samples were used. Any increase in line widths, due to any disorder on oriented bilayers or protein induced mosaic spread, would further reduce the resolution of spectral lines. Nevertheless, thoughtfully chosen labeling strategies (such as residue-specific labeling, segmental labeling, and selective unlabeling of amino acids) and utilizing higher dimensional solid-state NMR experiments could simplify the complexity of the 2D spectra. In addition, more experimental studies on peptides and small-size proteins would help to establish the spectroscopic aspects of this procedure.

In the simulations of PISEMA spectra of membrane proteins presented in this section, it was assumed that the proteins are immobile on solid-state NMR time scale for simplicity. However, peptides and proteins embedded in cell membranes are dynamics and therefore can have a range of orientations. As mentioned earlier, depending on the time scale of protein dynamics, span of anisotropic spin interactions of membrane proteins could be different from those observed for rigid solids. It has been shown that the librational motion of molecules in solids reduces the magnitude of anisotropic interaction measured using solid-state NMR experiments.[85] While this motional averaging is negligible in rigid solids, it is significant in semi-solids like hydrated bilayers. Therefore, the interpretation of a spectrum of an aligned sample based on tensor parameters determined from rigid samples could lead to some errors in the structural parameters.[55,56] In fact, variations of tilt and rotation of helices and librational motions of peptide planes have been observed experimentally.[86] Therefore, an experimental 2D PISEMA spectrum observed for a membrane protein embedded in hydrated lipid bilayers could be different from the simulations reported here. A recent study analyzed the effects of time and spatial averaging on PISEMA spectra of membrane bound peptides.[87] This study concluded that unambiguous identification of tilt and rotation of helices from PISA wheel spectrum without any resonance assignments may be difficult when the proteins are mobile on NMR time scale. Nevertheless, a careful analysis of PISEMA spectra could provide dynamics information in addition to the structure and topology of proteins in bilayers.

4.5. Structure determination using PISEMA

As mentioned earlier, resonance assignment is the most crucial step in the structure determination of proteins using NMR spectroscopy. PISA wheel patterns observed in the PISEMA spectra of uniaxially aligned samples overcome some of the difficulties related to the resonance assignment by

mapping the secondary structure onto a wheel-like PISEMA spectrum for a helix[32,33,78] or a loop pattern for a β-strand,[75] with each residue fit onto a resonance peak as discussed in the previous section; for example, no additional resonance assignments are needed to determine the tilt of a helix, and a single or partial assignment are sufficient to determine the helix rotation. Some of the approaches for the resonance assignment in the structural studies of membrane-associated proteins are discussed below.

4.5.1. *'Shotgun' approach*

Recently, a 'shotgun' method for simultaneous assignment and structure determination of membrane proteins has been proposed.[78] The shotgun approach solely relies on five PISEMA spectra from one uniformly and four selectively ^{15}N labeled protein samples, and utilizes the fundamental symmetry properties of PISA wheels to enable the simultaneous sequential assignment of resonances and measurement of orientational constraints. The fact that each resonance frequency in the PISEMA spectrum reflects molecular orientation relative to a fixed, and external, reference axis (defined by $\vec{B}_0$) enables the structures of isolated polypeptide segments of the protein to be determined independently from each other. It also prevents the propagation of any associated experimental errors or uncertainties in the magnitudes and orientations of the spin-interaction tensors. This approach was demonstrated using fd bacteriophage pVIII coat protein embedded in membrane bilayers (PDB ID: 1MZT).[78]

The PISEMA spectrum from uniformly labeled fd coat protein showed two PISA wheels (Fig. 10A and D), indicating two α-helices, one transmembrane helix with a tilt angle of 30° and another with an 87° tilt away from the bilayer normal.[78] The PISA wheel patterns then can be simulated, and each helix is rotated around its axis separately until the resonance pattern in the calculated PISA wheel spectrum qualitatively matches the resonances in the experimental spectra of selectively labeled samples (Fig. 10B). From this procedure, both the rotation of the two helices and the sequential assignment can be obtained. In the next step, the ^{15}N chemical shift and ^{1}H–^{15}N dipolar coupling frequencies are measured for each resonance and used to extract orientational constraints of the corresponding peptide plane. As the resonances are assigned, the dihedral angles are calculated, and then the backbone conformation of the protein is determined.

4.5.2. *Structural-fitting approach*

An alternative approach to structure determination is to fit structures to the resonance patterns in experimental PISEMA spectra when there is either no or only limited amounts of assignment information available.[88] It is necessary to relate the geometry of a peptide to its spectrum in order to perform a structural fitting. A chain propagator (rotation operator) is defined

that walks across the spectrum from the resonance of one residue (i) to that of the next residue in the sequence (i+1). No information from experimental assignments is used, and the 'assignments' selected by the algorithm will vary from those determined experimentally. However, the precision of the structural fitting can be improved by the addition of, e.g., residue type assignment from spectra of selectively labeled proteins.[88] In this algorithm, the resonance assignment is treated as an adjustable parameter, and the residues are linked together in a specific chemical manner (peptide bonds) and in defined order (sequence). In the most complete implementation of the algorithm, these intrinsic orientational and structural constraints, combined with the information about the overall orientation and conformation of the peptide domain obtained from the appearance of PISEMA spectra, can give a close set of structures that fit the solid-state NMR spectrum in an 'assignment-free' manner.

4.5.3. *Resolving ambiguities in angular constraints*

The use of angular constraints derived from anisotropic interactions is an attractive approach for structural studies of aligned molecules, e.g. mechanically oriented lipid bilayers. However, the inherent angular degeneracy of the orientational constraints can complicate the interpretation of NMR frequencies as angular constraints.[51] The observed chemical shift (δ_{obs}) and dipolar coupling (ν_{obs}) frequencies depend on the orientation of the molecular site with respect to $\vec{B}_0$, and on the magnitudes and orientations of the principal components of the spin-interaction tensors.[54] They can be expressed by the following equation.

$$\delta_{\text{obs}} = \delta_{11}\cos^2(\alpha' - \lambda)\sin^2\beta' + \delta_{22}\cos^2\beta' + \delta_{33}\sin^2(\alpha' - \lambda)\sin^2\beta' \qquad (10a)$$

$$D_{IS}^{\text{obs}} = \frac{h\gamma_I\gamma_S}{r^3}\left(3\sin^2\beta'\cos^2\alpha' - 1\right) \qquad (10b)$$

where γ_j is the gyromagnetic ratio of spin j, h is the Planck's constant, λ is the angle between δ_{11} and the N–H bond vector, α' (varied from 0 to 360°) is the angle between the N–H bond and the projection of $\vec{B}_0$ on the peptide plane, and β' (varied from 0 to 180°) is angle between $\vec{B}_0$ and the normal to the peptide plane. The angles α' and β' describe the peptide plane orientation with respect to $\vec{B}_0$. From these equations, it has been shown that there are four combinations of α' and β' angles that are consistent with the spectral parameters measured from the PISEMA experiment: (α'/β'), ($\alpha'/180-\beta'$), ($180+\alpha'/\beta'$), and ($180+\alpha'/180-\beta'$). PISEMA experiment does not distinguish between positive and negative dipolar couplings, resulting up to eight possible symmetry-related peptide plane orientations consistent with the ^{15}N chemical shift and the ^{1}H–^{15}N dipolar coupling frequencies. In addition, two pairs of ϕ/ψ dihedral angles to link two peptide planes can satisfy the

requirement of tetrahedral geometry and chirality at C_α atom. As a consequence, this will end up with 64 possible ϕ/ψ dihedral angle sets; of these, 32 are unique due to the indifference between positive and negative magnetic field directions in NMR experiments. A PISA pie method has been proposed to determine the correct set of angles, taking the advantage of the symmetry properties of PISA wheel.[89] In this method, the signs of individual dipolar couplings can be determined from their position in a PISA wheel, reducing the angular constraint ambiguities from eight to four symmetry related α/β orientations for each peptide plane, and from 32 to 16 sets of ϕ/ψ dihedral angles for each dipeptide combination. Then a single peptide plane orientation out of the symmetry-related set of four could be selected for each residue from the position of its resonance in the PISA wheel by generating four pie shaped sections in the helix and PISA wheel corresponding to four peptide plane orientations: (α'/β'), $(\alpha'/180-\beta')$, $(180+\alpha'/\beta')$, and $(180+\alpha'/180-\beta')$. Thus, a single set of ϕ/ψ dihedral angles connecting two peptide planes can be selected based solely on the piece of a PISA pie that it occupies.[89]

4.6. Dipolar waves

While the projection of the secondary structure on a plane is directly related to the 2D PISEMA spectrum of an aligned sample (called PISA wheels) as discussed in Section 4.4, its projection on a single axis can be correlated to the dipolar couplings values (called a 'dipolar wave') measured from either a weakly or completely aligned samples.[90] Both PISA wheels and dipolar waves originate from the orientational dependence of anisotropic spin-interactions and the periodicity inherent in the secondary structure elements in proteins. The magnitudes of the static heteronuclear dipolar couplings, D_{IS}, at a tilt angle, τ, as a function of residue number x demonstrate periodic wave like variations ($\rho = 2\pi x/3.6$) in the absence of chemical shift effects:

$$D_{IS}(x) = \frac{D_{||}}{2}\left[3(-0.326\cos\rho\sin\tau - 0.034\sin\rho\sin\tau - 0.946\cos\tau)^2 - 1\right] \quad (11)$$

For weakly aligned samples, the N–H bonds in a helix are distributed on a cone with axis defined by θ and ϕ with an aperture angle $\delta = 15.8^\circ$. The apparent residual dipolar coupling is parameterized as a function of the residue number (x) along the helix ($\rho = 2\pi x/3.6$).

$$D(x) = D_a\left\{\left[3\cos^2(\theta - \delta\cos\rho) - 1\right] + \frac{3}{2}R\sin^2(\theta - \delta\cos\rho)\cos 2(\phi + \delta\sin\rho)\right\} \quad (12)$$

where $R = D_r/D_a$ is the rhombicity, and D_a and D_r are the axial and rhombic components of the alignment tensor of the molecule.[91] The residual dipolar couplings in solution NMR spectra of weakly aligned samples give strikingly similar patterns of variations, representing a convergence of solid-state and solution NMR approaches in the structure studies of proteins (Fig. 16). The dipolar waves can, therefore, be applied to determine the

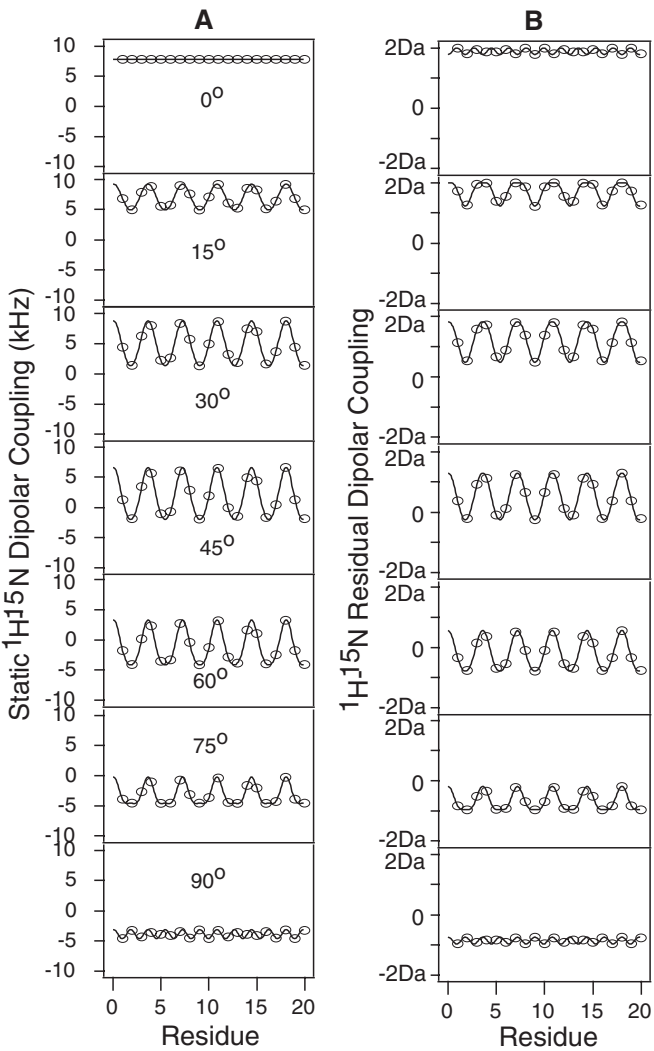

Fig. 16. Simulated amide ^{1}H–^{15}N dipolar couplings as a function of the residue position for a 20-residue ideal α-helix ($\phi = -65°$, $\psi = -40°$) for various slant angles: (A) a highly immobilized and (B) a weakly aligned helix. The rhombicity is $R = 0.25$.

orientation of structural domains of a protein when it is weakly aligned in liquid crystal media.

5. PROTON-DETECTED PISEMA

As discussed in the previous sections, 2D PISEMA has many advantages and therefore it will continue to be applied in the structural studies of biological solids. However, this technique depends on the detection of *S* nuclei which in general lowers the sensitivity of an NMR experiment as compared to a ^{1}H-detected experiment. ^{1}H-detected experiments have made great advances in sensitivity enhancement of dilute spins (^{2}H, ^{13}C, or ^{15}N) in solid-state NMR, for both very fast magic-angle-spinning (MAS) and static experiments.[40,92–96] This indirect-detection technique can be considered as an analogue of the 'inverse-detection' widely used in solution NMR.[97] Therefore, there is considerable interest in developing ^{1}H-detected PISEMA experiments. A one-dimensional ^{1}H-detected PISEMA method is developed in our laboratory to measure heteronuclear dipolar couplings from solids. This new pulse sequence has been experimentally demonstrated on single crystal and powder samples of peptides while the development of a family of ^{1}H-detected multi-dimensional experiments is in progress.[98] Details of the PISEMA pulse sequence and some experimental results are discussed below.

The 1D PISEMA pulse sequence is given in Fig. 17. In the pulse sequence, after cross-polarization from ^{1}H to *S* nuclei, the remaining ^{1}H magnetization in the proton reservoir is tilted to the magic angle by a 35.3° pulse. The delay time t_z, after CP in the pulse sequence, is used to manipulate the ratio of magnetization in ^{1}H and *S* channels. After t_z, SEMA pulse sequence is used to evolve the transverse *S*-spin magnetization under the scaled ^{1}H–*S* dipolar coupling. However, unlike in the original 2D PISEMA, the ^{1}H magnetization

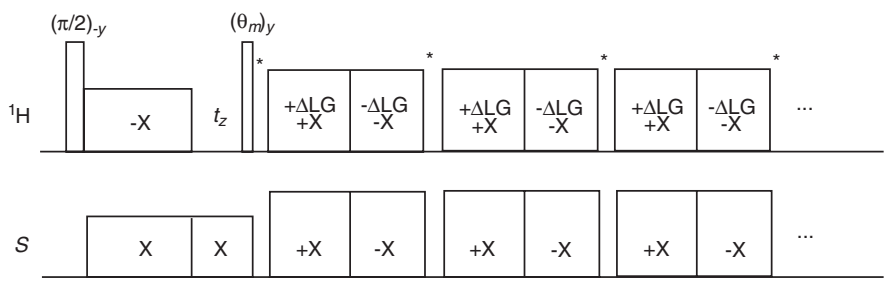

Fig. 17. A proton-detected one-dimensional PISEMA pulse sequence to measure heteronuclear *I*–*S* dipolar coupling parameters in solids. The pulse sequence is discussed in the text.

is detected during narrow windows after each FFLG cycle. The ^{1}H carrier frequency is brought back to zero frequency (or on resonance) at the beginning of the sampling interval, i.e., before detection. Since the magnetization is present in both ^{1}H and S channels during the SEMA sequence, stroboscopic detection of S-spin magnetization can also be employed for the measurement of heteronuclear dipolar couplings. However, detection of protons enhances the sensitivity of the experiment. Unlike previously reported indirect-detection methods that employ reverse cross-polarization from S to ^{1}H nuclei in order to acquire signal on the ^{1}H channel, the ^{1}H-detected PISEMA experiment utilizes the evolution under the ^{1}H–S dipolar coupling to acquire the signal in the ^{1}H channel. Therefore, this new sequence eliminates the sensitivity-loss due to the reverse cross-polarization step and could be used to develop a variety of ^{1}H-detected multi-dimensional solid-state NMR experiments.

The performance of the 1D ^{1}H-detected PISEMA technique has been examined on single crystalline and polycrystalline samples of peptides. As an example, experimental results obtained from *N*-acetyl-^{15}*N*-D,L-valine (NAV) powder sample are discussed. The experimental and simulated 1D heteronuclear dipolar coupling spectra of NAV powder sample are shown in Fig. 18. Both experimental and simulated spectra show a doublet separated by the magnitude of the scaled ^{1}H–^{15}N dipolar coupling (9.13 kHz) and a zero-frequency peak. A ^{1}H–^{15}N dipolar coupling of 11.2 kHz, corresponding to an N–H bond length of 1.05 Å, was used in the simulation to obtain the same dipolar splitting. The zero-frequency signal arises from the spin-locked pedestal ^{1}H magnetization that does not evolve under the heteronuclear dipolar coupling during the SEMA sequence while the doublet signal arises from those ^{1}H magnetizations that evolve under the heteronuclear dipolar coupling. The phases of these two components of the dipolar spectrum depend on the ^{1}H dephasing time t_z in the pulse sequence (see Fig. 17). With a very short ^{1}H dephasing time ($t_z \sim 1$ μs), where both ^{1}H and ^{15}N magnetizations exist before the evolution under the ^{1}H–^{15}N dipolar coupling during the SEMA pulse sequence, both the dipolar split doublet signal and the zero-frequency signal have the same phase (Fig. 18(A)). This is in complete agreement with the *in phase* peaks in the simulated spectrum (Fig. 18(C)) where a starting density matrix operator S_x–I_x was used; where I and S represent ^{1}H and ^{15}N nuclear spins respectively. Since polarization inversion, which inverts the ^{1}H magnetization after CP, is employed in the PISEMA experiment, the phases of I_x and S_x in the starting density operator differ by 180°. When the ^{1}H dephasing time was long ($t_z \sim 1$ ms), the ^{1}H magnetization vanishes leaving only the ^{15}N magnetization before the evolution under the ^{1}H–^{15}N dipolar coupling, and the phases of the resultant dipolar split and the zero-frequency signals differ by 180° (Fig. 18(B)). This spectrum was simulated using a starting density operator S_x (Fig. 18(D)). The simulations are in qualitative agreement with experiments in terms of

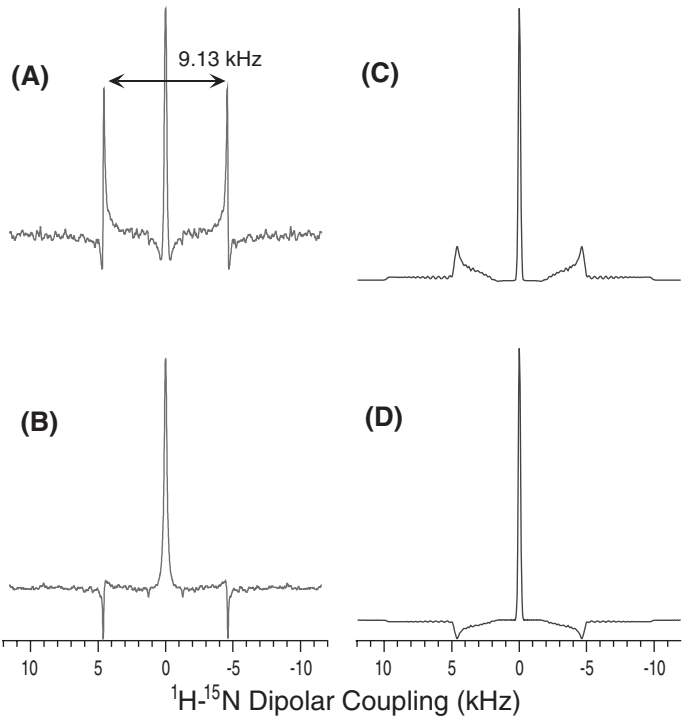

Fig. 18. Proton-detected 1D PISEMA spectra of a powder sample of *N*-acetyl-^{15}*N*-D,L-valine obtained using the pulse sequence shown in Fig. 17 under static condition. The experiments were performed with a ^{1}H Lee-Goldburg spin-lock RF power of 39.1 kHz, an offset frequency of 27.6 kHz, and a ^{15}N spin-lock RF power of 47.8 kHz. Other experimental parameters include: 2 μs stroboscopic sampling interval, 1 ms CP contact time, 35 kHz RF power for CP on both RF channels, and 1024 scans were acquired with a recycle delay of 3s. (A) Experimental spectrum with a very short dephasing time ($t_z \sim 1$ μs). (B) Experimental spectrum with a long dephasing time ($t_z \sim 1$ ms). (C) Simulated spectrum with an initial density matrix I_x–S_x. (D) Simulated spectrum with an initial density matrix S_x. An N–H bond length of 1.05 Å, ^{15}N CSA parameters ($\delta_{iso} = 125.9$ ppm, $\delta = 109.0$ ppm, $\eta = 0.2156$) and ^{1}H CSA parameters ($\delta_{iso} = 9.33$ ppm, $\delta = 8.67$ ppm, $\eta = 0.5767$) were used in simulations; where δ is the anisotropy ($\delta = \delta_{33} - \delta_{iso}$, if $|\delta_{33} - \delta_{iso}| \geq |\delta_{11} - \delta_{iso}| \geq |\delta_{22} - \delta_{iso}|$, or $\delta = \delta_{11} - \delta_{iso}$, if $|\delta_{11} - \delta_{iso}| \geq |\delta_{33} - \delta_{iso}| \geq |\delta_{22} - \delta_{iso}|$) and $\eta = (\delta_{22} - \delta_{33})/(\delta_{11} - \delta_{iso})$ if $|\delta_{11} - \delta_{iso}| \geq |\delta_{33} - \delta_{iso}|$, or $\eta = (\delta_{22} - \delta_{11})/(\delta_{33} - \delta_{iso})$ if $|\delta_{33} - \delta_{iso}| \geq |\delta_{11} - \delta_{iso}|$.

the relative phases of the peaks, although the peak intensity and line width are different. This difference may be attributed to the unsuppressed residual ^{1}H–^{1}H dipolar interactions and imperfection in the rf pulses that are not included in the simulations.

Our experimental results suggest that the sensitivity of the ^{1}H-detected PISEMA experiment was enhanced by many fold as compared to the

conventional 2D ^{15}N-detected PISEMA experiment, although it loses some advantages associated with the 2D PISEMA experiments, such as straightforward assignment using PISA wheel and the resolution associated with two-dimensional experiments. A two-dimensional ^{1}H-detected PISEMA pulse sequence that correlates ^{1}H or ^{15}N chemical shift and ^{1}H–^{15}N dipolar coupling could be developed to take advantage of the sensitivity of ^{1}H detection, as well as the resolution and straightforward assignment provided by the ^{1}H–^{15}N dipolar coupling and the ^{15}N chemical shift dimensions.

In ^{1}H-detected experiments, the data-sampling interval needs to be as short as possible in order to reduce the loss of ^{1}H magnetization, which depends on $T_{1\rho}$ of a sample during the SEMA sequence. A long interval also alters the scaling factor from 0.82, which is for a sequence with no interval, in addition to the loss of ^{1}H magnetization under T_2 process. This effect on the scaling factor of the SEMA sequence was studied using the SIMPSON simulations. We set the ^{1}H–^{15}N dipolar coupling to be constant (11.2 kHz), and varied the data-sampling interval from 0 to 10 μs. For data-sampling interval of 0 to 3 μs, the simulated scaling factor of the SEMA pulse sequence is very close to the theoretical value (0.82). When the interval is increased to 10 μs, the scaling factor is increased to $\sim$0.87. Therefore, a short data-sampling window <3 μs is recommended in order to obtain accurate dipolar coupling values, which could be technically demanding. On the other hand, experiments on a test sample for which the dipolar coupling is known through other sources could be used to determine the scaling factor of the sequence with sampling interval >3 μs. Setting a very large receiver filter frequency (ca. 500 MHz), and taking off the CRAMPS diode box from the ^{1}H transmission line in order to reduce the interference of rf pulses after such a short delay would be helpful to implement the ^{1}H-detected pulse sequences. Another difficulty in this experiment is that the spin exchange matching condition during the SEMA sequence has to be optimized very carefully. A mismatch suppresses the heteronuclear spin exchange process and increases the intensity of the zero-frequency signal in the dipolar coupling spectrum.

6. CONCLUDING REMARKS

The ability to retain anisotropic spin interactions and the power to selectively suppress unwanted interactions using pulse sequences such as PISEMA in aligned solids have played a significant role in the applications of solid-state NMR spectroscopy. In addition, the excellent control over the order parameter (ranging from isotropic to rigid solids) of a system and creation of model biological systems obviously invited, simplified, created, and amplified the applications of solid-state NMR techniques. Although solid-state NMR

techniques are beginning to be applied routinely, the intrinsic complex behaviour of nuclear spins present in solids continues to have the power to attract, engage, challenge, and excite the creative minds of spectroscopists. For example, understanding and manipulating spin physics under fast spinning and at ultra-high magnetic fields are wealthy area of fundamental research. Developing NMR methods to completely characterize the dynamics, the missing information to bridge the structure and function, of biological molecules is another challenging area of research.

It is interesting that the magic of obtaining high-resolution 'solution-like' spectra, either through aligning samples or MAS, of nearly all types of solids has significantly narrowed the gap between solution and solid-state NMR spectroscopy. This is evident from numerous recent studies using solid-state and solution NMR techniques. An example discussed in this review is the measurement of dipolar couplings from aligned samples using PISA wheels and residual dipolar couplings from weakly aligned samples using dipolar waves. Therefore, in the coming years, increased exchange of ideas from solution and solid-state NMR, combined with the advancements in instrumentation and materials, will create a new dimension for attractive scientific activities in this field of research.

In this review, we have made an effort to provide all aspects of PISEMA spectroscopy. Advantages, experimental aspects and difficulties, applications and limits of the PISEMA experiment are discussed. The capability of PISEMA to provide very high-resolution spectral lines and its sensitivity to the backbone conformation and topology of molecules have made it a useful and powerful technique, and it can be expected to provide even more exciting information in the time to come. The possibilities of using PISA wheels to study the structure and topology of large membrane proteins are illustrated using simulations of PISEMA spectra of uniformly labeled membrane-associated proteins. We believe that the recent developments in the preparation of well-aligned samples[99] will be useful to further enhance the resolution of PISEMA spectra of large membrane proteins. In the future, more efforts will probably be devoted to the development of new resonance assignment techniques, low temperature experiments on aligned samples, and proton-detected PISEMA experiments. Investigation of other liquid crystalline systems using PISEMA techniques will also be a likely focus of the future research.[100]

ACKNOWLEDGEMENTS

We thank Dr. Francesca Marassi for providing us the Figure 10 (A & B). We wish to acknowledge the funding support from NSF (CAREER development award for A.R) for our research in the area covered by this review.

REFERENCES

1. C. J. Gorter, *Physica*, 1936, **3**, 995.
2. U. Haeberlen, *High Resolution NMR in Solids, Selective Averaging*, Academic Press, New York, 1976.
3. M. Mehring, *High Resolution NMR Spectroscopy in Solids*, Springer-Verlag, New York, 1976.
4. K. Schmidt-Rohr and H. W. Spiess, *Multidimensional Solid-State NMR and Polymers*, Academic Press, New York, 1994.
5. A. Ramamoorthy, F. M. Marassi and S. J. Opella, *Dynamics and the Problem of Recognition in Biological Macromolecules*, Plenum Press, New York, 1996.
6. L. Frydman, *Annu. Rev. Phys. Chem*., 2001, **52**, 463.
7. R. Tycko, *Annu. Rev. Phys. Chem*., 2001, **52**, 575.
8. J. S. Santos, D. K. Lee, K. J. Hallock and A. Ramamoorthy, Recent Research Developments in Physical Chemistry. *Transworld Research Network*, 2002, **6** (Part I), 179.
9. M. Baldus, *Prog. Nucl. Magn. Reson. Spectrosc*., 2002, **41**, 1.
10. T. A. Cross and S. J. Opella, *Curr. Opin. Struc. Biol*., 1994, **4**, 574; S. J. Opella, A. Nevzorov, M. F. Mesleh and F. M. Marassi, *Biochem. Cell Biol*, 1994, **80**, 597.
11. S. J. Opella and J. S. Waugh, *J. Chem. Phys*, 1977, **73**, 4919.
12. R. K. Hester, J. L. Ackerman, B. L. Neff and J. S. Waugh, *Phys. Rev. Lett*, 1976, **36**, 1081.
13. (a) S. J. Opella and J. S. Waugh, *J. Chem. Phys*, 1977, **66**, 4919; E. F. Rybaczewski, B. L. Neff, J. S. Waugh and J. S. Sherfinski, *J. Chem. Phys*, 1977, **67**, 1231; (b) M. Linder, A. Hohener and R. R. Ernst, *J. Chem. Phys*, 1980, **73**, 4959; (c) M. G. Munowitz, R. G. Griffin, G. Bodenhausen and T. H. Huang, *J. Am. Chem. Soc*., 1981, **103**, 2529; J. A. Diverdi and S. J. Opella, *J. Am. Chem. Soc*., 1982, **104**, 1761; M. Munowitz, W. P. Aue and R. G. Griffin, *J. Chem. Phys*., 1982, **77**, 1686; B. S. A. Kumar and S. J. Opella, *J. Magn. Reson. A*, 1993, **101**, 333; S. J. Opella, *Annu. Rev. Phys. Chem*., 1994, **45**, 659; S. Caldarelli, M. Hong, L. Emsley and A. Pines, *J. Phys. Chem*., 1996, **100**, 18696.
14. A. Pine, M. G. Gibby and J. S. Waugh, *J. Chem. Phys*., 1973, **59**, 569.
15. O. B. Peersen, X. Wu, I. Kustanovich and S. O. Smith, *J. Magn. Reson. A*, 1993, **104**, 334.
16. M. H. Levitt, D. Suter and R. R. Ernst, *J. Chem Phys*., 1986, **84**, 4243.
17. S. C. Shekar and A. Ramamoorthy, *Chem. Phys. Lett*., 2001, **342**, 312.
18. S. C. Shekar, D.-K. Lee and A. Ramamoorthy, *J. Magn., Reson*., 2002, **157**, 223.
19. M. Munowitz and R. G. Griffin, *J. Chem. Phys*., 1982, **76**, 2848.
20. L. Muller, A. Kumar, T. Baumann and R. R Ernst, *Phys. Rev. Lett*., 1974, **32**, 1402.
21. R. K. Hester, J. L. Ackermann, V. R. Cross and J. S. Waugh, *Phys. Rev. Lett*., 1975, **34**, 993.
22. J. E. Roberts, S. Vega, and R. G. Griffin, *J. Am. Chem. Soc*., 1984, **106**, 2506; J. E. Roberts, G. S. Harbison, M. G. Munowitz, J. Herzfeld and R. G. Griffin, *J. Am. Chem. Soc*., 1987, **109**, 4163; J. Schaefer, R. A. McKay, E. O. Stejskal and W. T. Dixon, *J. Magn. Reson*., 1983, **52**, 123; J. Schaefer, R. A. McKay, E. O. Stejskal and W. T. Dixon, *J. Magn. Reson*., 1984, **57**, 85; A. C. Kolebert, M. H. Levitt, and R. G. Griffin, *J. Magn. Reson*., 1989, **85**, 42.
23. J. S. Waugh, L. M. Huber and U. Haeberlen, *Phys. Rev. Lett*., 1968, **20**, 180.
24. W. K. Rhim, D. D. Elleman and R. W. Vaughan, *J. Chem. Phys*., 1973, **58**, 1772.
25. M. Lee and W. I. Goldberg, *Phys. Rev. A*, 1965, **140**, 1261.
26. C. H. Wu, A. Ramamoorthy and S. J. Opella, *J. Magn. Reson. A*, 1994, **109**, 270.
27. A. Ramamamoorthy, C. H. Wu and S. J. Opella, *J. Magn. Reson. B*, 1995, **107**, 88.
28. A. Ramamamoorthy, L. M. Gierasch and S. J. Opella, *J. Magn. Reson. B*, 1995, **109**, 112.
29. A. Ramamamoorthy, L. M. Gierasch and S. J. Opella, *J. Magn. Reson. B*, 1996, **111**, 81.
30. Z. T. Gu and S. J. Opella, *J. Magn. Reson*., 1999, **138**, 193; Z. T. Gu and S. J. Opella, *J. Magn. Reson*., 1999, **140**, 340; W. M. Tan, Z. T. Gu, A. C. Zeri and S. J. Opella, *J. Biomol. NMR*, 1999, **13**, 337.
31. Y. Ishii and R. Tycko, *J. Am. Chem. Soc*., 2000, **122**, 1443.
32. F. M. Marassi and S. J. Opella, *J. Magn. Reson*., 2000, **144**, 150.

33. J. K. Denny, J. Wang, T. A. Cross and J. R. Quine, *J. Magn. Reson*., 2001, **152**, 217.
34. D. P. Burum and W. K. Rhim, *J. Chem. Phys*., 1979, **71**, 944.
35. M. Mehring and J. S. Waugh, *Phys. Rev. B*, 1972, **5**, 3459.
36. (a) A. Bielecki, A. C. Kolbert, H. J. M. de Groot, R. G. Griffin and M. H. Levitt, *Adv. Magn. Reson*., 1990, **14**, 111; A. Bielecki, A. C. Kolbert and M. H. Levitt, *Chem. Phys. Lett*., 1989, **155**, 341; M. H. Levitt, A. C. Kolbert, A. Bielecki and D. J. Ruben, *Solid State NMR*, 1989, **2**, 151; (b) E. Vinogradov, P. K. Madhu and S. Vega, *Chem. Phys. Lett*., 1999, **314**, 443.
37. P. Caravatti, L. Braunschweiler and R. R. Ernst, *Chem. Phys. Lett*., 1983, **100**, 305.
38. A. Ramamamoorthy, C. H. Wu and S. J. Opella, *J. Magn. Reson*., 1999, **140**, 131.
39. Z. Gan, *J. Magn. Reson*., 2000, **143**, 136.
40. Y. Wei, D.-K. Lee, K. J. Hallock and A. Ramamoorthy, *Chem. Phys. Lett*., 2002, **351**, 42.
41. P. Palmas, P. Tekely and D. Cadet, *J. Magn. Reson. A*, 1993, **104**, 26.
42. (a) Zumbulyadis, *J. Chem. Phys*., 1987, **86**, 1162; (b) N. Sinha and K. V. Ramanathan, *Chem. Phys. Lett*., 2000, **332**, 125.
43. S. C. Shekar, D. K-. Lee and A. Ramamoorthy, *J. Am. Chem. Soc*., 1995, **123**, 7467.
44. B. C. Gerstein and C. R. Dybowski, *Transient Techniques in NMR of Solids, An Introduction to Theory and Practice*, Academic Press, New York, 1985.
45. M. Bak, J. T. Rasmussen and N. C. Nielsen, *J. Magn. Reson*., 2000, **147**, 296.
46. A. Ramamamoorthy and S. J. Opella, *Solid State NMR*, 1995, **4**, 387.
47. R. Fu, C. I. Tian and T. A. Cross, *J. Magn. Reson*., 2002, **154**, 130.
48. R. Fu, C. I. Tian, H. N. Kim, S. A. Smith and T. A. Cross, *J. Magn. Reson*., 2002, **159**, 167.
49. M. Ravikumar and A. Ramamoorthy, *Chem. Phys. Lett*., 1998, **286**, 199.
50. A. Ramamoorthy, L. M. Gierasch and S. J. Opella, *J. Magn. Reson. B*, 1996, **110**, 102.
51. A. Ramamoorthy, F. M. Marassi, M. Zasloff and S. J. Opella, *J. Biomol. NMR*, 1995, **6**, 329.
52. R. Jelinek, A. Ramamoorthy and S. J. Opella, *J. Am. Chem. Soc*., 1995, **117**, 12348.
53. F. M. Marassi, A. Ramamoorthy and S. J. Opella, *Proc. Natl. Acad. Sci. USA*, 1997, **94**, 8551.
54. S. J. Opella, P. L. Stewart and K. G. Valentine, *Q. Rev. Biophys*., 1987, **19**, 7.
55. D.-K. Lee, R. J. Wittebort and A. Ramamoorthy, *J. Am. Chem. Soc*., 1998, **120**, 8868.
56. D.-K. Lee, J. S. Santos and A. Ramamoorthy, *J. Phys. Chem. B*, 1999, **103**, 8383.
57. K. J. Hallock, D. K. Lee, J. Omnaas, H. I. Mosberg and A. Ramamoorthy, *Biophys. J*., 2002, **83**, 1004; K. J. Hallock, D. K. Lee and A. Ramamoorthy, *Biophys. J*., 2003, **84**, 3052; F. M. Marassi, C. Ma, H. Gratkowski, S. K. Straus, K. Strebel, M. Oblatt-Montal, M. Montal and S. J. Opella, *Proc. Natl. Acad. Sci. USA*, 1999, **96**, 14336; S. Arumugam, S. Pascal, C. L. North, W. Hu, K. C. Lee, M. Cotten, R. R. Ketchem, F. Xu, M. Brenneman, F. Kovacs, F. Tian, A. Wang, S. Huo and T. A. Cross, *Proc. Natl. Acad. Sci. USA*, 1996, **93**, 5872; L. Grage, J. F. Wang, T. A. Cross and A. S. Ulrich, *Biophys. J*., 2001, **83**, 3336; J. F. Wang, S. Kim, F. Kovacs and T. A. Cross, *Protein Sci*., 2002, **10**, 2241; S. Yamaguchi, T. Hong, A. Waring, R. I. Lehrer and M. Hong, *Biochemistry*, 2001, **41**, 9852.
58. K. A. H. Wildman, D.-K. Lee and A. Ramamoorthy, *Biochemistry*, 2003, **42**, 6545.
59. A. Naito, S. Ganapathy, K. Akasaka and C. A. McDowell, *J. Chem. Phys*., 1981, **74**, 3190; G. S. Harbison, L. W. Jelinski, R. E. Stark, D. A. Torchia, J. Herzfeld and R. G. Griffin, *J. Magn. Reson*., 1984, **60**, 79; R. Gerald, T. Bernhard, U. Haeberlen, J. Rendell and S. J. Opella, *J. Am. Chem. Soc*., 1993, **115**, 777.
60. S. C. Shekar, A. Ramamoorthy and R. J. Wittebort, *J. Magn. Reson*., 2002, **155**, 257.
61. C. H. Wu, A. Ramamoorthy, L. M. Gierasch and S. J. Opella, *J. Am. Chem. Soc*., 1995, **117**, 6148.
62. A. Ramamoorthy, C. H. Wu and S. J. Opella, *J. Am. Chem. Soc*., 1977, **119**, 10479.
63. D.-K. Lee and A. Ramamoorthy, *J. Magn. Reson*., 1998, **113**, 204.
64. J. R. Brender, D. M. Taylor and A. Ramamoorthy, *J. Am. Chem. Soc*., 2001, **123**, 914.
65. D.-K. Lee, J. S. Santos and A. Ramamoorthy, *Chem. Phys. Lett*., 1999, **309**, 209; C. J. Hartzell, M. Whitfield, T. G. Oas and G. P. Drobny, *J. Am. Chem. Soc*., 1987, **109**, 5966; A. Shoji, S. Ando, S. Kuroki, I. Ando and G. A. Webb, *Ann. Reports on NMR Spectrosc*., Vol. 26, G. A. Webb, ed., Academic Press, London, 1993, 55.

66. Y. Wei, D.-K. Lee and A. Ramamoorthy, *J. Am. Chem. Soc*., 2001, **123**, 6118.
67. D. K. Lee, Y. Wei and A. Ramamoorthy, *J. Phys. Chem. B*, 2001, **105**, 4752.
68. Y. Wei, D.-K. Lee, A. E. McDermott and A. Ramamoorthy, *J. Magn. Reson*., 2002, **158**, 23.
69. X. L. Yao, S. Yamaguchi and M. Hong, *J. Biomol. NMR*, 2002, **24**, 51; X. L. Yao and M. Hong, *J. Am. Chem. Soc*., 2002, **124**, 2730.
70. G. A. Lorigan, R. McNamara, R. A. Jones and S. J. Opella, *J. Magn. Reson*., 1999, **140**, 315.
71. K. J. Hallock, D.-K. Lee and A. Ramamoorthy, *Chem. Phys. Lett*., 1999, **302**, 175; K. Srikanth and A. Ramamoorthy, *J. Phys. Chem. A*, 2003, **106**, 10363; K. Srikanth and A. Ramamoorthy, *Inorg. Chem*., 2002, **42**, 2200; K. Srikanth, D. K. Lee and A. Ramamoorthy, *Inorg. Chem*., 2003, **42**, 3142.
72. Z. Gan, *J. Am. Chem. Soc*., 1992, **114**, 8307.
73. F. M. Marassi, J. J. Gesell, A. P. Valente, M. Oblatt-Montal, M. Montal and S. J. Opella, *J. Biomol. NMR*, 1999, **14**, 141.
74. S. J. Opella, F. M. Marassi, J. J. Gesell, A. P. Valente, Y. Kim, M. Oblatt-Montal and M. Montal, *Nat. Struct. Biol*., 1999, **6**, 374.
75. F. M. Marassi, *Biophys. J*., 2001, **80**, 994.
76. M. Bak, R. Schultz, T. Vosegaard and N. C. Nielsen, *J. Magn. Reson*., 2002, **154**, 28.
77. M. Bierring, T. Vosegaard, A. Malmendal and N. C. Nielsen, *Concepts in Magn. Reson*., 2003, **18A**, 111.
78. F. M. Marassi and S. J. Opella, *Proteins Sci*., 2003, **12**, 403.
79. G. E. Schulz, *Adv. Protein Chem*., 2003, **63**, 47.
80. D. A. Doyle, J. Morais Cabral, R . A. Pfuetzner, A. Kuo, J. M. Gulbis, S. L. Cohen, B. T. Chait and R. MacKinnon, *Science*, 1998, **280**, 69.
81. R. Dutzler, E. B. Campbell, M. Cadene, B. T. Chait and R. MacKinnon, *Nature*, 2002, **415**, 287.
82. H. Luecke, B. Schobert, H.-T. Richter, J.-P. Cartailler and J. K. Lanyi, *J. Mol. Biol*, 1999, **291**, 899.
83. J. Vogt and G. E. Schulz, *Structure*, 1999, **7**, 1301–1309.
84. A. Pautsch and G. E. Schulz, *J. Mol. Biol*., 2000, **298**, 273–282.
85. K. J. Hallock, D.-K. Lee and A. Ramamoorthy, *J. Chem. Phys*., 2000, **113**, 11187.
86. C. L. North and T. A. Cross, *Biochemistry*, 1995, **34**, 5883; W. L. Hubbel, D. S. Cafisco and C. Altenbach, *Nat. Struct. Biol*., 2001, **7**, 735; D. Huster, L. Xiao and M. Hong, *Biochemistry*, 2001, **40**, 7662.
87. S. K. Straus, W. R. P. Scott and A. Watts, *J. Biomol. NMR*, 2003, **26**, 283.
88. A. A. Nevzorov and S. J. Opella, *J. Magn. Reson*., 2003, **160**, 33.
89. F. M. Marassi and S. J. Opella, *J. Biomol. NMR*, 2002, **23**, 239.
90. M. F. Mesleh, G. Veglia, T. M. DeSilva, F. M. Marassi and S. J. Opella, *J. Am. Chem. Soc*., 2002, **124**, 4206.
91. A. Bax, *Protein Sci*., 2003, **12**, 1.
92. Y. Ishii and R. Tycko, *J. Magn. Reson*., 2000, **142**, 199.
93. I. Schnell, B. Langer, S. H. M. Sontjens, M. H. P. van Genderen, R. P. Sijbesma and H. W. Spiess, *J. Magn. Reson*., 2001, **150**, 57.
94. M. Hong and S. Yamaguchi, *J. Magn. Reson*., 2001, **150**, 43.
95. K. Schmidt-Rohr, K. Saalwachter, S. F. Liu and M. Hong, *J. Am. Chem. Soc*., 2001, **123**, 7168.
96. A. K. Khitrin and B. M. Fung, *J. Magn. Reson*., 2001, **152**, 185.
97. A. Bax, *Curr. Opin. Struct. Biol*., 1994, **4**, 738.
98. Y. Wei, L. Waskall and A. Ramamoorthy, 43rd Rocky Mountain Conference, Denver, USA, 2001.
99. K. J. Hallock, K. H. Wildman, D. K. Lee and A. Ramamoorthy, *Biophys. J*., 2002, **82**, 2499.
100. C. S. Nagaraja and K. V. Ramanathan, *Liq. Cryst*., 1999, **26**, 12.

3D Structure Elucidation Using NMR Chemical Shifts

ULRICH STERNBERG[1], RAIKER WITTER[1] AND ANNE S. ULRICH[1,2]

[1]*IFIA, Forschungszentrum Karlsruhe, Hermann-von-Helmholtz-Platz 1, Postfach 3640, D-76021 Karlsruhe, Germany*
[2]*Institute of Organic Chemistry, University of Karlsruhe, Fritz-Haber-Weg 6, 76131 Karlsruhe, Germany; E-mail: anne.ulrich@ifia.fzk.de*

The NMR chemical shift is virtually always available from conventional NMR experiments. In contrast to X-ray diffraction it is caused by the density distribution of the valence electrons, hence it contains genuine information

ANNUAL REPORTS ON NMR SPECTROSCOPY
VOLUME 52 ISSN 0066 4103
DOI 10.1016/S0066-4103(04)52002-1

about the valence structure of the molecular system. This paper reviews the available theoretical, empirical and semi-empirical methods to obtain 3D structure information from chemical shifts. Besides direct empirical correlations of chemical shifts an overview of computational quantum chemical methods is presented. A critical survey is given how these methods can be used in structure refinement procedures. Special attention is paid to methods for protein and peptide structure analysis using chemical shifts. Computed and empirical chemical shift maps are discussed and compared to direct refinement methods. Chemical shift tensors or their principal components can provide additional data to characterise structural motifs in proteins. Furthermore, methods are discussed to extract orientational constraints from chemical shift tensors in macroscopically aligned samples. Applications are presented for structure elucidation in solution and in the solid state, including the first applications of chemical shifts to crystal structure refinements.

1. INTRODUCTION

The chemical shift (CS) phenomenon was first observed in 1951 by Arnold *et al.*,[1] and from this time on it was clear that the NMR chemical shifts contain a wealth of information on the structure of molecular systems. In the following years a vast amount of empirical chemical shift data for many nuclei was accumulated. Especially ^{13}C chemical shifts could be used as fingerprints of chemical structures. However, this basic information only reveals the molecular topology but not the three-dimensional geometry. The topology of simple molecules could often be readily deduced from NMR spectra using the empirical data of known compounds. Once the bond network was elucidated, the organic chemist had identified the target of the synthesis. Especially fruitful proved to be increment systems for chemical shift predictions,[2] which have lead in the meantime to the development of automated systems for structure identification. Up to this point, the three-dimensional arrangement of the atoms could only be resolved from crystals by diffraction analysis.

Yet, the chemical shift itself contains a lot of information about the three-dimensional atomic arrangement. Since the chemical shift of many nuclei depends strongly on the hybridization state h, we can estimate the bond angle θ from $h = -1/\cos\theta$. Another parameter that can be deduced from chemical shifts is the coordination number. For many nuclei the coordination number and hybridization state are tightly connected, although in inorganic compounds the measurement of coordination numbers only provides some narrow margins for the three-dimensional arrangement.

Empirical relationships between chemical shift and geometric parameters are of great value for larger molecules, because they reveal a wealth of information hidden in their complex NMR spectra. Extensive NMR data bases for proteins allow to derive detailed empirical models for the chemical

shift dependence of backbone carbons which can be used in 3D structure refinements. The ultimate goal would be to perform an accurate chemical shift calculation coupled to a 3D structure refinement. In many cases *ab initio* CS calculations are used to supplement NMR investigations to extract aspects of the spatial arrangement, but for complete structure refinement a number of severe problems still have to be solved. Quantum chemical calculations are hampered by their bad scaling in terms of the number of electrons. Chemical shift calculations often require extended basis sets or correlation corrections that may easily lead to multiples of the original computational times. If refinements are to be performed in addition to the chemical shift calculation, their derivatives with respect to the molecular coordinates need to be evaluated. This is again much more demanding than the chemical shift calculations alone. Concerning the basics of *ab initio* calculations of NMR shieldings and indirect coupling, we recommend the excellent and comprehensive review of Helgaker *et al.*[3] which also includes the calculation of various derivatives of NMR parameters.

This paper will discuss the state of the art in 3D structure refinement using empirical, semi-empirical and *ab initio* methods. We believe that the success story of liquid state NMR in protein structure elucidation is going to continue within the solid state (or membrane environment) if chemical shifts can be successfully exploited. Neutron and X-ray diffraction methods owe their success to a simple formula that connects the measured reflex intensities with the nuclear positions or the electron density, respectively. The better we understand how chemical shifts change with the three-dimensional arrangement of atoms, the more reliably we can construct molecular models from our NMR experiments. As we can in principle determine up to six numbers per nucleus if we perform a full chemical shift tensor analysis, we need to address the question whether whole CS tensor or at least its principal values can be used in structure calculations.

In many cases the chemical shift will be only one parameter amongst many others that can yield constraints for structure calculation. In solution we can measure Nuclear Overhauser Enhancements (NOEs), *J*-couplings and residual dipolar couplings, and for these parameters there exist well established relationships to aspects of the molecular structure. In solid state investigations we face the situation that up to now there is no general protocol for structure calculations from NMR data. Direct dipolar couplings are used in many solid state NMR structure investigations as distance constraints, provided that the interaction between two spins can be singled out. Chemical shift information, on the other hand, is highly useful to determine orientational constraints in macroscopically oriented samples such as membranes of fibres. For proteins structure investigations there are a number of excellent reviews[4,5,6,7] covering most aspects of chemical shift analyses.

The primary goal of this paper is to review methods that lead to the possibility of 3D structure refinement for molecules in solution and in the

solid state. Chemical shifts and CS tensors will be the essential data source within the rapidly growing field of solid state NMR investigations for 3D structure calculation.

2. BASIC CONCEPTS OF NUCLEAR SHIELDINGS AND CHEMICAL SHIFTS

Electrons shield or de-shield nuclei. For chemists the influence of core electrons is of no interest, hence they are disregarded. By referring only to the difference with respect to an appropriate shielding reference, $\sigma_{\mathrm{ref}} - \sigma$, their contribution is eliminated.

Let us consider the current density $j(r)$ of bond electrons. It is zero, when the molecular structure is isolated in free space

$$j(r) = \frac{e}{2m_e}\left\langle \chi \middle| \Big(p|r\rangle\langle r| + |r\rangle\langle r|p \Big) \middle| \chi \right\rangle = 0. \tag{1}$$

The bond electrons at position r are described by a real wave function $|\chi\rangle$ with momentum p. The coordinate vector r is the distance between the nucleus position and the electron location $r = r_O - R_N$. If the system is located in a homogenous magnetic field B_Z along the z-direction with $B_Z = \mathrm{rot}\, A_Z$ and $A_Z = 1/2 B_Z \times r$, then the current density becomes non-zero

$$j(r) = \frac{e}{2m_e}\left\langle \chi' \middle| \Big((p - eA_Z)|r\rangle\langle r| + |r\rangle\langle r|(p - eA_Z) \Big) \middle| \chi' \right\rangle \neq 0. \tag{2}$$

Now, the wave function $|\chi'\rangle$ is not real anymore and acquires an imaginary contribution. According to Biot-Savart's law the external magnetic field B_Z, in z-direction induces a local field B_{ind} at the position R due to the electron current $j(r)$

$$B_{\mathrm{ind}}(R) = \frac{\mu_0}{4\pi}\int dr^3 \frac{r - R}{|r - R|^3} \times j(r) = -\sigma(R) B_Z, \tag{3}$$

i.e., the magnetic shielding σ is the negative proportionality constant between the external magnetic field B_Z and the induced field B_{ind}. The total magnetic field at the nucleus N is given as the sum of the external and internal magnetic fields

$$B_{\mathrm{local}}(R_N) = B_Z + B_{\mathrm{ind}}(R_N) = (1 - \sigma(R_N)) B_Z. \tag{4}$$

The corresponding NMR resonance condition is

$$\Delta E = -\gamma_N (1 - \sigma_Z) B_Z \hbar I_Z = (-\omega_0 + \omega_{CS}) \hbar I_Z. \tag{5}$$

Due to the strong magnetic field B_Z the shielding tensor σ is truncated to its z-components

$$\sigma_Z = \sigma e_Z. \tag{6}$$

A more common way to represent the magnetic shielding tensor is an expectation value

$$\sigma = \langle \Psi_0 | \hat{\sigma}_N | \Psi_0 \rangle. \tag{7}$$

The wave function Ψ_0 is the solution of the Hamilton operator or Fock operator of the molecular system without external perturbations, and it is related to the ground state energy E_0. The shielding operator $\hat{\sigma}_N$ within the Coulomb gauge restriction yields in the general form introduced by Ramsey in 1950[8]

$$\hat{\sigma}_N = \hat{h}_N^{\text{dia}} - \frac{2}{m_e} \sum_{k \neq 0} \frac{\hat{h}_N^{\text{orb}} \left| \Psi_k^{(0)} \right\rangle \left\langle \Psi_k^{(0)} \right| \left(\hat{h}_N^{\text{pso}} \right)^T}{E_k - E_0}. \tag{8}$$

This expression was deduced by the Rayleigh-Schrödinger perturbation theory. The Ramsey expression contains the electron exited states $\Psi_k^{(0)}$ related to the energy E_k, and the operators $\hat{h}_N^{\text{dia}}$, $\hat{h}_N^{\text{orb}}$ and $\hat{h}_N^{\text{pso}}$ [3,9] which describe the involved electron interactions. The coupling of the external field to the orbital motion is expressed by a sum of orbital angular-momentum operators

$$\hat{h}_N^{\text{orb}} = \frac{1}{2a_0} \sum_k \hat{l}_{kO}. \tag{9}$$

The nuclear spin–orbit operator or orbital hyperfine operator describes the coupling of the nuclear magnetic moments to the orbital of the electrons

$$\hat{h}_N^{\text{pso}} = \alpha^2 a_0^2 \sum_k \frac{\hat{l}_k}{r_k^3}. \tag{10}$$

The diamagnetic electronic operator has the form

$$\hat{h}_N^{\text{dia}} = \frac{\alpha^2}{2} a_0 \sum_k \frac{(\hat{r}_{kO} \hat{r}_k) \hat{I} - \left(\hat{r}_k \hat{r}_{kO}^T \right)}{r_k^3}, \tag{11}$$

with the Sommerfeld's fine structure constant $\alpha \approx 1/37$, and the Bohr radius $a_0 \approx 0.53$ Å. The second order perturbation theory is included in the shielding operator itself. In principle, the calculation of this NMR parameter does

not depend on the exact wave function model. The Ramsey expression cannot be employed for most calculations, since it requires an explicit representation of the excited states. In practice, variational methods are used because all conventional *ab initio* methods can be cast into a variational form (HF, CI, MCSF, CC, MP, and DFT).[10–12] The magnetic shielding energy is a correction to the total molecular energy. The shielding can be represented by a Taylor expansion of the total energy with respect to the magnetic field B and the nuclear magnetic moment $\mu = \gamma\hbar I$

$$\begin{aligned} E(B,\mu) = E(0) &+ \sum_i \left(\frac{dE}{dB_i}\right)_{B=0} B_i + \sum_i \left(\frac{dE}{d\mu_i}\right)_{\mu=0} \mu_i \\ &+ \sum_{i,j} \left(\frac{d^2E}{dB_j dB_i}\right)_{B=0} B_j B_i + \sum_{i,j} \left(\frac{d^2E}{d\mu_j d\mu_i}\right)_{\mu=0} \mu_j \mu_i \\ &+ \sum_{i,j} \left(\frac{d^2E}{dB_j d\mu_i}\right)_{B,\,\mu=0} B_j \mu_i + \cdots \end{aligned} \tag{12}$$

The second derivative of the energy with respect to the magnetic field and the nuclear magnetic moment can be identified as the magnetic shielding

$$\sigma_{ij} = \left.\frac{d^2E}{dB_j d\mu_i}\right|_{B,\mu=0}. \tag{13}$$

The corresponding derivative of the Hamilton operator is

$$\frac{d^2h}{dB_j d\mu_i} = \frac{\mu_0}{4\pi}\frac{e^2}{2m}\frac{(r_e r)\delta_{ji} - (r_e)_i r_j}{|r|^3}. \tag{14}$$

The directly measured magnetic shielding tensor is symmetric, the anti-symmetric contribution is truncated. The symmetric part σ^s of

$$\sigma = \sigma^s + \sigma^a = \left(\sigma + \sigma^T\right)/2 + \left(\sigma - \sigma^T\right)/2 \tag{15}$$

can be diagonalized with the use of a transformation matrix $\mathbf{T}$ and its transpose $\mathbf{T}^{\mathbf{T}}$

$$\sigma^s = \begin{pmatrix} \sigma_{xx} & \sigma_{xy} & \sigma_{xz} \\ \sigma_{xy} & \sigma_{yy} & \sigma_{yz} \\ \sigma_{xz} & \sigma_{yz} & \sigma_{zz} \end{pmatrix} = \mathbf{T}^{\mathbf{T}} \begin{pmatrix} \sigma_{11} & 0 & 0 \\ 0 & \sigma_{22} & 0 \\ 0 & 0 & \sigma_{33} \end{pmatrix} \mathbf{T}. \tag{16}$$

As already mentioned, the vector potential can be chosen to satisfy the Coulomb gauge condition

$$A_Z = 1/2\ B_Z \times (r - R_0), \tag{17}$$

i.e., the magnetic field is independent of the origin, the gauge origin R_0, which was set to be zero. In order to be consistent with quantum mechanics the real wave function $|\chi\rangle$ of an electron has to be multiplied with a gauge factor and thus becomes complex

$$|\chi'(B_Z)\rangle = U(r)|\chi(0)\rangle \tag{18}$$

with

$$U(r) = \exp\left[-i\frac{e}{\hbar}(1/2\, B_Z \times (R_N - R_0))r\right]. \tag{19}$$

The magnetic shielding Hamilton operator has the form

$$\hat{H}_{\mathrm{MS}} = \omega_{\mathrm{MS}}\hbar\hat{I}_Z \tag{20}$$

with

$$\omega_{\mathrm{MS}} = \gamma B_Z\left(\sigma_{\mathrm{iso}} + \frac{\Delta_\sigma}{3}\left[\left(3\cos^2(\theta) - 1\right) - \eta_\sigma \sin^2(\theta)\cos(2\varphi)\right]\right). \tag{21}$$

θ and φ are the polar angles of the principal axis system with respect to the z-direction. The three independent parameters isotropy σ_{iso}, anisotropy Δ_σ, and asymmetry η_σ, are obtained from the principal tensor values σ_{11}, σ_{22} and σ_{33}, which fulfill the following condition

$$|\sigma_{33} - \sigma_{\mathrm{iso}}| \geq |\sigma_{11} - \sigma_{\mathrm{iso}}| \geq |\sigma_{22} - \sigma_{\mathrm{iso}}|. \tag{22}$$

The isotropic value is given by

$$\sigma_{\mathrm{iso}} = 1/3(\sigma_{11} + \sigma_{22} + \sigma_{33}), \tag{23}$$

while the anisotropic value is given by

$$\Delta_\sigma = 3/2(\sigma_{33} - \sigma_{\mathrm{iso}}). \tag{24}$$

The asymmetry is defined as

$$\eta_\sigma = \frac{\sigma_{22} - \sigma_{11}}{\sigma_{33} - \sigma_{\mathrm{iso}}}, \quad 0 \leq \eta_\sigma \leq 1. \tag{25}$$

In NMR spectroscopy, the chemical shifts δ are extracted from the spectra with frequencies ν instead of the magnetic shieldings σ

$$\delta\,[ppm] = 10^6 \frac{\nu - \nu_{\mathrm{ref}}}{\nu_{\mathrm{ref}}} = \frac{\sigma_{\mathrm{ref}} - \sigma}{1 - \sigma_{\mathrm{ref}}} \approx \sigma_{\mathrm{ref}} - \sigma. \tag{26}$$

These shifts δ are calculated from the shieldings σ or frequencies ν of standardized nucleus-specific references ν_{ref} or σ_{ref}. The chemical shift δ is positive towards high frequency, i.e., 'downfield' or 'low field'. The magnetic shielding σ is positive towards low frequency, i.e., 'upfield' or 'high field'.

The traditional definitions of the three principal value components (δ_{11}, δ_{22}, and δ_{33}), isotropy δ_{iso}, anisotropy Δ_δ and asymmetry η_δ of the chemical shift are equivalent to those of the magnetic shielding. This traditional scheme is indefinite. It leads to a loss of physical and chemical generality which is disadvantageous. Therefore, besides the isotropy two new parameters, span Ω and skew κ, are often introduced and used instead of the anisotropy Δ_δ and asymmetry η_δ.[13] The full range of the spectrum is called span Ω

$$\Omega = \sigma_{33} - \sigma_{11} = \delta_{11} - \delta_{33} > 0, \tag{27}$$

and the skew κ describes the asymmetry information of the magnetic shielding (chemical shift)

$$\kappa = 3\frac{\sigma_{\mathrm{iso}} - \sigma_{22}}{\sigma_{33} - \sigma_{11}} = 3\frac{\delta_{22} - \delta_{\mathrm{iso}}}{\delta_{11} - \delta_{33}}, \quad -1 \le \kappa \le 1. \tag{28}$$

3. COMPUTATIONAL METHODS FOR CHEMICAL SHIFT CALCULATIONS

3.1. General overview

In principle, a chemical shift calculation represents a perturbation theory, because of the presence of an external field B_Z and magnetic moments due to the dipole character of nuclei. Therefore, perturbations to the Hamiltonian and the wave function have to be considered. The next important point is that the origin of the vector potential A_Z is not fixed due to the relation $B_Z =$ rot A_Z. Any change of the gauge origin R_0 should not change any measurable observable. Therefore, a gauge transformation of the wave function $|\chi\rangle$ and Hamilton operator h is essential

$$|\chi\rangle \longrightarrow |\chi'\rangle = \exp(-i\Lambda(r))|\chi\rangle \tag{29}$$

$$h \longrightarrow h' = \exp(-i\Lambda(r))h\,\exp(i\Lambda(r)) \tag{30}$$

with the gauge factor defined by

$$\Lambda(r) = \frac{e}{\hbar}\left(1/2\, B_Z \times \left(R_0' - R_0\right)\right)r. \tag{31}$$

With this so-called gauge transformation, a shift of the gauge origin from R_0 to R_0' is achieved. Most of the theoretical methods differ in this point. The most important is the GIAO approach. For this, the atomic orbitals $|\chi'(B_Z)\rangle$ include the gauge, they are gauge dependent. This was first investigated by London.[14] Ditchfield adopted them to quantum chemical shift calculations and originally called them 'gauge-including atomic orbitals (GIAO)'.[15] Later Hansen and Bouman suggested the name 'gauge-invariant atomic orbitals'. Integrals are evaluated in terms of GIAOs with the result that R_0 is eliminated, hence the name 'gauge invariant'.

Other important local gauge origin schemes are 'individual gauge for localized orbitals (IGLO)',[16] 'localized orbital local origin (LORG)'[17] and 'second order LORG (SOLO)'.[18] All are based on individual gauges for molecular orbitals rather than atomic orbitals. However, as standard Hartree-Fock and density functional orbitals are usually delocalized they are not well suited for local gauge origin approaches. Therefore, these schemes use special localized orbitals. In practice, the most widely used method is the GIAO approach. Other methods are 'include individual gauges for atoms (IGAIM)'[19] or a 'continuous set of gauge transformations (CSGT)'.[20] All these methods are restricted to finite systems such as molecules and clusters that are isolated in free space. For pseudo-potentials and plane waves Mauri, Pfrommer, and Louie developed a method (MPL)[21] to compute the chemical shift in extended condensed matter systems using periodic boundary conditions. It can be applied to periodic systems, and with a super-cell technique also to disordered systems such as liquids.

Another major point in which the theoretical methods differ is the quantum chemical approach to solve the operator equation of the Hamilton operator itself. The most important schemes are Hartree-Fock self consistent field (HF-SCF), density functional theory (DFT) and multi-body second order perturbation theory (MP2). Different combinations have been established, so for instance GIAO-SCF,[22] GIAO-DFT,[23] GIAO-MP2,[24] or DFT-IGLO.[25] Most precise measurements on small systems were done with coupled cluster methods, as for instance GIAO-CCSDT-n.[26]

3.2. Bond polarization theory

The bond polarization theory is a semi-empirical approach applied within the context of COSMOS force field calculations.

According the Ramsey expression, the chemical shift tensor can be considered as a sum of one-electron operators, and within the BPT approach[27,28]

the chemical shift tensor is expressed by

$$\left\langle \Psi_0 | \hat{\delta}_{\alpha\beta} | \Psi_0 \right\rangle = \sum_{i}^{i \in A} \sum_{\alpha'\beta'} D^{i}_{\alpha\alpha'} D^{i}_{\beta\beta'} \left(n_i \delta_i^{\alpha'\beta'} + n_i^2 A_i^{\alpha'\beta'} \left[\left\langle \chi_A^i | \hat{V} | \chi_A^i \right\rangle - \left\langle \chi_B^i | \hat{V} | \chi_B^i \right\rangle \right] \right), \tag{32}$$

where the matrix elements $D_{\alpha\alpha'}$ describe the coordinate transformation from the bond orbital frame to the reference frame. The first sum runs over all bond contributions of atom A. The bond polarization matrix elements are given by

$$\left\langle \chi_\lambda^i | \hat{V} | \chi_\lambda^i \right\rangle = \sum_{x}^{\text{charges}} \sum_{k} h_k^2 \int dr^3 \phi_k^\lambda(r) \frac{Q_x}{|R_x - r|} \phi_k^\lambda(r), \tag{33}$$

with the charges Q_x at position R_x, the Slater type orbitals[29] $\phi_k^\lambda(r)$, and the bond coefficients h_k. The first sum runs over all polarizing atomic charges. The polarization parameters $\delta_i^{\alpha'\beta'}$ and $A_i^{\alpha'\beta'}$ are obtained by calibration procedures.[30,31] A collection of crystal structures and single crystal chemical shift measurements[32,33] is used to establish a set of linear equations. To some extent *ab initio* results are exploited (Fig. 1).

The correlation coefficient obtained from the parameter calibration is $R = 0.994$ with a standard deviation of SD = 7.2 ppm. If the parameters $\delta_i^{\alpha'\beta'}$

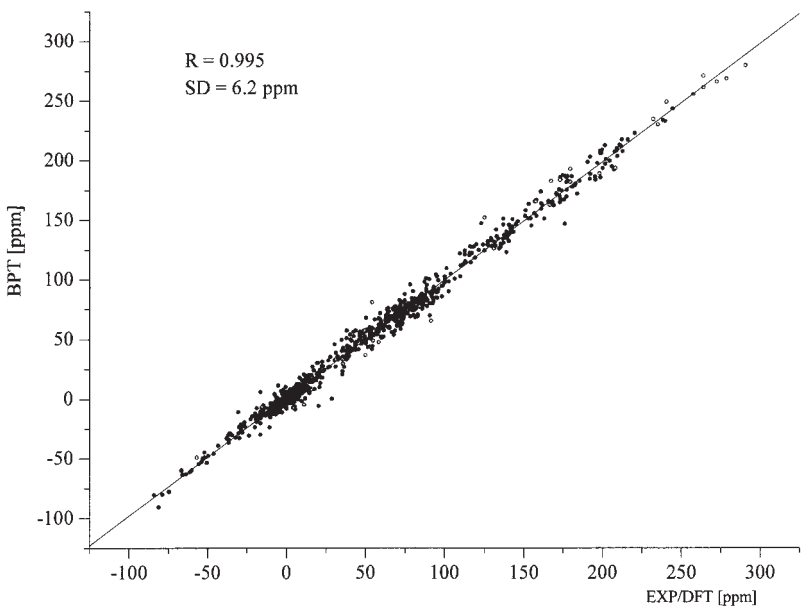

Fig. 1. Correlation of ^{13}C chemical shift tensor components obtained by BPT calculations with experimental values.

and $A_i^{\alpha'\beta'}$ are determined, only the matrix elements $\langle\chi_\lambda^i|\hat{V}|\chi_\lambda^i\rangle$ and the occupation numbers n_i[34,98] have to be calculated. As they are all expressed analytically, calculations with the BPT formula are highly efficient. In Eq. (32) there are two sums, the first runs over all bond contributions of the atom under consideration, and the second runs over all polarizing charges of $\hat{V}$. Hence, if the charges are known the computational cost for a chemical shift calculation is proportional to the number of atoms N.

For the chemical shift calculation, charges are essential. They are calculated within the BPT approach.[35]

$$Q_A = \sum_i^{i\in A}\left(n_i q_i + n_i^2 A_i^q\left[\left\langle\chi_A^i|\hat{V}|\chi_A^i\right\rangle - \left\langle\chi_B^i|\hat{V}|\chi_B^i\right\rangle\right]\right). \tag{34}$$

By investigating the charge equations, it is obvious that charges Q_A have to be estimated from charges Q_x.

$$Q_A = \sum_i^{i\in A}\left(n_i q_i + n_i^2 A_i^q\left[\left\langle\chi_A^i\left|\frac{Q_x}{|R_x - r|}\right|\chi_A^i\right\rangle - \left\langle\chi_B^i\left|\frac{Q_x}{|R_x - r|}\right|\chi_B^i\right\rangle\right]\right). \tag{35}$$

The parameters q_i and A_i^q were calibrated against natural population analysis charges of a set of 175 structures consisting of H, C, N, O, F, Si, P, S, Cl, and Zn atoms (Fig. 2).[36]

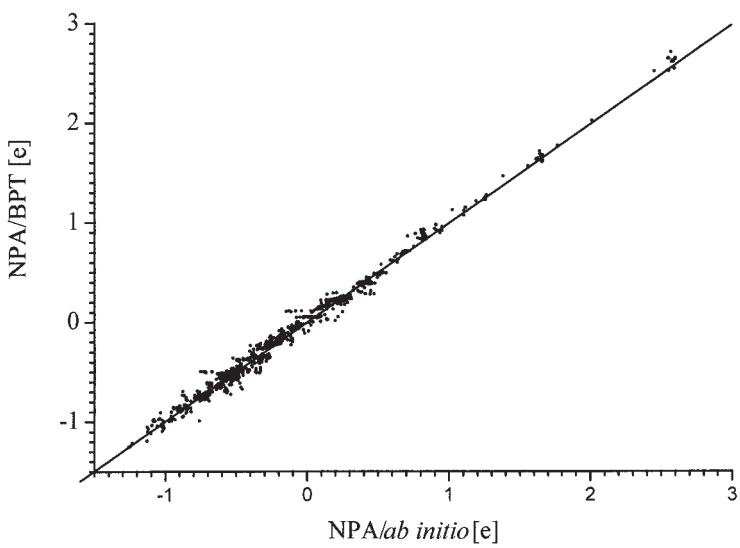

Fig. 2. Correlation of atomic charges obtained by BPT calculations with charges from 6-31G(d,p) calculations on a series of small molecules. The population analysis was performed using the NPA (Natural Population Analysis) method.

The computational time for setting up all charge equations is proportional to N^2. To calculate the charges means solving this set of linear equations for which the number of floating point operations is proportional to N^3.

4. EMPIRICAL AND SEMI-EMPIRICAL STRUCTURE DEPENDENCES OF CHEMICAL SHIFTS

4.1. Bond orbitals and chemical shifts

A number of extremely valuable direct correlations of the chemical shift with structural parameters have been discovered. In many cases it is problematic to provide a theoretical explanation for these relations. This is not readily achieved by standard quantum chemical calculations, since the environment of our nucleus of interest cannot be easily singled out, and the questions remains as to whether a result may be transferred to other molecular systems. In calculations were localized orbitals are used instead of canonical orbitals (as for instance IGLO), we can clearly distinguish between the local contributions of the bond that is directly connected to the nucleus of interest and other through-space contributions. The local bond contributions or bond increments obtained from IGLO calculations[37] have the general problem that their transferability is prohibited by the change of the shift generated by placing the bonds into different electronic environments. The largest influence is the redistribution of the electrons within the bonds by polarization and the conjugation of multiple bonds. In BPT calculations we account for both effects, hence the BPT bond increments are to a high degree transferable.

In many cases it was supposed that chemical shift changes of nuclei other than protons can be explained by the variations in bond angle upon changing the hybridization state. Within the light of the IGLO investigations[37] this is not a major influence. Schindler states that it is of much more concern whether the centre of the charge distribution within a bond is shifted towards or away from the nucleus.

According to the bond polarization theory we get the following major chemical shift contributions:

(i) bond increment AB, depending on the element A and B and on the bond type (σ or π);
(ii) occupation number n of the π bond connected to the bond length;
(iii) bond polarization by surrounding charges;
(iv) through-space contributions.

The latter contribution can play a major role in proton chemical shifts, but the much larger span of the chemical shifts of other nuclei is dominated by

effects (i)–(iii). Within the following chapters we will concentrate on empirical and semi-empirical correlations that possess predictive potential and have been used in structure elucidations.

4.2. Bond length dependences

One of the most striking examples for the bond length dependence of the chemical shift is the correlation of the $\delta_{||}$ CS tensor component of ^{29}Si nuclei in silicate compounds. This dependence was first observed by Grimmer.[38]

Figure 3 depicts this correlation with additional values of Heidemann.[39] The authors had restricted their values to tensors measured from nuclei with a local surrounding of virtual C_{3v} symmetry, and they correlated the values against the lengths of Si–O bonds lying along the parallel tensor direction. What we observe in this case is the change in the parallel CS tensor contribution caused by a redistribution of π electrons between the parallel bond and the other three Si–O d–p–π bonds. Silicon can acquire d electrons from π back-donation.

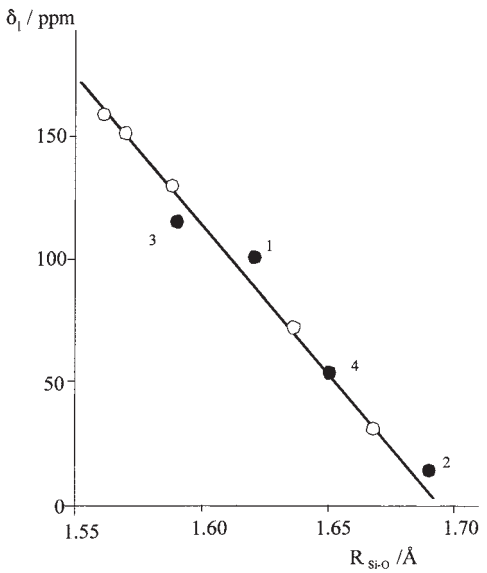

Fig. 3. Correlation of the $\delta_{||}$ CS tensor components of ^{29}Si nuclei in silicate compounds with the bond lengths of the Si–O bonds directed along the axially symmetric tensors. Only compounds with nearly or fully axially symmetric chemical shift tensors are included. The values of Grimmer[38] are supplemented with additional data from Heidemann[39] [1: Calcio-Chondrit (100 ppm, 1.62 Å); 2: α-Di-Calcium-Silicate-Hydrate (14 ppm, 1.69 Å); 3: Phyllo-Silic-Acid (115 ppm, 1.59 Å); 4: Dellait (54 ppm, 1.694 Å)].

The d–p–π valence v varies in our example within the range from $v = 0.1$ to 0.7 (see Fig. 3), and the contributions of the bond increments are directly proportional to the bond occupation number $n = 2v$.

The same principle was used to correlate ^{31}P CS tensors with P–O bond lengths. Olivieri[40] constructed the tensors of phosphate compounds from four additive bond contributions being proportional to the number of π electrons, and derived a formula to predict the three principal tensor components from the P–O bond lengths. Even if polarization and through-space terms are neglected, reasonable correlations are obtained since the π bond occupation is the leading term. For quantitative predictions, however, at least the polarizations should be included.[41] Since in the case of phosphates (and the same holds for silicates) the total number of d electrons does not vary appreciably, no good correlations between bond lengths and isotropic chemical shifts are observed.

4.3. Angular influences

One of the most frequently used geometric dependences was discovered by Smith and Blackwell[42] for ^{29}Si chemical shifts in silicates. It turned out that the Si–O–Si bond angle has a significant influence on the chemical shift.[43] According to Smith and Blackwell the ^{29}Si chemical shift should depend on the mean secants of the four Si–O–Si angles. Engelhardt and Radeglia[44] derived from the variation of the oxygen electronegativity with hybridization a $\cos\alpha/(\cos\alpha - 1)$ dependence. According to bond polarization theory[45] the central Si–O bonds are polarized mainly by the charges on the next neighbour silicons, and then the geometry dependence of the bond polarisation energy causes the change in chemical shifts [see Eq. (33)]. Again the oxygen hybridization is responsible for most of the change. Given the scatter of the data and the weak curvature, however, there is no clear preference for one or another formula. Nevertheless, this bond angle correlation had enough predictive force to solve assignment problems in silicates and to calculate angular distribution functions in vitreous silica.[46]

Keeping in mind the theoretical concept, is not surprising that correlations between Si–O–Al angles with ^{29}Si and ^{27}Al chemical shifts[47,48] were discovered. Since aluminum has a different atomic charge than silicon, one has to account for this fact by empirical correlations.[49] A theoretical investigation comparing calculations and empirical structure dependences was performed by Xue,[50] who reviewed many developments within the field of ^{29}Si, ^{17}O and ^{1}H NMR properties. For ^{31}P chemical shifts a dependence on the O–P–O angle is discussed, which can be of help in DNA/RNA structure investigations (see Ref. 51).

4.4. Through-space contributions

The external magnetic field B_0 induces currents in bonds, lone pairs and inner shell orbitals of our molecular systems, and these currents are the source of the chemical shifts. Adopting the picture of localized bond orbitals, through-space contributions are caused by charge distributions of bonds that are not directly connected to the nucleus under consideration. Provided that the charge distributions are sufficiently far away so that their electron density in the vicinity of the nucleus can be neglected, this type of interaction can be approximated by the McConnell equation[52]

$$\sigma_{\alpha\beta} = \frac{1}{N4\pi}\left(\frac{1}{R^3}\chi_{\alpha\beta} - \frac{3}{R^5}\chi_{\alpha\gamma}R_\gamma R_\beta\right), \tag{36}$$

and for the mean value

$$\sigma = \frac{1}{N4\pi}\frac{\Delta\chi}{R^3}\left(1 - 3\cos^2\vartheta\right). \tag{37}$$

R is the vector from the nucleus to the origin of the magnetic point dipole created by the charge distribution with the susceptibility χ.

There have been many attempts to trace back the effects observed in proton chemical shifts to these so-called magnetic neighbour susceptibility effects, but in some cases the wrong sign of the effect was predicted or unrealistically large magnetic bond susceptibilities were needed. Recent analysis of through-space contributions using GIAO-HF and IGLO-DFT calculations of simple systems revealed that electronic effects are dominant, and in the case of the interaction of a C–H bond with a π bond they are even of opposite sign than predicted from magnetic neighbour anisotropy considerations.[53]

Since polarization effects vanish with $1/R$ whereas the McConnell equation (2) contains $1/R^3$, it is obvious that polarisation effects can be observed when magnetic anisotropy effects are far beyond 0.1 ppm, hence polarizations should not be neglected when using the McConnell equation for isotropic chemical shifts.

Only the anisotropy of the magnetic susceptibility influences the isotropic mean value, whereas the complete susceptibility tensor contributes to the chemical shift anisotropy [see Eq. (36)]. The influence of the susceptibility of a spherical symmetric charge distribution on the isotropic chemical shift of a nearby nucleus will be zero, but there is a contribution to the chemical shift tensor. Especially in solid state proton chemical shift investigations this effect is quite remarkable and can be observed when studying proton chemical shift anisotropies.

In addition to the through-space influence, a ring current contribution is introduced in semi-empirical chemical shift calculations (see Section 4.6).

Ab initio calculations using the IGLO method were able to answer the question whether there is an extra contribution from real circulating aromatic currents.[54] Since the IGLO works with localized electrons, it must fail to include this effect since only orbital currents in localized orbitals are properly described. No special ring current effect in ^{1}H or ^{13}C shieldings could be detected.

4.5. Hydrogen bonds

Hydrogen bonding is of high interest because in many materials and biological molecules hydrogen bonds are responsible for the stability of secondary and tertiary structures. An overview on solid state NMR investigations of hydrogen bonds is given by Brunner and Sternberg.[55] Proton solid state measurements and diffraction investigations revealed a close relation between hydrogen bond distances $H\cdots X$ and chemical shifts. From theoretical considerations[56] there should be a $1/R$-dependence of the chemical shift. The correlation that included only hydrogen bonded O–H protons gave a correlation coefficient of $R = 0.92$, and the correlation to the bond polarization energies was even better ($R = 0.95$) (see Fig. 4).

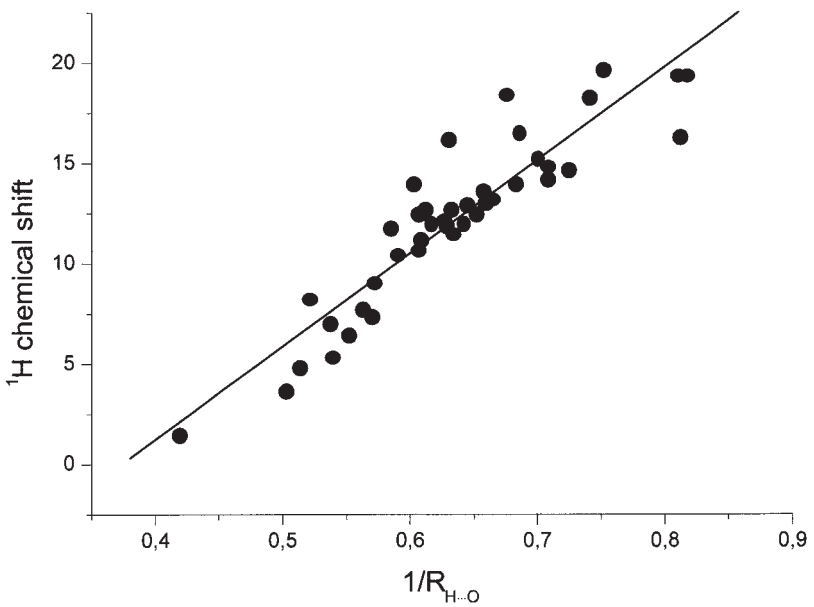

Fig. 4. ^{1}H NMR chemical shifts of $O–H\cdots O$ hydrogen bonded protons in different compounds plotted versus $1/R_{H\cdots O}$. All distances R are obtained from neutron diffraction investigations.

From these results it was concluded that hydrogen bonds are dominated by polarization, but in general the proton chemical shift is influenced by through-space contributions (see previous chapter) as well. Since through-space contributions affect the anisotropy even more than the chemical shift mean value, no good correlations between distances and proton CS anisotropies are observed.

There is clear evidence for a distinctive influence of hydrogen bonds on carbonyl carbons in peptides. Wei *et al.*[57] performed solid state NMR investigations on 17 different polypeptides with known structure. They found a correlation of the δ_{22} tensor component (using the convention $\delta_{11} > \delta_{22} > \delta_{33}$) with the N···O hydrogen bond distance:

$$\delta_{22}^{C^*=O}(\text{Ala}) = 366.8 - 63.8 R_{N\cdots O}\ (\text{ppm}) \quad (R = -0.83) \tag{38}$$

$$\delta_{22}^{C^*=O}(\text{Gly}) = 285.0 - 37.4 R_{N\cdots O}\ (\text{ppm}) \quad (R = -0.81) \tag{39}$$

δ_{22} is the tensor component that is in close relation to the direction of the carbonyl C=O bond. Similar observations are reported from Kameda *et al.*[58] The correlations to isotropic carbonyl chemical shifts are found to be much weaker.

4.6. Empirical and semi-empirical chemical shift prediction models

There are numerous attempts to channel the different empirical observations and geometry dependences chemical shifts into predictive schemes, and some of them have been successfully used in structure elucidation. One of these models is CHARGE(X) where X reached 5 in recent publications.[59] The central point is that for protons and certain other resonances a correlation of atomic charges with chemical shifts was observed. Within the framework of the bond polarization theory we arrive in the case of a proton at a linear dependence with just one parameter for its chemical shift and for the atomic charge. Therefore, one dependence can be easily calculated from the other.

Within the CHARGE program an elaborated scheme for α, β, and γ effects on the proton charges is established depending on electronegativity differences. In addition to the charge dependence δ^{e} the authors included three more terms in their chemical shift formula to account for other effects, namely: (i) steric shift δ^{steric}, (ii) neighbour anisotropy shift δ^{ani}, and (iii) electric field effect shift δ^{E}.

In models that are used for protein chemical shift prediction (see e.g., Williamson and Asakura,[60] and Asakura *et al.*[61]) the influence of the

environment on the chemical shift is decomposed into the following terms:

$$\delta^{\text{exp}} = \delta^{\text{random}} + \delta^{\text{rc}} + \delta^{\text{ani}} + \delta^{E}. \tag{40}$$

The first term is the so-called random coil shift, and the second term is a ring current term to account for susceptibility effects caused by aromatic rings. From a general point of view, the common source of δ^{rc} and δ^{ani} are currents induced by distant charge distributions. Unfortunately there is no closed theory for all these terms that would allow *a priori* to exclude or to include any one interaction or to give a ranking of the terms. Each term has a theoretical background, but the formulae are used with empirical parameters derived from experiment. Therefore, Williamson and Asakura[62] performed a statistical analysis for $C^{\alpha}H$ protons to assess the influence of the different terms and various approximations on their calculation. This paper gives a very comprehensive overview of environmental influences on chemical shifts. Since only one type of hydrogen atom was investigated, the charge effect δ^{e} could not be included into the analysis. No statistical improvement was found upon including a steric term depending on $1/R^6$. For the electric field term

$$\delta^{E} = \varepsilon_1 E_{||} + \varepsilon_2 E^2 \tag{41}$$

it was found[63] that it was sufficient to include the first term which is proportional to the electric field in the direction of the C–H bond direction $E_{||}$ (for a discussion of this equation see Section 5.3). Into the magnetic anisotropy term δ^{ani} only backbone C–N and C=O bonds had to be included. Raynes and Ratcliffe[64] pointed out that even for a molecular system with $C_{\infty v}$ and C_{3v} symmetry, as for instance an idealised X–H bond, the above formula is not correct and the following equation has to be used:

$$\sigma = \sigma^{(0)} - AE_{||} - B_{||}E_{||}^2 - B_{\perp}E_{\perp}^2. \tag{42}$$

The field prefactors are in most papers denoted by A and B, carrying an opposite sign with respect to the original development.

For the ring current shift δ^{rc} three models are discussed: the Haigh–Maillion[65] and the Johnson–Bovey (for review see Ref. 65) formula, and the application of the magnetic point dipole formula for the aromatic ring.[66] All three models establish a proportionality between the chemical shift and the anisotropic magnetic susceptibility as well as a geometric term. In the case of the point dipole model the formula is nearly identical with the McConnell equation (37). The preference for any one of the three models seems to depend on the selected data. Abraham and Griffiths found a preference for the simpler Johnson–Bovey model, whereas in recent investigations[67] the Haigh–Maillion formula was preferred. In general all equations yield correlations to experimental data with correlation coefficients $R < 0.9$ and standard deviation (sd) > 0.2. Investigations

for ^{1}H chemical shifts in DNA with similar methods[68] gave better standard deviations of sd = 0.17 for a span of shifts of 4 ppm.

The starting point for many investigations on peptides and proteins is the famous paper of Spera and Bax,[69] who revealed a clear distinction between the ^{13}C secondary shifts of α and β carbons in α-helical or β-sheet environments (see Fig. 5). The characteristic shift difference between a random coil and the observed value was used in many investigations to identify α-helical or β-sheet regions. Wishart and Sykes[70] transformed these data into a predictive tool to identify α-helices and β-sheets. The authors established rules in the form of a protocol that can be used together with a special shift table, and they also made a program available. Using thoroughly referenced shift data, structural motifs in proteins can thus be identified with a success rate of ~90%. Finally a database of uniformly referenced protein chemical shifts was developed[71] that will be of great value in future protein investigations, because predictions using chemical shift contour maps depend heavily on the reliability of the data. Labudde *et al.*[72] used this database to predict not only the secondary structure of proteins but additionally the amino acid types. Up to now the amino acid prediction has not reached the high validity of the secondary structure prediction, with one exception. Most peptide bonds in proteins are in *trans* conformation. If an amino acid is followed by proline, the *cis* configuration is preferred in 5% of all Xaa–Pro bonds. The probability of these *cis* Xaa–Pro bonds can be predicted using the difference $\delta_{\Delta}(cis, trans)$ of the $^{13}C^{\beta}$ and $^{13}C^{\gamma}$ chemical shifts.[73] For the *cis* conformation the authors found $\delta_{\Delta}(cis) = 4.51\ \text{ppm} \pm 1.17\ \text{ppm}$, while $\delta_{\Delta}(trans) = 9.64\ \text{ppm} \pm 1.27\ \text{ppm}$.

Interesting prospects are opened up by the observation of Tjandra and Bax[74] that the $^{13}C^{\alpha}$ anisotropy is obviously even more dependent on the

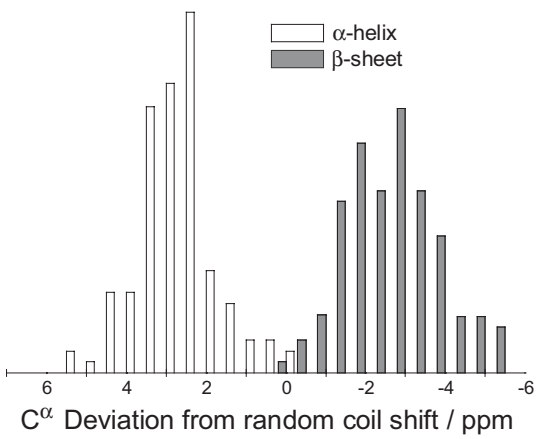

Fig. 5. Analysis of the distribution of $^{13}C^{\alpha}$ and $^{13}C^{\beta}$ chemical shifts as a function of the protein secondary structure (adapted from a figure of Spera and Bax[69]). The authors counted the deviations from random coil chemical shits of carbons in α-helical and β-sheet environments using an empirical chemical shift map.

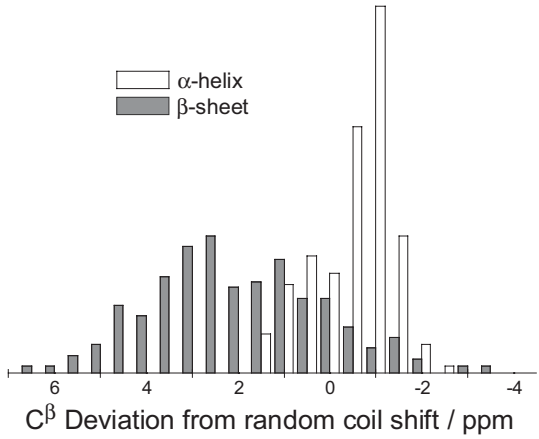

Fig. 5. Continued.

α-helical or β-sheet environment than the isotropic mean value. Eventually, it is possible to train neuronal networks on databases of proteins and use them for chemical shift predictions of proteins with known structure. This task was performed by Meiler[75] for ^{1}H, ^{13}C, and ^{15}N chemical shifts, which can now help to assign chemical shifts and to support or reject proposed structures.

5. CHEMICAL SHIFT DERIVATIVES

5.1. Chemical shift coordinate derivatives

In geometry optimizations or molecular dynamics calculations the NMR data are used as target functions, by defining proper pseudo-energies as a function of measurements and calculated data. From these energies forces have to be derived that are used to drive the system into the desired direction. In the case of chemical shifts these pseudo-energies depend on the calculated values, hence we need to calculate the derivatives of the chemical shifts with respect to the molecular coordinates.

There is also an immediate interest in coordinate derivatives of chemical shifts in situations where temperature effects, isotope chemical shifts, vibrational or rotational corrections are investigated. For these purposes chemical shielding hyper-surfaces have been calculated using *ab initio* methods (for a discussion see Jameson,[76] Bennett and Raynes,[77] Raynes and Bennett,[78] Chesnut and Wright,[79] de Dios *et al.*,[80] Sundholm *et al.*,[81] Sundholm and Gauss,[82] and Auer *et al.*[83]), and the slope with respect to any internal coordinate can be calculated numerically.

For polyatomic molecules the computational burden grows rapidly, since for every combination of internal coordinates a single point calculation has to be performed. Moreover, there are two other problems: (i) the *ab initio* calculations have to be performed for non-equilibrium states, and (ii) strong environmental influences on the chemical shifts will change the hyper-surfaces so that only weakly interacting molecules can be discussed on the basis of a hyper-surface of a single molecule. Therefore, it would be much more desirable to calculate the analytical shift derivatives directly.

In proteins the main influence on the C^{α} and C^{β} chemical shifts is exerted by the type of amino acid and the backbone dihedral angles (φ, ψ). In this case it is possible to limit the calculation of the derivatives to these relevant effects.

A special case occurs for macroscopically oriented samples, when the change of the shift along the field direction δ_{zz} is monitored as a function of the sample tilt angle:

$$\delta_{zz} = \mathbf{D}_{z\alpha}\mathbf{D}_{z\beta}\delta_{\alpha\beta}. \tag{43}$$

Here **D** is the matrix for the transformation of the tensor to the laboratory system. If the δ_{zz} values are used as constraints in structure refinement, we have to calculate derivatives of the transformation matrices **D** with respect to the coordinates.[84]

5.2. Chemical shift polarizabilities

The following chemical shielding concept is used in many papers to discuss the influence of uniform electric fields E (Einstein's sum convention is applied for double Greek indices):

$$\sigma_{\alpha\beta} = \sigma^{(0)}_{\alpha\beta} + \sigma^{(1)}_{\alpha\beta\gamma}E_{\gamma} + \frac{1}{2}\sigma^{(2)}_{\alpha\beta\gamma\delta}E_{\gamma}E_{\delta}, \tag{44}$$

where $\sigma^{(1)}$ is the chemical shielding polarizability tensor, and $\sigma^{(2)}$ is the chemical shielding hyperpolarizability tensor. Equations (41) and (42) in Section 4.6 were derived from the above formula (44) for molecules in solution that re-orient quickly on the NMR time scale. To account for the non-uniformity of molecular electric fields, further terms have to be added to Eq. (44) containing not only the electric field but also its gradients with respect to the tensor directions.[85]

Buckingham and Pople[86] derived the equation from a perturbation treatment of atoms or molecules in a magnetic and a uniform electric field. This treatment requires that the perturbations of the magnetic and the electric field should be of the same order of magnitude. Because of the 1/c prefactor of the magnetic field, only weak electric fields should be considered. In semi-empirical considerations this equation is used to treat perturbations from

nearby charged groups, thereby violating the prerequisites of its derivation. To determine the field prefactors in Eq. (41) (Section 4.6) empirically by fitting them to experimental data is no cure for this principal mistake. These limitations have to be borne in mind when using the formalism to treat molecules in reaction field calculations or to study the influence of charged crystal lattices on chemical shifts. Within the bond polarization theory (Section 3.2) the equations are derived for strong perturbations from electrostatic potentials, hence this formalism should be preferred.

Grayson and Raynes[87] performed *ab initio* calculations on the shielding polarizabilities for protons in C–H bonds and compared their values to other calculations and to empirical values. Applying the nomenclature of Eq. (42) the A value varies from $A = 44.1$ (ppm au) to $A = 111$ (ppm au), thus comparing rather well with the value of $A = 70.0$ (ppm au) obtained by the authors. From this result one has to conclude that it is justified to apply the formalism even to chemic shift changes caused by the strong electric fields of substituents or charged groups. For the second order terms [denoted with B in Eq. (42)] the values scatter over a wide range if different methods are examined. For empirical proton chemical shift formulae it is thus recommended to employ the theoretically derived value of $A = 70.0$ ppm au, and to drop all other than the linear terms of the electric field dependence.

Similar investigations on the influence of electric fields on ^{13}C chemical shieldings were carried out by Grayson and Raynes.[88] As found in former calculations there is no correspondence of their *ab initio* results to experimental observations. In a paper on fluorine chemical shift calculations using the electric field dependence [Eq. (42)]. Pearson *et al.*[89] showed that uniform field terms dominate at $R > 7$ Å and field gradient terms become important at shorter distances of $R < 5$ Å. Generally, it therefore has to be stated that the influence of strong molecular electric fields and crystal lattices should not be treated using Eq. (42). In modern quantum chemical calculations the influence of the surrounding is taken into account by a lattice of point charges around the region of interest. These QM/MM methods are discussed in Section 6.1.

Nymand *et al.*[90] performed molecular dynamics simulations on liquid water, and they used the electric field effect formalism [Eq. (6)] to explain the gas to liquid shifts of the ^{1}H and ^{17}O nuclei. For the proton it turned out that the resulting gas to liquid shift of -3.86 ppm at 300 K compared well with the experimental value of -4.70 ppm, whereas for ^{17}O the method failed to reproduce the experiment. Even if electric field gradient terms are introduced, requiring additional quadrupolar shielding polarizabilities, no better results could be obtained for the ^{17}O gas to liquid shifts.[91] Isotropic proton chemical shifts are obviously a special case where many higher order terms cancel, hence it is justified to use the simple electric field equations in these chemical shift calculations.

5.3. BPT chemical shift derivatives

In the BPT approach the derivative[36,92] of the chemical shift tensor can be analytically derived with respect to the corrdinates:

$$\frac{\partial \delta_{\alpha\beta}}{\partial x_j} = \frac{\partial \left\langle \Psi_0 | \hat{\delta}_{\alpha\beta} | \Psi_0 \right\rangle}{\partial x_j}$$
$$= \sum_{i}^{i\in A} \sum_{\alpha'\beta'} D^i_{\alpha\alpha'} D^i_{\beta\beta'} \left(\frac{\partial n_i}{\partial x_j} \delta_i^{\alpha'\beta'} + 2 \frac{\partial n_i}{\partial x_j} A_i^{\alpha'\beta'} \left[\left\langle \chi^i_A | \hat{V} | \chi^i_A \right\rangle - \left\langle \chi^i_B | \hat{V} | \chi^i_B \right\rangle \right] \right.$$
$$\left. + n_i^2 A_i^{\alpha'\beta'} \left[\frac{\partial \left\langle \chi^i_A | \hat{V} | \chi^i_A \right\rangle}{\partial x_j} - \frac{\partial \left\langle \chi^i_B | \hat{V} | \chi^i_B \right\rangle}{\partial x_j} \right] \right). \qquad (45)$$

Since analytical expressions for the simple one center integrals in Eq. (45) have been worked out, their derivatives can be obtained in a straightforward manner. As for the chemical shift, when the charges are known the computational cost of the chemical shift derivative calculation is proportional to N. Most time consuming is the charge calculation which goes with N^3.

6. STRUCTURE REFINEMENT METHODS

6.1. Molecular force fields and chemical shift pseudo-forces

Given that the chemical shift depends on the atomic coordinates, we face the situation that this is a highly complicated implicit dependence. As in the case of other NMR parameters such as NOEs or J-couplings we will rarely have enough experimental data to determine 3N-6 coordinates. The most promising way to solve this problem is to introduce NMR parameters as constraints into energy calculations. In the search for the most probable structure of a polyatomic molecule like a peptide, one has to find an energy minimum on a hyper-surface possessing a vast multitude of minima. Every experimental constraint will limit the free configurational space and drive the system into the direction of the experimental structure. Even with a large number of constraints we have to search for a global minimum on a multidimensional energy hyper-surface. It is important to realize that the minimum structure will not be the most probable structure, because this will depend on ΔG containing not only the enthalpy but also the entropy. Broad shallow minima may thus be preferred because of the entropic term. Our NMR constraints on the other hand will contain an average over the most probable structures in solution or the solid state. Therefore, in most cases the experimental constraints will drive our molecular system energetically uphill.

One of the most fundamental problems caused by the NMR time scale is discussed by Torda and van Gunsteren.[93] The MD simulation is run in steps of femto seconds, whereas the experimental structure constraints are mean values over several Larmor periods at least (some nanoseconds). NMR constraints should therefore be calculated from mean values of the properties and not from the actual values at each MD time step. For NOEs this means that the pseudo-energies should be calculated from time averaged mean values. The same holds for chemical shifts, which depend heavily on bond length changes caused by vibrations. These effects have to be averaged out, although not over the long time scale of conformational changes. To keep the system responsive to changes in the instantaneous values it is therefore preferable to use a running average. The authors thus propose to use a memory function with a built-in exponential decay:

$$\overline{\delta}(t) = \frac{1}{\tau}\int_0^t e^{-t'/\tau}\delta(t-t')\,dt'. \tag{46}$$

The time constant τ has to be chosen in such way that the influences of rapid motions like vibrations are averaged out while slow conformational changes prevail.

To account for experimental constraints, in most calculations the following pseudo-energy term is added to the total energy:

$$E^{\text{pseudo}} = \frac{k^{\text{CS}}}{2}\sum_n (\delta_n^{\text{theo}} - \delta_n^{\text{exp}})^2. \tag{47}$$

This pseudo-energy depends harmonically on the differences between calculated chemical shifts and experimental values, and it will disappear if these values match. The force constant k^{CS} [in the range of 5 in kJ/(mol ppm^2)] can be chosen such that the pseudo-energies are weighted appropriately, although in principle it would be better to derive individual constants from theoretical starting points. Within the BPT framework it is possible to derive different constants for different types of bond environments and hybridization (see Section 3.2). To calculate chemical shift pseudo-energies we have to assign all chemical shifts, but from a theoretical point of view it would be possible to derive pseudo-forces from measured intensities:

$$E^{\text{pseudo}} = \frac{k_I^{\text{CS}}}{2}\sum_n \left(I_n(\ldots,\delta_m^{\text{theo}},\ldots) - I_n^{\text{exp}}\right)^2. \tag{48}$$

The index k runs over all measured values of the intensity I. This equation does not contain the index i of the experimental chemical shift, because to the intensity at some points of the spectrum may consist of contributions from several nuclear sites. On the other hand, we can only analyze spectra in which the intensities are not biased by experimental conditions such as cross polarization effects. Furthermore, the method only seems to make sense in solid state NMR investigations with broad overlapping lines.

In MD simulations or geometry optimizations pseudo-forces are needed in addition to the pseudo-energies:

$$F_j = k^{\mathrm{CS}} \sum_m \left(\delta_m^{\mathrm{theo}} - \delta_m^{\mathrm{exp}}\right) \frac{\partial \delta_m^{\mathrm{theo}}}{\partial x_j} \tag{49}$$

These forces which drive the system under investigation into the direction of the minimum pseudo-energy contain derivatives of the theoretical chemical shifts with respect to the coordinates. As pointed out in Section 5, the calculation of chemical shift derivatives is even more time consuming than the calculation of the chemical shifts itself. The calculations should be performed at least on the same theoretical level as the chemical shifts. If theoretical or empirical chemical shift contour maps have been worked out in advance, their derivatives can be calculated numerically. If the contour maps are constructed as a function of the dihedral angles (see Sections 6.3–6.4), only the forces with respect to these inner coordinates are readily obtained.

The most desirable approach would be to perform the calculations of the energy, the chemical shifts and their derivatives using *ab initio* methods. Even on fast computers this does not seem to be feasible for systems with much more than 10 heavy atoms. With the advent of DFT calculations the situation improved, but a breakthrough in chemical shift calculations was not achieved. One of the most promising developments is the combination of quantum mechanical *ab initio* methods with molecular mechanics calculations (QM/MM). Cui and Karplus[94] combined the empirical CHARMM force field[95] with HF and DFT calculations. In this framework the chemical shielding calculations can be performed on the GIAO-DFT, -HF or -MP2 level in the QM part of the system under the influence of a larger MM surrounding. The electrostatic perturbations of all relevant matrix elements are treated by a point charge distribution from the MM part of the system, and their influence on the chemical shielding can be studied. Even with the limitations on the size of the QM part this method will be of great value, especially in the treatment of reaction centres in large molecules.

The traditional method for the treatment of large molecular systems using NMR constraints are molecular mechanics force fields like DYANA.[96] It was demonstrated that such empirical force field reproduces the 3D structure rather well and can compete in this aspect with elaborate *ab initio* calculations.

The limitations of molecular mechanics in system size are due to the calculation of the intermolecular energy terms, which scale with the second power of the number of atoms. Hundreds or even thousands of atoms are no real problem for molecular mechanics force field calculations. The most popular method for the search of global minima in NMR force field calculations is to run MD simulations at elevated temperatures (1000 K). At these temperatures the molecules should surmount all conformational barriers and populate extended areas of the configurational space. A larger number of coordinate snapshots is then cooled down in a so-called simulated annealing procedure, or the energy minimum is determined by geometry optimization. The latter method has the advantage that we can weight every structure by its minimum energy. A combination of simulated annealing and geometry optimization is preferred in some investigations to avoid side minima. A short overview on protein structure analysis using NMR constraints is given by Williamson.[97]

The problem of all previous force field methods is that electronic properties cannot be calculated without wave function or electron distribution. Even atomic charges are mostly fixed parameters of the force field, and polarizations of the electron distribution are excluded. One possibility to overcome the limitations of the traditional molecular mechanics is the combination of the BPT with a force field. Within the COSMOS force field (Möllhoff and Sternberg,[98] and Sternberg *et al.*[99]) a two centre bond orbital is constructed for every bond defined in the force field. If the hybridization coefficients and the bond occupation numbers n are calculated from the geometry only the bond polarities are left as free parameters [see Eq. (32)]. Within the framework of the BPT, bond polarities or atomic charges can be readily calculated. Therefore, this force field works with charges that depend in the same way on the 3D structure of the molecular systems as the *ab initio* charge values that were used in the parametrization. The atomic charges are parametrized to reproduce the values obtained by NPA (Natural Population Analysis) analyses of *ab initio* 6-31G(d,p) calculations (for the method see Sternberg *et al.*[100]), and the BPT will reproduce these charges with a correlation of $R = 0.996$ (see Fig. 2). For σ-bonds the occupation number is set as 2, and for conjugated π-bonds the value is estimated from the bond distance.[98] Another interesting feature of the COSMOS force field is the possibility to divide the molecular system into an MM part and a BPT-QM part, which considers only the polarizations caused by the point charges of the MM part. BPT calculations are very fast and scale with the number of atoms multiplied by the number of bonds. Nevertheless the BPT atomic charge calculation is most time consuming step in the force field cycle, hence cutoffs or smaller QM parts help to run efficient simulations. Since all polarizations can be included into the Coulomb energy, the COSMOS force field can be used to study interactions of highly charged systems as for instance ions and peptides.[99]

6.2. Semi-empirical ^{1}H chemical shift prediction methods

To predict proton chemical shifts, methods had been developed using theoretically derived formulae with an empirical parametrization (see Section 4.6). Despite the relatively large scatter of the predictions when plotted versus the experimental values, it was found that the deviations were reduced when calculating the shifts from better refined structures. Proton chemical shifts were thus included as target functions into force field calculations. Kuszewski *et al.*[101] included a harmonic pseudo-energy term into XPLOR.[102] The ^{1}H chemical shifts were calculated according to Eq. (40) with the parametrization of Williamson and Asakura.[62] Derivatives of the theoretical chemical shifts with respect to Cartesian coordinates could be derived more or less easily from the shift formulae. An ensemble of 40 structures was obtained by simulated annealing using restraints consisting of interproton distances, torsion angles, and $^{3}J_{\mathrm{HNH}\alpha}$ coupling constants. This total number of 2933 data points had been collected for human thioredoxin. The authors first studied the impact of a chemical shift refinement with ^{13}C chemical shifts (see Ref. 101) and then using additionally the proton shifts. The final result showed that the rms deviation of the proton chemical shifts decreased from 0.31 to 0.25, but hardly any effect was detected on the coordinates.

This result is in stark contrast to a study of Moyna *et al.*[67] who applied nearly the same formalism for calculating the proton chemical shifts [Eq. (40)]. For the tripeptide under investigation only a limited set of intra-residue proton distances was available. The definition of structure was therefore greatly improved when the proton chemical shift constraints were switched on. The chemical shift refinement reduced the rmsd for the backbone atoms from 1.2 Å to 0.2 Å, and it revealed a single set of conformers with both peptide bonds in *trans* conformation. The shift constraints drove the molecule energetically uphill by 3.9 kcal/mol but produced a well-defined minimum within the energy hyper-surface. Obviously, chemical shift constraints will produce well-defined structures when other constraints are not available from experiment.

6.3. Chemical shift hyper-surfaces from quantum chemical calculations

6.3.1. *Derivation of ^{13}C chemical shifts*

In 1995 Oldfield[103] reviewed the applications of *ab initio* methods to chemical shift structure refinement, with special emphasis on the construction of ^{13}C chemical shift hyper-surfaces $\delta(\varphi, \psi)$ for proteins. de Dios[104] further discussed the range of *ab initio* calculations using NMR chemical shifts, focussing on the construction of computed chemical shift hyper-surfaces for proteins. In a more recent review, Ando *et al.*[105] presented an overview of the interplay

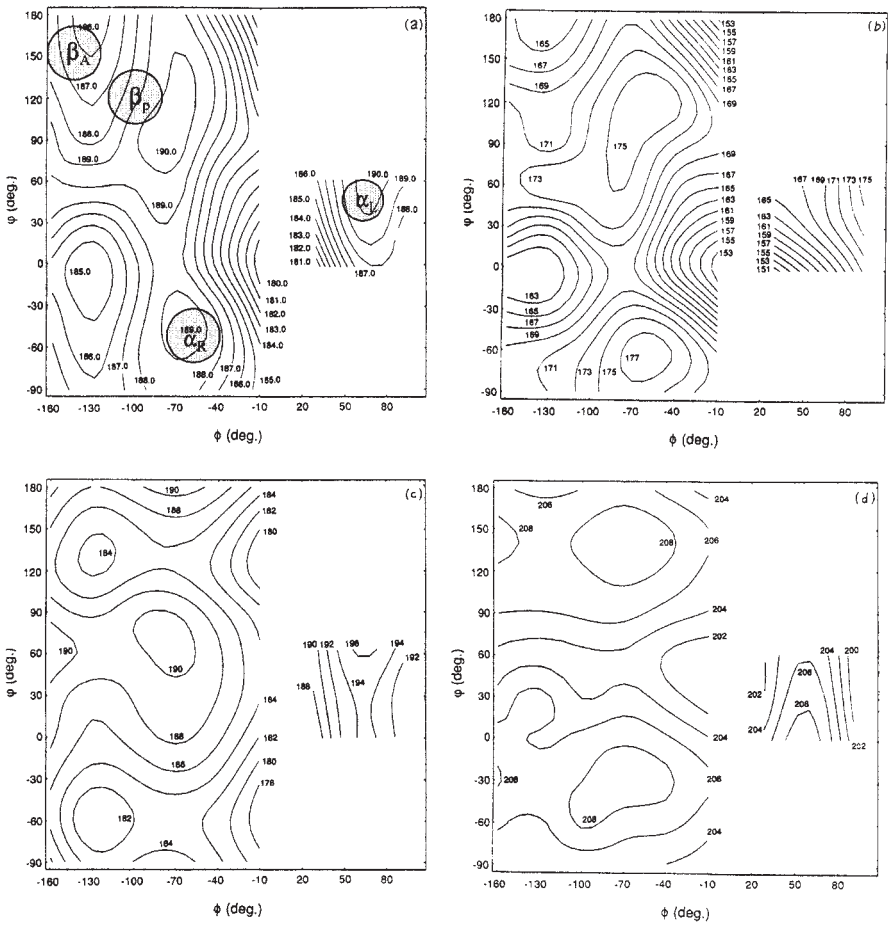

Fig. 6. Dependence of the chemical shielding on the dihedral angles (φ, ψ) for $^{13}C^{\alpha}$ carbons of L-alanine in peptides. The chemical shieldings are calculated with the GIAO-CHF method using a 4-31G basis set. The geometry of *N*-acetyl-*N*′-methyl L-alanine amide was optimized on the 4-31G HF level. The different panels show (a) the isotropic value, as well as the tensor components, (b) σ_{11}, (c) σ_{22}, and (d) σ_{33} (adapted from Asakawa *et al.*[106] with permission of the authors).

between the development of methods for chemical shift calculations and the interpretation of polymer structures. In the present paper we will deal mainly with questions concerning the limitations of pre-calculated chemical shift hyper-surfaces and new developments in this field. Therefore, only a short introduction of the basic concepts will be presented. Figures 6 and 7 illustrate the calculated chemical shift surface $\delta(\varphi, \psi)$ for proteins containing the isotropic values and the principal tensor components for $^{13}C^{\alpha}$ and $^{13}C^{\beta}$, to

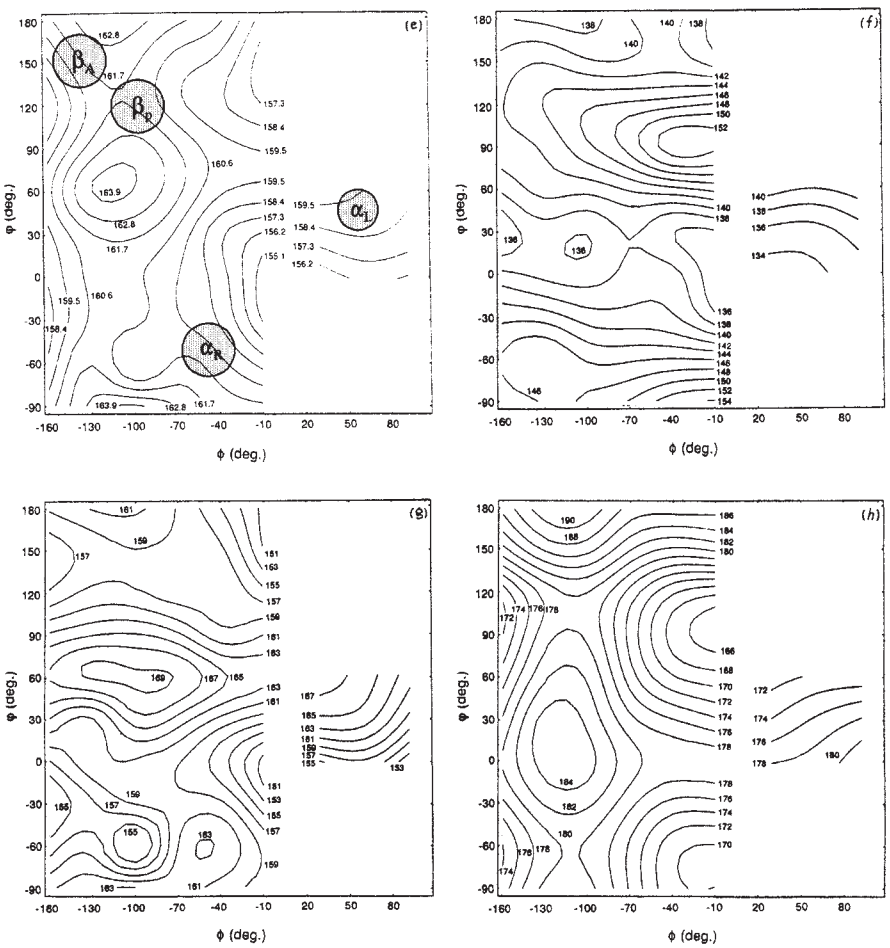

Fig. 7. Figure 6 continued, presenting analogous values for $^{13}C^{\beta}$ carbons, namely the (e) isotropic value, as well as the tensor components (f) σ_{11}, (g) σ_{22}, and (h) σ_{33}.

allow an easy comparison throughout the discussion in this chapter (see also Asakawa *et al.*[106]).

Le *et al.*[107] constructed C^{α} and C^{β} surfaces for peptides from *ab initio* calculations on the Hartree-Fock/GIAO level. Even if considering only the dihedral angles out of all internal degrees of freedom, the computational burden is very high. A separate hyper-surface has to be constructed for each type of amino acid, by calculating the chemical shift dependence on the geometry for small fragments or single amino acids. The results are presented for the formyl-derivatives of glycine, alanine, valine and isoleucine. For the latter two also the side chain dihedral angles are varied. The probability that

a pair of dihedral angles (φ, ψ) leads to a particular experimental chemical shift is given by Z:

$$Z = e^{-\left((\delta_{\exp} - \delta(\phi,\varphi))/(2\varepsilon)\right)^2}, \tag{50}$$

where ε is a width parameter accounting for the error range of the shift surface. If there are two different independent measurements, say C^{α} and C^{β} shifts, then the Z values of the two corresponding surfaces may be multiplied to give a Bayesian consensus or ${}^2Z$ surface. The more of these Z surfaces are being multiplied, the higher becomes the probability for the correct combination of dihedrals. A single Z surface generally displays several regions of possible combinations of dihedrals, but in higher Z surfaces only the overlapping areas of all single surfaces remain. The error range of 10–15° of a ${}^3Z$ surface for the predicted angles seems acceptable, although it is not possible to construct a complete protein backbone from this data source alone. It is much more appropriate to include the data directly into standard force field procedures and seek for solutions that fulfill both the chemical shift and other constraints like NOE derived distances. For this purpose the calculated chemical shielding surfaces $\sigma(\varphi, \psi)$ were scaled to chemical shifts, and derivative surfaces with respect to (φ, ψ) were calculated. The authors[108] included an alanine and three valine surfaces with different side chain conformations into the force field. The solution structures of the protein were refined using combinations of different sets of constraints: the chemical shift hyper-surface (S), the chemical shift Z surface (Z), NOE distance constraints (N), NOE derived hydrogen bonds (H), and ${}^3J$ couplings (J). Inclusion of the chemical shift constraints (S) produced in all cases better defined structures that were closer to the X-ray results. ${}^3J_{\mathrm{HNH}\alpha}$ coupling constraints and N or S constraints are to a certain extent complementary. J constraints depend only on φ, but in proteins φ and ψ are highly correlated. In many cases no J couplings can be determined because of overlapping signals, line width problems, or the values being too small. Therefore, it seems in most cases justified to apply S constraints. Z constraints are apparently not flexible enough to be coupled with other constraints.

For ${}^{13}C^{\alpha}$ and ${}^{13}C^{\beta}$ the shielding hyper-surfaces for the principal tensor components $\sigma_{ii}(\varphi, \psi)$ and $\sigma_{ii}(\varphi, \psi, \chi_1)$ have been worked out in some peptide fragmenxts.[109] On average, the ${}^{13}C^{\alpha}$ tensors of residues in β-sheet regions have a span (~34 ppm) that is larger than for nuclei in α-helical residues (~22 ppm). However, this does not apply for glycine and alanine which exhibit large spans in helical environments (~35–40 ppm). These results can be of great value in solid state structure investigations of peptides (see Section 7.2). This was demonstrated by Heller *et al.*[110] who predicted the backbone angles of a tripeptide from a solid state investigation of the ${}^{13}C^{\alpha}$ chemical shift anisotropy. First the authors computed alanine Ramachandran

chemical shift surfaces for the principal tensor components $\sigma_{ii}(\varphi, \psi)$. These HF/GIAO calculations were performed for N-formyl-L-alanine fragments using local dense basis sets for the carbon under study. NMR solid state experiments were performed on the two tripeptides Gly–*Ala–Val and Ala–*Ala–Ala with C^{α} labelled alanines. The G*AV crystal structure contained only a single molecule per unit cell, whereas A*AA crystallized in two different forms with two molecules per unit cell in each case. Correlation of the experimental chemical shift data to the theoretical shieldings yielded a good coefficient ($R = 0.99$), but the slope of -0.67 raises some questions (as the correct value has to be -1). The correlation was used to scale the shielding surface to the shift values. Then three Z surfaces according to Eq. (8) were constructed: one Z-isotropic, one Z for (δ_{33}–δ_{11}), and finally a Z surface for (δ_{22}–δ_{11}). Superimposing these surfaces gave a $^{3}Z(\varphi, \psi)$ that allowed to determine the backbone dihedral angles. In the case of Gly–*Ala–Val the authors obtained $(\varphi, \psi) = (-79.9, -47.8)$ which compares rather well with the values from the crystal structure $(\varphi, \psi) = (-68.7, -38.1)$. The investigation demonstrates that measuring tensorial chemical shift data can provide the constraints needed to determine the backbone angles in a peptide. The predictive force of this method was proven for a peptide whose data were not used to construct the theoretical Z surfaces.

The first problem that needs to be discussed is the accuracy of the *ab initio* calculation. Laws *et al.*[111] studied the influence of the basis set size on the ^{13}C shielding calculations, by comparing calculations with small basis sets with the results of a large local dense basis set (C^{α} and C^{β}: 6-311G++(2d,2p)/6-31G). The calculated C^{α} and C^{β} shieldings with smaller basis sets correlate well with the large basis set, so that it seems possible to improve the shift surfaces by scaling to elaborate basis sets. As test of this procedure a valine shielding hyper-surface $\delta(\varphi, \psi, \chi^1)$ was used to predict the C^{α} chemical shifts of two proteins with known structure. The correlation with $R^2 = 0.84$ and a slope -0.8 seems to be reasonable, but a scatter of 2 ppm within a total span of 7 ppm indicates the limitations of the method.

The second problem that arises from the use of pre-calculated CS hypersurfaces is the neglect of the molecular environment in the calculation of small model systems. For ^{13}C chemical shift tensors of zwitterionic amino acids this effect was studied by de Dios *et al.*[112] Quite large effects were observed for the carbonyl carbons when the crystal lattice was included in the *ab initio* calculations in the form of a point charge distribution. The σ_{11} tensor component of L-tyrosine changed by 16 ppm and the σ_{22} tensor component by 37 ppm. The changes for L-threonine were only slightly smaller.

It is therefore not surprising that the chemical shifts of ^{13}C carbonyl groups are influenced by other features of the structure more or at least to the same extent as they are by the main chain dihedral angles. Performing *ab initio* calculations on small amino acid-like models, de Dios and Oldfield[113] detected a strong dependence on hydrogen bonds. The authors found a variation of

3 ppm with hydrogen bond distance, while experimental hydrogen bond shifts of up to 8 ppm are observed.

Chemical shift maps for 1-substituted pentanes were worked out by Barfield,[114] who could analyse various substitution effects in dependence on the molecular conformation. Of special interest was the origin of the δ- and ε-effect.

6.3.2. *Derivation of ^{15}N chemical shifts*

An excellent overview concerning the use of solid state ^{15}N NMR data for structure analysis was given by Shoji *et al.*[115] For several reasons the interpretation of ^{15}N chemical shifts and CS tensors attracted much attention in the last years. The total span of ^{15}N chemical shifts is almost an order of magnitude larger than that of the observed carbon chemical shifts. Therefore, this relatively easily measurable nucleus bids fair to be an excellent structural probe in proteins and peptides. Furthermore, the ^{15}N principal values and the tensor orientation of the backbone nitrogen atoms are prerequisites for the interpretation of spectra of peptides in oriented membranes (see Secton 7.2). On the other hand, severe problems often arise in chemical shielding calculations due to the nitrogen lone pair and its conjugated double bonds. As in the case of ^{13}C carbonyl chemical shifts, a strong dependence of calculated values on the long range molecular surrounding is observed. If for instance the influence of the crystal lattice was neglected in a calculation of solid imidazole,[116] one tensor component was wrong by as much as 68 ppm which is more than 1/3 of its total chemical shift. Results in a similar direction were obtained by Scheurer *et al.*[117] who performed DFT chemical shift calculations on asparagine side-chain nitrogens and Ala–Ala peptide bond nitrogens. The structures were extracted from a molecular dynamics trajectory to obtain nitrogen tensor MD trajectories. The charge distribution in the environment had a more pronounced influence on the tensor components than on the directions of the principal axes. In chemical shift calculations for ^{15}N atoms in the bases of nucleic acids with comparable hybridization states, differences in the tensor components of up to 50 ppm were observed depending on the molecular geometry and environment.[118]

The orientation of amide ^{15}N chemical shift tensors in peptides was investigated by Brender *et al.*[119] As shown in Fig. 8, the orientation of this tensor is described by three angles: α is the angle between δ_{11} and the projection of the N–H bond onto the δ_{11}–δ_{22} plane, β is the angle between δ_{33} and the N–H bond, and γ is the angle between δ_{33} and the projection of δ_{33} onto the peptide plane. Especially the last angle γ is not accessible from the solid-state NMR spectra of powder samples. For nearly axially symmetric tensors the determination of α relies on the readily interchangeable assignment of δ_{11} and δ_{22}. For an idealized amide nitrogen the δ_{33} component is set parallel to the N–H bond keeping the other two components within the

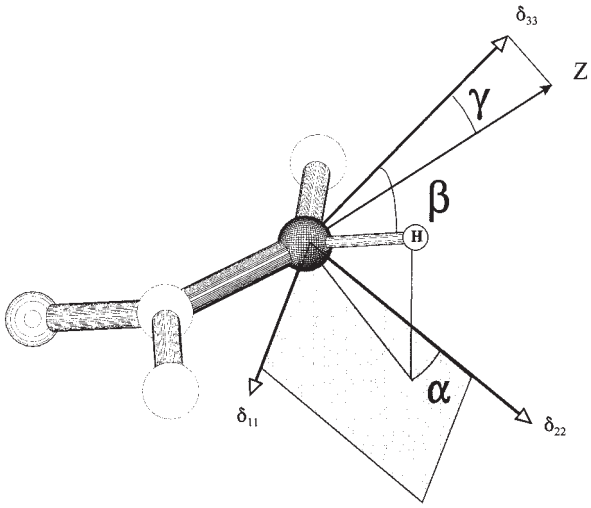

Fig. 8. Orientations of the principal axies of the ^{15}N chemical shift tensor relative to the N–H bond and the peptide plane. The angle γ is defined by the direction of the δ_{33} tensor component and its projection onto the peptide plane, β is the angle between the direction of δ_{33} and the N–H bond direction, and α is the angle between δ_{11} and the projection of the N–H bond vector onto the δ_{11}–δ_{22} plane.

plane such that α, $\gamma = 0°$. The calculations of Brender *et al.*[119] yielded a range of 0° to 35° for α with most values between 10° and 20°. Most of the β angles are clustered in the narrow range between 17.5° and 18.5°, which is in good agreement with solid state NMR experiments. Most of the γ angles are less than 5°. In a study of the basis set dependence of the tensor orientations only weak influences are found. Surprisingly even with small basis sets the orientations are predicted rather well. Since the tensor directions are not too strongly influenced by the environment, they can be predicted even for larger molecular fragments much better than the principal values. The individual tensor components show quite large discrepancies, but they average out in the calculation of isotropic values because errors in the σ_{11} and σ_{33} components compensate. The largest source of error stems from the poorly defined coordinates. Not only is the uncertainty in the proton position of concern, but in the case of conjugated π-systems the shielding depends strongly on the bond length. This effect can be as high as 300 ppm per Å.[120]

A further problem of ^{15}N chemical shift calculations is the influence of electron correlation. In calculations on the Hartree-Fock level the error is typically 20 ppm for isotropic nitrogen values. The observed range of backbone nitrogen chemical shifts is also about 20 ppm, hence only calculations on the MP2 level or better are suitable for structure elucidation – or it must be assumed that the correlation effects are constant within the pool of studied structures.

First attempts to construct amide ^{15}N chemical shift surfaces additionally face the problem that at least five angles have to be studied: the peptide bond planarity ω, and one pair each of (φ, ψ) angles on each side of the nitrogen. The only encouraging result is that the influence of the two pairs is practically additive.[121] A study of the main influence of (φ_i, ψ_i) and $(\varphi_{i-1}, \psi_{i-1})$ revealed that ψ_{i-1} and φ_i dominate.[122] Only minor effects from N–H hydrogen bonds and the side chain torsion angle were observed. A strong correlation between the calculated and experimental ^{15}N chemical shifts of non-helical residues was observed on the HF and DFT level. Reliable applications require maximum differences lower than 18 ppm, since the total range of ^{15}N chemical shifts in proteins is only 20 ppm.

6.4. Empirical chemical shift contour maps

Over the last decades a large number of protein structures were solved using diffraction methods, and for some of them also the ^{1}H NMR chemical shifts were completely assigned. Cornilescu *et al.*[123] selected 20 proteins and created a database containing the $^{13}C^{\alpha}$, $^{13}C^{\beta}$, $^{13}C'$, $^{1}H^{\alpha}$ and ^{15}N chemical shifts, together with the backbone torsion angles φ and ψ. The authors developed a program (TALOS) that searches for triplets of neighbour chemical shifts within the data base. This way it is possible to predict backbone dihedral angles from NMR measurements of proteins with unknown 3D structure. Wishart and Nip[124] presented a guide for obtaining unbiased chemical shift data, and they also gave a critical view on the use of empirical chemical shift contour maps.

Kuszewski *et al.*[125] constructed a $^{13}C^{\alpha}$ shift surface from the Spera and Bax[69] database, by assigning Gaussian weights such that every (φ, ψ) data point includes weighted information on the next neighbours [truncated form of Eq. (51)]. Harmonic and square well penalty functions were tested in a refinement of human thioredoxin. Since several $^{3}J_{\mathrm{HNH}\alpha}$ couplings could not be determined, chemical shift constraints improved the structure and the atomic rmsd dropped for sites without J-coupling from 0.25 Å to 0.06 Å.

Similar $^{13}C^{\alpha}$ and $^{13}C^{\beta}$ contour maps were constructed by Asakura *et al.*:[126]

$$\Delta(\phi, \varphi) = \frac{\sum_k \delta(\varphi_k, \psi_k) e^{-\left((\phi-\phi_k)^2+(\psi-\psi_k)^2\right)/2\varepsilon^2}}{\sum_k e^{-\left((\phi-\phi_k)^2+(\psi-\psi_k)^2\right)/2\varepsilon^2}}. \tag{51}$$

The error in the representation of the angles was set to $\varepsilon = 15^{\circ}$, and k runs over all observed shifts. These contour maps were used to confirm structure models of silk obtained from solid state chemical shifts (see Section 7.2). In the construction of the empirical contour maps the question was raised whether ring currents could influence the ^{13}C chemical shifts.[127] No ring current

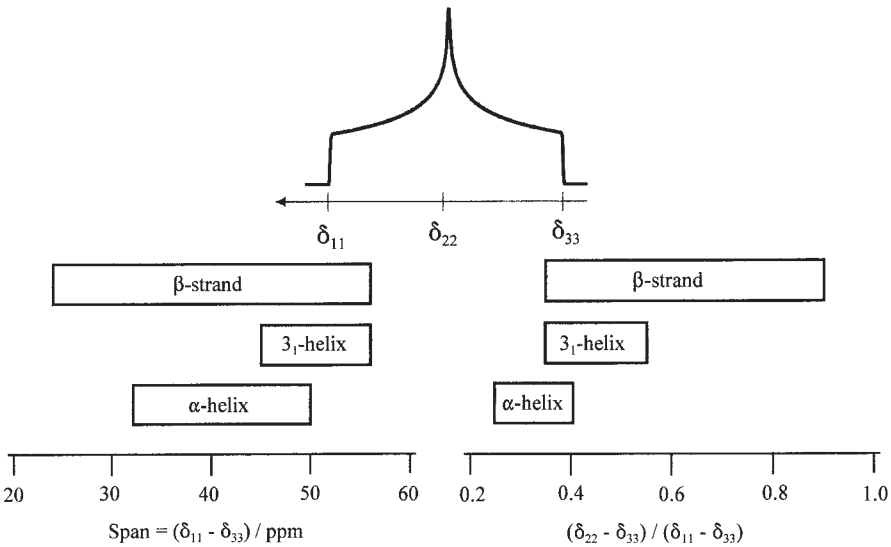

Fig. 9. Dependence of the $^{13}C^{\alpha}$ chemical shift tensor in glycine on different types of peptide secondary structure motifs, from an experimental investigation of tripeptides.[128]

influence was detected, and the inclusion of this effect did not lower the rms deviation of back-calculated values. On the other hand, an influence of hydrogen bonds on $^{13}C^{\alpha}$ in helical surroundings was observed.

Studying the glycine $^{13}C^{\alpha}$ chemical shift tensors in various tripeptides, Chekmenev *et al.*[128] established rules to distinguish between different structural motifs. They proposed that the span $s = (\delta_{11}–\delta_{33})$ can distinguish in most cases between an α-helix and a 3_{10}-helix. And if the value of $(\delta_{22}–\delta_{33})$/span is larger than 0.5, the structure is definitely a β-sheet (see Fig. 9).

6.5. BPT pseudo-forces[36]

In order to obtain energetic corrections, the contribution of the bonds around nucleus A to the polarisation energy has to be calculated. The total energy can be approximated by

$$E = \sum_{A} \sum_{i}^{i \in A} \left(2n_i E_0^i + n_i^2 \frac{\left\langle \chi_A^i | \hat{V} | \chi_A^i \right\rangle - \left\langle \chi_B^i | \hat{V} | \chi_B^i \right\rangle}{E_0 - E_{i^*}} \right). \tag{52}$$

E_0^i are the energies of un-polarized bond contributions, E_0 is the total ground state energy of the molecular system, E_{i^*} is the excited state energy for the

polarized bond contribution i, and n_i is the occupation number. In a force field approach we are only interested in relative energies and disregard the constant contributions, hence we introduce the molecular polarisation energy E^P as well as the atomic polarization energy E_A^P

$$E^P = \sum_A \sum_i^{i\in A} n_i^2 \frac{\left\langle \chi_A^i | \hat{V} | \chi_A^i \right\rangle - \left\langle \chi_B^i | \hat{V} | \chi_B^i \right\rangle}{E_0 - E_{i^*}} = \sum_A E_A^P. \tag{53}$$

For the chemical shift it turns out that it can be expressed in terms of the atomic polarization energy.[36] Expanding it with respect to the chemical shift tensor $\delta_{\alpha\beta}^{\text{theo}}$ around the experimental value $\delta_{\alpha\beta}^{\text{exp}}$ and taking the gradient, the BPT pseudo-force can be deduced

$$F_j = k_{\alpha\beta}^{\text{CS}} (\delta_{\alpha\beta}^{\text{theo}} - \delta_{\alpha\beta}^{\text{exp}}) \frac{\partial \delta_{\alpha\beta}^{\text{theo}}}{\partial x_j}. \tag{54}$$

The force constant is

$$k_{\alpha\beta}^{\text{CS}} = \sum_A \sum_i^{i\in A} \frac{2A_i^q}{n_i^2 \left(\sum_{\alpha'\beta'} D_{\alpha\alpha'}^i D_{\beta\beta'}^i A_{\alpha'\beta'}^i \right)^2}. \tag{55}$$

For the isotropic chemical shift it follows

$$F_j = k^{\text{CS}} (\delta^{\text{theo}} - \delta^{\text{exp}}) \frac{\partial \delta^{\text{theo}}}{\partial x_j}. \tag{56}$$

In this case the force constant becomes

$$k^{\text{CS}} = \sum_A \sum_i^{i\in A} \frac{2A_i^q}{n_i^2 (A^i)^2}. \tag{57}$$

The computational cost depends, to the first degree, on the charge calculation which is proportional to the cube of the number of atoms, N^3. Calculations on systems of about 10^4 atoms are feasible within a day on current standard GHz machines with an average performance of about 500 Mflops/s.

7. APPLICATIONS IN PEPTIDE AND PROTEIN STRUCTURE INVESTIGATIONS

7.1. Biomolecular structure investigations in solution

The application of NMR chemical shift constraints in the structure refinement of soluble proteins is now a standard procedure, since the ^{1}H, ^{15}N and ^{13}C chemical shifts have to be assigned to produce NOE constraints. The empirical $^{13}C^{\alpha}$ and $^{13}C^{\beta}$ shift surfaces from Kuszewski *et al.*[131] and the proton chemical shift formulae[129] were included into X-PLOR[130] and thus belong to the standard procedures in protein structure analysis.

In a structure investigation of the SH2 domain from $p55^{bkl}$ kinase, Metzler *et al.*[131] performed geometry optimizations with distance restraints from NOEs plus torsion angle restraints. They compared these results with calculations where additionally $^{13}C^{\alpha}$, $^{13}C^{\beta}$ and non-exchangeable ^{1}H chemical shift constraints were applied. Introducing the CS constraints it was observed that the rmsd of all restraints dropped, except for the NOEs. The most significant deviations came from regions where the structures were least well-defined and only few NOEs had been observed. Luginbühl *et al.*[132] investigated the validity of the dihedral angle prediction using secondary $^{13}C^{\alpha}$ shifts $\Delta\delta(^{13}C^{\alpha})$. They came to the conclusion that the $\Delta\delta(^{13}C^{\alpha})$ database should only be used for protein structure refinements if no ^{3}J couplings or NOE values can be measured. Therefore, in solid state investigations chemical shift constraints are of great value.[133] Similar observations were reported from Wittekind *et al.*[134] who investigated the complex of a decapeptide with the Grb2 N-terminal SH3 domain. The inclusion of $^{13}C^{\alpha}$, $^{13}C^{\beta}$ and ^{1}H constraints slightly raised the rmsd of the NOE and $^{3}J_{HNH\alpha}$ data. The use of ^{1}H chemical shifts in this refinement was of special interest because the complex formation showed up in dominant contact shifts. A number of protons in this SH3 domain exhibited extreme upfield deviations from the random coil ^{1}H chemical shift values, which could be readily explained by the refined structures.

An interesting approach of structure refinement is based on the use of NOEs plus ^{1}H chemical shifts that are caused by intermolecular interactions. Iwadate *et al.*[135] performed calculations on the geometry of a melittin tetramer at different temperatures. The structural models rely on a relatively small number of intermolecular ^{1}H chemical shifts caused by the interaction of special groups such as tryptophan rings with protons. There are even a number of examples where aggregation chemical shifts are used to build and refine molecular models.[136] For example, van Rossum *et al.*[137] used the shift differences between solution values and the solid state to construct a model of the chlorosomal antennae complex of green bacteria. It is tempting to assign these changes solely to ring current contributions from aromatic rings, but from a theoretical point of view the question still remains open whether any single chemical shielding contribution would dominate.

Chemical shift target functions proved their power especially in the refinement of smaller peptides as for example a vasopressin derivative.[138] Using only traditional constraints, this cyclic peptide switched in MD simulations between two conformations. $^{1}H^{\alpha}$ chemical shift constraints forced the structure into a single conformation that not only fits the chemical shift constraints well but also satisfies the NOE constraints better than in their absence. Despite the fact that the accuracy of this type of chemical shift calculation for protons is still relatively low (about 0.25 ppm), chemical shift constraints can significantly reduce the conformational space allowed for the structures.

The ^{13}C chemical shift structure elucidations using the COSMOS-NMR force field[92] differ in several general aspects from the former calculations: (i) the chemical shifts and their derivatives are calculated 'on the fly' during the molecular mechanics simulations, (ii) pseudo-forces act on all sites that polarise the bonds of the NMR nuclei, (iii) the derivatives are calculated in Cartesian space, and (iv) the calculations are not limited to peptides or any special types of nuclei. The only prerequisite is a proper parametrization for the NMR nuclei. The first application of the COSMOS-NMR force field was concerned with a cyclic pseudo-tripeptide, which had been designed to mimic the catalytic centre of carboanhydrase and should therefore form a complex with zinc ions.[139] By solution state NMR all ^{13}C and ^{1}H chemical shifts were assigned in the complex, and 18 NOE were observed. The original computer model of the peptide and a zinc ion were used as the starting structure for a 1 ns molecular dynamics calculation at a temperature of 2000 K to surmount the conformational energy barriers. The COSMOS-NMR force field works with atomic charges that are computed in every step of the simulation, hence the non-bonded energy contains all polarizations. This is necessary if highly charged systems such as metal ions and their interactions are to be studied by molecular mechanics. To search for a stable complex structure it was necessary to introduce the metal as an ion without predefined bonds. Thousand structures originating from the MD simulation were then selected and cooled to 0 K by applying simulated annealing methods including NOE pseudo-forces. For the NOE pseudo-potential the method of Torda and van Gunsteren[93] was used. In this potential the energy depends on the time-averaged $H \cdots H$ distances and it is only half-side harmonic, i.e., if any proton pair distance is equal to or closer than the desired NOE distance then the forces are set to zero. The functional behavior of the potential and its gradient are kept continuous by this assumption. With 18 NOEs only approximate proximities could be obtained, which cannot result in well resolved structures. In order to obtain highly defined structures, 1000 geometry optimizations with additional ^{13}C chemical shift pseudo-forces were performed. From the 22 possible ^{13}C chemical shifts 17 were used. The rms NOE distance deviation after refinement was about 0.5 Å and the rms difference between restricted ^{13}C chemical shifts and experimental values was 0.1 ppm. If the originally excluded $-CH_2$ carbon sites were also considered, the deviation was 1.2 ppm.

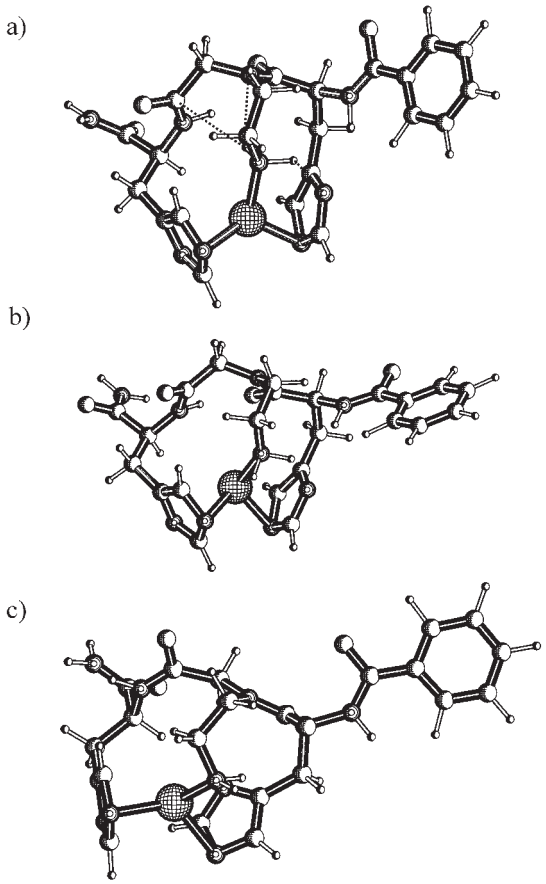

Fig. 10. The three best COSMOS-NMR force field results of a peptide-zinc complex obtained with NOE as well as chemical shift pseudo-forces. Zn–X bonds are shown if the distance is shorter than 2.5 Å. The force field search for the most stable complex was run with a free Zn^{2+} ion.

The energetically most stable structure is illustrated in Fig. 10(a). The NH_2-group position of the N-alkyl chain is important since it is the most obvious structural difference between the first two conformations. Complex 6(a) possesses two additional hydrogen bonds as compared to conformation (b), thus stabilizing (a). In contrast to (a) and (b), structure (c) shows two *trans–cis* alterations and an imidazole ring flip.

In order to find energetic minima of the free complex closes to the NMR optimized structures, B3LYP/6-31G(d,p) full geometry optimizations were carried out with the GAUSSIAN98 program package using the COSMOS-NMR structures as a starting point. The DFT optimized structure 6(a) is shown in Fig. 11. It can be seen that the position of the NH_2-group has

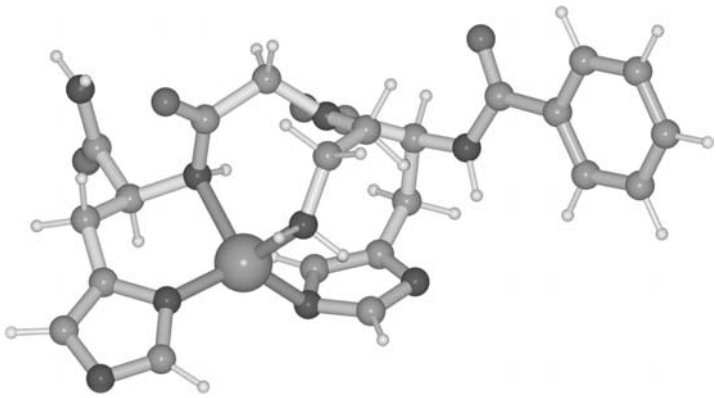

Fig. 11. B3LYP/6-31G(d,p) DFT optimized structure starting with the conformation of Fig. 10(a).

changed and the hydrogen bonds have disappeared. This might be due to the fact that no diffuse functions were used. The DFT energy difference between 6(a) and (b) is rather small (6.3 kJ/mol). The corresponding energy difference in the COSMOS force field approach amounts to 77.5 kJ/mol, mainly originating from the three hydrogen bonds (see Fig. 7). The main difference between the DFT optimized structures 6(a) and (b) is the position of the $-CONH_2$ group in His^2. The average Zn–X bond length is about 2.0 Å ± 0.1 Å. For the tetrahedral complex of 6(a) and (b), the bond angle is 109° ± 12°. The theoretically expected angle would be 109.3°.

These calculations demonstrate that it is possible to obtain highly refined structures using chemical shift pseudo-forces. The resulting differences between measured and calculated BPT chemical shifts are in the range of the experimental error. BPT pseudo-forces are in the same range as electrostatic interactions, and they act on all atoms that contribute to the chemical shift of a site.

7.2. Biomolecular structure investigations in the solid state

Chemical shifts are extensively applied in the structure analysis of biomolecules in the solid state, being especially informative for biomembranes and fibres. There are two fundamentally distinct approaches of how either isotropic chemical shifts or chemical shift anisotropies, respectively, are utilized: Isotropic chemical shifts of ^{13}C, ^{15}N or ^{1}H are typically available from high resolution MAS and can be correlated with the local chemical environment and geometry of the protein of interest, as outlined in detail above. Alternatively, aligned membranes or drawn fibres are ideally suited to prepare macroscopically oriented samples, in which the anisotropy of the ^{15}N,

^{13}C or ^{19}F chemical shift can be analysed directly in terms of orientational constraints. We will review the applications of these two different strategies with special attention to the pioneering work since the 1980s and more recent examples from the past 5 years. Several biological systems will then be presented which have been comprehensively characterized, followed by a brief outlook on the further development of biomolecular solid state NMR.

7.2.1. *Analysis of isotropic chemical shifts by MAS NMR*

The first protein to be comprehensively studied by solid state NMR was the robust membrane protein bacteriorhodopsin, as it could be readily reconstituted with specifically labelled retinal. For example, Griffin and coworkers deduced the conformation of the chromophore from its isotropic ^{15}N and ^{13}C chemical shifts[140,141] and monitored its changes throughout the photocycle.[142–144] The high sensitivity of aromatic chemical shifts to the environment was also exploited with other chromophores in more complex systems, such as retinal in visual rhodopsin,[145] pheophytin in a photosynthetic reaction centre,[146] or an entire bacterial light harvesting chlorosome.[137] As it is also relatively straightforward to observe a labelled ligand in the binding-site of an unlabelled enzyme or receptor, many elegant MAS studies have been performed on protein–ligand interactions.[147–149] For example, the chemical shifts of an inhibitor complexed with citrate synthase revealed information about H-bonding.[150] Working with reconstituted membranes, acetylcholine was localized in the binding pocket of its receptor,[151] and the conformational transition of neurotensin upon receptor binding was characterized.[152,153]

Moving on to uniformly labelled peptides and proteins, the partially resolved spectrum of gramicidin A confirmed its unusual β-helical conformation.[154] The partial assignment of larger proteins progressed with ubiquitin[155] and BPTI.[156] Recently, Oschkinat *et al.* succeeded to assign nearly all backbone and side chain ^{13}C and ^{15}N resonances of the spectrin SH3 domain,[157] as well as its non-exchangeable and amide protons.[158,159] On this basis, the complete three-dimensional structure of the 62-residue protein could be calculated from ^{13}C–^{13}C and ^{15}N–^{15}N distance restraints.[160] Further improvements in labelling strategy[161] and sample preparation[162] suggest that structure analysis of microcrystalline and even membrane-bound proteins[163] may soon be practical by MAS NMR.

7.2.2. *Analysis of the chemical shift anisotropy in oriented samples*

The basic concept of utilizing anisotropic chemical shifts in macroscopically aligned membranes, pioneered by Opella and Cross, was initially developed using gramicidin A. The 15 amino acid peptide is readily synthesized with selective ^{15}N or ^{13}C-labels in the backbone,[164,165] or with ^{15}N or ^{19}F-labels in the side chains[166,167] (as well as ^{2}H for quadrupolar couplings). Numerous individual orientational constraints were thus used to determine the detailed β-helical structure of the membrane-bound ion channel,[168,169] which was refined

to quasi-atomic resolution using the CHARMM force field.[170] Since then, many other investigation of α-helical peptides have extensively relied on the ^{15}N chemical shift, which is a valuable indicator of the peptide's tilt angle in the membrane.[171,172] Since the δ_{33} component of the chemical shift tensor is aligned reasonably well with the N–H bond ($\beta \approx 18^\circ$, see Section 6.3.2 and Fig. 8) and thus with the overall helical axis, a simple 1D spectrum suffices to estimate the alignment of the α-helix with respect to the lipid bilayer normal. That way integral peptides have been shown to span the membrane at certain tilt angles,[173] while many antimicrobial peptides were found to lie flat on the surface.[174–176]

Given the small but significant deviation of the δ_{33} component from the α-helical axis (see Section 6.3.2 and Fig. 8), additional information is gained by including the ^{15}N–^{1}H dipolar coupling as a second orientational constraint. Correlation of the ^{15}N-chemical shifts with these couplings in early DIPSHIFT experiments was vastly improved in terms of resolution by the PISEMA experiment[177–179] and its more recent 'magic sandwich' version.[180] The 2D spectra have even been correlated with ^{1}H chemical shifts for 3D resolution.[181] Using this general approach it was possible to assign group-specifically and uniformly ^{15}N-labelled resonances of several proteins and to determine the precise tilt angles of their helical segments in the membrane. Self-assembly into bundles, which is often associated with ion channel activity, was elegantly demonstrated by the structures of Vpu from HIV[182–184] and the M2 protein from influenza A.[185,186]

7.2.3. *Examples of comprehensively characterized biological systems*

Several structural proteins have been thoroughly characterized. Silk from the cocoon of silkworms or the dragline of spiders has a unique tensile strength, which is attributed to the co-existence of crystalline and amorphous regions in the fibre. Asakura *et al.* have resolved many structural features of silk proteins from various sources, using synthetic model peptides as well as biosynthetically labelled protein from cultivated silk worms. The characteristic antiparallel β-sheet structure was evident from the anisotropic ^{15}N chemical shifts of macroscopically aligned fibres.[187] The analysis of ^{13}C chemical shift contour plots revealed distinct changes in secondary structure before and after spinning.[126,188–190] A different kind of cross-β-sheet structure is formed by amyloid fibrils, which are associated with neurodegenerative diseases and often represent the aggregated state of other folded protein conformations. The local and supramolecular structure of the Alzheimer peptide has been recently characterized by Tycko *et al.*, starting from conformation-dependent chemical shifts and including many further distance and torsion angle constraints.[191–193]

Structural transitions between functionally distinct α-helical and β-sheet conformations have also been observed for several membrane-interacting peptides. For example, fusogenic peptides tend to assume helical structures at low concentration in certain membrane compositions, while they switch to

extended sheets when they self-assemble. This behaviour was evident from orientational constraints derived from ^{19}F-labelled analogues,[194] and from conformation-dependent isotropic chemical shifts of ^{13}C-labels.[195,196] Yet another example of functionally relevant structural transitions is provided by several different antimicrobial peptides, which have been recently reported to re-align from a surface-bound to a membrane-spanning state in response to changes in concentration or membrane composition.[197–201]

7.2.4. *Future perspectives for solid state NMR of biomolecules*

The general feasibility of assigning uniformly labelled proteins by either MAS-NMR[202] or in oriented samples[203] has been explored by spectral simulations,[204] revealing certain bottlenecks that may be overcome by a suitable combination of experiments. One of the remaining experimental challenges for measuring precise chemical shifts lies – besides the need to further improve spectral resolution – in suitable referencing procedures. Recently, several innovative referencing approaches have been suggested for MAS,[205] for static oriented samples,[206,207] and for MAS of aligned specimen.[208] The most critical aspect for a reliable protein structure analysis remains the accurate knowledge of its chemical shift tensors. Various 1D and 2D experiments have been used to resolve the principal axis values and Euler angles of ^{15}N[209,210] and ^{13}C tensors[211–214] in crystalline amino acids and solid peptides (see Section 6.3). Given their significant dependence on the backbone conformation and local environment, a combination of such experimental input with computational analysis promises to be the best route towards the structural refinement of proteins in the solid state.

8. APPLICATIONS IN CRYSTAL STRUCTURE REFINEMENT

To apply molecular mechanics calculations to crystal structures, the force field has to represent the influence of the crystal lattice in an adequate way. This is achieved by surrounding a central unit cell by 26 translationally created images of itself. In most crystal structures some of the bonds span the borders of the unit cell; therefore one also has to account for these periodic intramolecular contributions besides the intermolecular energy. Within the COSMOS-NMR force field[92] the molecules are allowed to extend from the central unit cell into the neighbouring cells. For every atom in each of the 26 cells the program stores a code for the translation that was used to generate the coordinates from the central unit cell. Using this code it is possible to update the forces, charges and positions of the atoms in the 26 neighbouring cells from the values of the central cell. Therefore, all energies and forces are only calculated for the central unit cell, but are then taken into account by the 26 neighbouring cells. Space group symmetry was not

enforced, but the chemical shift constraints conserve the symmetry relations within the unit cell if two or more sites display the same chemical shift value.

The first application of the COSMOS-NMR force field to a crystallographic problem was the refinement of proton positions from ^{13}C chemical shifts.[92] Proton positions are not that readily derived from X-ray investigations, especially for large molecules, because of the lack of core electron interaction with the radiation field. But even if good X-ray data are available, the refinement of the proton sites using NMR chemical shifts will lead to better defined structures and can provide valuable insight into the formation of hydrogen bonds. In our first example of β-D-mannitol, both the high resolution X-ray structure and the solid state ^{13}C chemical shifts were known. The BPT calculation of the chemical shifts from the X-ray atomic position gave a mean deviation from experiment of 1.7 ppm and a maximum difference of 2.7 ppm. A force field optimization of the protons, while keeping the positions of the heavy atoms unchanged, lead to a structure with an even larger mean deviation of 2.5 ppm for the calculated ^{13}C chemical shifts from their experimental values. Next, ^{13}C chemical shift pseudo-forces were switched on to act only on the proton positions. The pseudo-forces were scaled in a range starting from 10^{-3} up to 10^{3}. Significant changes started to show up around 10^{-1}, and at for a scaling constant of 10^{2} a lower limit of 0.02 ppm for the chemical shift difference is reached. At higher scaling factors the negative pseudo-forces start to dominate all other contributions, but the structure stays stable. This means that the proton positions are controlled exclusively by the chemical shift pseudo-forces. The errors in the experimental NMR data and the chemical shift calculations then limit the precision of the structure determination. Notably the refined proton positions do not violate the limits of the X-ray diffraction. The average proton displacement parameter derived from the temperature factor is about 0.2 Å. The standard deviation of the refined structure ($S = 100$, $S = 1000$) with respect to the X-ray structure is only about 0.13 Å.

In Fig. 12 the superposition of the X-ray and the H-refined structure ($S = 1000$) is shown. The spheres at the proton positions are the isotropic 50% probability ellipsoids. It is thus possible to refine crystal structures using chemical shifts as target functions and thereby resolve structural features that are not well represented in diffraction investigations. These new ^{1}H-refined crystal structures will now fulfil the requirements of both the diffraction investigation and the NMR.

The lack of crystalline order in polymers such as cellulose or silk significantly reduces the number of interference spots in diffraction investigations; hence the patterns often cannot be analysed unambiguously. In these cases a crystal structure refinement using NMR chemical shifts will be of great value, because NMR spectroscopy does not require long-range crystalline order. In our second example of cellulose, the situation occurred that the C4 values in BPT ^{13}C chemical shift calculations deviated seriously from

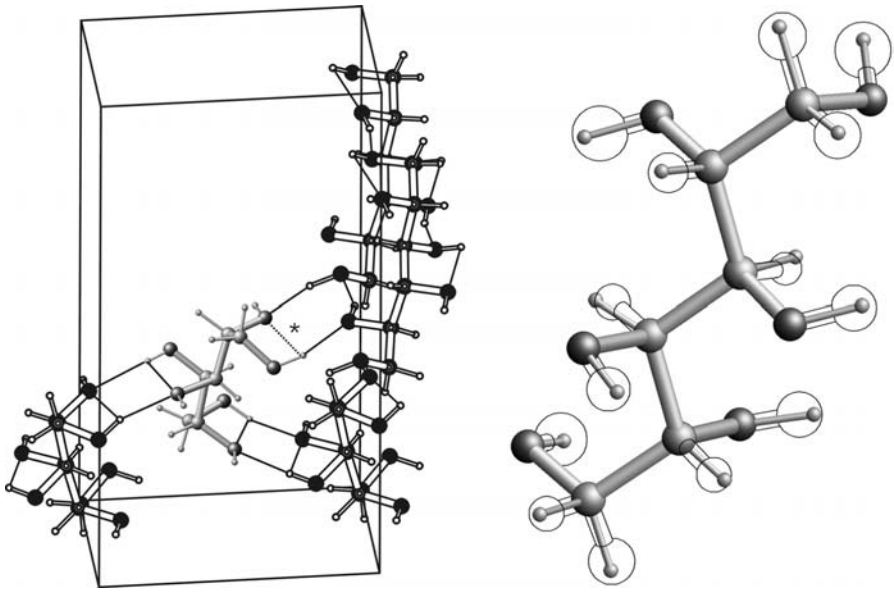

Fig. 12. Superposition of the X-ray structure of D-mannitol with its refinement from ^{13}C NMR chemical shifts. Only the proton positions are refined (left), and their 50% probability spheres from the X-ray investigation are shown for comparison. The refined β-D-mannitol crystal structure (left) illustrates the hydrogen bond system.

experiment for all of the three proposed crystal structures (cellulose Iα, Iβ, and II).[215] Since the BPT parametrization had been thoroughly performed on the experimental data from many sugars, the deviations of 10 ppm were beyond the error range of the former calculations. The optimizations with ^{13}C chemical shift target functions succeeded to produce structures which fulfil the requirements of both the NMR and the diffraction methods. The method thus provides additional criteria for the ranking of the proposed structural models. It turns out that some inner chain hydrogen bonds cause geometry changes of the glycosidic linkage, leading to the C4 shift from the amorphous value of about 75 ppm to the crystalline value of about 88 ppm. Since this value is observed in all cellulose I and II polymorphs, the arrangements of these hydrogen bonds have to be similar. In Fig. 13 an experimental ^{13}C MAS NMR spectrum of bacterial cellulose is compared with the chemical shifts after structure refinement. Bacterial cellulose contains mainly cellulose Iα with two glucose units per unit cell plus a minor amount of cellulose Iβ with four glucose units.

The question whether there exist any other structural models that fulfil all X-ray and NMR criteria still remains open to discussion. Additionally, the influence of molecular motions of the ring segments or CH_2–OH groups

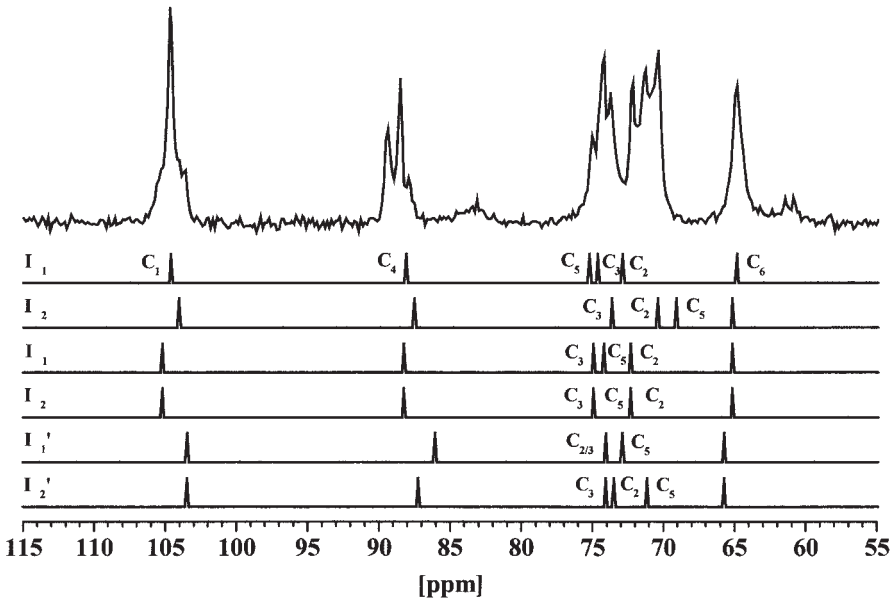

Fig. 13. ^{13}C-CPMAS spectrum of bacterial cellulose containing mainly the Iα and a minor amount of the Iβ polymorphs. Below the calculated chemical shift values according to the ^{13}C chemical shift crystal structure refinement are shown.

should be investigated, and it is obviously critical that the chemical shifts are correctly assigned to the crystallographic sites.

There are specific differences between structure data obtained by NMR methods and diffraction methods. Not only the time scale of the NMR experiment and therefore the time average is different, but chemical shifts depend mostly on the valence electrons whereas X-ray diffraction looks mainly at the inner shell electrons. It is well conceivable that these differences become a valuable source of new information. The same is true when neutron and X-ray data are comparatively analysed to produce density difference distributions. As far as NMR methods are concerned, the investigations reported here represent the first steps towards crystal structure refinement.

REFERENCES

1. J. T. Arnold, S. S. Dharmatti and M. E. Packard, *J. Chem. Phys.*, 1951, **19**, 507.
2. D. M. Grant and E. G. Paul, *J. Am Chem. Soc.*, 1964, **86**, 2984.
3. T. Helgaker, M. Jaszuński and K. Ruud, *Chem. Rev.*, 1999, **99**, 293.
4. D. A. Case, H. J. Dyson and P. E. Wright, *Methods Enzymol.*, 1994, **239**, 392.
5. L. Szilagyi, *Prog. Nucl. Magn. Reson. Spectrosc.*, 1995, **27**, 325.
6. M. P. Williamson and T. Asakura, *Methods Mol. Biol.*, 1997, **60**, 53.

7. D. S. Wishart and B. D. Sykes, *Methods Enzymol*., 1994, **239**, 363.
8. N. F. Ramsey, *Phys. Rev*. 1950, **91**, 303; *Phys. Rev*., 1959, **78**, 699.
9. W. Kutzelnigg, *J. Mol. Struct*. (Theochem), 1989, **202**, 11.
10. T. Helgaker and P. Jorgensen, *Methods in Computational Molecular Physics*, S. Wilson and G. H. F. Diercksen, eds., Plenum Press, New York, 1992, 353.
11. W. Kutzelnigg, *Theor. Chim. Acta*, 1992, **83**, 263.
12. J. Grotendorst, Modern Methods and Algorithm of Quantum Chemistry, NIC, Forschungszentrum Jülich, 2000.
13. J. Mason, *Solid State NMR*, 1993, **2**, 285.
14. F. London, *J. Phys. Radium*, 1937, **8**, 397.
15. R. Ditchfield, *Mol. Phys*., 1974, **27**, 789.
16. M. Schindler and W. Kutzelnigg, *J. Chem. Phys*., 1982, **76**, 1919.
17. A. E. Hansen and T. D. Bouman, *J. Chem. Phys*., 1985, **82**, 5035.
18. T. D. Bouman and A. E. Hansen, *Chem. Phys. Lett*., 1990, **175**, 292.
19. T. A. Keith and R. F. W. Bader, *Chem. Phys. Lett*., 1992, **194**, 1.
20. J. R. Cheeseman, G. W. Trucks, T. A. Keith and M. J. Frisch, *J. Chem. Phys*., 1996, **104**, 5497.
21. F. Mauri, B. G. Pfrommer and S. G. Louie, *Phys. Rev. Lett*., 1996, **77**, 5300.
22. K. Wolinski, J. F. Hinton and P. Pulay, *J. Am. Chem. Soc*., 1990, **112**, 8251.
23. J. R. Cheeseman, G. W. Trucks, T. A. Keith and M. J. Frisch, *J. Chem. Phys*., 1996, **104**, 5497.
24. J. Gauss, *J. Chem. Phys*., 1993, **99**, 3629.
25. V. G. Malkin, O. L. Malkina and D. R. Salahub, *Chem. Phys. Lett*., 1993, **204**, 80.
26. J. Gauss and J. F. Stanton, *Phys. Chem. Phys. Lett*., 2000.
27. U. Sternberg, *J. Mol. Phys*., 1988, **63**, 249.
28. U. Sternberg and W. Priess, 1999, Modelling NMR Chemical Shifts ACS Symposium Ser. *732*, Ed. A. C. Facelli and A. C. de Dios.
29. J. C. Slater, *Phys. Rev*., 1930, **36**, 57.
30. U. Sternberg and W. Priess, *J. Magn. Reson*., 1997, **125**, 8.
31. W. Priess and U. Sternberg, *J. Mol. Struct. (Theochem)*, 2001, **544**, 181.
32. W. S. Veeman, *Progr. NMR Spec*, 1984, **20**, 193.
33. M. H. Sherwood, D. W. Alderman and M. G. Grant, *J. Magn. Reson*., 1989, **84**, 466.
34. M. O'Keefe and N. E. Brese, *J. Am. Chem. Soc*., 1991, **113**, 3226.
35. F.-T. Koch, M. Möllhoff and U. Sternberg, *J. Comp. Chem*., 1994, **15**, 524.
36. R. Witter, Three Dimensional Structure Elucidation with the COSMOS-NMR Force Field, thesis, 2003. dissertation.de.
37. M. Schindler, Die Berechnung magnetischer Eigenschaften unter Verwendung individuell geeichter lokalisierter Molekülorbitale, thesis, Bochum 1980.
38. A.-R. Grimmer, *Chem. Phys. Lett*., 1985, **119**, 416.
39. D. Heidemann, 19Si und 1H-Festkörper-NMR-Untersuchungen an kristallinen Hydrosilikaten, thesis, Berlin 1986.
40. A. Olivieri, *J. Magn. Res*., 1990, **88**, 1.
41. U. Sternberg, F. Pietrowski and W. Priess, *Z. f. Phys. Chem. Neue Folge*., 1990, **168**, 115.
42. J. V. Smith and C. S. Blackwell, *Nature*, 1983, **303**, 223.
43. A.-R. Grimmer, F. von Lampe, M. Mägi and E. Lippmaa, *Montshefte für Chemie*, 1983, **114**, 1053.
44. G. Engelhardt and R. Radeglia, *Chem. Phys. Lett*., 1984, **108**, 271.
45. U. Sternberg and W. Priess, *J. Magn. Res*., 1993, **102**, 160.
46. R. F. Pettifer, R. Dupree, I. Farnan and U. Sternberg, *J. Non-Cryst. Solids*, 1988, **106**, 408.
47. E. Lippmaa, A. Samoson and M. Mägi, *J. Am. Chem. Soc*., 1986, **108**, 1730.
48. E. Hallas and U. Sternberg, *Mol. Phys*., 1989, **68**, 315.
49. R. Radeglia and G. Engelhardt, *Chem. Phys. Lett*., 1985, **114**, 28.
50. X. Xue and M. Kanzaki, *Phys. Chem. Miner*., 1998, **26**, 14.
51. D. G. Gorenstein, *Chem. Rev*., 1994, **94**, 1315.

52. H. M. McConnell, *J. Chem. Phys*., 1957, **27**, 226.
53. N. H. Martin, J. D. Brown, K. H. Nance, H. F. Schaefer III, P. v. R. Schleyer, Z.-X. Wang and H. L. Woodcock, *Organ. Lett*., 2001, **3**, 3823.
54. U. Fleischer, W. Kutzelnigg, P. Lazzeretti and V. Mühlenkamp, *J. Am. Chem. Soc*., 1994, **116**, 5298.
55. E. Brunner and U. Sternberg, *Prog. Nucl. Magn. Res. Spectr*., 1988, **32**, 21.
56. U. Sternberg and E. Brunner, *J. Magn. Res*., 1994, **A108**, 142.
57. Y. Wei, D.-K. Lee and A. Ramamoorthy, *J. Am. Chem. Soc*., 2001, **123**, 6118.
58. T. Kameda, N. Takeda, S. Kuroki, H. Kurosu, S. Ando, I. Ando, A. Shoji and T. Ozaki, *J. Mol. Struct*., 1996, **384**, 17.
59. R. J. Abraham, M. A. Warne and L. Griffiths, *Magn. Res. Chem*., 1998, **36**, 179.
60. M. P. Williamson and T. Asakura, *J. Magn. Reson*., 1991, **94**, 557.
61. T. Asakura, Y. Niizawa and M. Williamson, *J. Magn. Reson*., 1992, **98**, 646.
62. M. P. Williamson and T. Asakura, *J. Magn. Res*., 1993, **B101**, 63.
63. A. D. Buckingham, *Can. J. Chem*., 1960, **38**, 300.
64. W. T. Raynes and R. Ratcliffe, *Mol. Phys*., 1979, **37**, 571.
65. C. W. Haigh and R. B. Mallion, *Prog. NMR Spectros*., 1980, **13**, 303.
66. J. A. Pople, *J. Chem. Phys*., 1956, **24**, 1111.
67. G. Moyna, R. J. Zauhar, H. J. Williams, R. J. Nachman and A. I. Scott, *J. Chem. Inf. Comput. Sci*., 1998, **38**, 702.
68. S. S. Wijmenga, M. Kruithof and C. W. Hilbers, *J. Biomol. NMR*, 1997, **10**, 337.
69. S. Spera and A. Bax, *J. Am. Chem. Soc*., 1991, **113**, 5490.
70. D. S. Wishart and B. D. Sykes, *J. Biomol. NMR*, 1994, **4**, 171.
71. H. Zhang, S. Neal and D. S. Wishart, *J. Biomol. NMR*, 2003, **25**, 173.
72. D. Labudde, D. Leitner, M. Krüger and H. Oschkinat, *J. Biomol. NMR*, 2003, **25**, 41.
73. M. Schubert, D. Labudde, H. Oschkinat and P. Schmieder, *J. Biomol. NMR*, 2002, **24**, 149.
74. N. Tjandra and A. Bax, *J. Am. Chem. Soc*., 1997, **119**, 9576.
75. J. Meiler, *J. Biomol. NMR*, 2003, **26**, 25.
76. C. J. Jameson, *J. Chem. Phys*., 1977, **66**, 4977.
77. B. Bennett and W. T. Raynes, *Magn. Res. Chem*., 1991, **29**, 946.
78. W. T. Raynes and B. Bennett, *Magn. Res. Chem*., 1991, **29**, 955.
79. D. B. Chesnut and D. W. Wright, *J. Comp. Chem*., 1991, **12**, 546.
80. A. C. de Dios, J. G. Pearson and E. Oldfield, *J. Am. Chem. Soc*., 1993, **115**, 9768.
81. D. Sundholm, J. Gauss and A. Schäfer, *J. Chem. Phys*., 1996, **105**, 11051.
82. D. Sundholm and J. Gauss, *Mol. Phys*., 1997, **92**, 1007.
83. A. A. Auer, J. Gauss and J. F. Stanton, *J. Chem. Phys*., 2003, **118**, 10407.
84. R. Bertram, J. R. Quine, M. S. Chapman and T. A. Cross, *J. Magn. Res*., 2000, **147**, 9.
85. J. G. Batchelor, *J. Am. Chem. Soc*., 1975, **97**, 3410.
86. A. D. Buckingham and J. A. Pople, *Trans. Faraday Soc*., 1963, **59**, 2421.
87. M. Grayson and W. T. Raynes, *Magn. Res. Chem*., 1995, **33**, 138.
88. M. Grayson and W. T. Raynes, *Mol. Phys*., 1994, **81**, 533.
89. J. G. Pearson, E. Oldfield, F. S. Lee and A. Warshel, *J. Am. Chem. Soc*., 1993, **115**, 6851.
90. T. M. Nymand, P.-O. Åstrand and K. V. Mikkelsen, *J. Phys. Chem. B*, 1997, **101**, 4105.
91. T. M. Nymand and P.-O. Åstrand, *J. Chem. Phys*., 1997, **106**, 8332.
92. R. Witter, W. Prieß and U. Sternberg, *J. Comp. Chem*., 2002, **23**, 298.
93. A. E. Torda and W. F. van Gunsteren, *Comp. Phys. Commun*., 1991, **62**, 289.
94. Q. Cui and M. Karplus, *J. Phys. Chem. B*, 2000, **104**, 3721.
95. Q. Cui and M. Karplus, *J. Chem. Phys*., 2000, **112**, 1133.
96. P. Güntert, *Q. Rev. Biophys*. 1009, **31**, 145.
97. M. P. Williamson, *Nat. Prod. Rep*., 1993, 207.
98. M. Möllhoff and U. Sternberg, *J. Mol. Model*., 2001, **7**, 90.
99. U. Sternberg, F.-Th. Koch, M. Bräuer, M. Kunert and E. Anders, *J. Mol. Model*., 2001, **7**, 54.

100. U. Sternberg, F.-Th. Koch and M. Möllhoff, *J. Comp. Chem.*, 1994, **15**, 524.
101. J. Kuszewski, A M. Groenenborn and G. M. Clore, *J. Magn. Res.*, 1995, **B107**, 293.
102. A. T. Brünger, G. M. Clore, A. M. Gronenborn and M. Karplus, *Proc. Natl. Acad. Sci. USA*, 1983, **83**, 3801.
103. E. Oldfield, *J. Biomol. NMR*, 1995, **5**, 217.
104. A. C. de Dios, *Prog. NMR Spectrosc.*, 1996, **29**, 229.
105. I. Ando, S. Kuroki, H. Kurosu and T. Yamanobe, *Prog. Nucl. Magn. Res. Spec.*, 2002, **39**, 79.
106. N. Asakawa, H. Kurosu and I. Ando, *J. Mol. Struct.*, 1994, **323**, 279.
107. H. Le, J. G. Pearson, A. C. de Dios and E. Oldfield, *J. Am. Chem. Soc.*, 1995, **117**, 3800.
108. J. G. Pearson, J.-F. Wang, J. L. Markley, H. Le and E. Oldfield, *J. Am. Chem. Soc.*, 1995, **117**, 8823.
109. R. H. Havlin, H. Le, D. D. Laws, A. C. de Dios and E. Oldfield, *J. Am. Chem. Soc.*, 1997, **119**, 11951.
110. J. Heller, D. D. Laws, M. Tomaselli, D. S. King, D. E. Wemmer, A. Pines, R. H. Havlin and E. Oldfield, *J. Am. Chem. Soc.*, 1997, **119**, 7827.
111. D. D. Laws, H. Le, A. C. de Dios, R. H. Havlin and E. Oldfield, *J. Am. Chem. Soc.*, 1995, **117**, 9542.
112. A. C. de Dios, D. D. Laws and E. Oldfield, *J. Am. Chem. Soc.*, 1994, **116**, 7784.
113. A. C. de Dios and E. Oldfield, *J. Am. Chem. Soc.*, 1994, **116**, 11485.
114. M. Barfield, *Magn. Reson. Chem.*, 1998, **36**, S93.
115. A. Shoji, S. Ando, S. Kuroki, I. Ando and G. A. Webb, *Annu. Rep. NMR Spectr.*, 1993, **26**, 55.
116. M. B. Ferraro, V. Repetto and J. C. Facelli, *Solid State NMR*, 1998, **10**, 185.
117. C. Scheurer, N. R. Skrynnikov, S. F. Lienin, S. K. Straus, R. Brüschweiler and R. R. Ernst, *J. Am. Chem. Soc.*, 1999, **121**, 4242.
118. J. Z. Hu, J. C. Facelli, D. W. Alderman, R. J. Pugmire and D. M. Grant, *J. Am. Chem. Soc.*, 1998, **120**, 9863.
119. J. R. Brender, D. M. Taylor and A. Ramamoorthy, *J. Am. Chem. Soc.*, 2001, **123**, 914.
120. T. B. Wolf, V. G. Malkin, O. L. Malkina, D. R. Salahub and B. Roux, *Chem. Phys. Lett.*, 1995, **239**, 186.
121. N. R. Luman, M. P. King and J. D. Augspurger, *J. Comp. Chem*, 2001, **22**, 366.
122. H. Le and E. Oldfield, *J. Phys. Chem.*, 1996, **100**, 16423.
123. G. Cornilescu, F. Delaglio and A. Bax, *J. Biomol. NMR*, 1999, **13**, 289.
124. D. S. Wishart and A. M. Nip, *Biochem. Cell Biol.*, 1998, **76**, 153.
125. J. Kuszewski, J. Qin, A. M. Gronenborn and G. M. Clore, *J. Magn. Reson.*, 1995, **B106**, 92.
126. T. Asakura, M. Iwadate, M. Demura and M. P. Williamson, *Int. J. Biol. Macromol.*, 1999, **24**, 167.
127. M. Iwadate, T. Asakura and M. P. Williamson, *J. Biomol. NMR*, 1999, **13**, 1999.
128. E. Y. Chekmenev, R. Z. Xu, M. S. Mashula and R. J. Wittebort, *J. Am. Chem. Soc.*, 2002, **124**, 1198.
129. J. Kuszewski, A. M. Gronenborn and G. M. Clore, *J. Magn. Reson.*, 1995, **107**, 293.
130. A. T. Brünger, X-PLOR 3.1 Manual, Yale University, New Haven, CT.
131. W. J. Metzler, B. Leiting, K. Pryor, L. Mueller and B. T. Farmer, *Biochemistry*, 1996, **35**, 6201.
132. P. Luginbühl, T. Szyperski and K. Wüthrich, *J. Magn. Reson.*, 1995, **B109**, 229.
133. K. Nishimura, A. Naito, S. Tuzi, H. Saito, C. Hashimoto and M. Aida, *J. Phys. Chem.*, 1998, **B102**, 7476.
134. M. Wittekind, C. Mapelli, V. Lee, V. Goldfarb, M. S. Friedrichs, C. A. Meyers and L. Mueller, *J. Mol. Biol.*, 1997, **267**, 933.
135. M. Iwadate, T. Asakura and M. P. Williamson, *Eur. J. Biochem.*, 1998, **257**, 479.
136. P. Brown and H. W. Spiess, *Chem. Rev.*, 2001, **101**, 4125.
137. B.-J. van Rossum, D. B. Steensgaard, F. M. Mulder, G. J. Boender, K. Schaffner, A. R. Holzwarth and H. J. M. de Groot, *Biochemistry*, 2001, **40**, 1587.

138. M. Iwadate, E. Nagano, M. P. Williamson, M. Ueki and T. Asakura, *Eur. J. Biochem.*, 2000, **267**, 4504.
139. R. Witter, L. Seyfart, G. Greiner, S. Reissmann, J. Weston, E. Anders and U. Sternberg, *J. Biomol. NMR*, 2002, **24**, 277.
140. G. S. Harbison,, J. Herzfeld and R. G. Griffin, *Biochemistry*, 1983, **22**, 1.
141. G. S. Harbison, S. O. Smith, J. A. Pardoen, P. P. Mulder, J. Lugtenburg, J. Herzfeld, R. Mathies and R. G. Griffin, *Biochemistry*, 1984, **23**, 2662.
142. S. O. Smith, H. J. de Groot, R. Gebhard, J. M. Courtin, J. Lugtenburg, J. Herzfeld and R. G. Griffin, *Biochemistry*, 1989, **28**, 8897.
143. S. O. Smith, J. Courtin, E. van den Berg, C. Winkel, J. Lugtenburg, J. Herzfeld and R. G. Griffin, *Biochemistry*, 1989, **28**, 237.
144. A. T. Petkova, J. G. Hu, M. Bizounok, M. Simpson, R. G. Griffin and J. Herzfeld, *Biochemistry*, 1999, **38**, 1562.
145. S. O. Smith, I. Palings, M. E. Miley, J. Courtin, H. de Groot, J. Lugtenburg, R. A. Mathies and R. G. Griffin, *Biochemistry*, 1990, **29**, 8158.
146. T. A. Egorova-Zachernyuk, B. van Rossum, G. J. Boender, E. Franken, J. Ashurst, J. Raap, P. Gast, A. J. Hoff, H. Oschkinat and H. J. de Groot, *Biochemistry*, 1997, **36**, 7513.
147. L. M. McDowell and J. Schaefer, *Curr. Opin. Struct. Biol.*, 1996, **6**, 624.
148. L. K. Thompson, *Curr. Opin. Struct. Biol.*, 2002, **12**, 661.
149. A. Watts, *Mol. Membr. Biol.*, 2002, **19**, 267.
150. Z. Gu, D. G. Drueckhammer, L. Kurz, K. Liu, D. P. Martin and A. McDermott, *Biochemistry*, 1999, **38**, 8022.
151. P. T. Williamson, G. Grobner, P. J. Spooner, K. W. Miller and A. Watts, *Biochemistry*, 1998, **37**, 10854.
152. P. T. Williamson, S. Bains, C. Chung, R. Cooke and A. Watts, *FEBS Lett.*, 2002, **518**, 111.
153. S. Luca, J. F. White, A. K. Sohal, D. V. Filippov, J. H. van Boom, R. Grisshammer and M. Baldus, *Proc. Natl. Acad. Sci. USA*, 2003, **100**, 10706.
154. P. O. Quist, *Biophys. J.*, 1998, **75**, 2478.
155. M. J. Hong, *J. Biomol. NMR*, 1999, **15**, 1.
156. A. McDermott, T. Polenova, A. Bockmann, K. W. Zilm, E. K. Paulson, R. W. Martin, G. T. Montelione and E. K. Paulsen, *J. Biomol. NMR*, 2000, **16**, 209–219.
157. J. Pauli, M. Baldus, B. van Rossum, H. de Groot and H. Oschkinat, *Chembiochem*, 2001, **2**, 272.
158. B. J. van Rossum, F. Castellani, K. Rehbein, J. Pauli and H. Oschkinat, *Chembiochem*, 2001, **2**, 906.
159. B. J. van Rossum, F. Castellani, J. Pauli, K. Rehbein, J. Hollander, H. J. De Groot and H. Oschkinat, *J. Biomol. NMR*, 2003, **25**, 217.
160. F. B. Castellani, B. van Rossum, A. Diehl, M. Schubert, K. Rehbein and H. Oschkinat, *Nature*, 2002, **420**, 98.
161. F. Castellani, B. J. van Rossum, A. Diehl, K. Rehbein and H. Oschkinat, *Biochemistry*, 2003, **42**, 11476.
162. R. W. Martin and K. W. Zilm, *J. Magn. Reson*, 2003, **165**, 162.
163. A. T. Petkova, M. Baldus, M. Belenky, M. Hong, R. G. Griffin and J. Herzfeld, *J. Magn. Reson.*, 2003, **160**, 1.
164. R. Smith, D. E. Thomas, F. Separovic, A. R. Atkins and B. A. Cornell, *Biophys. J.*, 1989, **56**, 307.
165. Q. Teng, L. K. Nicholson and T. A. Cross, *J. Mol. Biol.*, 1991, **218**, 607.
166. W. Hu, K. C. Lee and T. A. Cross, *Biochemistry*, 1993, **32**, 7035.
167. S. L. Grage, J. Wang, T. A. Cross and A. S. Ulrich, *Biophys. J.*, 2002, **83**, 3336.
168. T. A. Cross, *Methods Enzymol.*, 1997, **289**, 672.
169. R. Ketchem, B. Roux and T. Cross, *Structure*, 1997, **5**, 1655.
170. F. Kovacs, J. Quine and T. A. Cross, *Proc. Natl. Acad. Sci. USA*, 1999, **96**, 7910.

171. B. Bechinger, Y. Kim, L. E. Chirlian, J. Gesell, J. M. Neumann, M. Montal, J. Tomich, M. Zasloff and S. J. Opella, *J. Biomol. NMR*, 1991, **1**, 167–173.
172. B. Bechinger, *Mol. Membr. Biol.*, 2000, **17**, 135–142.
173. A. Mascioni, C. Karim, G. Barany, D. D. Thomas and G. Veglia, *Biochemistry*, 2002, **41**, 475–482.
174. F. M. Marassi, S. J. Opella, P. Juvvadi and R. B. Merrifield, *Biophys. J.*, 1999, **77**, 3152.
175. S. Yamaguchi, D. Huster, A. Waring, R. I. Lehrer, W. Kearney, B. F. Tack and M. Hong, *Biophys. J.*, 2001, **81**, 2203.
176. M. S. Balla, J. H. Bowie and F. Separovic, *Eur. Biophys. J.*, 2003, **10**, 10.
177. F. M. Marassi and S. J. Opella, *J. Magn. Reson.*, 2000, **144**, 150.
178. S. J. Opella, A. Nevzorov, M. F. Mesleb and F. M. Marassi, *Biochem. Cell Biol.*, 2002, **80**, 597.
179. F. M. Marassi and S. J. Opella, *Protein Sci.*, 2003, **12**, 403.
180. A. A. Nevzorov and S. J. Opella, *J. Magn. Reson.*, 2003, **164**, 182.
181. F. M. Marassi C. Ma, J. J. Gesell and S. J. Opella, *J. Magn. Reson.*, 2000, **144**, 156.
182. V. Wray, R. Kinder, T. Federau, P. Henklein, B. Bechinger and U. Schubert, *Biochemistry.*, 1999, **38**, 5272.
183. P. Henklein, R. Kinder, U. Schubert and B. Bechinger, *FEBS Lett.*, 2000, **482**, 220–224.
184. S. H. Park, A. A. Mrse, A. A. Nevzorov, M. F. Mesleh, M. Oblatt-Montal, M. Montal and S. J. Opella, *J. Mol. Biol.*, 2003, **333**, 409.
185. Z. Song, F. A. Kovacs, J. Wang, J. K. Denny, S. C. Shekar, J. R. Quine and T. A. Cross, *Biophys. J.*, 2000, **79**, 767.
186. C. Tian, K. Tobler, R. A. Lamb, L. H. Pinto and T. A. Cross, *Biochemistry*, 2002, **41**, 11294.
187. L. K. Nicholson, T. Asakura, M. Demura and T. A. Cross, *Biopolymers*, 1993, **33**, 847.
188. T. Asakura, R. Sugino, J. Yao, H. Takashima and R. Kishore, *Biochemistry*, 2002, **41**, 4415.
189. Y. Nakazawa and T. Asakura, *J. Am. Chem. Soc.*, 2003, **125**, 7230.
190. J. Ashida, K. Ohgo, K. Komatsu, A. Kubota and T. Asakura, *J. Biomol. NMR*, 2003, **25**, 91.
191. J. J. Balbach, Y. Ishii, O. N. Antzutkin, R. D. Leapman, N. W. Rizzo, F. Dyda, J. Reed and R. Tycko, *Biochemistry*, 2000, **39**, 13748.
192. R. Tycko, *Methods Enzymol.*, 2001, **339**, 390.
193. R. Tycko and Y. Ishii, *J. Am. Chem. Soc.*, 2003, **125**, 6606.
194. S. Afonin, U. H.N. Dürr, R. W. Glaser and A. S. Ulrich, *Magn. Reson. Chem.*, 2004, **42**, 195.
195. P. Barre, O. Zschornig, K. Arnold and D. Huster, *Biochemistry*, 2003, **42**, 8377.
196. J. Yang and D. P. Weliky, *Biochemistry*, 2003, **42**, 11879.
197. U. Harzer and B. Bechinger, *Biochemistry*, 2000, **39**, 13106.
198. B. Bechinger, D. A. Skladnev, A. Ogrel, X. Li, E. V. Rogozhkina, T. V. Ovchinnikova, J. D. O'Neil and J. Raap, *Biochemistry*, 2001, **40**, 9428.
199. J. Salgado, S. L. Grage, L. H. Kondejewski, R. S. Hodges, R. N. McElhaney and A. S. Ulrich, *J. Biomol. NMR*, 2001, **21**, 191.
200. Y. Hori, M. Demura, M. Iwadate, A. S. Ulrich, T. Niidome, H. Aoyagi and T. Asakura, *Eur. J. Biochem.*, 2001, **268**, 302.
201. K. J. Hallock, D. K. Lee, J. Omnaas, H. I. Mosberg and A. Ramamoorthy, *Biophys. J.*, 2002, **83**, 1004.
202. R. Tycko, *J. Biomol. NMR*, 1996, **8**, 239–251.
203. R. Bertram, T. Asbury, F. Fabiola, J. R. Quine, T. A. Cross and M. S. Chapman, *J. Magn. Reson.*, 2003, **163**, 300.
204. M. Bak, R. Schultz, T. Vosegaard and N. C. Nielsen, *J. Magn. Reson.*, 2002, **154**, 28.
205. C. R. Morcombe and K. W. Zilm, *J. Magn. Reson.*, 2003, **162**, 479.
206. R. W. Glaser and A. S. Ulrich, *J. Magn. Reson.*, 2003, **164**, 104.
207. R. Ulrich, R. W. Glaser and A. S. Ulrich, *J. Magn. Reson.*, 2003, **164**, 115.
208. O. Soubias, V. Reat, O. Saurel and A. Milon, *J. Magn. Reson.*, 2002, **158**, 143.

209. D. K. Lee and A. Ramamoorthy, *J. Magn. Reson.*, 1998, **133**, 204.
210. J. R. Brender, D. M. Taylor and A. Ramamoorthy, *J. Am. Chem. Soc.*, 2001, **123**, 914.
211. R. H. Havlin, D. D. Laws, H. M. Bitter, L. K. Sanders, H. Sun, J. S. Grimley, D. E. Wemmer, A. Pines and E. Oldfield, *J. Am. Chem. Soc.*, 2001, **123**, 10362.
212. L. Odgaard, M. Bak, H. J. Jakobsen and N. C. Nielsen, *J. Magn. Reson.*, 2001, **148**, 298.
213. Y. Wei, D. K. Lee and A. Ramamoorthy, *J. Am. Chem. Soc.*, 2001, **123**, 6118.
214. X. Yao, S. Yamaguchi and M. Hong, *J. Biomol. NMR*, 2002, **24**, 51.
215. U. Sternberg, F.-Th. Koch and W. Prieß and R. Witter, *Cellulose*, 2003, **10**, 189.

^{77}Se NMR Spectroscopy and Its Applications in Chemistry

HELMUT DUDDECK

Hannover University, Institute of Organic Chemistry, Schneiderberg 1B, D-30167 Hannover, Germany

1. INTRODUCTION

Selenium has attracted the widest NMR spectroscopic interest among the group 16 elements. A number of reviews have appeared during the 1980s and the mid-1990s.[1] In the meantime, many new important reports and applications have appeared. Thus, it deemed desirable to prepare an updated ^{77}Se NMR review with particular emphasis on chemical applications. It should be noted that a comprehensive ^{77}Se NMR data collection[2] covering the literature into the year 2000 is in print.

For many decades selenium chemistry remained an exotic field of research and only a few selenium compounds, as for example SeO_2, saw frequent application as a reagent. Although selenium was quite popular in inorganic chemistry,[3] modern organoselenium chemistry commenced only in the early 1970s and the first reviewing reports appeared in 1972–1974.[4] During the seventies it became clear that organoselenium compounds are valuable intermediates in a great variety of reactions since they often react

ANNUAL REPORTS ON NMR SPECTROSCOPY
VOLUME 52 ISSN 0066 4103
DOI 10.1016/S0066-4103(04)52003-3

regio- and/or stereoselectively with high efficiency under mild conditions producing selenium-free molecules. Consequently, a substantial number of reviews and monographs were published at the end of the seventies and during the eighties.[5] A comprehensive list of important organoselenium chemistry literature has been compiled by Krief and Hevesi in 1988.[6] Nowadays, this field is a well-established area in the arsenal of methods for functional group transformation. Stereoselectivity and stereospecifity as well as chirality effects play an ever increasing role.[7]

While reports of ^{77}Se NMR reach back to the early fifties[8] the first systematic investigations in this field were published between 1965 and 1971.[9] Thereafter, the interest in this nucleus increased steadily when it was noticed that its NMR properties were comparable to those of ^{13}C making it rather easily accessible under routine pulse Fourier transform recording conditions. At the end of the century, the number of papers reporting ^{77}Se NMR data exceeded 1200.

In the beginning, the interest was focused on the exploration of the general ^{77}Se NMR characteristics, and only a part of these publications dealt with the chemistry of organoselenium compounds. Later, more and more reports were published with studies on the chemical reactions, the stereochemistry, molecular dynamics and – last but not least – biochemical applications of various compounds. Needless to say that ^{77}Se NMR spectroscopy is an important tool in the investigation of inorganic selenium compounds as well. During the 1990s, ^{77}Se NMR gained increasing attention in studying metal complexes with organic or inorganic selenium-containing ligands; in 2002 the number of such papers exceeded 500.

In order to avoid data overflow, the present article is designed to be an update of the author's previous review[1e] which covered the literature up to 1994. Nevertheless, it contains some selected pre-1995 literature to make the article self-consistent.

2. ^{77}Se NMR PARAMETERS

The most important ^{77}Se NMR parameter is the chemical shift $\delta(^{77}\mathrm{Se})$ reflecting the chemical environment around the selenium atom. Chemical shift tensors can be obtained from the rotational side-band pattern in solid-state ^{77}Se NMR spectra and offer more detailed information. Reports on coupling constants involving ^{77}Se are comparably rare although at least $^{1}J(^{77}\mathrm{Se},^{1}\mathrm{H})$ and $^{1}J(^{77}\mathrm{Se},^{13}\mathrm{C})$ can often be read easily from the ^{77}Se-satellites in the ^{1}H and ^{13}C NMR spectra, respectively. On the other hand, $^{1}J(^{77}\mathrm{Se},^{31}\mathrm{P})$ values are popular because they reflect the bond order within the P=Se group. However, these coupling constants are often extracted from the ^{31}P NMR peaks and, unfortunately, many author's refrained from direct ^{77}Se NMR measurements.

2.1. Nuclear properties, experimental techniques and calculations

2.1.1. *NMR properties*

The element selenium consists of six natural isotopes: ^{74}Se (0.87%), ^{76}Se (9.02%), ^{77}Se (7.58%), ^{78}Se (23.52%), ^{80}Se (49.82%), and ^{82}Se (9.19%). Only one of them, ^{77}Se, is NMR-active having a nuclear spin quantum number of $I = 1/2$; i.e., it has no quadrupolar moment, and high-resolution NMR spectroscopy is possible. The resonance frequency (at $B_0 = 2.3$ T, corresponding to 100 MHz for ^{1}H) is 19.07 MHz, and the receptivity R_C is 2.9 relative to ^{13}C (recorded under identical external conditions, i.e., magnetic field, molar concentration etc.). Thus, ^{77}Se is about three times more NMR sensitive than ^{13}C. Taking into account that longitudinal relaxation times (T_1) are in the range of seconds (similar to ^{13}C) and NOE effects are generally absent (except in selenols, R–Se–H), the sensitivities of ^{13}C and ^{77}Se are comparable in routine NMR experiments.

In the early days there was a sensitivity problem when using CW techniques which has been overcome – at least in part – by indirect multiple-resonance experiments,[10] but with the advent of pulse Fourier Transform spectrometers (ca. 1970) sensitivity is no longer an obstacle.

2.1.2. *Two-dimensional NMR experiments*

A number of papers contain two-dimensional NMR spectra involving ^{77}Se nuclei. The first was an exchange experiment (^{77}Se 2D-EXSY) which proved that exchange processes in 1:1 mixtures of S_2Cl_2 and $SeBr_2$ take place predominantly via chalcogen–halogen bond cleavages, and any other mechanisms involving chalcogen–halogen radicals or four-centre-intermediates can be excluded.[11] The second instance discusses ^{77}Se-detected 2D ^{77}Se,^{13}C correlation spectra by which the stereoisomeric compounds **1** and **2** could be differentiated.[12] It was possible to detect ^{77}Se,^{13}C couplings over one and over two to four bonds. In addition, a ^{77}Se-detected ^{77}Se,^{1}H HOESY experiment was described which revealed a steric contact between the nucleus Se^a and the *ortho*-protons of the vicinal *cis* phenyl ring in **2**, a contact which does not exist in the corresponding *trans* configuration (Scheme 1).[12]

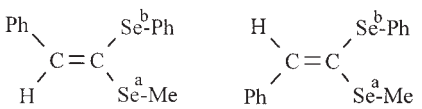

1 **2**

$^2J(^{77}Se,^{1}H)$ = H-Se^a : 5.3 Hz H-Se^a : 11.0 Hz

H-Se^b : 11.6 Hz H-Se^b : 8.9 Hz

Scheme 1

Glass *et al.*, were the first to mention the enormous sensitivity gain achievable by ^{1}H-detected {^{77}Se} correlation spectroscopy.[13–15] They showed for a number of representative organoselenium compound that the theoretical *S*/*N* ratio enhancement factor of 72, as compared to direct ^{77}Se detection, can nearly be achieved so that this technique should be applied for recording biomolecules in low concentration, e.g., in selenoproteins. If inverse detection is combined with isotopic enrichment of ^{77}Se, the factor may be increased up to 800.[13] Selenomethionine, selenocysteine, and related compounds have been recorded using ^{77}Se,^{1}H HETCOR experiments.[16]

Silks *et al.*, have proven the existence of through-space N–H $\cdots$ Se=C coupling and, for the first time at all, C–H $\cdots$ Se=C interactions by recording ^{1}H,^{77}Se HMQC spectra.[17,18] In the case of compound **3**, a signal splitting of 13 Hz was registered being much too high for a through-bond ^{5}J(^{77}Se,^{1}H) coupling constant.[18] In compounds like **4** it was found that there is no hydrogen bonding between the OH group and selenium as originally expected. Rather, it is the CH proton which undergoes a through-space ^{77}Se,^{1}H coupling of 5–7 Hz (Scheme 2).[17]

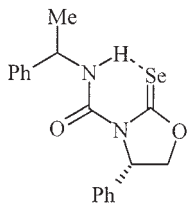

3

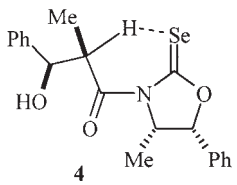

4

Scheme 2

Selenoureas have been used for applying gradient-enhanced ^{1}H,^{77}Se HSQC experiments.[19,20] One-dimensional ^{77}Se HMQC detection has been applied in a ditungsten complex with bridging $>$Se–CH_2Ph substituents allowing to determine precisely the two-bond 77Se,^{1}H coupling as 20.6 Hz.[21] Recently, ^{1}H,^{77}Se HMBC spectroscopy has been used for the unequivocal assignment of ^{77}Se signals when organoselenium ligands form adducts with dirhodium complexes and the signals of free and ligated selenium atoms have to be discerned.[22]

Interestingly, even small ^{77}Se,^{13}C coupling constants *via* two to four bonds (13.7–1.7 Hz) could be identified benzoselenadiazoles by 1D ^{13}C-detected {^{77}Se} HMBC spectroscopy.[23]

2.1.3. *Temperature-dependent ^{77}Se NMR spectroscopy*

Various medium effects[1e] – such as temperature, concentration, and pH – play an important role, as for many other heavy nuclei. Consequently, ^{77}Se chemical shifts are medium-dependent. Signal shifts of several ppm over a temperature range of 100° have been reported for various classes of

organoselenium compounds. Thus, it is advisable to keep the temperature constant within the sample, otherwise line shape distortions and considerable line broadening can be observed. Even broad-band ^{1}H-decoupling can be the origin of such unwanted effects.

Conformational analysis of selenium-containing compounds by temperature-variable NMR spectroscopy (DNMR) is facilitated by the great sensitivity of the ^{77}Se chemical shift. Generally, chemical shift differences of selenium atoms in different conformers (at low temperatures) are much larger than those of carbon or hydrogen atoms. Therefore, the coalescence temperature in ^{77}Se NMR spectra is higher than in ^{1}H or ^{13}C NMR experiments of the same compounds. However, it should be noted that the temperature range in which line broadening occurs, is larger than that of ^{1}H and ^{13}C. So, the gain in rising temperatures for the observation of coalescence is often not accompanied by the same temperature gain in reaching the low-temperature regime when the conformers are frozen and the spectra show the signals of the individual conformers without line broadening. This devalues the advantage of ^{77}Se DNMR to some extent. On the other hand, a larger temperature range for changes in the appearance of the signals allows a higher precision in the computer-simulation for extracting the thermodynamic and kinetic data of the conformational process.

The coalescence of ^{77}Se signals for the ring inversion process of cyclohexanes with phenylselenenyl substituents occurs at ca. 283 K whereas those of ^{1}H or ^{13}C signals appear at least 60° lower at the same external field strength.[24,25] The equilibrium is in favour of the equatorial conformer and a free energy difference of 4.6 kJ/mol (A-value = 1.1) has been determined.[24] The ring inversion barrier is ca. 49 kJ/mol (equatorial → axial isomer), a value similar to that of other monosubstituted cyclohexanes indicating that the substituent has no significant influence.[24]

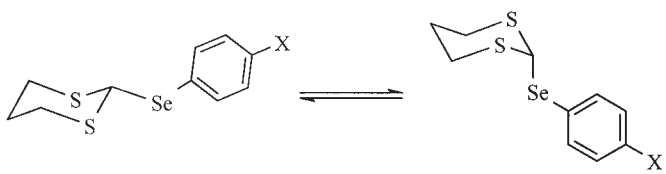

5 (X = NMe_2, OMe, H, CF_3, NO_2)

Scheme 3

Third-row anomeric effects of arylselenenyl substituents were studied in 2-arylseleno-1,3-dithianes (**5**) (Scheme 3). This effect favours the axial conformer by 6.7–9.2 kJ/mol, and an intramolecular $n_S \rightarrow \sigma^*_{C-Se}$ interaction is held responsible.[26,27] Interestingly, this stabilizing interaction depends clearly on the nature of the substituent X; the strongest effect is observed for the nitro (9.2 kJ/mol) and weakest for dimethylamino (6.7 kJ/mol). This can

be interpreted in terms of Dual Substituent Parameters (DSP) analysis showing that the anomeric effect is indeed based on an orbital and not an electrostatic interaction.[26] The existence of an anomeric effect has also been determined in analogous 1,3-diselenanes (endocyclic sulphur atoms in **5** replaced by Se).[28]

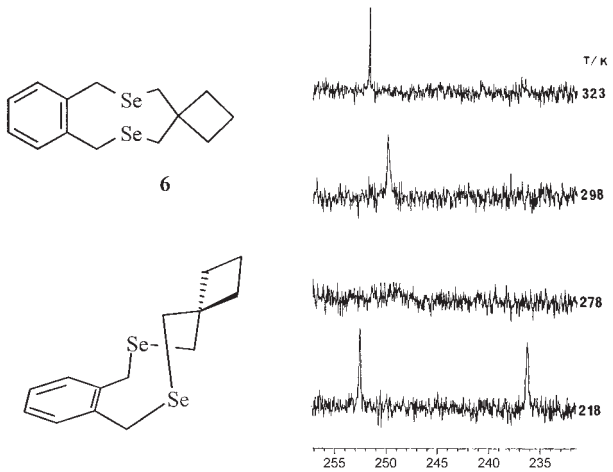

Scheme 4

A variable-temperature ^{77}Se NMR study confirmed earlier reports that the 1,4,5,7-tetrahydro-3*H*-2,6-benzodiselenine derivative **6** (Scheme 4) exists as a racemic mixture of two interconverting enantiomeric conformers with chemically non-equivalent selenium atoms.[29]

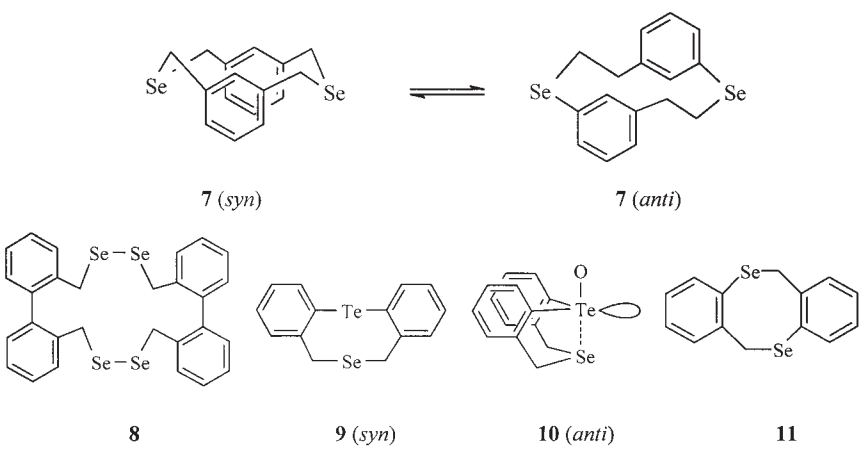

7 (*syn*) **7** (*anti*)

8 **9** (*syn*) **10** (*anti*) **11**

Scheme 5

The conformational equilibrium of 2,11-diselena[3.3]metacyclophane (**7**) has been investigated (Scheme 5). It involves a *syn*,*anti*-interconversion with a barrier of ca. 33.5 kJ/mol and a strong predominance of the *syn*-conformer.[30] In addition, there is a 'bridge wobble' (up and down motion of the selenium atoms) which, however, could not be measured in contrast to the respective wobble of the groups in [3.3]metacyclophane.[30] A great variety of other diselena[3.3] cyclophanes with benzene and other heteroaromatic rings (furyl, pyridyl, and thiophenyl) and one tetraselena[4.4]cyclophane (**8**) have been studied, and again the *syn*-conformers are more stable.[31] 5*H*,7*H*-Dibenzo[*b*,*g*][1,5]telluraselenocin (**9**) exists in two different conformers, a boat (58%) and a chair form (42%), whereas its oxidation product **10** adopts exclusively the boat conformation stabilized by a transannular interaction[32] (compare Section 3.4). Boat and chair conformers of dibenzosiselenocins **11** were identified.[33] Conformational interconversion in the selenocarbamates **12** is observed by variable-temperature ^{13}C and ^{77}Se NMR spectroscopy (Scheme 6).[34]

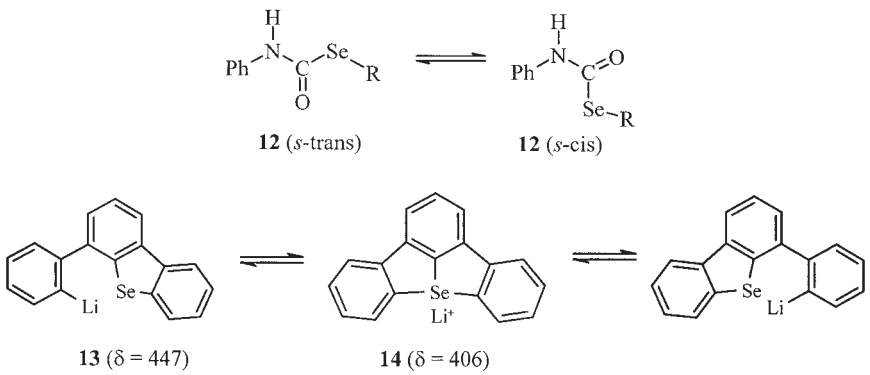

Scheme 6

Intramolecular interactions between charged species can be investigated as well. For example, the exchange equilibrium of the ate complex **13** and the hypervalent lithiumorganyls **14** has been monitored by ^{77}Se DNMR spectroscopy (Scheme 6).[35,36] Selenium–hydrogen contacts in selenoarsinous (**15**) and in related diselenoarsinic acid ion pairs were proven by inspecting the low-temperature ^{77}Se signals (Scheme 7).

A coalescence has been detected in the variable-temperature ^{77}Se NMR spectra of the tungsten complex **16**. One signal ($\delta = 874$) broadens on lowering the temperature and finally splits into two with approximately equal intensity ($\delta = 967$ and 754 at 183 K). This observation was attributed to a stereochemical non-rigidity of the five-membered rings containing Se[a] rather than to a dissociative process.[37] The dynamic behaviour of some other platinum[38]

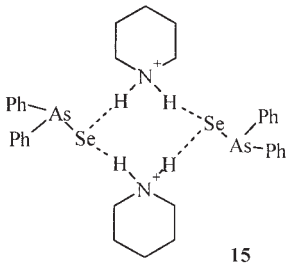

15

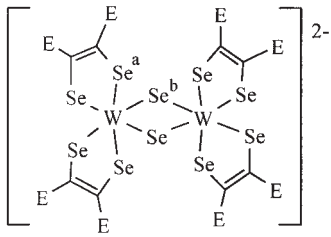

16 (E = $COOCH_3$)

Scheme 7

and manganese[39] complexes observed by low-temperature NMR has been described.

The mechanisms and kinetics of ligand exchange in adducts of selenoethers and a chiral dirhodium tetraacylate were investigated using 3-phenylselenenyl-1-phenyl-1-propene[40] and a variety of phenylselenylcyclohexane derivatives.[22] It was shown that the selenium atom is the binding site of all ligands and that different exchange mechanisms exist depending on the molar ratio of ligand relative to the dirhodium complex.

2.1.4. *Solid-state ^{77}Se NMR**

The ^{77}Se NMR chemical shift tensors of a selection of inorganic and organic selenium-containing compounds have been obtained from solid-state NMR, partly involving cross-polarization (CP) and magic angle spinning (MAS). Some early data have been previously compiled before.[1e] Later (after 1994), this technique was recognized as a valuable tool for structural investigations in the solid state. Se_5^{2-} and Se_6^{2-} anions appeared to have similar ^{77}Se chemical shifts and conformations in the liquid and the solid state.[41] Some selenates (VI) were measured by ^{77}Se MAS NMR; the isotropic chemical shifts are $\delta = 1024$ for Li_2SeO_4 and $\delta = 876$ for the pentavalent selenium in Li_4SeO_5 (slightly distorted trigonal bipyramid).[42] Details of the structure and dynamics (reorientation) of selenate ($\delta_{iso} \approx 1050$) and selenite in hydrotalcite-like compounds (mixed-metal layered hydroxides) were investigated.[43] The isotropic ^{77}Se chemical shift of $Se(SCN)_2$ is $\delta = 997$ in good agreement with data obtained for various solutions ($\delta = 960$–993).[44] Selenium atoms in phosphorus–selenium glasses could be differentiated according to absent or existing P–Se links by solid-state ^{77}Se NMR at various temperatures.[45] $^{31}P \rightarrow {}^{77}Se$ cross polarization and MAS was used for detecting the solid-state ^{77}Se resonance of β-P_4Se_3, an inorganic glass with $\delta \approx 1290$.[46]

*Although not directly related to ^{77}Se NMR, a very recent review on what high-resolution solid-state NMR spectroscopy can offer is recommended: M. J. Porzebowski, *Eur. J. Org. Chem.*, **2003**, 1367–1376.

A surprising observation was the fact that the solid-state ^{77}Se CP/MAS NMR spectrum of diphenyldiselenide (Ph–Se–Se–Ph, **17**) (Scheme 8) afforded two resonances at $\delta_{iso} = 425$ and 350, far distant from each other, whereas there is only one signal at $\delta = 463$ in the liquid state.[47] Clearly, the molecule adopts a chiral conformation with different torsion angles Se(1)–Se(8)–C(9)–C(14) vs. Se(8)–Se(1)–C(2)–C(7) leading to a 75-ppm-chemical shift differerence.[47]

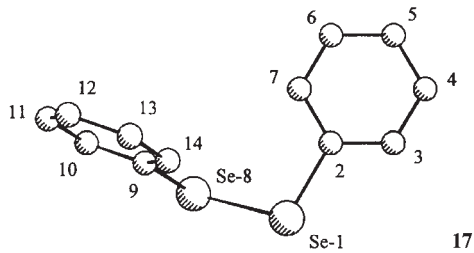

17

Scheme 8

Porzebowski emphasized the merits of high-resolution solid-state ^{77}Se NMR spectroscopy demonstrating that it is complementary to X-ray studies by comparing various classes of organoselenium compounds.[48] An example is the structure of bis[(2,3,4,6)-tetra-*O*-acetyl-β-D-glucopyranosyl] diselenide and its solid-state conformation with respect to the central C–C–Se–Se–C–C fragment.[49] Characteristic chemical shift tensors were determined and interpreted. Another paper reports on the ^{77}Se CP/MAS NMR spectral data of the amino acid selenomethionine as pure L-enantiomer and as racemate including an investigation of the packing effects in the crystal and molecular dynamics.[50]

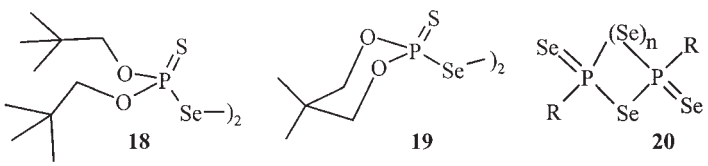

18 **19** **20**

Scheme 9

Further pioneering work has been published by Porzebowski and his group on bis-phosphoryl diselenides [–P(=X)–Se–Se–P(=S)] and phosphine selenides [XYZP(=Se)]. For bis(dineopentoxythiophosphoryl) diselenide **18** and *anti-anti*-conformation of the Se–Se–P=Se fragment was found.[51] In a structurally related dioxaphosphorinanyl diselenide **19** a *syn*-clinal arrangement of the P–Se–Se–P fragment was found.[52] It turned out from experiments of these and some related diselenides that ^{77}Se parameters obtained from ^{77}Se CP/MAS reflect molecular packing effects sensitively.[51–54] Anisotropies of ^{77}Se chemical shift

tensors in molecules containing P=Se groups were determined as well.[55,56] Very recently, this technique was applied by Grossmann *et al.*, to some phosphetane **20** ($n = 1$) and phospholane **20** ($n = 2$) analogues (Scheme 9).[57]

2.1.5. *Theory and calculations*

Since 1993 considerable effort has been taken to reproduce ^{77}Se chemical shifts by *ab initio* calculations. Japanese authors reported a study describing the calculation of ^{77}Se chemical shifts of various selenides R–Se–R′ by the Hartree–Fock finite perturbation method; they found that the shielding is dominated by the contribution of the 4p orbital of Se to the paramagnetic term σ_p.[58] Gas-phase ^{77}Se chemical shifts of H_2Se, CH_3SeH, and $(CH_3)_2Se$ were published in the same year,[59] and in 1994 Magyarfalvi and Pulay reported principal values of the shielding tensors for the same compounds on the basis of GIAO calculations.[60] More detailed studies including comparisons between different calculations methods (GIAO, IGLO etc.) appeared in 1995 when Bühl *et al.* described their results for small selenium-containing compounds including selenols, CSe_2, selenoketones (RR′C=Se), fluoridated selenides, selenoxides, SeF_6, and selenophene.[61] In 1996, other authors showed that $\delta(^{77}Se)$ can also be reproduced over a great span of the ^{77}Se chemical shift range with sufficient accuracy by density functionol theory (DFT) calculations using GIAOs.[62] In the following years, ^{77}Se shieldings of even larger molecules were reported including diphenyl diselenide,[47] various aryl and diaryl selenides[63] and halogen adducts (molecular complex vs. trigonal bipyramid) thereof,[64] phosphorothioyl diselenides (P=Se),[57,65] Se_nS_{8-n} ring molecules[66] and diselenins;[67] and further optimization of the DFT calculation method has been proposed by Wilson.[68]

2.2. ^{77}Se chemical shifts

As for most other nuclei, the ^{77}Se chemical shift, i.e., the signal position relative to that of a chosen standard reference, is the most important NMR parameter since it reflects the chemical environment of the selenium atom in terms of attached atoms/groups, oxidation state and other effects influencing the electronic situation around the ^{77}Se nucleus. Under ^{1}H-decoupling condition, ^{77}Se signals are singlets if no other spin-1/2 nucleus with sufficient natural abundance (V) is present, as in ^{19}F or ^{31}P. ^{13}C with V = 1.1% is generally not sufficient to observe ^{13}C-satellites; rather, ^{77}Se-satellites (^{77}Se: V = 7.58%) can be seen from the ^{13}C resonances if the signal-to-noise ratio is good enough. However, ^{77}Se chemical shifts are quite sensitive to medium effects (solvent, temperature, pH etc.) so that careful sample preparation and constant temperature during sampling are mandatory in order to avoid chemical shift errors of several ppm and severe line broadening.

2.2.1. *Referencing and medium effects*

Referencing is not uniform in ^{77}Se NMR spectroscopy; a number of compounds have been used as standards. A solution of Me_2Se in $CDCl_3$ (60% v/v) as an external probe has been proposed and accepted as a universal reference.[69] Me_2Se, however, is volatile, has a very unpleasant smell and is toxic, and an accidental spilling or a breaking of the sample tube will be hazardous. Therefore, it is advisable to use other selenium compounds as external standard samples and refer the obtained experimental chemical shifts to Me_2Se in $CDCl_3$ (60% v/v). For example, diphenyl diselenide (Ph_2Se_2) with a ^{77}Se chemical shift of $\delta = 463$ is well-suited, because it is a commercially available, stable solid which is a popular starting material in organoselenium chemistry and can be handled conveniently. A saturated solution of H_2SeO_3 in H_2O at 20°C with a selenium chemical shift of $\delta = 1300.0$ has been recommended.[70] Recently, ditetradecyl selenide, $(C_{14}H_{29})_2Se$, was suggested as an alternative to Me_2Se as a reference compound in organic solvents because it is easy to prepare, non-odorous and stable.[71]

The δ-values of some commonly employed standard compounds are collected in Table 1 and can be used to convert reported ^{77}Se chemical shifts relative to Me_2Se in $CDCl_3$ (60% v/v; $\delta = 0$). However, this procedure implies inaccuracies of several ppm since re-referencing of literature data often has to ignore medium effects on the ^{77}Se chemical shift.

Often ^{77}Se chemical shifts are given with a precision of 0.1 ppm. The above mentioned reasons and the fact that $\delta(^{77}Se)$-values are reproducible only within a few tenths of a ppm prompted the author of this review to present all ^{77}Se chemical shift values as integers only. This is comparable to the generally accepted notation in ^{13}C NMR spectroscopy where $\delta(^{13}C)$-values are given in decimals; the ^{77}Se resonance range is about ten times larger than that of ^{13}C.

Table 1. ^{77}Se chemical shifts of compounds used as references, relative to Me_2Se in $CDCl_3$ (60% v/v)[69]

Compound	Solvent	$\delta(^{77}Se)$
Me_2Se	$CDCl_3$ (60% v/v)	0
	neat	+4
(n-$C_{14}H_{29})_2Se$	$CDCl_3$	+162
Ph_2Se_2	$CDCl_3$	+463
$SeOCl_2$	neat	+1479
H_2SeO_3	H_2O (saturated)	+1300
Na_2SeO_3	H_2O (infinite dilution)	+1260
$(NH_4)_2SeO_4$	solid state	+1040
Selenophene	$CDCl_3$	+605
	C_6D_6 (20% v/v)	+605
Benzo[b]selenophene	$CDCl_3$	+530
$Ph_3P{=}Se$	$CDCl_3$	−262

An absolute shielding scale for the ^{77}Se nucleus has been established on the basis of gas-phase T_1 measurements of ^{19}F and ^{77}Se in SeF_6.[72] Using this scale the ^{77}Se chemical shift of liquid Me_2Se is $\delta = 2069$.

2.2.2. *^{77}Se chemical shift ranges and substituent effects – a general survey*

^{77}Se chemical shifts span a wide range of ca. 3300 ppm; the extremes are marked by selenoaldehydes, some molybdenum selenides, and cationic heterocycles (up to $\delta = 2434$) at the high-frequency end and bridging selenium (μ) in tungsten complexes ($\delta = -900$) at the low-frequency end. A detailed discussion of electronic influences on ^{77}Se chemical shifts and its variation in different classes of compounds has been published.[1e] In the following, some general characteristic tendencies are collected.

Electronegativities of attached atoms:

$$\begin{aligned}&\text{Ph–Se–Cl } (\delta = 1039) > \text{Ph–Se–Br } (\delta = 867) > \text{Ph–Se–NEt}_2 \ (\delta = 617)\\ &> \text{Ph–Se–SMe } (\delta = 514) > \text{Ph–Se–SeMe } (\delta = 447) > \text{Ph–Se–CH}_3 \ (\delta = 202)\\ &> \text{Ph–Se–H } (\delta = 145) > \text{Ph–Se–SnMe}_3 \ (\delta = 11)\end{aligned}$$

or

$$\begin{aligned}&\text{Ph–Se(=O)–Ph } (\delta = 863) > \text{Ph–Se(Cl}_2\text{)–Ph } (\delta = 586)\\ &> \text{Ph–Se(Br}_2\text{)–Ph } (\delta = 545) > \text{Ph–Se–Ph } (\delta = 420)\end{aligned}$$

Excitation energy:

$$\begin{aligned}&\text{Selenoketones, R–C(=Se)–R}' > \text{Selenophenes} > \text{Dialkylselenides, R–Se–R}'\\ &\text{Dialkyldiselenides, R–Se–Se–R}' > \text{Dialkylselenides, R–Se–R}'\end{aligned}$$

Electron density:

$$\text{Me}_3\text{Se}^+(\delta = 258) > \text{Me–Se–Me } (\delta = 0) > \text{Me–Se}^-(\delta = -330)$$

Generally, the δ-values of ^{77}Se in P=Se bonds of organophosphine selenides are negative. ^{77}Se chemical shifts of transition metal complexes cover the whole range. In most cases the selenium atom is deshielded ($\delta = 200$–1500) as compared to the free selenium-containing ligand but exceptions with negative complexation shifts exist.

Substituent effects in organoselenium compounds (e.g., in Ph–Se–R with various R) are qualitatively similar as compared to homologous carbon analogues (Ph–CH_2–R) but they are 3–5 times larger on the ppm-scale. The diagnostically valuable γ-gauche effect in olefins has attracted some attention.[73]

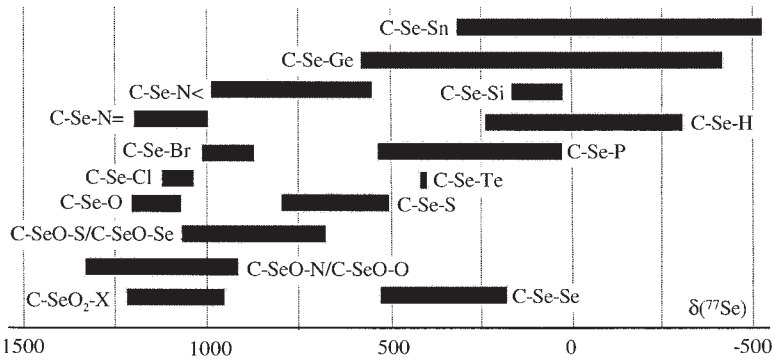

Fig. 1. Schematic view of ^{77}Se chemical shift ranges in compounds containing C–Se–X bonds.

2.2.3. *^{77}Se chemical shifts in various functionalities*

As noted before, the ^{77}Se chemical shift range is about 3300 ppm and ^{77}Se signals reflect changes in the steric and electronic environment of the selenium sensitively, even over long distances. In this section, typical shift ranges for ^{77}Se in Se–X fragments including selenoxides and -dioxides, selenocarbonyl (C=Se) derivatives, heterocycles, medio-, and macrocycles, as well as charged species are presented. This is followed by selenonium ions and hypervalent compounds. In most cases, literature prior to 1994 will be referred to in the author's previous review article.[1e]

2.2.3.1. Compounds with various Se–X bonds (X = B, Si, Ge, N, P, As, Sb, Bi, O, S, Se, Te, and halogens)

An overview of ^{77}Se chemical shift ranges shows that this parameter is strongly dependent on the electronegativity of X. This is exemplified in Fig. 1 for C–Se–X fragments. However, individual molecular structures may cause variations of several hundreds of ppm.

Selenium–boron bonds. Boron as a low-electronegativity element does not deshield attached selenium atoms.[1e] On the contrary, the ^{77}Se NMR spectrum of H_3B–Se–Se–BH_3 shows two resonances at $\delta = -392$ and -509 which were

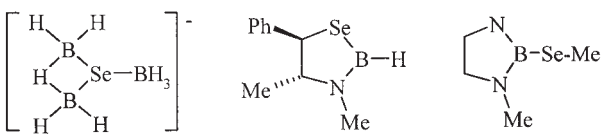

21 (δ = -474) **22** (δ = +223) **23** (δ = -242)

Scheme 10

ascribed to two different rotamers, and in the anion **21** with three boron atoms coordinated to Se it is $\delta = -474$ (Scheme 10).[74] When the selenium-containing group is –SeCN attached to boron polyhedra it is between $\delta = -23$ and -73 and in $(PPh_4)[B_3H_7(SeCN)]$ even -347[75] whereas selenocyanates with Se bound to carbon usually resonate at $\delta = +120$ to $+400$.[1e]

In cases with C–Se–B groups the δ (^{77}Se)-values are mostly between $+50$ and $+250$,[1e] see e.g., **22**,[76] but exceptions may occur caused by the rest of the molecule; for example $\delta = -242$ in **23**.[77]

Selenium–silicon and selenium–germanium bonds. Similar to boron, silicon shields ^{77}Se nuclei when attached. In addition to those compounds published prior to 1995,[1e] a large number of papers have appeared reporting Se–Si and Se–Ge bonds in various constellations, a representative choice of which is illustrated below.

Whereas $H_3Si–Se–SiH_3$ and related oligosilylated selanes show ^{77}Se resonances at $\delta = -620$ to 666,[1e,78] the selenium nuclei are more deshielded in corresponding alkylated derivatives, e.g., $Me_3Si–Se–SiMe_3$ with $\delta = -332$[79] or -337,[80] $Me_3Si–Se–Et$ with $\delta = -65$ and $Me_3Si–Se–Ph$ with $\delta = +86$,[79] whereas further trimethylsilylation of the silicon atoms cause shielding again, e.g., $[(Me_3Si)_3Si]_2Se$ with $\delta = -629$.[80] As expected, chlorine atoms attached to Si in the β-position to Se leads to deshielding: $Me_3Si–Se–Bu$ with $\delta = -108$, $Me_2Si(Cl)–Se–Bu$ with $\delta = -28$, $MeCl_2Si–Se–Bu$ with $\delta = +5$ and $Cl_3Si–Se–Bu$ with $\delta = +63$.[81]

A number of cyclic structures with Se–Si bonds have been contributed in recent years (Scheme 11). Beside one substituted three-membered ring consisting of C, Si, and Se ($\delta = +49$),[82] some four- and five-membered rings (**24**–**28**) were published.[83] Further examples are **29**–**31** and **33**–**36**,[84] **37**,[85] **39**,[86] **41**,[87] the propellane-type **43**[88] and the 'double-decker' tricyclus **44**.[89] For many of the silicon compounds, corresponding germanium analogues have been reported as well: **32**,[84] **38**,[85] **40**,[86] **42**,[87] and **45** (Scheme 11).[89] Evidently, the effects of Ge are mostly less shielding as compared to Si.

The first selenagermirane **46** (Tbt = 2,4,6-tris[bis(trimethylsilyl)methyl]-phenyl and Mes = mesityl),[90] a 1-selena-2,5-digermacyclopentane derivative **47**[91] – presumably as a mixture of *cis-syn-cis*- and *cis-anti-cis*-isomers – have been characterized. A series of bicyclic systems **48**–**51** consisting of germanium atoms at the bridgehead position and selenium atoms in the bridges were introduced.[92] It seems that internal ring strain increases the ^{77}Se shielding very strongly; compare Ge–**Se**–Ge in the series **48**–**51** ($\delta = -97$, -7, $+406$, and $+995$, respectively).

Stable germaneselenones **52** and **53**, congeners of ketones, were presented and structurally characterized (Tbt = 2,4,6-tris[bis(trimethylsilyl)methyl]-phenyl, Tip = 2,4,6-tris(isopropyl)phenyl) and Dis = bis(trimethylsilyl)methyl) (Scheme 12).[93] These high-frequency resonances support the interpretation of a ketone-analogous sp^2-hybridized germanium atom with germanium–selenium

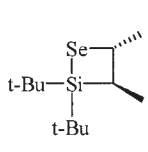

24 (δ = +4)

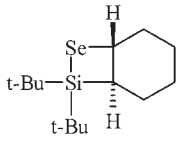

25 (δ = +55)

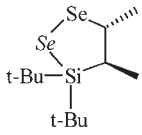

26 (δ = -133)

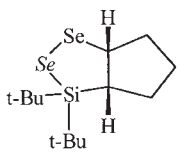

27 (δ = -58)

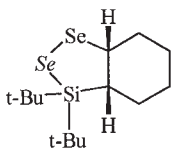

28 (δ = -72)

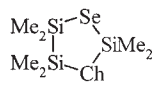

Ch = S : δ = -312
Ch = Se: δ = -302
Ch = Te: δ = -288

29, 30, 31

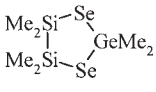

32 (δ = -294)

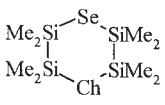

33 - 36

Ch = O: δ = -317
Ch = S : δ = -370
Ch = Se: δ = -369
Ch = Te: δ = -366

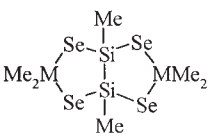

37 (M = Si: δ = -208)
38 (M = Ge: δ = -217)

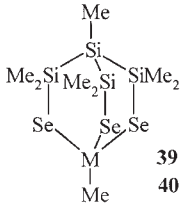

39 (M = Si: δ = -101)
40 (M = Ge: δ = -29)

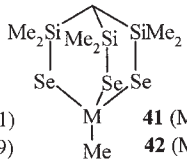

41 (M = Si: δ = -180)
42 (M = Ge:δ = -130)

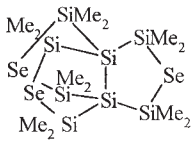

43 (δ = -189)

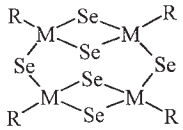

(R = CMe_2-$CHMe_2$)
44 (M = Si: δ = -52, -122)
45 (M = Ge: δ = -3, +154)

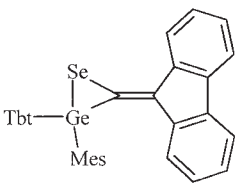

46 (δ = +128)

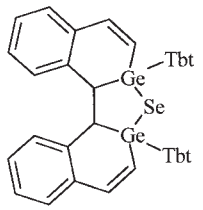

47 (δ = -451, -447)

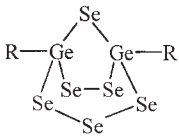

48 (δ = -97,+278, +443)

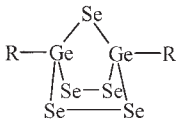

49 (δ = -7, +434)

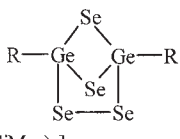

50 (δ = +406, +478)

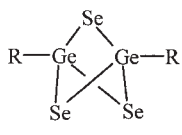

[R = $C(SiMe_3)_3$]

51 (δ = +995)

Scheme 11

double bond.[93,94] The ^{77}Se atom in another germaneselone (**54**) which has two additional stabilizing nitrogen coordinations is much more shielded ($\delta = -98$).[95] The X-ray data of **54** reveal that the geometry about Ge is pseudotrigonal bipyramidal and the Ge–Se bond length indicates that it is between single and double bond.[95]

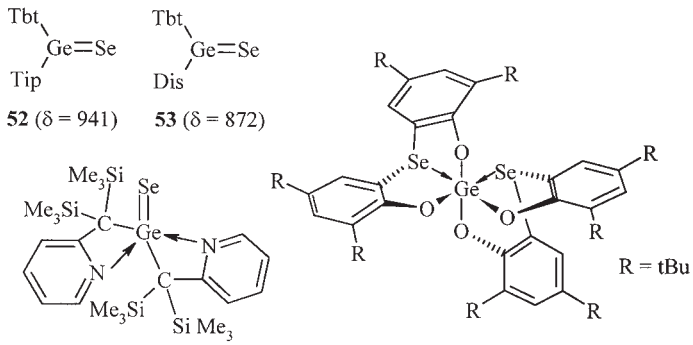

Scheme 12

Finally, the hexacoordinateed germanium(IV) complex **55** is worth mentioning. It is produced by reaction of $GeCl_4$ with the corresponding selenobisphenol widening the coordination sphere of germanium from 4 to 6 *via* intramolecular transannular Se···Ge interaction (Scheme 12).[96]

Selenium–nitrogen bonds. Due to the large electronegativity of nitrogen, the resonances of selenium atoms attached to N have generally high frequencies; δ-values between 900 and 1800 may appear depending on the rest of the molecule, its charge and the bond properties.[1e] Many of these compounds can be regarded as analogues of selenium dioxide or selenite which resonate in that range as well (Scheme 13). Examples are a selenium (IV) diimide **56** (Ad = 1-adamantyl)[97] and a tris(*tert*-butylimido)selenite anion **57**.[98] High chemical shift values are observed for Se(II) compounds as well: some open-chain compounds with Se–N bonds **58** and **59**,[99] the series of bis-disilylamino selenides **60–63**[100] (in **62** and **63** the chemical shifts of ^{77}Se attached to N are in italics) and an aminoselenolate **64**[101] have been reported. New Se–N heterocycles are **65**,[102] **66**,[99,102] **67**,[102] and **68**.[102] $(Se_2SN_2)Cl$, a planar five-membered ring has been proven to be a dimer **69**,[103,104] and 1,5-$Se_2S_2N_4$ (**70**) has been characterized as well.[104,105] Solid-state ^{77}Se MAS NMR spectra of **70** were reported as well: two isotopic lines at $\delta = 1455$ and 1409 were found.[104]

Selenium–phophorus bonds. Chemical shifts of selenium atoms bound to phosphorus spans a wide rage of far more than 1000 ppm depending on the bond order and the existence of further atoms attached. At the low-frequency area of that range are P=Se derivatives with three organyl (phosphines) or alkoxy groups at P (phosphinates, phosphonate, or phosphates); the δ (^{77}Se)-values range from −256 for trimethylphosphine selenide (Me_3P=Se) to −497 for triisopropylphosphine selenide.[1e] Halogen atoms at P, however, deshield selenium considerably so that even positive chemical shifts may occur; e.g., $PhCl_2P$=Se, $\delta = +149$.[106] This trend was recently confirmed by the resonance

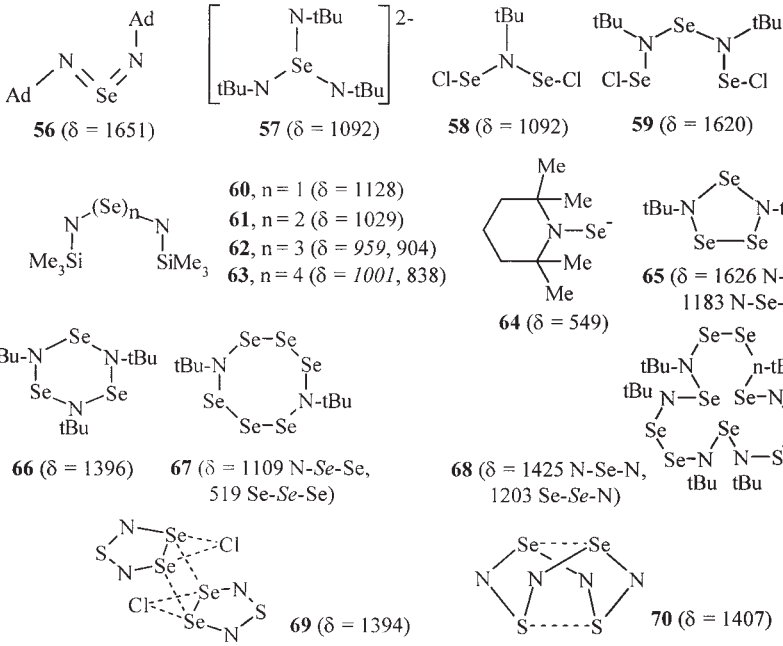

Scheme 13

of 1-adamantyldichlorophosphine selenide [1-Ad(Cl_2)P=Se] with δ (^{77}Se) = +61.[107] In addition to the ^{77}Se chemical shift, the one bond ^{77}Se,^{31}P coupling constant is an interesting parameter in this class of compounds (see Section 2.3.4).

Triselenophosphonates, R−PSe_3^{2-}, have ^{77}Se chemical shifts of +243 (R = Me), +295 (R = Et), and +273 (R = *i*Pr) but if R = Ph the selenium atoms are much more deshielded (δ = +390).[108] Metaphosphates, -phosphonates, and -phosphinates are interesting compounds although they are generally instable. Seleno analogues, however, could be identified. They have trigonal planar geometries and can, in contrast to their analogues with lower chalcogens (O, S), exist as monomers (Scheme 14). The reaction of P_4Se_3 with Li_2Se_2 and grey Se affords the lithium salt of triselenometaphosphate **71** in solution; the thio analogues **72** and **73** can be prepared in a similar way; all compounds show positive ^{77}Se chemical shifts of moderate magnitudes.[109] By ylide substitution, arylselenometaphosphonates and -phosphinates can be isolated without dimerization; examples are **74** and **75** with two non-equivalent selenium atoms differing considerably by their ^{77}Se chemical shift.[108,110] Nitrogen stabilization is possible as well (for example in **76**) forming a C–C–P–N four-membered ring as proven by X-ray analysis.[111] Some related derivatives with different *ortho*-amino substituents have been published as well;[111–113] in general, the δ(^{77}Se)-values are in the range of 195–500 and the

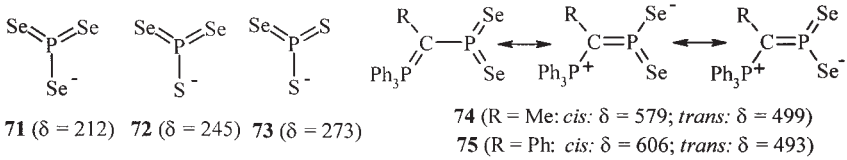

71 (δ = 212) **72** (δ = 245) **73** (δ = 273)

74 (R = Me: *cis:* δ = 579; *trans:* δ = 499)
75 (R = Ph: *cis:* δ = 606; *trans:* δ = 493)

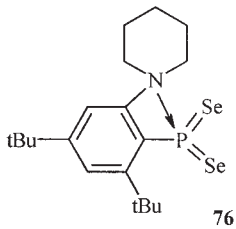

76 (δ = 397)

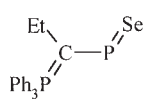

77 (δ = 813)

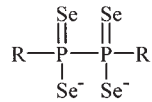

78 (R = Me: δ = -73)
79 (R = tBu: δ = +68)
80 (R = Ph: δ = -85)

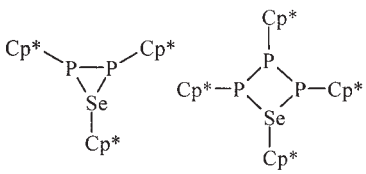

81 (δ = -89) **82** (δ = -149)

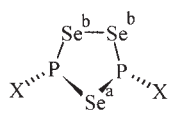

83 (X = Br: δ = 889)
84 (X = I: δ = 918)

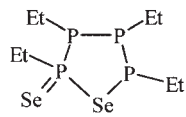

85 (δ = 448, P-Se-P; δ = -43, P=Se)

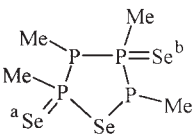

86 (δ = 407, P-Se-P; δ = 165, P=Se[a]; δ = -117, P=Se[b])

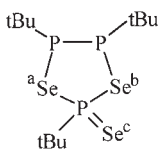

87 (δ = 492, Se[a]; δ = 480, Se[b]; δ = 276, Se[c])

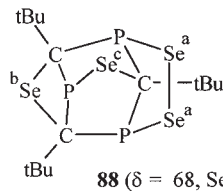

88 (δ = 68, Se[a]; δ = 514, Se[b]; δ = 257, Se[c])

Scheme 14

difference of the non-equivalent Se atoms may be ca. 50 ppm or even indetectable.[113] Ylide stabilized selenometaphosphinates, such as **77**, have also been identified[108] as well as some tetraselenohypodiphosphonates like **78**–**80**.[108]

The lithium salt of $Ph_2P–Se^-$, stabilized by TMEDA (tetramethylethylenediamine) resonates at $\delta = -233$, that of $Ph_2P-Se_2^-$ at $\delta = -41$ and that of $Cy_2P-Se_3^-$ (Cy = cyclohexyl) at $\delta = -166$.[114]

Some new phosphorus–selenium cycles have been described (Scheme 14). Examples are the three- and four-membered rings **81** and **82**[115] (Cp* = σ-bonded pentamethylcyclohexadienyl) as well as the five-membered rings **83** and **84**; the ^{77}Se chemical shifts given in the Scheme refer to the P–Se–Se–P atoms (Se^b), that of P–Se–P (Se^a) was not observed.[116] Some other five-membered rings are **85**–**87**[108] and a carbon-containing oligocycle **88**[117] are worth mentioning. Since the δ (^{77}Se)-values in such cycles often show large positive values,[1e] the negative ones in **81** and **82** are somewhat surprising

inspite of the bulky residues. A few further compounds with C–Se–P bonds, e.g., $(CF_3Se)_3P$ with δ (^{77}Se) = 541,[118] have been summarized before;[1e] the chemical shifts are positive as well.

Selenium–arsenic and selenium–antimony bonds. $(CF_3Se)_3As$ with $\delta = 505$ has a chemical shift very similar to that of the phosphorus analogue.[118] The same holds for the comparison of tetraphosphorus triselenide ($\delta = 759$) and the arsenic analogue ($\delta = 764$).[1e,119]

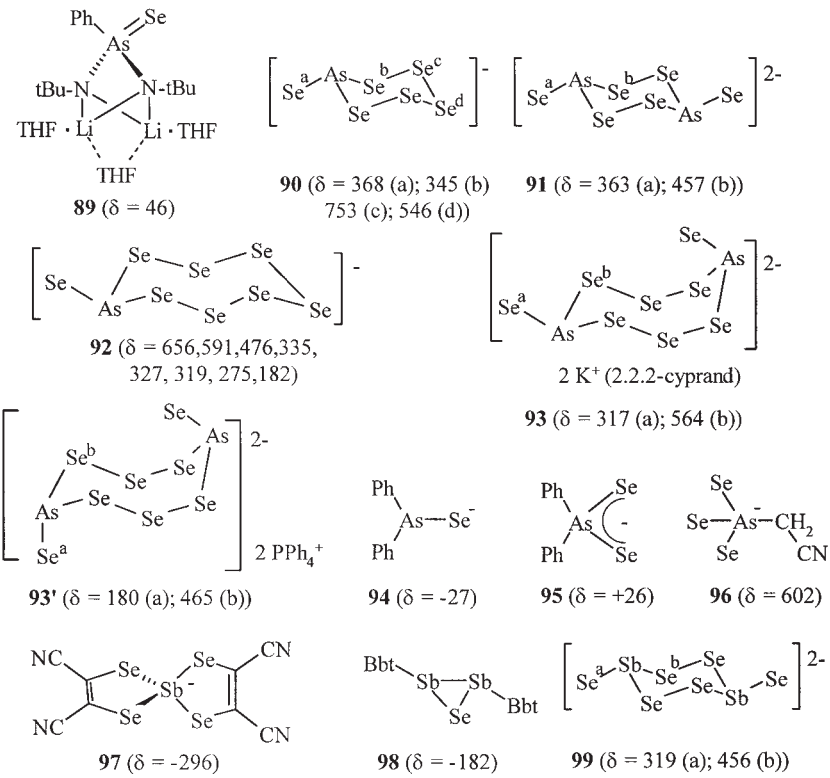

Scheme 15

The ^{77}Se chemical shift of the arsine selenide **89** with a formal As=Se double bond (THF = tetrahydrofurane) is slightly positive (Scheme 15).[120] Several arsenic–selenium ring anions have been described by ^{77}Se NMR and X-ray crystallography: **90** (as PPh_4^+ salt)[121] but in the enH^+ salt (en = ethylenediamine) $\delta = 366$, 418, 779, and 569, respectively,[122] **91** (as PPh_4^+ salt)[123] but as NEt_4^+ salt with $\delta = 167$ and 461, respectively,[122] **92** (as NEt_4-salt)[122] and **93**.[124] Interestingly, the stereochemical position of the Se^a-atoms attached to the eight-membered ring of **93** differs depending on

which counterion has been used and so do the chemical shifts; the ring itself, however, does not show conformational changes in the normal NMR temperature range.[124]

Diphenylselenoarsinous (**94**) and -diselenoarsinic acid pyridinium salts (**95**) have been identified at −90°C.[125] The ^{77}Se chemical shift of the dimethyl analogue of **95**, $Me_2AsSe_2^-$, is 113 ppm.[126] A systematic study of arsenic selenide liquids with varying stoichiometries has been performed. At high temperatures, an averaged signal representing As–Se and Se–Se bonds can be identifed, and chemical ordering can be monitored.[127] The arsenide anion **96** has a large ^{77}Se chemical shift indicating that, indeed, the negative charge is located at the As atom.[128]

Some interesting antimony–selenium ring compounds have been published recently (Scheme 15), among them **97** with a spiro-antimony atom, a selenadistibirane **98**[129] stabilized by bulky groups (Bbt = 2,6-bis[bis(trimethylsilyl)methyl]-4-[tris(trimethylsilyl)methyl]phenyl) and the dianion **99**,[130] a congener of **91**, with similar ^{77}Se chemical shifts.

Selenium–oxygen bonds. The ^{77}Se chemical shifts of some inorganic selenium–oxygen compounds are listed in the Tables 2 and 3. It is apparent that Se (VI)-species are much more shielded ($\delta = 944$–1076; Table 2) than the Se (IV)-species ($\delta = 1263$–1559; Table 3). This holds as well for SeO_3, the anhydride of selenic acid (H_2SeO_4), the halogen derivatives and its alkyl esters and amides.

Highly fluorinated Se(VI) compounds, however, resonate in a much lower chemical shift range, $\delta = 600$–650 (Table 2). The first hexaoxoselenate SeO_6^{6-} with octahedral geometry has been described recently by X-ray analysis and ^{77}Se NMR.[137] Interestingly, its chemical shift ($\delta = 667$) is about 350–400 ppm lower than those of selenates inspite of the high oxygen coordination.

Table 2. ^{77}Se chemical shifts in various selenium(VI)–oxygen compounds

	δ (^{77}Se)	Solvent	Ref.
SeO_3	944	Neat	131
H_2SeO_4	1001	Water	131,132
Na_2SeO_4	1033	Water	133
$(NH_4)_2SeO_4$	1024	Solid-state	134
$(Me_2N)_2SeO_2$	1076	Choroform	135
Cl–SeO_3H	1003	SO_2	131
F–Se(=O)$_2$–F	948	Neat	131,136
F_5Se–O–SeF_5	597	Neat	136
F_5Se–O–O–SeF_5	634	Neat	136
$Na_{12}(SeO_6)(SeO_4)_3$	667 (SeO_6^{6-})	Solid-state	137
	1045,1044,1033 (SeO_4^{2-})		
$(MeO)_2SeO_2$	1053	dichloromethane	139

Table 3. ^{77}Se chemical shifts in various selenium(IV)–oxygen compounds

	δ (^{77}Se)	Solvent	Ref.
H_2SeO_3	1300	Water	131,133,138
Na_2SeO_3	1263	Water	133
$(MeO)_2SeO$	1339	Neat	139
$F_2Se{=}O$	1378	Neat	131
$Cl_2Se{=}O$	1479/1501	Neat	131,140
$Br_2Se{=}O$	1559	Neat	131

An analogous sequence appears in trifluoroseleninic acid as compared to -selenonic acid: CF_3SeO_3H resonates at $\delta = 981$ whereas the ^{77}Se chemical shift of CF_3SeO_2H is only $\delta = 1231$.[135] The δ-value of benzeneseleninic acid Ph–SeO_2H in a chloroform–methanol mixture is 1188 ($\delta = 1152$, 1182)[1e] and its methyl ester $\delta = 1236$; protonation leads to a ca. 20 ppm shielding.[141] Recently, some further arylseleninic acids have been reported with ^{77}Se chemical shifts between $\delta = 1200$ for Ar = 2,4,6-triisopropylphenyl and $\delta = 1276$ for Ar = 2,4,6-triethylphenyl.[142] These were optically resolved, partially to 100% e.g., on a chiral column and their racemization studied.[142]

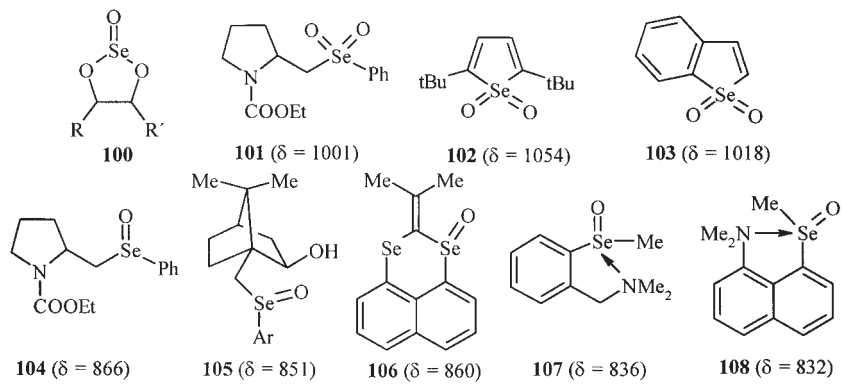

Scheme 16

The ^{77}Se chemical shifts of cyclic selenite esters **100** (R=$(CH_2)_4$COOMe, R′=$C_{11}H_{23}$) are δ = 1338–1339 without a significant difference between *cis*/-*trans*-4,5-disubstituted stereoisomers (Scheme 16).[143] ^{77}Se NMR data of diorganyl selendioxides (R–SeO_2–R′) are rare; their chemical shifts are between 1000 and 1054; for example see **101**,[144] **102** and **103**[145]). Only few data of selenoxides are available, because they easily undergo elimination if a β-hydrogen is present in the molecule. At low temperature, however, some phenylalkylselenoxides, Ph–SeO–R, were recorded and ^{77}Se chemical shifts between $\delta = 800$ and 950 were found.[1e] Some new data were presented for **104**,[144] **105** (Ar = 4-Tol)[146] and **106** (the selenide atom resonates at $\delta = 263$).[147]

The selenoxide **107** as well as its benzyl ($\delta = 890$) and phenyl analogues ($\delta = 879$) were separated into the enantiomers and their chiroptical properties investigated; intramolecular nitrogen coordination stabilizes the selenoxide so that no bulky substituents were required.[148] Another selenoxide with *N*-stabilization is **108**.[149]

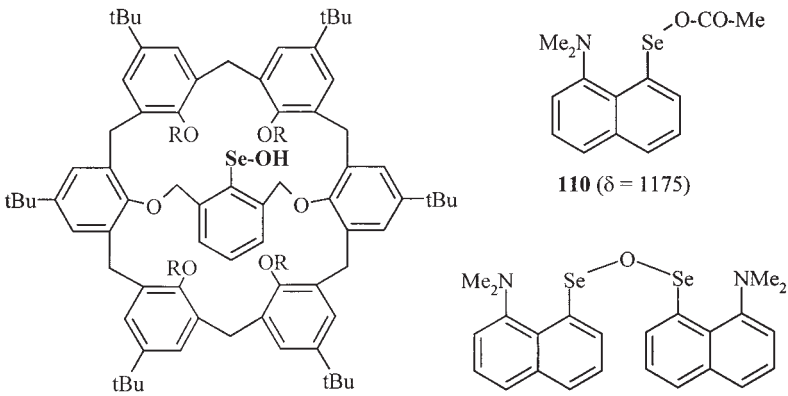

109, R = CH_2Ph ($\delta = 1134$)

110 ($\delta = 1175$)

111 ($\delta = 1191$)

Scheme 17

The first stable arylselenenic acid, Ar–Se–OH (**109**) as a bridged calix[6]arene, was synthesized and characterized by an X-ray study (Scheme 17).[150] ^{77}Se chemical shifts of selenenic acids seem to be comparable to those of selenonic acids. This is confirmed by the data of the selenoperacetate **110** (same δ-value for the selenoperbenzoate) and the selenenic anhydride **111**.[151]

Selenium–sulfur, selenium–selenium, and selenium–tellurium bonds. The ^{77}Se chemical shift of a terminal Se in tetramethylammonium selenosulfate (VI) tetrahydrate $(Me_4N^+)_2SO_3Se^{2-}$ was recently determined to be $\delta = 650$.[152] However, the majority of data on molecules containing Se–Ch groups (Ch = S, Se, Te) were reported from neutral acyclic or cyclic oligo- and polychalcogenides. A number of such examples including charged species thereof together with their ^{77}Se NMR properties has been collected and reviewed in detail before.[1e,153] The ^{77}Se chemical shift range of the neutral species is large, $\delta = 560$–700 but values up to 1100 and even somewhat higher may occur.[1e,153,154] It was shown that ^{77}Se chemical shifts in Se_nS_{8-n} ring molecules[155,156] can be predicted satisfactorily by factor analysis[155] and by theoretical calculation.[157] Selenium–tellurium rings show resonances in an analogous range.[158] Introduction of nitrogen atoms into a six-membered ring SeS_3N_2 does not significantly affect the ^{77}Se shielding ($\delta = 780$) if Se is flanked by two sulfur atoms.[159] The ^{77}Se data of acyclic $H_2S_nSe_{m-n}$ compounds provide similar values; they are between $\delta = 527$ and 749 if selenium is

attached to at least one sulfur but somewhat higher (up to 954) if selenium is attached to two other selenium atoms.[160]

Selenium atoms in cationic oligochalcogen rings are even more deshielded (Scheme 18); if the ring consist of selenium exclusively or if sulfur is involved, δ-values up to 2000 may occur (for example, **110** and **111**), but selenium attached to tellurium is less deshielded ($\delta = 1600$–1700, e.g., **112**). Dicationic organoselenium species have been compiled and reviewed as well.[1e,161] Typically, a strong deshielding is associated with an oxidative ring closure, e.g., the formation of **114** from **113**.[161,162] Some benzo-annelated analogues show similar trends.[163,164]

110 (δ = 1951) **111** (δ = 1939) **112** (δ = 1429) **113** (δ = 141) **114** (δ = 806)

Scheme 18

Selenium–halogen bonds. A brief survey of binary and ternary selenium–halogen compounds has been presented before.[1e] It emerged that ^{77}Se chemical shifts are high with a strong dependence on the electronegativity of the halogen(s). This can be exemplified in the series SeX_2[1e]: $\delta = 1738$, 1758 for X = Cl, $\delta = 1495$ for X = Br and $\delta = 814$ for X = I. Recently, it was shown that thiourea and tetrahydrothiophene adducts of $SeCl_2$, with the sulfur atoms coordinating at Se and forming T-shaped molecules with nearly linear Cl–Se–Cl fragments, have considerable higher δ (^{77}Se)-values, namely 1042 and 1299, respectively.[156] Se(IV) atoms in halides are also strongly deshielded ($\delta = 1000$–1700) and this holds also for corresponding anions;[1e] compare also $SeCl_3^+$ AsF_6^- with $\delta = 1419$[165] and $SeCl_6^{2-}$ ($\delta = 1407$–1428), $Se_2Cl_6^{2-}$ ($\delta = 1618$–1698) and $Se_2Cl_{10}^{2-}$ ($\delta = 930$–966).[166] Various cationic species of $[Se_6I_2]^{2+}$ have been described as existing in a SO_2 solution equilibrium.[167]

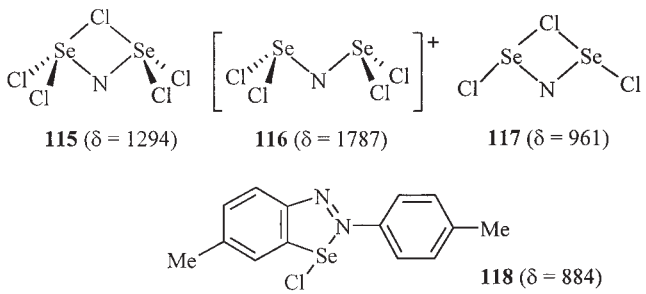

115 (δ = 1294) **116** (δ = 1787) **117** (δ = 961)

118 (δ = 884)

Scheme 19

A new selenium nitride halide (**115**) with a ^{77}Se chemical shift of $\delta = 1294$ has been reported (Scheme 19).[168] In accordance with general trends, this

value is much smaller than that of the corresponding cation **116**[169] but larger than that of the analogue **117** with selenium in a lower oxidation state.[170] Surprisingly, a ^{77}Se chemical shift of only $\delta = 884$ has been reported for the selenadiazole halide **118**[171] whereas the typical resonance range of selenadiazoles themselves is 1400–1600; see also Section 2.2.3.4.[1e]

Large halogenation-induced deshieldings of the selenium atom in dialkyl selenides (R–Se–R′) are associated with the formation of a trigonal bipyramid (**TB**) with the selenium atom in the center; in that case the signal shifts are > 100 ppm, whereas they are ≤ 10 ppm if only a molecular complex (**MC**: $RR'Se\cdots X_2$) is formed.[1e,172,173] The criterion for the **TB** vs. **MC** decision is the electronegativity balance ('effective electronegativity'). It turned out that chlorine and bromine adducts are **TB**s whereas the iodine adduct is an **MC**. However, it was claimed that there are exceptions of this rule in the case of Br_2-adducts which may be **TB** or **MC** depending on the selenium compounds structure. This study has been continued by the group investigating **TB** vs. **MC** stability,[174] the effect of bulkiness introduced by *ortho*-substituents[175] and by theoretical calculations.[176] It turns out that the **MC** bond follows the 3c–4e description.[174,176] In the case of *N*-methylthiazolidine-2(3*H*)-selone and its Br_2-adduct (**119**), it has been shown that the result of the bromine-addition is strongly dependent on the molar ratio of the components and the salt **120** is produced at higher Br_2 proportions (Scheme 20).[177]

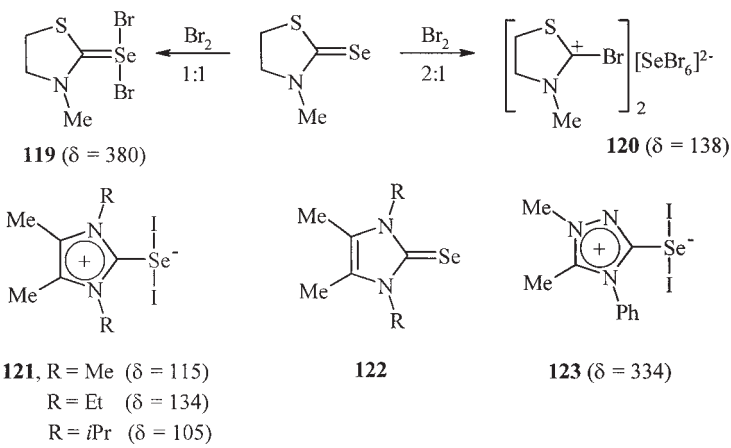

Scheme 20

Interestingly, an exceptional I_2–**TB**–adduct (**121**) can be isolated after iodine-addition to a mesoionic imidazolylidene selenide. Stabilization of the trigonal bipyramid is presumed to result from the enhanced C–Se bond.[178] The corresponding precursors **122** resonate at $\delta = 34$, 10, and 19, respectively,[179] so that a considerable gross deshielding results from diiodo adduct formation which, however, is probably due to the charge separation in the mesoionic **121**.

A related mesoionic Ar−SeI_2^- anion **123** was reported to have a much higher ^{77}Se chemical shift.[180]

2.2.3.2. Selenols and selenolates, selenides, diselenides, and related functional groups

Selenols (R–SeH) have rather small ^{77}Se chemical shifts which are strongly dependent on the alkyl or aryl residue attached to Se, and incremental influences of individual groups in α, β, or γ position can be identified.[1e] The chemical shifts range from $\delta = -130$ for MeSeH to +278 for *t*BuSeH; the δ-value of PhSeH is+152.[139,181]

As expected, selenium atoms are considerably more shielded (−150 to −200 ppm) in sodium alkylselenolates as compared to the respective selenols[139] but the shielding is much less (−12 to −50 ppm) in $PhSe^-$ as compared to PhSeH.[182,183] Much larger shieldings have been found for a lithium salt of *n*Bu–SeH, stabilized by TMEDA [$(Me_2N–CH_2)_2$]. Whereas the selenol resonates at $\delta = +22$ (in THF at 195 K),[184] the chemical shift of $[n\text{BuSeLi} \cdot \text{TMEDA}]_2$ is $\delta = -660$; probably fluxional aggregates exist in solution.[185] On the other hand, the sign of the selenolate formation shift may even be reversed (deshielding) and adopt large positive values; the ^{77}Se chemical shifts of the sterically crowded 2,6-$Trip_2$-C_6H_3–SeH (Trip = 2,4,6-*i*Pr–C_6H_2–) is $\delta = +108$ whereas that of the K^+ is $\delta = +178$ and that of the Rb^+salt even $\delta = +216$.[186]

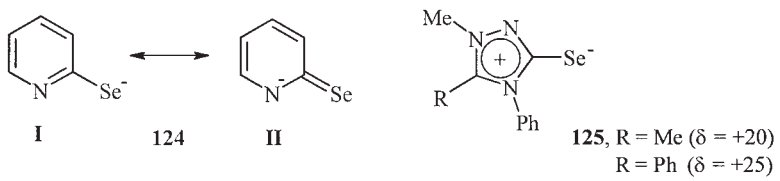

Scheme 21

Selenium in 2-pyridineselenolate (**124**) is even more deshielded; it resonates at $\delta = +360$ (Et_4N^+ salt) and +442 [(18-crown-6)K^+ salt].[187] This can be explained by a contribution of the canonical form **II**; an interpretation which is confirmed by the low δ(^{77}Se)-values of the mesoionic selenolates **125** in which such delocalization of the negative charge is not possible (Scheme 21).[180]

Diorganyl selenides and diselenides (R–Se–R′ and R–Se–Se–R′, respectively; R/R′ = alkyl and/or aryl) were subjects of intensive investigations in the early years of ^{77}Se NMR investigation.[1a–1f] The chemical shifts are in the range of $\delta = 0$–550 and 200–600, respectively, and are strongly dependent on the structure of the organyl residues[1a–1f] in a way similar to that mentioned above for the selenols. This has been summarized before in detail.[1e] Organic selenocyanates (R–Se–C≡N) belong to this group as well; they resonate at

$\delta = 120$–400, and there is a strong dependence on substituents attached to the aromatic ring in phenylselenocyanates.[1e]

If the group next to the selenium atom is a carbonyl, thiocarbonyl, or selenocarbonyl [selenoesters: C–Se–C(=X)–C; X = O, S, Se], the selenium atom is deshielded and its chemical shift becomes larger; δ-values between 400 and 1100 may occur;[1e] for example **126**–**128** (Scheme 22).[1e,188] This can be rationalized qualitatively by assuming a considerable contribution of the dipolar mesomeric form (see **126**).

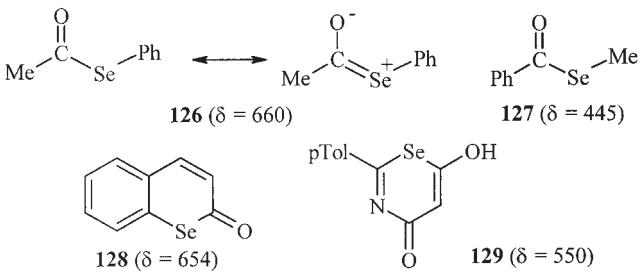

Scheme 22

Acyl carbamoyl selenides R–C(=O)–Se–C(=O)NHR′ (R = alkyl or aryl and R′ = aryl) display high ^{77}Se chemical shifts ranging from $\delta = 633$ (R = 4-anisyl, R′ = Ph) to $\delta = 708$ (R = 2-anisyl, R′ = Ph).[189] The selenium atom in the selenacinone **129** is in a similar molecular arrangement and has a similar chemical shift ($\delta = 550$).[190] Cs^+ and Rb^+ salts of selenocarboxylates, R–C(=O)–Se^- (R = alkyl or aryl) have been investigated, and ^{77}Se chemical shifts were reported to be between $\delta = 340$ (4-MeO–C_6H_4–C(=O)–Se^- Rb^+) and 517 (2-Cl–C_6H_4–C(=O)–Se^- Cs^+).[191] A small but significant influence of the counterion on ^{77}Se chemical shift of the selenocarboxylate Ph–C(=O)–Se^- M^+ seems to exist: M = Li, $\delta(^{77}Se) = 371$, M = Na, $\delta(^{77}Se) = 362$, M = K, $\delta(^{77}Se) = 363$, M = Rb, $\delta(^{77}Se) = 371$, and M = Cs, $\delta(^{77}Se) = 389$.[191]

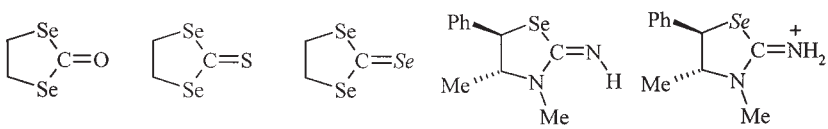

130 (δ = 565) **131** (δ = 805) **132** (δ = 855) **133** (δ = -315) **134** (δ = -275)

Scheme 23

The series of diselenocarbonates **130**–**132** shows how strong the influence of the doubly bonded chalcogen on the chemical shifts of the endocyclic selenium atoms is: $\delta = 585$ (C=O), $\delta = 805$ (C=S), and $\delta = 855$ (C=Se); the $\delta(^{77}Se)$-value of the C=Se atom of **132** is 1455 (Scheme 23).[192] In contrast, selenium atoms in monoselenocarbonates are less deshielded;[1e] for example, the ^{77}Se chemical

shifts of various Ph–Se–C(=O)–O–R (R = alkyl or aryl) are between $\delta = 500$ and 520.[193,194] Selenocarbamates R–NH–C(=O)–Se–R′ (R/R′ = alkyl or aryl) have a similar resonance range; values between $\delta = 307$–498 were reported; *s*-cis-/*s*-trans equilibria could be studied at low temperatures.[195] A few data of selenocarbamate salts have been reported:[196] Me_2N–C(=O)–Se^-Na^+, $\delta = 121$; Et_2N–C(=O)–Se^-Na^+, $\delta = 119$; Ph_2N–C(=O)–Se^-Na^+, $\delta = 225$; Me_2N–C(=O)–Se^- K^+, $\delta = 121$. Here, selenium is clearly more shielded that in selenocarboxylates (see above). Even more, the iminoselenazolidine **133** has a negative δ-value (−315) and protonation to the minimum derivatives **134** is associated with a deshielding of only 40 ppm (Scheme 23).[76]

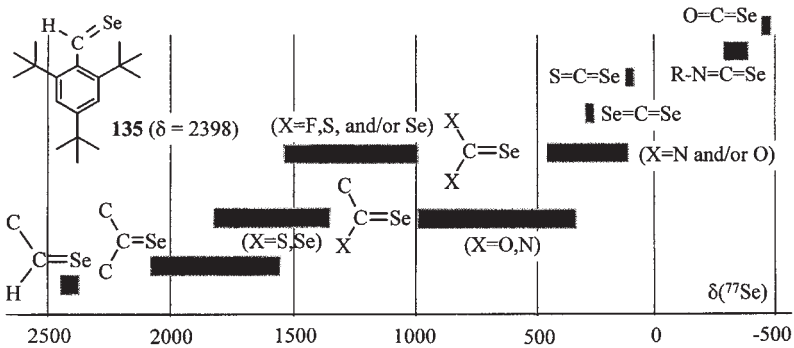

Figure 2. 77Se NMR signals of compounds containing C=Se groups.

2.2.3.3. Compounds with carbon–selenium double bonds

Signals of compounds containing C=Se groups are spread over nearly the whole range of ^{77}Se chemical shifts (Fig. 2).

Very large δ (^{77}Se)-values have been reported for some sterically crowded selenoaldehydes; e.g., **135** ($\delta = 2398$; Fig. 2)[197] or ketones; $\delta = 2131$ was measured for di-*tert*-butylselone (tBu$_2$C=Se).[198] It is interesting to note that the selenoformyl proton in **135** is extraordinarily deshielded as well, it resonates at $\delta = 17.38$; the ^{13}C chemical shift is $\delta = 258.2$.[197a] On the other hand, the lowest δ (^{77}Se)-value has been recorded in O=C=Se ($\delta = -447$).[199]

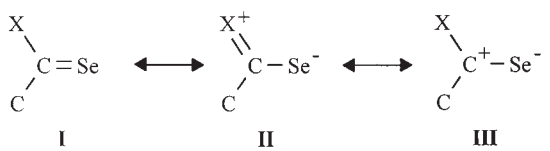

Scheme 24

The atoms directly attached to the C=Se group play a decisive role in determining the ^{77}Se shielding. Hydrogen and/or carbon atoms (selenoaldehydes and selenoketones) appear at the high-frequency end of the spectrum

($\delta > 1600$)[200] whereas heteroatoms shield the selenium nucleus. A simple qualitative rationalization of this finding is the concept of a back-donation from the heteroatom X (mesomeric form **II**) and a C=Se double bond polarization (mesomeric form **III**) which both increase the electron density at Se (Scheme 24). Note that the ^{77}Se chemical shifts of analogous germaneselones (**52** and **53**; RR′Ge=Se) are more than 1000 ppm lower.[93]

Second-row elements like oxygen and, particularly, nitrogen are easily capable of undergoing a back-donation so that very small ^{77}Se chemical shifts result in selenoureas ($\delta = 150$–245);[181,199,200] see for example the oxazolidine-2-selone **235** (Section 3.1). Fluorine is an exception; the ^{77}Se chemical shift of $F_2C{=}Se$ is $\delta = 688$.[199] CF_3–C(=Se)–F with $\delta = 1560$ is another example.[201] Apparently, the relative importance of form **II** (Scheme 24) is lower here owing to the high electronegativity of fluorine.

Analogous trends, although to a lesser extent, appear in selenocarboxylic acid derivatives; as soon as third- and/or higher-row elements (sulphur or selenium) are involved, the δ (^{77}Se) reach up to $\delta =$ ca. 1500.[200,202–205] It seems that the interaction of the lone-pairs of these chalcogen atoms with the C=Se π-bond (formula **II** in Scheme 24) is less effective.[205] These trends may be demonstrated in a series of selenoesters Ph–C(=Se)–X: X = NMe_2, $\delta = 733$; X = OMe, $\delta = 910$; X = SeMe, $\delta = 1787$.[200,202–205] Good correlations of ^{77}Se chemical shifts in C=Se compounds with $n \rightarrow \pi^*$ transitions have been found indicating that the shieldings are dominated by the local paramagnetic term and particularly by ΔE^{-1}, i.e., inverse of the mean electronic excitation energy.[200] Moreover, ^{77}Se shieldings correlate nicely with ^{17}O shieldings in C=O analogues.[200]

These trends have been confirmed by recent reports. The selenoester derivatives with the highest chemical shifts are diselenolates, Ar–(C=Se)–Se–R′, with δ-values between 1650 and 1800; the single-bond selenium atoms (–Se–) resonate at $\delta = 860$–955 in these compounds.[206] However, the carboxylate salts, $R - CSe_2^-$, are inbetween ($\delta = 1360$–1500).[206] In the imidazolidiniodiselenocarboxylate **136** (Scheme 25), however, the selenium atoms are much more shielded ($\delta = 946$), probably because any delocalization is impossible.[207] Selenothioic *S*-alkyl esters, R–C(=Se)–S–R′, are next with chemical shifts δ (^{77}Se) = 1406–1634.[208,209]

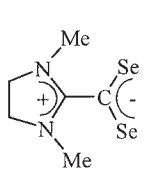

136 (δ = 946)

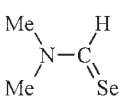

137 (δ = 522)

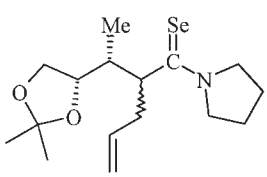

138 (δ = 497)

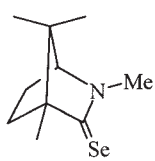

139 (δ = 312)

Scheme 25

Selenoesters, R–C(=Se)–O–R′, on the other hand, have much higher shieldings according to the interaction model mentioned above (Scheme 24).

They resonate in the range of $\delta = 900$–1000; for example $PhCH_2$–C(=Se)–OMe, $\delta = 956$,[209] and Ph–C(=Se)–O–CH_2–*t*Bu, $\delta = 933$.[210] Selenocarboxamides, R–C(=Se)–NR′R″, show even lower ^{77}Se chemical shifts. Since they are quite stable, a number of reports on these compounds have recently appeared. They show a typical chemical shift range of $\delta = 700 \pm 100$,[210–216] depending on the organyl residues attached, but lower values nearly down to $\delta = 300$ may occur; see for example compounds **137**,[217] **138**,[218] and **139** (Scheme 25).[219]

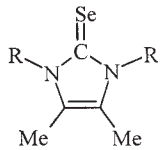

140, R = Me (δ = 34)
R = Et (δ = 10)
R = *i*Pr (δ = 19)

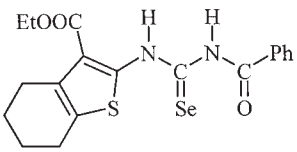

141 (δ = 480)

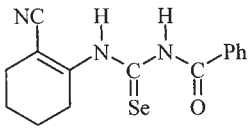

142 (δ = 481)

Scheme 26

It has been mentioned before[1] that selenourea and its derivatives have comparatively low ^{77}Se chemical shifts: $\delta = 150$–245.[181,199,200] Two molecular structures have been reported which are exceptions (Scheme 26): the δ-values are even smaller in 2-selenoimidazolines (**140**),[179] probably due to enhanced conjugation and delocalization; on the other hand, in substituted acylselenoureido derivatives, such as **141**[19] and **142**,[20] the selenium atoms are exceptionally deshielded, a fact which may be explained by perturbed conjugation between the C=Se group and the amide nitrogen.

Selenium atoms in cumulated double bonds (X=C=Se) show the lowest chemical shifts of all of the C=Se groups or other organoselenium compounds; e.g., O=C=Se, $\delta = -447$.[1e,199]

2.2.3.4. Heterocycles

143 (δ = 605)

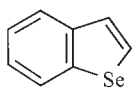

144 (δ = 530)

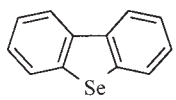

145 (δ = 451)

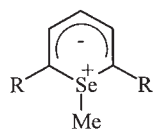

146 (δ = 310)

Scheme 27

Selenophene (**143**) and its benzoannelated analogues (**144** and **145**) are among the most intensively studied selenium-containing heterocycles and this holds also for a great variety of derivatives thereof (Scheme 27).[1e,220–225] It was shown that any benzoanullation or substitution causes large chemical shift

changes of the selenium atom; compare the ^{77}Se chemical shifts of **143** with those of **144** and **145**. A large number of derivatives with anullated thiophene, selenphene, and pyrane ring have been reported as well.[1e]

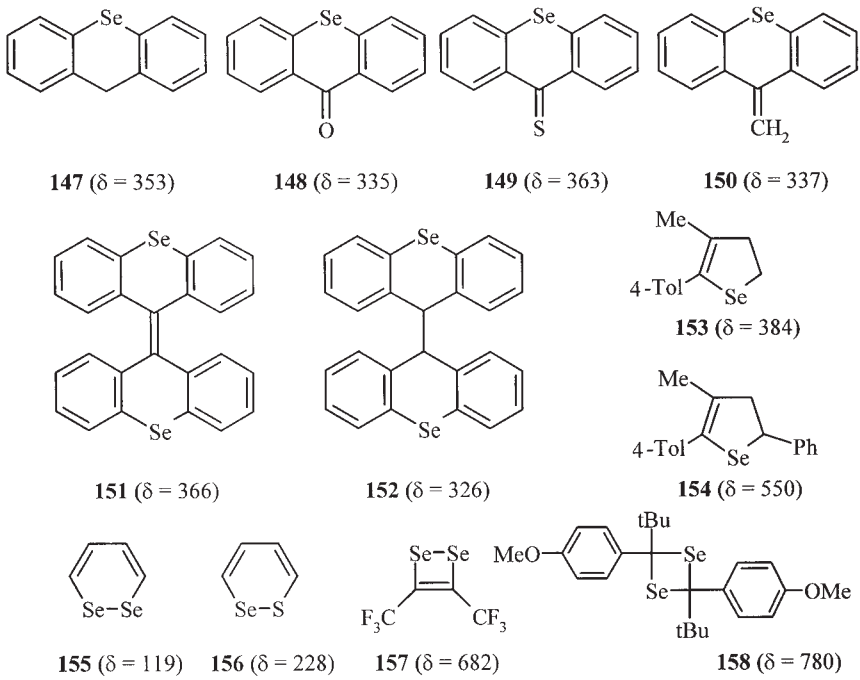

147 (δ = 353) **148** (δ = 335) **149** (δ = 363) **150** (δ = 337)

151 (δ = 366) **152** (δ = 326) **153** (δ = 384) **154** (δ = 550)

155 (δ = 119) **156** (δ = 228) **157** (δ = 682) **158** (δ = 780)

Scheme 28

During the last decade many more heterocyclic systems have appeared in the literature. Recently, some derivatives of selenabenzene were reported for the first time; e.g., **146** with R=COOMe.[226,227] A variety of selenopyrane derivatives, such as **147–152**[228–230] are collected in Scheme 28. It is interesting to note that the bis(selenoxanthones) **151** and **152** adopt folded conformations, i.e., there is no coplanarity within the tricyclic units. Some dihydroselenophenes bearing alkyl, alkenyl, and/or phenyl substituents were introduced, see e.g., **153** and **154**.[231] As expected, a change in the substituent in the α-position with respect to Se causes a large ^{77}Se chemical shift change. Finally, 1,2-diselenin **155**, its monothia analogue **156** and a number of their derivatives[232,233] as well as 1,2-diselenacyclobutene (**157**)[234] and a 1,3-diselenetane **158**[235] deserve attention.

The ^{77}Se NMR parameters of 1,2- (**159**)[236] and 1,3-selenazoles (e.g., **160**)[223] have been mentioned before (Scheme 29). [1e] Due to its large electronegativity, the nitrogen atom deshields the ^{77}Se nucleus to a great extent. Recently, the synthesis of further 1,3-selenazole derivatives, such as **161**[237] and **162**[238] have been reported confirming this trend. Acylation of the amino group of **162**

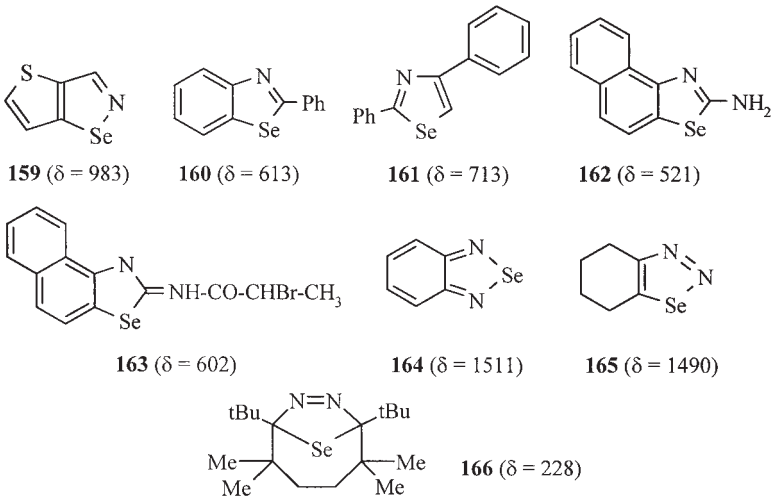

159 (δ = 983) **160** (δ = 613) **161** (δ = 713) **162** (δ = 521)

163 (δ = 602) **164** (δ = 1511) **165** (δ = 1490)

166 (δ = 228)

Scheme 29

leads to the formation of tautomeric selenazolines like **163** accompanied by a significant deshielding of the selenium atom.[238] The deshielding is much larger in 1,2- and 1,3-selenadiazoles as exemplified by **164**[239] and **165**;[240] such chemical shifts are among the largest for selenium atoms in this oxidation state. For a detailed analysis of the substituent, strain and chirality effects on 1,2-selenadiazole derivatives see Ref. 240. Derivatives of **164** with various substituents at the benzenoic ring have been reported.[23,239,241,242] Finally, a sterically congested selenadiazoline **166** with a remarkably shielded ^{77}Se nucleus is mentioned.[243]

2.2.3.5. Medio- and macrocycles

Selenium-containing medio- and macro-cyclic compounds were studied intensively. Basically, three research groups were involved in this topic during the last one to two decades.

Levason *et al.*, studied mono-, di-, tri-, and polydentate selenoethers as ligands in various metal complexes; a recent review compiles papers in this field.[244] In the course of this project they developed many complexes of the medio- and macrocyclic selenoethers (coronands) like **167** ([8]aneSe$_2$), **168** ([16]aneSe$_4$), and **169**, a benzodiselenonine derivative (Scheme 30).[245–251]

Pinto's group introduced a variety of selenium coronands, e.g., **170**,[252] **171**,[252] **172**,[253,254] and **173**[254,255] and focused on their conformation in solution and in the solid state. Moreover, they studied some copper and mercury complexes thereof.[256–258] Polymethylated selenium coronands **174–176** have been synthesized.[259] Some crown ethers **177** (and its palladium complex)[260] and **178–180**,[261] macrocycles containing oxygen as well as selenium atoms, deserve mentioning (Scheme 30).

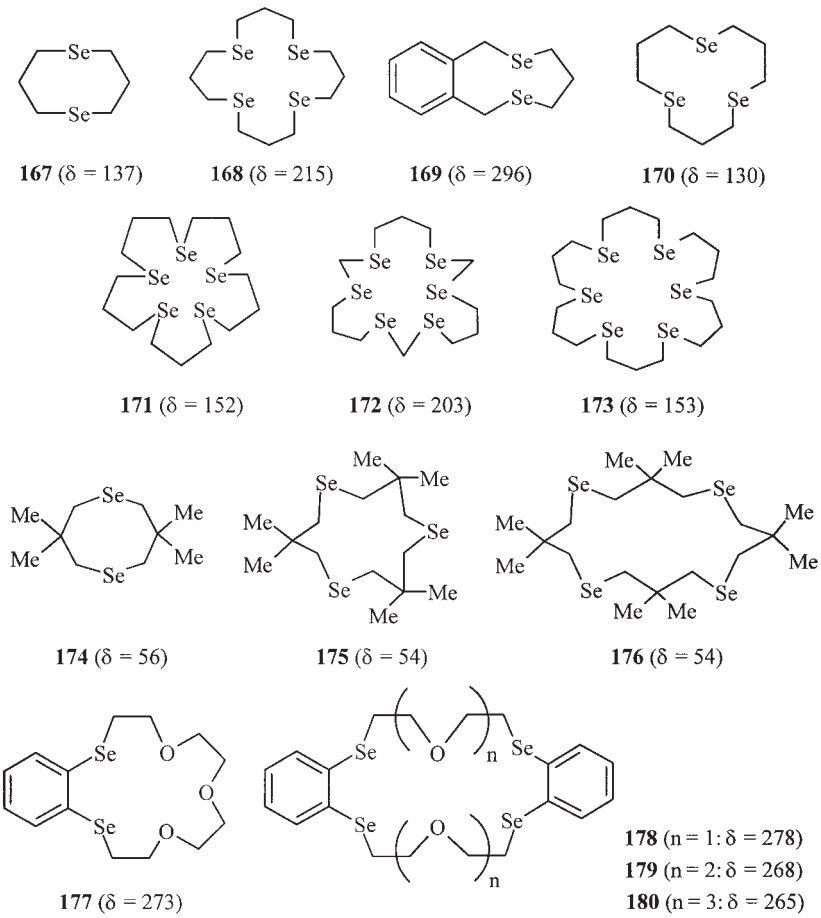

Scheme 30

The third group constantly active in this field is that of Furukawa and co-workers (Scheme 31). Starting from aromatic systems with two selenium atoms and other chalcogens in the *peri*-position (e.g., **181**–**183**),[262,263] they studied oxidation reactions (e.g., producing **184**),[263] intramolecular interactions of spatially close atoms (see also Section 3.4), included selenocins and diselenocins (e.g., **185**[264] and **186**,[265] respectively) with respect to their conformational behaviour and oxidized them to produce dications (e.g., **187** → **188**).[266] Moreover, derivatives with other endocyclic heteroatoms were investigated, such as telluraselenocins (**189**; two ^{77}Se signals at −50°C due to the existence of two conformations, chair and boat),[267] selenazocines[268–271] such as **190**[141] and **191**,[273] phosphaselenocines **192**[264] and even stannamacrocycles like **193**.[274] A review of the chemistry of such compounds summarizes the results.[275]

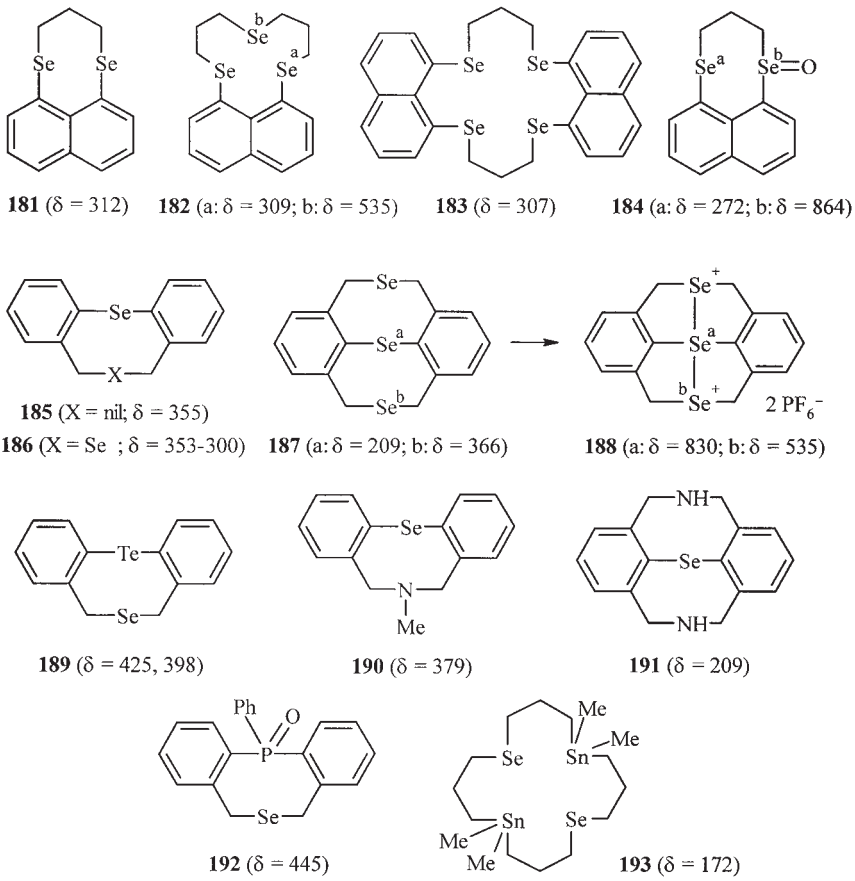

181 (δ = 312) **182** (a: δ = 309; b: δ = 535) **183** (δ = 307) **184** (a: δ = 272; b: δ = 864)

185 (X = nil; δ = 355)
186 (X = Se ; δ = 353-300) **187** (a: δ = 209; b: δ = 366) **188** (a: δ = 830; b: δ = 535)

189 (δ = 425, 398) **190** (δ = 379) **191** (δ = 209)

192 (δ = 445) **193** (δ = 172)

Scheme 31

Some very interesting tetraselenaporphyrin analogues, the ionic **194** and **195**, complete the section of macrocycles (Scheme 32).[276] It is interesting to see that large charge differences do not lead to very significant ^{77}Se chemical shift changes, apparently, due to delocalization. And finally, some related selenoethers **196**–**197** and their analogues with replacing the 1-naphthyl by 9-anthryl residues should be mentioned; they are not macrocycles but tweezer-like molecules and have been used as ligands in platinum (II) complexes (Scheme 32).[277]

2.2.3.6. Selenonium ions, selenides, selenuranes, and other charged species

As expected, alkylation, alkenylation, and arylation of selenides to selenonium salts leads to selenium deshieldings,[1e] compare for example $(CH_3)_3Se^+I^-$, $\delta = 258$ relative to $\delta = 0$ for $(CH_3)_2Se$.[278] The magnitude of the deshielding can reach upto ca. 180–250 ppm and depends on the substituent introduced as well as on those already present.[279–281] However, it seems to be smaller for

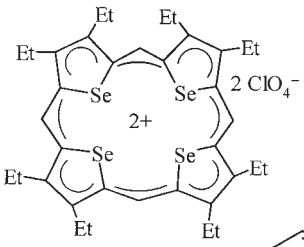

194 (δ = 747)

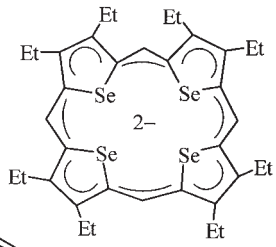

195 (δ = 586)

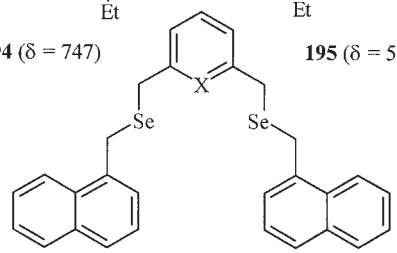

196 (X = CH; δ = 325)
197 (X = N ; δ = 325)

Scheme 32

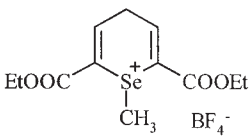

198 (δ = 268)

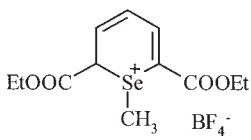

199 (δ = 268)

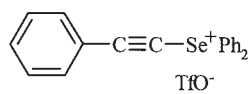

200 (δ = 470)

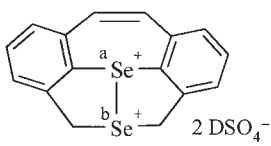

201 (a: δ = 777; b: δ = 737)

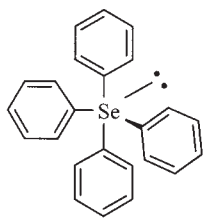

202 (δ = 374)

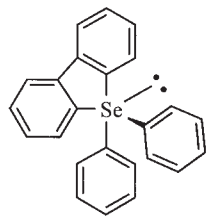

203 (δ = 397)

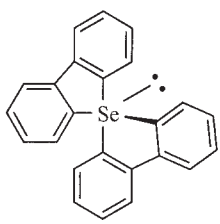

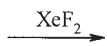

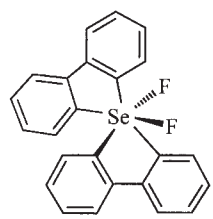

204 (δ = 427)

205 (δ = 490)

Scheme 33

triarylselenonium salts due to a better delocalization of the positive charge; see for example: $Ph_3Se^+Br^-$, $\delta = 484$, relative to Ph_2Se, $\delta = 414$.[282] In the mono–*Se*–methyl derivative of **193**, two ^{77}Se signals are observed, one at $\delta = 310$ for the selenonium atom and $\delta = 163$ for the selenide.[274] More recently, some 1-methylselenopyranium salts, e.g., **198** and the two diastereomers of **199**, were reported (Scheme 33).[283] Ethynylselenonium salts, such as **200**, were used in a stereoselective reaction with active methylene compounds and amides[284] or with thiols and thiophenols.[285] The methylselenonium derivatives of the amino acids cysteine and methionine have been characterized,[286] and some related multication species, such as **114**,[162] **188**,[266] or **201**,[287] deserve attention.

Organic compounds possessing hypervalent selenium atoms are called selenuranes. Although selenuranes with four organyl residues had been originally considered to be unstable, tetraphenylselenurane **202**[288] and some

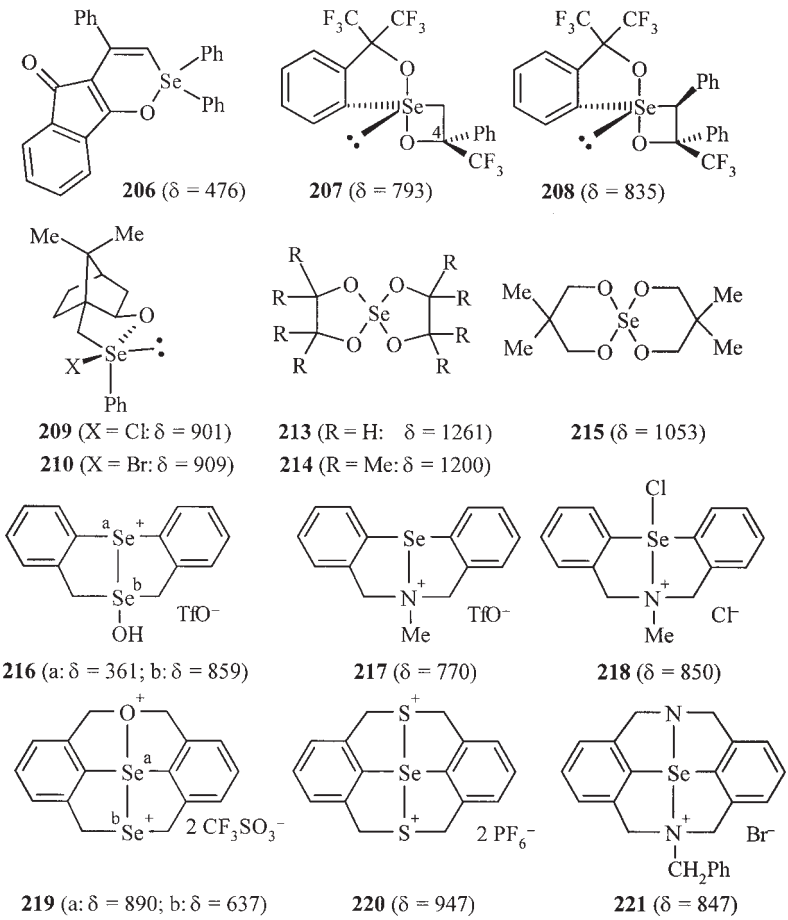

Scheme 34

reactive derivatives like **203**[288–290] (Scheme 33) have been reported to be stable at low temperatures as trigonal bipyramids and were identified by low-temperature NMR when the pseudorotation is frozen (on the NMR time-scale) which makes all four phenyl groups equivalent. For example, **202** affords diphenylselenide and biphenyl. Surprisingly, the addition of the two phenyl groups to diphenylselenide ($Ph_2Se \rightarrow$ **202**) shields the selenium atom by 35 ppm. A detailed review on the synthesis, structure, and dynamics of chalcogenuranes appeared in 1998.[291] The difluoroperselenurane **205** with a hexavalent selenium atom can be prepared from the corresponding selenurane **204**[289] by adding two fluorine atoms with XeF_2.[292]

Selenuranes with at least one carbon replaced by oxygen have been reported as well. The reaction of ethynylselenonium salts with 1,3-indanedione afforded the oxyselenurane **206**.[284] Further oxyselenetane derivatives were reported, e.g., **207** and its diastereomer with opposite configuration at C-4 differ by 12 ppm in their ^{77}Se chemical shifts[293] or its phenyl derivative **208**.[294] Optically pure halogenated oxyselenuranes such as **209** and **210** and others, derived from the bornane system, have been described.[295,296] Tetraalkoxyselenuranes like $Se(OCH_3)_4$ (**211**, $\delta = 1176$), $Se(O–CH_2–t–Bu_3)_4$ (**212**, $\delta = 1256$), the spiro analogues **213**–**215** and some others have ^{77}Se chemical shifts ranging up to nearly $\delta = 1300$.[297] Cationic selenuranes have already mentioned before: **188**[266,298] and **201**.[287] Some further examples are **216** and **217**,[299] **218**,[300] **219**,[301] **220**,[298] and **221** (Scheme 34).[273]

2.3. Scalar couplings involving ^{77}Se

In earlier reviews[1] detailed descriptions of the nature of dipolar coupling (through-space; coupling constant D) and scalar coupling (through-bond; coupling constant J) between NMR-active nuclei have been presented. Scalar coupling constants between a ^{77}Se nucleus and its partner X [$^nJ(^{77}Se,X)$] can be extracted quite easily in the case of first-order spectra, either from the ^{77}Se signals if X has a satisfactory natural abundance (typical for ^{1}H, ^{19}F, ^{31}P) or from the spectra of X by inspecting the ^{77}Se satellites (typical for ^{13}C, ^{15}N, and ^{31}P). Each of the ^{77}Se satellites has about 4% intensity compared to the respective main signal of nucleus X.

The following section presents short summaries in the first paragraph for each subsection taken from the author's earlier review.[1e] This is supplemented by reports which appeared between 1994 and 2002 if they contain significant new information.

2.3.1. *^{77}Se,^{1}H couplings*

One-bond coupling constants, $^1J(^{77}Se,^1H)$, requiring an Se–H fragment in the molecule are positive, and values between 65.4 (H_2Se) and 38 ± 1 Hz (*t*-Bu–SeH) have been reported. In general, they are smaller in aliphatic (41–45 Hz)

and larger in aromatic selenols (48–58 Hz). $^{2}J(^{77}Se,^{1}H)$-values (*geminal* couplings) are between 4 and 16 Hz for hydrogens in aliphatic fragments, in divinyl selenide it is 22.0 Hz, and they can increase up to more than 50 Hz if there are further geminal heteroatoms or if they are in aromatic rings. On the other hand, smaller ^{2}J-values are found in selenoacetals; for example, it is only 4.4 Hz in $(PhSe)_2CH–Me$. Oxidation of the selenium atom has apparently no significant effect: $^{2}J = 10.5$ Hz in Me_2Se and 11.7 Hz in Me_2SeO. There seems to be a stereochemical dependence in this parameter. Three-bond (*vicinal*) couplings, $^{3}J(^{77}Se,^{1}H)$, tend to be positive. They are rather small in aliphatic fragments, e.g., 8–12 Hz across sp^3 carbons. If, however, a selenium atom involved in a three-bond coupling has no free electron pair, the ^{3}J-value becomes much larger: 37.9 Hz in $Et–SeO_3^-$ and 24.8 Hz in $(MeO)_2SeO_2$. *Vicinal* couplings are rather small in selenophenes (5–10 Hz), and there is clearly a stereochemical Karplus-type dependence of the $^{3}J(^{77}Se,^{1}H)$ parameter.

2.3.2. *^{77}Se,^{13}C couplings*

One-bond couplings, $^{1}J(^{77}Se,^{13}C)$, are negative and depend strongly on the hybridization state, i.e., the *s*-character of the carbon atom involved. Typical ranges are −45 to 100 Hz for selenium attached sp^3-carbon atoms (larger absolute values if heteratoms are attached to C), −90 to 174 Hz for C=*C*–Se (sp^2-carbon atoms; aromatic or olefinic), −203 to −249 Hz in C=Se bonds, −184 to 193 Hz for C≡*C*–Se (sp-carbon atoms), −240 to 292 Hz for N≡*C*–Se-, ca. −274 Hz for –N=*C*=Se, and ca. −287 Hz for O=*C*=Se. Exceptionally low values were found for selenonic acids, e.g., −13 Hz for $Me–SeO_3^-\ K^+$. The coupling constants in C=Se fragments of a number of selenoketones can be correlated with the wavelengths of the $n \rightarrow \pi^*$ transitions in the UV spectra. Coordination to transition-metals can reduce the $^{1}J(^{77}Se,^{13}C)$-values severely. Two-bond couplings, $^{2}J(^{77}Se,^{13}C)$, have not been studied very intensively. Generally, they are positive, much smaller than $^{1}J(^{77}Se,^{13}C)$, and rarely exceed 15 Hz in acyclic diorganyl selenides. Even oxidation of the selenides to dichlorides, selenoxides, and selenium dioxides can hardly affect them. Little is known about $^{3}J(^{77}Se,^{13}C)$-values. They are in the range of 3–12 Hz but a decrease to less than 3 Hz occurs if the selenium atom is oxygenated.

2.3.3. *^{77}Se,^{19}F couplings*

One-bond $^{77}Se,^{19}F$ coupling constants, $^{1}J(^{77}Se,^{19}F)$, are presumably negative and can be very large, exceeding 1000 Hz considerably. If fluorine atoms are in different stereochemical positions, they can be discerned easily. $^{2}J(^{77}Se,^{19}F)$-values can be substantial; large values have been observed in $CF_3–C(=Se)–F$ (314.7 Hz) or in $F_2C=Se$ (256 Hz). However, they are much smaller in CF_3Se groups (5–50 Hz). Trifluoromethylselenonic acid and its derivatives such as $CF_3–SeO_3–Et$, $CF_3–SeO_3H$, and $CF_3–SeO_2–NMe_2$ are exceptions with $^{2}J(^{77}Se,^{19}F) = 153.3$, 134, and 113 Hz, respectively. In $(CF_3)F_3Se=O$, however,

it is only 2.1 Hz. $^{3}J(^{77}Se,^{19}F)$ coupling constants of 5–29 Hz have been reported in trifluoromethylated derivatives but a Karplus-type dependence has not yet been established. Four-bond $^{77}Se,^{19}F$ coupling constants of 11–12 Hz exist in fluorinated 1,3-diselenetanes.

The one-bond coupling $^{1}J(^{77}Se,^{19}F)$ in the selenurane **205** is 503 Hz[292] and 1428 Hz in $[XeOSeF_5]^{+}[AsF_6]^{-}$.[302] Recently, it was found in fluoro- and difluorovinyl selenides ($F_2C{=}CH{-}SePh$) that $^{3}J(\text{trans}) > {}^{3}J(\text{cis})$; 40.8 and 3.2 Hz, respectively).[303,304] For some through-space scalar couplings of ^{77}Se and ^{19}F nuclei under steric compression see Section 3.4 (intermolecular interactions).

2.3.4. *$^{77}Se,^{31}P$ couplings*

One-bond coupling, $^{1}J(^{77}Se,^{31}P)$, are negative. The absolute value of this coupling constant is an excellent indicator of the bond order between P and Se. Large absolute values (−800 to 1200 Hz) are normal in the case of P=Se fragments whereas they are much smaller across P–Se single bonds (−200 to 620 Hz). Moreover, $^{77}Se,^{31}P$ couplings contain stereochemical information, for example with respect to the axial or equatorial positions in phosphorinane rings. Coordination of selenium in a P=Se fragment to metals may significantly reduce the absolute value of the coupling. Both positive and negative values for two-bond $^{2}J(^{77}Se,^{31}P)$ coupling constants were found. The absolute values might be very small, like −3.8 Hz in $Me_2P(=Se){-}P(=Se)Me_2$, but much larger ones are found as well, for example 41 Hz Ar–Se–Au–PPh (Ar = 2,4,6-*t*–Bu_3–C_6H_2–), 87 Hz in $Ph_3P{=}N{-}SeCl_3$ and 102.9 Hz in a compound containing a Se–Pt–P fragment. Apparently, three-bond $^{3}J(^{77}Se,^{31}P)$ coupling constants are negative and can have absolute values up to 14 Hz.

As mentioned above, one-bond $^{77}Se,^{31}P$ coupling constants in compounds with Se–P single bonds are relatively small, e.g., 124.7 Hz in the three-membered ring of **81** and 62.1 Hz in the four-membered ring of **82**; $^{2}J(^{77}Se,^{31}P) = 27.5$ in **82**.[115] The respective values in the five-membered **83** (dibromide) are: $^{1}J(^{77}Se^{a},^{31}P^{a}) = -285.3$ Hz, $^{1}J(^{77}Se^{b},^{31}P^{a}) = -196.9$ Hz, and $^{2}J(^{77}Se^{b},^{31}P^{b}) = -0.1$ Hz; the corresponding values of the diiodide **84** are −264.5, −181.0, and −3.9 Hz.[116] The couplings of the bridged cyclic **88** are: $^{1}J(^{77}Se^{a},^{31}P) = 317.4$ Hz, $^{1}J(^{77}Se^{b},^{31}P) = 177.8$ Hz, $^{2}J(^{77}Se^{a},^{31}P) = 40.3$ and 15.4 Hz, $^{2}J(^{77}Se^{b},^{31}P) = 52.5$ Hz, and $^{2}J(^{77}Se^{c},^{31}P) = 23.2$ Hz.[117] On the other hand, the one-bond $^{77}Se,^{31}P$ coupling in the adamantoid tetraphosphorhexaoxidiselenide **222**, 1148.8 Hz, is one of the highest hitherto reported (Scheme 35).[305] The TMEDA-stabilized lithium salt of $Ph_2P{-}Se^{-}$ mentioned in Section 2.2.3.1, shows not only a reduction in the ^{77}Se-chemical shift as compared to the respective neutral P=Se analogue but also a reduced coupling constant: $^{1}J(^{77}Se,^{31}P) = 321$ Hz. This can be attributed to a localization of the negative charge at the selenium atom.[114] It has been mentioned that electronegative substituents attached to a P=Se group increase the absolute

values of the ^{77}Se,^{31}P coupling constant. This tendency is confirmed by 1-adamantyldichlorophosphine selenide [1-Ad(Cl_2)P=Se]: $^{1}J(^{77}Se^{a},^{31}P) = 910$ Hz.[107] Various iodine–selenium adducts of phosphine selenides with organyl or amino substituents at the phosphorus atoms show $^{1}J(^{77}Se^{a},^{31}P)$-values between 500 and 700 Hz depending of the adduct structure which is of three-centre, four-electron bonding characteristics.[306,307] Some phosphonium salts of the structure $(MeO)_2(Ph)P^{+}SeClX^{-}$ ($X^{-} = Cl^{-}$, SO_2Cl^{-}) and $(MeO)(Ph)_2P^{+}SeClX^{-}$ are in the same range.[308] Selenoxophosphines Ar–P=Se[112] and diselenoxophosphoranes Ar–P(=Se)$_2$[111–113,309] can be isolated if Ar is a steric demanding substituent, such as 2,4,6-tri-*t*-butylphenyl and others; the one-bond ^{77}Se,^{31}P couplings are in the expected range: 700–855 Hz. In the selenometaphosphates **71**–**73**[109] as well as the ylides **74**, **75**, and **77**,[108,110] the pertinent values are in the upper part of this range (788–855 Hz) whereas tetraselenopyrodiphosphates **78**–**80** show smaller one-bond couplings of 591.9–683.5 Hz; the $^{2}J(^{77}Se^{a},^{31}P)$-values are small (−4.7–+0.8 Hz) (Scheme 35).[108]

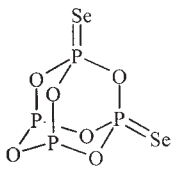

222: $^{1}J(^{77}Se,^{31}P) = 1148.8$ Hz

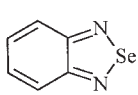

223: $^{1}J(^{77}Se,^{15}N) = 75.5$ Hz

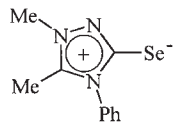

224: $^{3}J(^{77}Se,^{15}N) = 4.9$ Hz

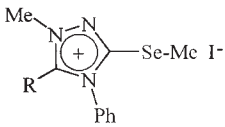

225, R = Me: $^{3}J(^{77}Se,^{15}N) = 5.5$ Hz
226, R = Ph : $^{3}J(^{77}Se,^{15}N) = 5.5$ Hz

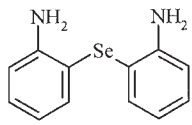

227: $^{3}J(^{77}Se,^{15}N) = 9.1$ Hz

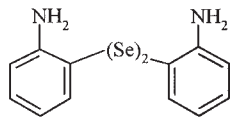

228: $^{3}J(^{77}Se,^{15}N) = 23.8$ Hz

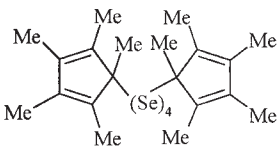

229: $^{1}J(^{77}Se,^{77}Se) = 89$ Hz

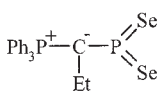

230: $^{2}J(^{77}Se,^{77}Se) = 133.0$ Hz

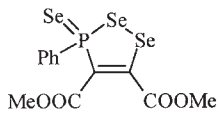

231: $^{1}J(^{77}Se,^{77}Se) = 271$ Hz

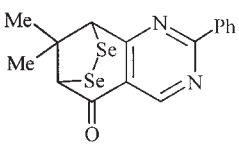

232: $^{1}J(^{77}Se,^{77}Se) = 361.2$ Hz

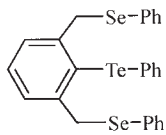

233: $^{1}J(^{125}Te,^{77}Se) = 100$ Hz

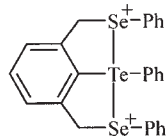

234: $^{1}J(^{125}Te,^{77}Se) = 433, 462$ Hz

Scheme 35

2.3.5. *^{77}Se couplings to other nulcei*

$^{n}J(^{77}Se,^{15}N)$: Only few reports on ^{77}Se,^{15}N couplings exist. One-bond coupling constants, $^{1}J(^{77}Se,^{15}N)$, are probably positive: 60.1 Hz for $CF_3Se–NH_2$, 74.7 Hz for $(CF_3Se)_2NH$, 89.8 Hz for **165**, and 74.2 Hz for $Se[N(Tms)_2]_2$ (Tms≡trimethylsilyl). Two-bond coupling constants, $^{2}J(^{77}Se,^{15}N)$, are rare, a value of 3.66 Hz has been reported for $H_3Si–^{15}N{=}C{=}^{77}Se$, and so are three-bond coupling constants, $^{3}J(^{77}Se,^{15}N)$.

^{77}Se,^{15}N coupling constants reported for the eight-membered $Se_6(N–tBu)_2$ (**67**) are in the expected range: $^{1}J(^{77}Se,^{15}N) = 96.9$ Hz and $^{2}J(^{77}Se,^{15}N) = 9.7$ Hz.[102] The one-bond ^{77}Se,^{15}N coupling constant of 2,1,3-benzoselenadiazole (**223**) is 75.5 Hz, and the corresponding coupling constant involving the quadrupolar ^{14}N is ca. 1 Hz larger, an $^{14}N/^{15}N$ isotope effect.[23,310] Three-bond ^{77}Se,^{15}N coupling constants were reported for the mesoionic 1,3,4-triazolium-5-selenolates **224**–**226**,[180] the selenide **227**, and the diselenide **228** (Scheme 33).[311]

$^{n}J(^{77}Se,^{29}Si)$: One-bond ^{77}Se,^{29}Si coupling constants are positive. Only few data have been published before 1994, e.g., 110.6 Hz in $H_3Si–Se–SiH_3$, and values between 45 and 80 Hz in some cyclic Si–Se compounds. A two-bond coupling constant $^{2}J(^{77}Se,^{29}Si) = 2.7$ Hz has been reported for $Se[N(Tms)_2]_2$ (Tms≡trimethylsilyl).

$^{1}J(^{77}Se,^{29}Si) = 107.7$ Hz in $Me_3Si–Se–SiMe_3$, and similar values were reported for $EtSe–SiMe_3$ (107.3 Hz) and $PhSe–SiMe_3$ (103.3 Hz).[79,80] Herzog and collaborators described a large number of silanes and halosilanes containing organoselenium groups. They found that the number of chlorine atoms attached to silicon has an enormous effect on $^{1}J(^{77}Se,^{29}Si)$. For example, $Me_3Si–SeBu$, 110.8 Hz; $Me_2SiCl–SeBu$, 146.8 Hz; $MeSiCl_2–SeBu$, 183.2; $SiCl_3–SeBu$, 217.4 Hz. Other effects could be identified for changing the number of SeBu and phenyl substituents.[81] One-bond ^{77}Se,^{29}Si coupling constants in organosilanylselenols and bis(organosilanyl)selenides are in the same range (100–160 Hz) but the corresponding parameters in alkali selenides are somewhat larger (165–173 Hz).[80] Analogous values exist for mono- and bicyclic derivatives such as **33**–**43**.[84–88,312] Two-bond ^{77}Se,^{29}Si couplings are between 10 and 22 Hz[80] and three-bond ^{77}Se,^{29}Si coupling constants are ca. 15–17 Hz.[86]

$^{n}J(^{77}Se,^{77}Se)$: One-bond ^{77}Se,^{77}Se couplings have been measured for a number of diselenides, and $^{1}J(^{77}Se,^{77}Se)$-values between +22 Hz (Ph–Se–Se–Me) and −66.5 Hz ($CF_2Cl–Se–Se–CF_2Cl$) have been found. Much larger $^{1}J(^{77}Se,^{77}Se)$-values are found if a charged selenium atom is involved. In cyclic sulphur–selenium compounds their absolute values are even larger: $^{1}J(^{77}Se,^{77}Se) = 95$–114 Hz. In the same class of compounds, three-bond couplings are noticeable (3–16 Hz). Two-bond couplings can adopt large values; in geminally diseleno-substituted alkenes, they are between 20 and 55 Hz. Interesting cases of a stereochemical differentiation by $^{3}J(^{77}Se,^{77}Se)$-values are

found in the pair in tetraselenafulvalenes. Four-bond couplings vary between 0 and 16 Hz in sulphur–selenium cycles.

Recent reports provide further data (Scheme 33). For example, the ^{77}Se,^{77}Se coupling constants in the tetraselenide **229** are $^{1}J = 89$ Hz and $^{2}J = 109$ Hz; the latter parameter is an exceptionally large value[313] but that in the ylide **230** is even larger ($^{2}J = 133.0$ Hz).[314] Further surprisingly high one-bond ^{77}Se,^{77}Se coupling constants were reported for **231** (271 Hz)[315] and for the bridged diselenide **232** (361.2 Hz).[316] So, the influence of structure and substitution on the $^{1}J(^{77}\text{Se},^{77}\text{Se})$ parameter is far from being understood.

$^{n}J(^{125}Te,^{77}Se)$: One-bond couplings have been reported for Me–Se–Te–Me (-169 ± 2 Hz). Some polychalcogen cations and anions afford substantial one- and two-bond ^{125}Te,^{77}Se coupling constants (189–670 Hz).

Only few recent ^{125}Te,^{77}Se coupling data are to be cited (Scheme 33). In the telluride **233**, the coupling constant $^{1}J(^{125}\text{Te},^{77}\text{Se}) = 100$ Hz, whereas in the corresponding dicationic hypervalent telluride **234** the $^{1}J(^{125}\text{Te},^{77}\text{Se}) = 443$ and 462 Hz and $^{2}J(^{77}\text{Se},^{77}\text{Se}) = 71$ Hz.[163]

$^{n}J(^{129}Xe,^{77}Se)$: A two-bond coupling of 153.8 Hz between ^{77}Se and ^{129}Xe has been reported for $Xe(OSeF_5)_2$.[1e]

As mentioned before,[1e] coupling constants of ^{77}Se to metal nuclei (M) can adopt a vast range of several kHz. Comparing such parameters within a certain group of analogous or isomeric compounds may be indicative of substitution and stereochemistry. On the whole, however, ^{77}Se,M couplings are hardly of great value in a more general sense although a careful investigation in this field may be rewarding. Here, however, we refrain from a detailed compilation and refer previous reviews[1] and to a comprehensive data collection.[2]

3. CHEMICAL APPLICATIONS

^{77}Se NMR spectroscopy is more and more recognized as a useful tool for the elucidation of molecular structures of selenium-containing compounds and intermediates. In other applications, ^{77}Se nuclei were used as probes for detecting molecular chirality, intramolecular interactions, or bond situations. In addition, some methods have been invented where selenium-containing auxiliaries are applied to selenium-free compounds. In the following, applications in those fields are presented.

3.1. Chirality

Gronowitz and co-workers were the first to report that ^{77}Se NMR is an excellent tool for chiral recognition. They found two resonances at $\delta = 136.6$ and 134.5 in the ^{77}Se NMR spectrum of a mixture of diastereomeric esters produced from (*R*)-2-phenylselenenylpropanoic acid and (*R,S*)-2-octanol. [317]

The first chiral selenium-containing derivatizing agent, enantiomerically pure (4*S*,5*R*)-(–)-4-methyl-5-phenyloxazolidine-2-selone (**235**), designed for the determination of enantiomeric purities by ^{77}Se NMR spectroscopy, was introduced by Dunlap *et al.*, 1990 (Scheme 36).[318–320] It is shown that the ^{77}Se signal is split into two with a separation of 5.3 Hz (external field: 7.05 T) when the oxazolidine selone derivative **235** reacts with the racemic mixture of 5-methylheptanoic acid to produce a diastereomeric mixture of **236**. This is a chiral recognition across seven bonds, five of them in a flexible chain! Moreover, the stereochemical difference in **237** caused by the position of a deuterium atom five bonds away from the selenium atom could clearly be recognized by a 5.0 Hz deuterium isotope shift.[318] Further related examples were published by the same group[319–325] including a review.[326]

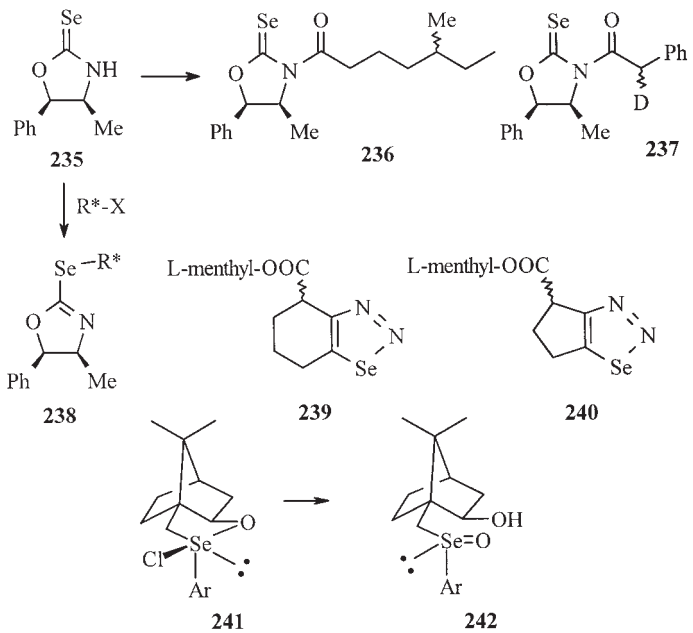

Scheme 36

The use of **235** has been extended to chiral recognition of alcohols and alkyl halides by forming 4,5-dihydrooxazoles **238**.[327]

Another example for the potential of this method is demonstrated by the L-menthyl ester **239** of a racemic cyclohexenoselenadiazole carboxylic acid which shows a 10–11 Hz splitting of the ^{77}Se NMR signal (Scheme 36). [240b] Here, the distance between the selenium atom and the nearest chirality center in the menthyl residue is six bonds, and they are on opposite sides of the cyclohexeno ring. Interestingly, the chiral recognition ability of selenium is practically lost in the corresponding cyclopenteno analogue **240**.[240b]

Apparently, molecular rigidity is indispensible in these molecular models, and this is provided by the half-chair cyclohexeno ring but is missing is the much more flexible cyclopenteno ring.

During the last decade a large number of asymmetric syntheses involving selenium-containing reagents have been studied and diastereomeric ratios were determined by ^{77}Se NMR. For example, complexes of chiral diamines with α-phenylselenenylalkyllithium compounds were prepared.[328] Optically pure haloselenuranes, such as **241**, were synthesized starting from optically pure borneol derivatives (Scheme 36).[329] These were converted to γ-hydroxyselenoxides (**242**) which served as enantioface-differentiating protonation reagents.[146] Highly stereoselective [2,3]sigmatropic rearrangements were observed when Ar in **242** is replaced by an allylic group.[146] Di(*endo*-3-camphoryl) diselenides were converted to their dioximes which are electrophiles for asymmetric oxyselenenylation of alkenes providing diastereomeric ratios of 9:1 and higher.[330] The method has been extended to methoxyselenenylations and some unusual cyclizations.[331] Other authors used chiral nitrogen-containing diselenides (e.g., **243**) for the oxy- and methoxyselenenylation of olefins (Scheme 37).[332]

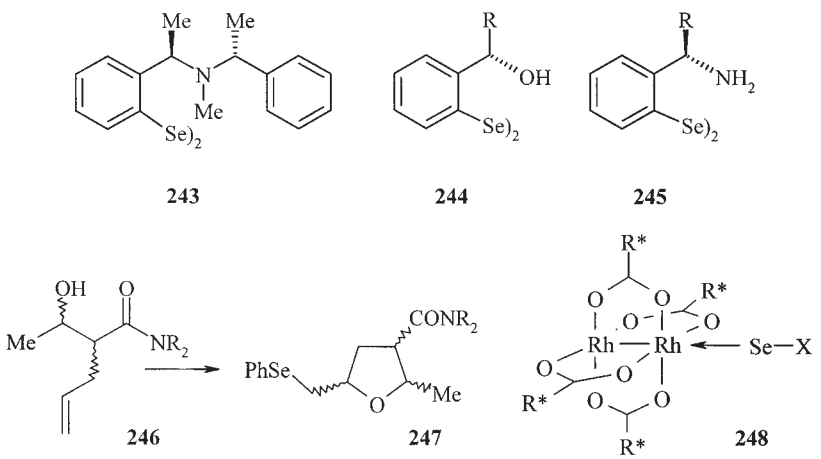

Scheme 37

A large number of chiral α,α′-*ortho*-disubstituted diphenyldiselenides with hydroxy and amino functions (e.g., **244** and **245**) have been prepared by Wirth and co-workers. They were used as electrophiles for a number of asymmetric addition and cyclization reactions[333–337] including the total synthesis of the lignan derivatives (+)-samin[338] and (+)-membrine[339] as well as catalysts in the asymmetric diethylzinc addition to aldehydes.[340]

Some β-hydroxyamides (**246**) in different diastereomic mixtures were cyclized to tetrahydrofurane derivatives (**247**) in the presence of Ph–SeCl, and subsequently, their diastereomeric ratios could be determined by ^{77}Se NMR analysis.[341] Some arylseleninic acids (Ar–SeO_2H; δ = 1200–1276) were optically resolved by chiral columns and their racemization studied.[142]

Table 4. ^{77}Se signal dispersions in Hz (at 76.3 MHz) of 1:1 mixtures of racemic α-phenylselenenylbutanoic acid and enantiomerically pure amines (in $CDCl_3$)[343]

(*R*)-(+)-1-Phenylethylamine	22 Hz
(*R*)-(+)-*N*,*N*-Dimethyl-1-phenylethylamine	8 Hz
(*R*)-(+)-1-(1-Naphthyl)ethylamine	347 Hz
(*R*)-(−)-1-Cyclohexylethylamine	95 Hz
Brucin	159 Hz
Strychnin	37 Hz
Chinin	107 Hz
Cinchonin	99 Hz
Cinchonidin	240 Hz
(−)-Nicotin	25 Hz
(1*R*,2*S*)-(−)-Ephedrin	211 Hz
L-Valinol [(*S*)-2-amino-3-methyl-1-butanol]	72 Hz

In analogy to the Pirkle-Method[342] stereochemical recognition is possible even in solution in the presence of a chiral selenium-containing solvating reagent. Racemic α-phenylselenenylalkanoic acids and enantiomerically pure amines have been examined as salts. Strong signal splittings could be detected which are clearly superior to any related effects observed by ^{1}H or ^{13}C NMR (Table 4).[343] The method works excellently even with tertiary amines and amines without aromatic groups where the Pirkle-method fails due to the lack of an additional intramolecular stabilization.

Chiral recognition of organoselenium compounds lacking any other functional group can easily be achieved by forming kinetically labile adducts **248** with the chiral dirhodium complex Rh_2[(*R*)-MTPA]$_4$ [MTPA–H = (*R*)-(+)-methoxytrifluoromethylphenylacetic acid≡Mosher's acid] (Scheme 37). Se–X may be any phenylselenenylalkane and -cycloalkane (Ph–Se–R)[22,344] or phosphine selenide ($R^1R^2R^3P$=Se; R = organyl or heteroatom residues).[345] Large diastereomeric dispersions can often be seen at the ^{77}Se signal although line broadening due to coalescence may occur. In such cases, other nuclei such as ^{1}H, ^{13}C, and eventually ^{31}P will be available for chiral recognition.

3.2. Syntheses

Selenium-containing compounds attract increasing interest as selenation reagents or as intermediates during exploration of reaction pathways. Some interesting recent examples are presented in the following.

The reaction products obtained when dissolving elemental selenium in aqueous sulphite solution were found to be $SeSO_3^{2-}$, and some reactions using similar sulphur or selenium reagents afforded the $Se(SO_3)_2^{2-}$ isomers with O- and with S-bonded Se as well as other related species, as determined by ^{77}Se NMR and Raman spectroscopy.[346–348] Selenium dioxide, SeO_2, is the

oldest selenium-containing reagent used for oxidation reactions and has provided unexpected products in two cases. Instead of affording an α-diketone from a six-membered ring ketone with a –CH_2–CO– fragment, the bridged diselenido ketone **232** was formed and characterized by its ^{77}Se NMR spectra.[316] Cyclic selenites, e.g., **249**, were obtained in a [4+2]cycloaddition when 1,3-diene precursors were treated with SeO_2; these can be converted into selenium-free diols in a stereospecific reaction (Scheme 38).[349]

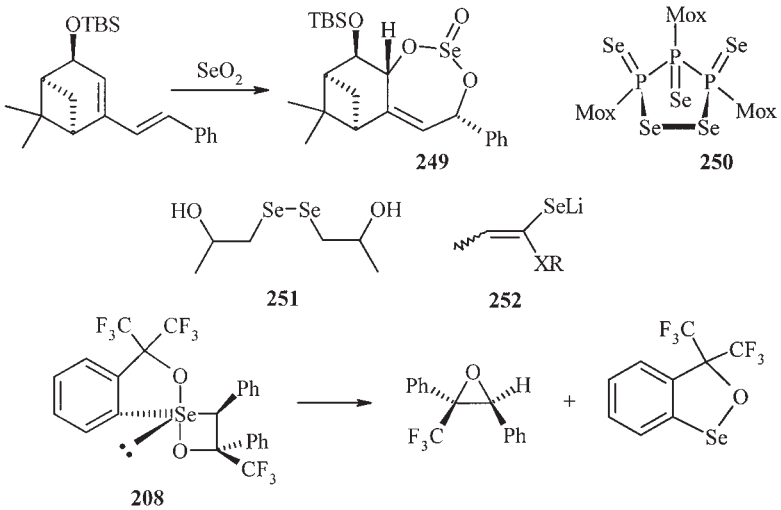

Scheme 38

A mixture of triphenylphosphine and dichloroselenuranes (R_2SeCl_2; R=Me or Ph) has been introduced as a new reagent for converting alcohols into the corresponding chlorides.[350] A new selenation reagent **250** (Mox = 2,4-di-*t*-butyl-6-methoxyphenyl) was introduced by which carboxamides R–C(=O)–NMe_2 can be converted conveniently into the corresponding selenoamides R–C(=Se)–NMe_2 with satisfactory yield (Scheme 38).[351]

Radical reactions can be observed when alkyl radicals are trapped by phenylselenol, PhSeH, produced *in situ* by reducing diphenyl diselenide, PhSeSePh, with tributyltinhydride, Bu_3SnH.[352] Barton *et al.*, used tributylphosphine in aqueous solution for converting PhSeSePh into PhSeH which, then, underwent a phenylselenation of alkenes in the presence 30% hydrogen peroxide, H_2O_2.[353] The water soluble diselenide **251** was proposed by Barton *et al.*, as an efficient radical trap.[354] Lithium alkeneselenolates **252** have proven to be precursors in reactions leading to substituted selenophenes (X = O)[355] or selenothioacetals and selenothioesters (X = S).[356] Pyrolysis of oxaselenetanes, such as **208**, leads to oxiranes with retention of configuration (Scheme 38).[293] The effect of amino groups on the antioxidant activity of glutathione peroxidase was tested by the model reaction H_2O_2+2 PhSH → 2 H_2O+PhSSPh catalyzed

by various diaryl diselenides containing amino groups.[357,358] Three intermediates, a selenenyl sulphide (R–Se–S–R′), a selenolate (R–Se$^-$), and selenenic acid (R–SeOH) were identified by ^{77}Se NMR.[357] It was found that differences in the activity depend on the intramolecular Se $\cdots$ N interaction.[357,358]

3.3. Selena analogues of natural products and biochemical applications

Although selenium compounds are notorious for being toxic and often have a particularly unpleasant smell, the element selenium has significant biological relevance.[1e,359] Selenium is an essential trace element and some selenium-containing proteins, e.g., glutathione peroxidase, have been discovered.[1e,359] Very recently, a comprehensive review on the chemistry of biologically important synthetic organoselenium compounds has been published.[360] However, biochemically oriented ^{77}Se NMR investigations are still rare; those which appeared prior to 1995 have been reviewed before.[1e] The following section contributes to this aspect and quotes later work on selenium-containing natural products or selena analogues thereof.

^{77}Se NMR spectroscopy has been considered a suitable method for tracing selenium metabolites[286] or the fate of organoselenides in a hydrobromic acid – bromine digestion system.[361] In particular, selena analogues of the amino acids

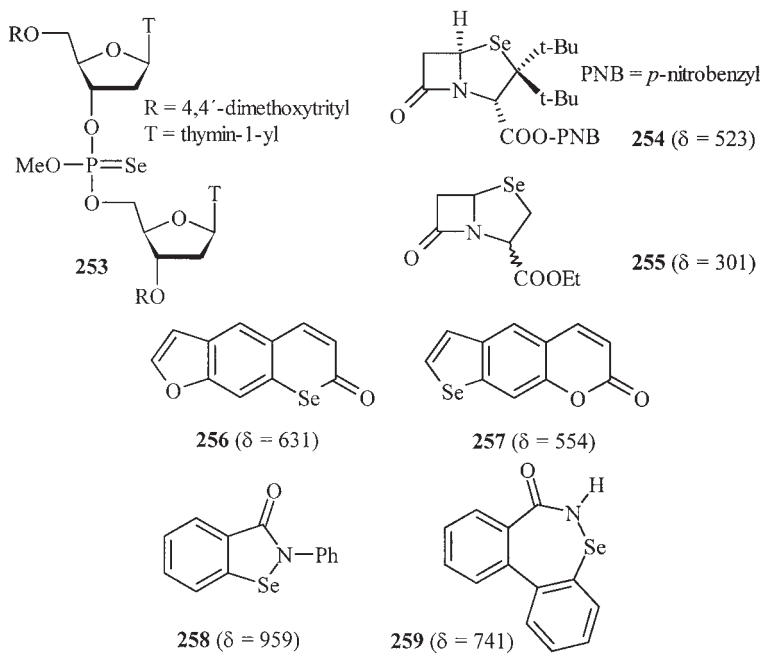

Scheme 39

methionine[50] and cystine[362,363] were studied as such and in peptides.[364,365] Per-*O*-acetylated bis(β-D-glucopyranosyl) diselenide[48b,49] and 5-selenopentopyranose derivatives (with endocyclic selenium)[366] have been reported. Synthetic methods have been described by which nucleoside selenophosphates and -selenophosphites, e.g., **253**, can be prepared (Scheme 39).[367–369]

Selenapenams (selena analogues of penicillin), such as **254** and **255**, have been synthesized and their ^{77}Se NMR spectra recorded.[370,371] Tetraselenaporphyrin analogues (**194** and **195**)[276] have already been mentioned before, and some selenapsoralen derivatives (**255** and **256**) were reported.[372] Ebselen (**258**), a heterocyclic compound with anti-inflammatory and glutathione-peroxidase-like activity, as well as a bis-homoebselen (**259**; dibenzo[*d*,*f*]-1,2-selenazepin-3-one) have been described.[373]

3.4. Intramolecular interactions

The ^{77}Se nucleus with its large sensitivity is well-suited for detecting intramolecular interactions. This has been demonstrated in a large number of cases during the last decade so that a separate section is devoted to this topic.

For an effective interaction the nuclei involved have to be close in space. This can be achieved by the topology of the molecular constitution, e.g., in 1,8-disubstituted naphthalenes, or by adopting suitable conformations where a small distance between the respective atoms is easily obtained or even cannot be avoided. Both approaches have been followed.

3.4.1. *Se · · · H interaction*

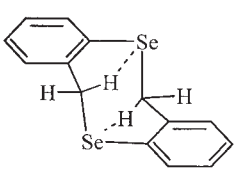

260 (chair)

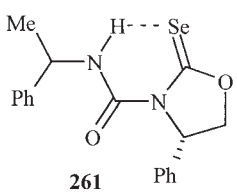

261

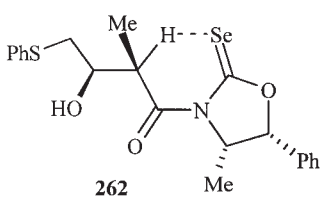

262

Scheme 40

C–H · · · Se interactions occur when steric transannular congestion exists in mediocycles. For example, through-space scalar couplings $J(^{77}Se,^{1}H) = 34.0$ Hz and 25.4 Hz could be detected in the frozen chair and boat conformations of the dibenzo[1,5]diselenocin **260** (Scheme 40).[33,374] In addition, shielding deuterium isotope effects of 4.0 and 4.2 ppm, respectively, on the ^{77}Se chemical shifts were noted.[33] An N–H · · · Se=C hydrogen bond was detected in **261** and related derivatives giving rise to a 12–13 Hz one-bond ^{77}Se,^{1}H coupling.[324] In a very similar molecular system, such as **262**, even C–H · · · Se=C interactions

could be identified with couplings $^{1}J(^{77}Se,^{1}H) = 5–6$ Hz, good enough for a polarization transfer in an HMBC experiment (Scheme 40).[375]

3.4.2. *Se · · · N interaction*

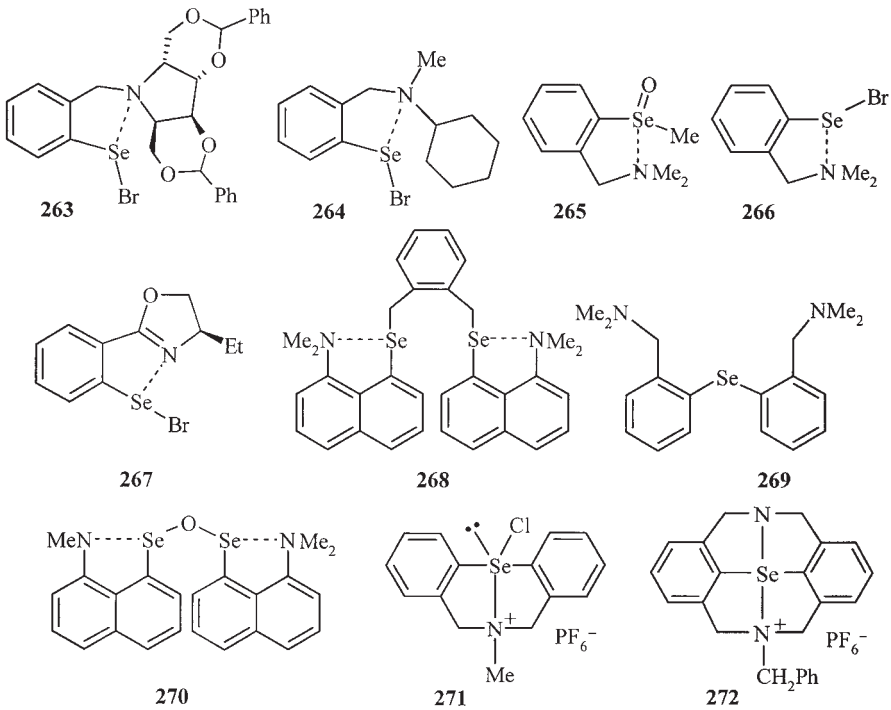

Scheme 41

Intramolecular interaction between selenium and nitrogen is the most frequently investigated one of all (Scheme 41). A favourable testbed are benzylamines with selenium in *ortho* position. An early report is the ^{77}Se chemical shift of $\delta = 1019$ found in the benzeneselenenyl bromide **263**, as compared to $\delta = 869$ for benzeneselenenyl bromide itself without the benzylamino residue. This large difference of 150 ppm cannot be explained unless by an interatomic Se · · · N contact.[376] Soon thereafter, even $^{77}Se,^{15}N$ couplings in the range of 13.0–59.3 Hz were reported in similar molecular systems like **264**.[377] An analogous interaction was also found for selenium in selenoxides (**265**).[148] Further interesting examples were contributed by Singh *et al.* e.g., the selenenyl bromide **266** and corresponding tribromides and diselenides[378] and oxazolines like the selenenyl bromide **267** as well as iodide and diselenide analogues.[358,379,380] The large ^{77}Se chemical shift ($\delta = 546$) of **268** as compared to that of **269** ($\delta = 341$) was taken as proof for the existence of an intramolecular Se · · · N interaction in **268**.[381] An unusually short Se · · · N

distance in **270**, as determined by X-ray diffraction, proves an intramolecular interaction and the hypervalency of the selenium atoms.[149] Finally, the fact that transannular oxidation reactions of **190** and **191** readily form selenazocins (such as **271**)[272] or diazaselenuranes (such as **272**),[273] respectively, is another proof for this type of interaction.

3.4.3. *Se · · · O interaction*

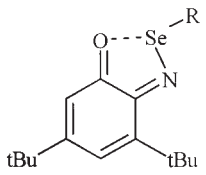

273 (R = Me: δ = 986)
274 (R = Ph: δ = 1064)
275 (R = Cl: δ = 1402)

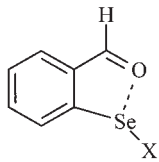

276

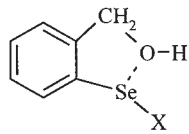

277

Scheme 42

Two examples of Se · · · O interaction are worth noting (Scheme 42). One is the selenoiminoquinone system **273**–**275**.[382] Here, its existence is taken from short intramolecular atom distances. Since proper molecules without such interaction are not available to compare with, it is not yet possible to say how the ^{77}Se chemical shifts reflect it. The second example involves *ortho*-selenated benzaldehydes **276** with X = Cl, Br, CN, SPh, SeAr, and Me.[383] The ^{17}O chemical shift of the formyl oxygen atom undergoes a significant deshielding when going from X = Cl to X = Me. This is opposite to what one would expect from an inductive effect of X upon the oxygen so that the existence of an intramolecular Se · · · O contact has to be postulated.[383] On the other hand, the ^{77}Se nuclei are shielded in the same series; from $\delta = 1114$ for X = Cl to $\delta = 260$ for X = Me. In addition, corresponding benzyl alcohols **277** were studied giving analogous but weaker effects.[383]

3.4.4. *Se · · · F interaction*

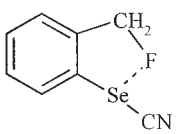

278

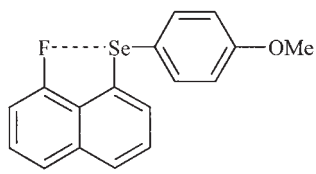

279

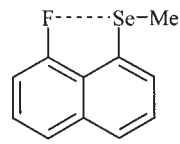

280

Scheme 43

It is not surprising that intramolecular Se · · · F interactions have been reported (Scheme 43). Here, the ^{77}Se,^{19}F coupling is an excellent monitoring parameter. J(^{77}Se,^{19}F)-values up to 84.2 Hz for the selenocyanate **278** are found; Se–Hal,

Se–R, Se–Ar derivatives give smaller but still significant coupling constants.[384] Calculation suggest that an $n_F \rightarrow \sigma^*_{Se-X}$ interaction (X = CN in **278**) is responsible.[385] Later, it has been shown that an analogous interaction exists in derivatives where fluorine is replaced by chlorine or bromine but it decreases with a lower electronegativity value of the halogen: Se···F > Se ···Cl > Se···Br.[386] A strong interaction involving the same orbitals produces a large $^{77}Se,^{19}F$ coupling in 1,8-disubstituted naphthalenes **279** and **280**: $J(^{77}Se,^{19}F) = 285.0$ and 276.7 Hz, respectively.[387] Moreover, the ^{77}Se nuclei experience a pronounced shielding when the fluorine atom is replaced by hydrogen. Thus, the Se···F interaction leads to ca. 90-ppm deshielding of the ^{77}Se nuclei in **279** and **280**.[387]

3.4.5. *Se···Se and Se···Te interaction*

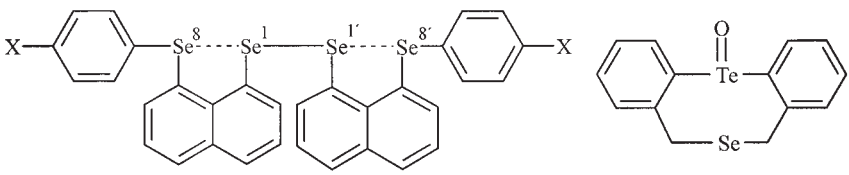

281 **282**

Scheme 44

An interesting type of a 4c–6e interaction between four linear selenium atoms was derived from inverse substituents effects of X (X = OMe, Me, H, Cl, Br, COOEt, and NO_2) and long-range $^{77}Se,^{77}Se$ coupling constants in *peri*-substituted bis(naphthyl) diselenides **281** (Scheme 44).[388,389] A bonding involving the p-orbitals of Se-8 and Se-8′ and the σ^* orbital of the Se-1–Se-1′ bond is invoked. Selenuranes,[298,301,390] such as **216** or **219** have been mentioned before; their synthesis is assisted by a transannular interaction. Finally, a strong unprecedented transannular interaction between selenium and tellurium in **282** is noteworthy, evidenced by an unusually large $^{125}Te,^{77}Se$ coupling of 467 Hz.[267]

3.5. Metal complexes

Papers containing ^{77}Se NMR data of metal complexes appear in the literature in increasing numbers. Their ^{77}Se chemical shifts cover the whole range of known values, from ca. −1000 to +1500 and the same holds for pertinent coupling constants.[1e] Although some trends can be deduced in certain compound families, a general view which would go beyond earlier summaries[1] or allow reliable ^{77}Se chemical shift prediction is not yet available and may be

the subject of a future review specially devoted to this topic. For the time being, the reader is referred to the comprehensive data collection of ^{77}Se NMR parameters[2] which covers the data of metal complexes up to the end of 1999.

REFERENCES

1. (a) H. C. E. McFarlane and W. McFarlane, *NMR of Newly Accessible Nuclei*, Vol. 2, P. Laszlo, ed., Academic Press, New York, 1983, p. 275; (b) M. Baiwir, *Proc. Int. Conf. Org. Chem. Selenium Tellurium*, 4th, B. Frank and W. R. McWhinnie, eds., Univ. Aston, Birmingham, UK, 1983, p. 406; (c) N. P. Luthra and J.D. Odom, *The Chemistry of Organic Selenium and Tellurium Compounds*, Vol. 1, S. Patai and Z. Rappoport, eds., Wiley, Chichester, 1986, p. 189; (d) H. C. E. McFarlane and W. McFarlane, *Multinuclear NMR*, J. Mason, ed., Plenum Press, New York, 1987, p. 417; (e) H. Duddeck, *Progr. NMR Spectrosc.*, 1995, **27**, 1; (f) T. M. Klapötke and M. Broschag, *Compilation of Reported ^{77}Se NMR Chemical shifts – Up to the Year 1994*, Wiley, Chichester, 1996.
2. H. Duddeck, *Chemical Shifts and Coupling Constants for Selenium-77*, Landolt-Börnstein, New Series, Volume III/35G, Springer, Berlin, Heidelberg, New York, 2004.
3. *Gmelin Handbook on Inorganic and Organometallic Chemistry*, 8th edition. Se. Selen. Selenium (System-Nr. 10). Springer, Berlin, Heidelberg, New York, 1949–1981.
4. (a) *Organic Selenium Compounds: Their Chemistry and Biology*, D. L. Klayman and W. H. H. Günther, eds., Wiley, New York, 1973; (b) *Organic Selenium and Tellurium Chemistry*, Y. Okamoto and W. H. H. Günther, eds., *Ann. N.Y. Acad. Sci.*, **192**, 1972; *Selenium*, R.A. Zingaro and W. C. Cooper eds., Van Nostrand Reinhold, New York, 1974.
5. (a) D. L. J. Clive, *Tetrahedron*, 1978, **34**, 1049; (b) H. J. Reich, *Acc. Chem. Res.*, 1979, **12**, 22; (c) A. Krief, *Tetrahedron*, 1980, **36**, 2531; (d) D. Liotta, *Acc. Chem. Res*, 1984, **17**, 28; (e) C. Paulmier, *Selenium Reagent and Intermediates in Organic Synthesis*, Pergamon Press, Oxford (1986); (f) *The Chemistry of Organic Selenium and Tellurium Compounds*, S. Patai and Z. Rappoport, eds., Wiley, Chichester, Vol. 1 (1986) and Vol. 2 (1987); (g) *Organoselenium Chemistry*, D. Liotta, ed., Wiley, New York, 1987.
6. A. Krief and L. Hevesi, *Organoselenium Chemistry I, Functional Group Transformation*, Springer, Berlin, Heidelberg, 1988.
7. (a) T. Wirth, *Tetrahedron*, 1999, **55**, 1; (b) T. Wirth ed., *Organoselenium Chemistry, Modern Developments in Organic Synthesis, Topics in Current Chemistry*; Vol. 208, Springer, Berlin, Heidelberg, New York, 2000.
8. (a) S. S. Dharmatti and H. E. Weaver, *Phys. Rev.*, 1952, **86**, 259; (b) H. E. Walchli, *Phys. Rev.*, 1953, **90**, 331.
9. (a) T. Birchall, R. J. Gillespie and S. L. Vekris, *Can. J. Chem.*, 1965, **43**, 1672; (b) P. Bucci, V. Bertini, G. Ceccarelli and A. De Munno, *Chem. Phys. Lett.*, 1967, **1**, 473; (c) W. McFarlane, *Mol. Phys.*, 1967, **12**, 243; (d) W. McFarlane, *Chem. Commun.*, 1968, 755; (e) R. A. Dwek, R. E. Richards, D. Taylor, G. J. Penney and G. M. Sheldrick, *J. Chem. Soc. [A]*, 1969, 935; (f) W. McFarlane, *J. Chem. Soc. A*, 1969, 670; (g) W. McFarlane and J. A. Nash, *J. Chem. Soc. D*, 1969, 913; (h) K. Olsson and S. O. Almqvist, *Acta Chem. Scand.*, 1969, **23**, 3271; (i) G. Pfisterer and H. Dreeskamp, *Ber. Bunsenges. Physikal. Chem.*, 1969, **73**, 654; (k) A. Bugge, B. Gestblom and O. Hartmann, *Acta Chem. Scand.*, 1970, **24**, 1953; (l) B. M. Dahl and P. H. Nielsen, *Acta Chem. Scand.*, 1970, **24**, 1468; (m) M. Lardon, *J. Am. Chem. Soc.*, 1970, **92**, 5063; (n) J. Morel and G. Martin, *Bull. Soc. Chim. France*, 1971, 4497.
10. (a) W. McFarlane and R. J. Wood, *J. Chem. Soc. Dalton Trans.*, 1972, 1397; (b) W. McFarlane and D. S. Rycroft, *J. Chem. Soc., Chem. Commun.*, 1972, 902; (c) W. McFarlane and D. S. Rycroft, *J. Chem. Soc. Dalton Trans.*, 1973, 2162.
11. J. Milne and A. J. Williams, *Inorg. Chem.*, 1992, **31**, 4534.

12. T. Fäcke, R. Wagner and S. Berger, *J. Org. Chem.*, 1993, **58**, 5475.
13. T. B. Schroeder, C. Job, M. F. Brown and R. S. Glass, *Magn. Reson. Chem.*, 1995, **33**, 191.
14. R. S. Glass, *Phosphorus Sulfur and Silicon*, 1998, **136–138**, 159.
15. F. Farooqui, M. Sabahi, T. B. Schroeder and R. S. Glass, *Scientia Iranica*, 1997, **4**, 121.
16. T. W.-M. Fan, A. N. Lane, D. Martens and R. M. Higashi, *Analyst*, 1998, **123**, 875.
17. R. Wu, G. Hernández, J. D. Odom, R. B. Dunlap and L. A. Silks, *J. Chem. Soc., Chem. Commun.*, 1996, 1125.
18. R. M. Michalczyk, J. G. Schmidt, E. Moody, Z. Li, R. Wu, R. B. Dunlap, J. D. Odom and L. A. Silks, III, *Angew. Chem. Int. Ed.*, 2000, **39**, 3067.
19. R. Marek, L. Králik and V. Sklenař, *Tetrahedron Lett.*, 1997, **38**, 665.
20. J. Šibor, D. Žůrek, R. Marek, M. Kutý, O. Humpa, J. Marek and P. Pazdera, *Coll. Czech. Chem. Commun.*, 1999, **64**, 1673.
21. F. Du, M. Liu, X. Miao, and L. Song, *Meas. Sci. Technol.*, 1999, **10**, 170; *Chem. Abstr.* 130:290452.
22. S. Malik, S. Moeller, G. Tóth, T. Gáti, M. I. Choudhary and H. Duddeck, *Magn. Reson. Chem.*, 2003, **41**, 455.
23. E. H. Mørkved, O. Bjørlo,W. Schilf and P. Bernatowicz, *Bull. Pol. Acad. Sci., Chem.*, 2000, **48**, 47. for a review see: T. Fäcke, R. Wagner and S. Berger, *Concepts Magn. Reson.*, 1994, **6**, 293.
24. H. Duddeck, P. Wagner and S. Gegner, *Tetrahedron Lett.*, 1985, **26**, 1205.
25. W. J. Boyko, F. J. Duarte and R. M. Giuliano, *Magn. Reson. Chem.*, 1994, **32**, 259.
26. B. M. Pinto, J. Sandoval-Ramirez and R. D. Sharma, *Tetrahedron Lett.*, 1985, **26**, 5235.
27. B. M. Pinto, B. D. Johnston, J. Sandoval-Ramirez and R. D. Sharma, *J. Org. Chem.*, 1988, **53**, 3766.
28. B. M. Pinto, B. D. Johnston and R. Nagelkerke, *Heterocycles*, 1989, **28**, 389.
29. B. Rys, H. Duddeck and M. Hiegemann, *J. Heterocycl. Chem.*, 1992, **29**, 967.
30. R. H. Mitchell and K. S. Weerawarna, *Tetrahedron Lett.*, 1988, **29**, 5587.
31. M. Hojjatie, S. Muralidharan and H. Freiser, *Tetrahedron*, 1989, **45**, 1611.
32. H. Fujihara, T. Uehara, T. Erata and N. Furukawa, *Chem. Lett.*, 1993, 263.
33. M. Iwaoka, H. Komatsu and S. Tomoda, *Bull. Chem. Soc. Jap.*, 1996, **69**, 1825.
34. M. Koketsu, M. Ishida, N. Takamura and H. Ishihara, *J. Org. Chem.*, 2002, **67**, 486.
35. H. J. Reich, B. Ö. Gudmundsson and R. R. Dykstra, *J. Am. Chem. Soc.*, 1992, **114**, 7937.
36. H. J. Reich, B. Ö. Gudmundson, D. P. Green, M. J. Bevan, I. L. Reich and H. J. Reich, *Helv. Chim. Acta.*, 2002, **85**, 3748.
37. M. A. Ansari, C. H. Mahler and J. A. Ibers, *Inorg. Chem.*, 1989, **28**, 2669.
38. J. P. Fackler, Jr. and W.-H. Pan, *J. Am. Chem. Soc.*, 1979, **101**, 1607.
39. A. M. Bond, R. Colton and P. Panagiotidou, *Organometallics*, 1988, **7**, 1767.
40. (a) H. Duddeck, S. Malik, T. Gáti, G. Tóth and M. I. Choudhary, *Magn. Reson. Chem.*, 2002, **40**, 153; (b) S. Malik, S. Moeller, G. Tóth, T. Gáti, M. I. Choudhary and H. Duddeck, *Magn. Reson. Chem.*, 2003, **41**, 455.
41. P. J. Barrie, R. J. H. Clark, D.-Y. Chung, D. Chakrabarty and M. G. Kanatzidis, *Inorg. Chem.*, 1995, **34**, 4299.
42. H. Haas and M. Jansen, *Z. Anorg. Allg. Chem.*, 2000, **626**, 1174.
43. X. Hou and R. J. Kirkpatrick, *Chem. Mater.*, 2000, **12**, 1890.
44. C. Milne and J. Milne, *Can. J. Chem.*, 1996, **74**, 1889.
45. R. Maxwell, D. Lathrop and H. Eckert, *J. Non-Cryst. Solids*, 1995, **180**, 244.
46. T. Pietraß, R. Seydoux, R. E. Roth, H. Eckert and A. Pines, *Solid State Nucl. Magn. Reson.*, 1997, **8**, 265.
47. G. Balzer, H. Duddeck, U. Fleischer and F. Röhr, *Fresenius J. Analyt. Chem.*, 1997, **357**, 473.
48. (a) For reviews see: M. J. Porzebowski, *Wiad. Chem.*, 1995, **49**, 777 (in Polish); (b) M. J. Porzebowski, *Bull. Pol. Acad. Sci. Chem.*, 1998, **46**, 61.
49. M. J. Porzebowski, M. Michalska, J. Blaszczyk, M. W. Wieczorek, W. Ciesielski, S. Kazmierski and J. Pluskowski, *J. Org. Chem.*, 1995, **60**, 3139.

50. M. Porzebowski, R. Katarzynski and W. Cieselski, *Magn. Reson. Chem.*, 1999, **37**, 173.
51. M. J. Porzebowski, *Magn. Reson. Chem.*, 1995, **33**, 8.
52. M. J. Porzebowski, G. Grossmann, J. Blaszczyk, M. W. Wieczorek, J. Sieler, P. Knopik and H. Komber, *Inorg. Chem.*, 1994, **33**, 4688.
53. M. J. Porzebowski, J. Blaszczyk, M. W. Wieczorek and J. Klinowski, *J. Phys. Chem. A*, 1997, **101**, 8077.
54. M. J. Porzebowski, J. Blaszczyk, W. R. Majzner, M. W. Wieczorek, J. Baraniak and W. J. Stec, *Solid State Nucl. Magn. Reson.*, 1998, **11**, 215.
55. M. J. Porzebowski, J. Blaszczyk, M. W. Wieczorek, K. Misiura and W. J. Stec, *J. Chem. Soc., Perkin Trans. 2*, 1997, 163.
56. G. Grossmann, M. J. Porzebowski, U. Fleischer, K. Kruger, O. L. Malkina and W. Ciesielski, *Solid State Nucl. Magn. Reson.*, 1998, **13**, 71.
57. G. Großmann, G. Ohms, K. Krüger, K. Karaghiosoff, K. Eckstein, J. Hahn, A. Hopp, O. L. Malkina and P. Hrobarik, *Z. Anorg. Allg. Chem.*, 2001, **627**, 1269.
58. H. Nakatsuji, T. Higashioji and M. Sugimoto, *Bull. Chem. Soc. Jap.*, 1993, **66**, 3235.
59. P. D. Ellis, J. D. Odom, A. S. Lipton, Q. Chen and J. M. Gulick, *NATO ASI Ser., Ser. C*, 1993, **386**, 386.
60. G. Magyarfalvi and P. Pulay, *Chem. Phys. Lett.*, 1994, **225**, 280.
61. (a) M. Bühl, J. Gauss and J. F. Stanton, *Chem. Phys. Lett.*, 1995, **241**, 248; (b) M. Bühl, W. Thiel, U. Fleischer and W. Kutzelnigg, *J. Phys. Chem.*, 1995, **99**, 4000.
62. G. Schreckenbach, Y. Ruiz-Morales and T. Ziegler, *J. Chem. Phys.*, 1996, **104**, 8605.
63. (a) W. Nakanishi and S. Hayashi, *Chem. Lett.*, 1998, 523; (b) W. Nakanishi and S. Hayashi, *J. Phys. Chem. A*, 1999, **103**, 6074.
64. (a) W. Nakanishi, S. Hayashi and H. Kihara, *J. Org. Chem.*, 1999, **64**, 2630; (b) W. Nakanishi and S. Hayashi, *J. Organomet. Chem.*, 2000, **611**, 178.
65. G. Grossmann, D. Scheller, O. L. Malkina, V. G. Malkin, G. Zahn, H. Schmitt and U. Haeberlen, *Solid State Nucl. Magn. Reson.*, 2000, **17**, 22.
66. J. Komulainen, R. S. Laitinen and R. J. Suontamo, *Can. J. Chem.*, 2002, **80**, 1435.
67. E. Block, M. Birringer, R. DeOrazio, J. Fabian, R. S. Glass, C. Guo, C. He, E. Lorance, Q. Qian, T. B. Schroeder, Z. Shan, M. Thiruvazhi, G. S. Wilson and X. Zhang, *J. Am. Chem. Soc.*, 2000, **122**, 5052.
68. P. J. Wilson, *Mol. Phys.*, 2001, **99**, 363.
69. N. P. Luthra, D. B. Dunlap and J. D. Odom, *J. Magn. Reson.*, 1983, **52**, 318.
70. J. Milne, *Magn. Reson. Chem.*, 1993, **31**, 652.
71. K. I. Doudin, N. A. Fröystein and J. Songstad, *Magn. Reson. Chem.*, 2000, **38**, 975.
72. C. J. Jameson and A. K. Jameson, *Chem. Phys. Lett.*, 1987, **135**, 254.
73. (a) H. A. Stefani, I. P. de Arruda Campos, L. C. Roque and A. L. Braga, *J. Chem. Res. (S)*, 1994, 112; (b) I. P. de Arruda Campos, H. A. Stefani, L. C. Roque, M. A. Montoro and A. L. Braga, *J. Chem. Res. (S)*, 1995, 112; (c) I. P. de Arruda Campos and H. A. Stefani, *Phosphorus Sulfur, and Silicon*, 1995, **105**, 73; (d) J. V. Comasseto, P. H. Menezes, H. A. Stefani, G. Zeni and A. L. Braga, *Tetrahedron*, 1996, **52**, 9687.
74. H. Binder, I. Duttlinger, H. Loos, K. Locke, A. Pfitzner, H.-J. Flad, A. Savin and M. Kohout, *Z. Anorg. Allg. Chem.*, 1995, **621**, 400.
75. C. Nachtigal, B. Steuer and W. Preetz, *Chem. Ber.*, 1996, **129**, 1531.
76. A. Cruz, D. Macias-Mendoza, E. Barragan-Rodriguez, H. Tlahuext, H. Noth and R. Contreras, *Tetrahedron: Asymm.*, 1997, **8**, 3903.
77. (a) H. Fußstetter, H. Nöth and B. Wrackmeyer, *Chem. Ber.*, 1977, **110**, 3172; (b) R. Köster, G. Seidel, R. Boese and B. Wrackmeyer, *Chem. Ber.*, 1988, **121**, 1955.
78. (a) D. E. J. Arnold, J. S. Dryburgh, E. A. V. Ebsworth and D. W. H. Rankin, *J. Chem. Soc., Dalton Trans.*, 1972, 2518; (b) A. Haas, R. Süllentrup and C. Krüger, *Z. Anorg. Allg. Chem.*, 1993, **619**, 819.
79. H. Poleschner, M. Heydenreich and U. Schilde, *Eur. J. Org. Chem.*, 2000, 1307.

80. H. Lange and U. Herzog, *J. Organomet. Chem.*, 2002, **660**, 36.
81. U. Herzog, *J. Prakt. Chem.*, 2000, **342**, 379.
82. A. G. Brook, R. Kumarathasan and A. J. Lough, *Organometallics*, 1994, **13**, 424.
83. P. Boudjouk, E. Black, R. Kumarathasan, U. Samaraweera, S. Castellino, J. P. Oliver and J. W. Kampf, *Organometallics*, 1994, **13**, 3715.
84. U. Herzog and G. Rheinwald, *J. Organomet. Chem.*, 2001, **627**, 23.
85. U. Herzog, U. Böhme, E. Brendler and G. Rheinwald, *J. Organomet. Chem.*, 2001, **630**, 139.
86. U. Herzog and G. Rheinwald, *Organometallics*, 2001, **20**, 5369.
87. U. Herzog, G. Rheinwald and H. Borrmann, *J. Organomet. Chem.*, 2002, **660**, 27.
88. U. Herzog and G. Rheinwald, *Eur. J. Inorg. Chem.*, 2001, 3107.
89. M. Unno, Y. Kawai, H. Shioyama and H. Matsumoto, *Organometallics*, 1997, **16**, 4428.
90. K. Kishikawa, N. Tokitoh and R. Okazaki, *Organometallics*, 1997, **16**, 5127.
91. N. Nakata, N. Takeda and N. Tokitoh, *Chem. Lett.*, 2002, 818.
92. W. Ando, S. Watanabe and N. Choi, *J. Chem. Soc., Chem. Commun.*, 1995, 1683.
93. (a) T. Matsumoto, N. Tokitoh and R. Okazaki, *Angew. Chem., Int. Ed. Engl.*, 1994, **33**, 2339; (b) T. Matsumoto, N. Tokitoh and R. Okazaki, *J. Am. Chem. Soc.*, 1999, **121**, 8811.
94. R. Okazaki and N. Tokitoh, *Acc. Chem. Res.*, 2000, **33**, 625.
95. G. Ossig, A. Meller, C. Broenneke, O. Mueller, M. Schaefer and R. Herbst-Irmer, *Organometallics*, 1997, **16**, 2116.
96. T. Thompson, S. D. Pastor and G. Rihs, *Inorg. Chem.*, 1999, **38**, 4163.
97. R. Laitinen and T. Chivers, *Chem. Commun.*, 2002, 1812.
98. T. Chivers, M. Parvez and G. Schatte, *Inorg. Chem.*, 1996, **35**, 4094.
99. T. Maaninen, T. Chivers, R. Laitinen and E. Wegelius, *Chem. Comm.*, 2000, 759.
100. J. Siivari, A. Maaninen, E. Haapaniemi, R. S. Laitinen and T. Chivers, *Z. Naturforsch.*, 1995, **50b**, 1575.
101. T. Nothegger, K. Wurst, M. Probst and F. Sladky, *Chem. Ber.*, 1997, **130**, 119.
102. A. Maaninen, T. Chivers, R. Laitinen, G. Schatte and M. Nissinen, *Inorg. Chem.*, 2000, **39**, 5341.
103. A. Maaninen, J. Konu, R. S. Laitinen, T. Chivers, G. Schatte, J. Pietikaeinen and M. Ahlgren, *Inorg. Chem.*, 2001, **40**, 3539.
104. A. Maaninen, M. Ahlgren, P. Ingman and R. S. Laitinen, *Phosphorus Sulfur Silicon Relat. Elem.*, 2001, **169**, 161.
105. A. Maaninen, R. S. Laitinen, T. Chivers and T. A. Pakkanen, *Inorg. Chem.*, 1999, **38**, 3450.
106. K. M. Enikeev, E. V. Bayandina, I. É. Ismaev, N. A. Buina, A. V. Il'yasov and I. A. Nuretdinov, *Zh. Obshch. Khim*, 1983, **53**, 2143, *Chem. Abstr.*, 1984, **100**, 22721.
107. J. R. Goerlich, H. Thönnessen, P. G. Jones and R. Schmutzler, *Phosphorus Sulfur*, 1996, **114**, 143.
108. K. Karaghiosoff, personal communication, 1994.
109. K. Karaghiosoff and M. Schuster, *Phosphorus Sulfur Silicon Relat. Elem.*, 2001, **168–169**, 117.
110. A. Schmidpeter, G. Jochem, K. Karaghiosoff and C. Robl, *Angew. Chem., Int. Ed. Engl.*, 1992, **31**, 1350.
111. M. Yoshifuji, S. Sangu, K. Kamijo and K. Toyota, *J. Chem. Soc., Chem. Commun.*, 1995, 297.
112. M. Yoshifuji, M. Hirano and K. Toyota, *Tetrahedron Lett.*, 1993, **34**, 1043.
113. M. Yoshifuji, S. Angu, K. Kamijo and K. Toyota, *Chem. Ber.*, 1996, **129**, 1049.
114. R. P. Davies and M. G. Martinelli, *Inorg. Chem.*, 2002, **41**, 348.
115. P. Jutzi, N. Brusdeilins, H.-G. Stammler and B. Neumann, *Chem. Ber.*, 1994, **127**, 997.
116. P. Loennecke and R. Blacknik, *Phosphorus Sulfur Silicon Rel. Elem.*, 1997, **131**, 191.
117. P. B. Hitchcock, J. F. Nixon and N. Sakarya, *Chem. Commun.*, 2000, 1745.
118. W. Gombler, *Z. Naturforsch.*, 1981, **36B**, 535.
119. B. W. Tattershall, R. Blachnik and H. P. Baldus, *J. Chem. Soc., Dalton Trans.*, 1989, 977.
120. G. G. Briand, T. Chivers and M. Parvez, *J. Chem. Soc., Dalton Trans.*, 2002, 3785.
121. W. Czado and U. Müller, *Z. Anorg. Allg. Chem.*, 1998, **624**, 239.

122. D. M. Smith, M. A. Pell and J. A. Ibers, *Inorg. Chem*., 1998, **37**, 2340.
123. M. A. Ansari, W. T. Pennington and J. A. Ibers, *Polyhedron*, 1992, **11**, 1877.
124. D. M. Smith, C.-W. Park and J. A. Ibers, *Inorg. Chem*., 1996, **35**, 6682.
125. T. Kanda, K. Mizoguchi, S. Kagohashi and S. Kato, *Organometallics*, 1998, **17**, 1487.
126. J. Gailer, G. N. George, H. H. Harris, I. J. Pickering, R. C. Prince, A. Somogyi, G. Buttigieg, R. S. Glass and M. B. Denton, *Inorg. Chem*., 2002, **41**, 5426.
127. C. Rosenhahn, S. E. Hayes, B. Rosenhahn and H. Eckert, *J. Non-Cryst. Solids*, 2001, **284**, 1.
128. D. M. Smith, T. E. Albrecht-Schmitt and J. A. Ibers, *Angew. Chem., Int. Ed. Engl*., 1998, **37**, 1089.
129. N. Tokitoh, T. Sasamori and R. Okazaki, *Chem. Lett*., 1998, 725.
130. D. M. Smith, C.-W. Park and J. A. Ibers, *Inorg. Chem*., 1997, **36**, 3798.
131. T. Birchall, R. J. Gillespie and S. L. Vekris, *Can. J. Chem*., 1965, **43**, 1672.
132. M. Lamoureux and J. Milne, *Polyhedron*, 1990, **9**, 589.
133. W. Koch, O. Lutz and A. Nolle, *Z. Naturforsch*., 1978, **33A**, 1025.
134. M. J. Collins, C. I. Ratcliffe and J. A. Ripmeester, *J. Magn. Reson*., 1986, **68**, 172.
135. A. Haas and K. Schinkel, *Chem. Ber*., 1990, **123**, 685.
136. R. Damerius, P. Huppmann, D. Lentz and K. Seppelt, *J. Chem. Soc., Dalton Trans*., 1984, 2821.
137. H. Haas and M. Jansen, *Z. Anorg. Allg. Chem*., 2001, **627**, 1313.
138. O. Lutz, *The Multinuclear Approach to NMR Spectroscopy*, J.B. Lambert and F. G. Riddell, eds., Reidel, Dordrecht, 1983, p. 389.
139. W. McFarlane and R. J. Wood, *J. Chem. Soc. Dalton Trans*., 1972, 1397.
140. W. Gombler, *Z. Naturforsch*., 1981, **36B**, 535.
141. L. Henriksen and N. Stuhr-Hansen, *Phosphorus Sulfur Silicon Rel. Elem*., 1998, **136–138**, 175.
142. T. Shimizu, Y. Nakashima, I. Watanabe, K. Hirabayashi and N. Kamigata, *J. Chem. Soc., Perkin Trans. 1*, 2002, 2151.
143. G. Knothe, R. S. Glass, T. J. Schroeder, M. O. Bagby and D. Weisleder, *Synthesis*, 1997, 57.
144. M. A. Cooper and A. D. Ward, *Aust. J. Chem*., 1997, **50**, 181.
145. T. Matsui, J. Nakayama, N. Sato, Y. Sugihara, A. Ishii and S. Kumakura, *Phosphorus Sulfur*, 1996, **118**, 227.
146. T. Takahashi, N. Nakao and T. Koizumi, *Tetrahedron: Asymm*., 1997, **8**, 3293.
147. K. Kobayashi, S. Shinhara, M. Moriyama, T. Fujii, E. Horn, A. Yabe and N. Furukawa, *Tetrahedron Lett*., 1999, **40**, 5211.
148. T. Shimizu, M. Enomoto, H. Taka and N. Kamigata, *J. Org. Chem*., 1999, **64**, 8242.
149. H. Fujihara, H. Tanaka and N. Furukawa, *J. Chem. Soc., Perkin Trans. 2*, 1995, 2375.
150. T. Saiki, K. Goto and R. Okazaki, *Angew. Chem., Int. Ed. Engl*., 1997, **36**, 2223.
151. H. Fujihara, H. Tanaka and N. Furukawa, *J. Chem. Soc., Perkin Trans. 2*, 1995, 2375.
152. A. J. Blake, V. Consterdine, M. F. A. Dove, S. Lammas and L. H. Thompson, *J. Chem. Soc., Dalton Trans*., 1998, 3.
153. R. S. Laitinen, P. Pekonen and R. J. Suontamo, *Coord. Chem. Rev*., 1994, **130**, 1.
154. A. K. Verma and T. B. Rauchfuss, *Inorg. Chem*, 1995, **34**, 6199.
155. P. Pekonen, J. Taavitsainen and R. S. Laitinen, *Acta Chem. Scand*., 1998, **52**, 1188.
156. A. Maaninen, T. Chivers, M. Parvez, J. Pietikaeinen and R. S. Laitinen, *Inorg. Chem*., 1999, **38**, 4093.
157. J. Komulainen, R. S. Laitinen and R. J. Suontamo, *Can. J. Chem*., 2002, **80**, 1435.
158. J. J. Pietikäinen and R. S. Laitinen, *Phosphorus Sulfur and Silicon*, 1997, **124&125**, 453.
159. A. Maaninen, J. Siivari, R. J. Suontamo, J. Konu, R. S. Laitinen and T. Chivers, *Inorg. Chem*., 1997, **36**, 2170.
160. J. Hahn and R. Klünsch, *Angew. Chem., Int. Ed. Engl*., 1994, **34**, 1770.
161. N. Furukawa, *Phosphorus Sulfur and Silicon*, 1998, **136–138**, 43.
162. H. Fujihara, R. Akaishi, T. Erata and N. Furukawa, *J. Chem. Soc., Chem. Commun*., 1989, 1789.

163. A. B. Bergholdt, K. Kobayashi, E. Horn, O. Takahashi, S. Sato, N. Furukawa, M. Yokoyama and K. Yamaguchi, *J. Am. Chem. Soc.*, 1998, **120**, 1230.
164. H. Naka, M. Shindo, T. Maruyama, S. Sato and N. Furukawa, *Chem. Lett.*, 1999, 723.
165. J. Passmore, T. S. Cameron, P. D. Boyle, G. Schatte and T. Way, *Can. J. Chem.*, 1996, **74**, 1671.
166. W. Czado, M. Maurer and U. Mueller, *Z. Anorg. Allg. Chem.*, 1998, **624**, 1871.
167. S. Brownridge, L. Calhoun, R. S. Laitinen, J. Passmore, J. Pietikainen and J. Saunders, *Phosphorus Sulfur Silicon Relat. Elem.*, 2001, **168**, 105.
168. C. Lau, B. Neumüller, W. Hiller, M. Herker, S. F. Vyboishchikov, G. Frenking and K. Dehnicke, *Chem. Eur. J.*, 1996, **2**, 1373.
169. M. Broschag, T. M. Klapötke, I. C. Tornieporth-Oetting and P. S. White, *J. Chem. Soc., Chem. Commun.*, 1992, 1390.
170. R. Wollert, A. Höllwarth, G. Frenking, D. Fenske, H. Goesmann and K. Dehnicke, *Angew. Chem. Int. Ed. Engl.*, 1992, **31**, 1251.
171. P. G. Jones and M. C. Ramírez des Arellano, *Chem. Ber.*, 1995, **128**, 741.
172. W. Nakanishi, S. Hayashi, H. Tukada and H. Iwamura, *J. Phys. Org. Chem.*, 1990, **3**, 358.
173. W. Nakanishi, Y. Yamamoto, S. Hayashi, H. Tukada and H. Iwamura, *J. Phys. Org. Chem.*, 1990, **3**, 369.
174. W. Nakanishi, S. Hayashi and H. Kihara, *J. Org. Chem.*, 1999, **64**, 2630.
175. W. Nakanishi and S. Hayashi, *Chem. Lett.*, 1995, 75.
176. W. Nakanishi and S. Hayashi, *J. Organomet. Chem.*, 2000, **611**, 178.
177. M. Arca, F. Demartin, F. A. Devillanova, A. Garau, F. Isaia, V. Lippolis, S. Piludu and G. Verani, *Polyhedron*, 1998, **17**, 3111.
178. N. Kuhn, T. Kratz and G. Henkel, *Chem. Ber.*, 1994, **127**, 849.
179. N. Kuhn, G. Henkel and T. Kratz, *Z. Naturforsch.*, 1993, **48B**, 973.
180. W. Bocian, J. Jazwinski and L. Stefaniak, *Pol. J. Chem.*, 1995, **69**, 85.
181. J. D. Odom, W. H. Dawson and P. D. Ellis, *J. Am. Chem. Soc.*, 1979, **101**, 5815.
182. E. S. Lewis, T. I. Yousaf and T. A. Douglas, *J. Am. Chem. Soc.*, 1987, **109**, 2152.
183. B. M. Jacobson, A. M. Kook and E. S. Lewis, *J. Phys. Org. Chem.*, 1989, **2**, 410.
184. A. Krief, C. Delmotte and W. Dumont, *Tetrahedron Lett.*, 1997, **38**, 3079.
185. W. Clegg, R. P. Davies, R. Snaith and A. E. H. Wheatley, *Eur. J. Org. Chem.*, 2001, 1411.
186. M. Niemeyer and P. P. Power, *Inorg. Chim. Acta*, 1997, **263**, 201.
187. J. Laube, S. Jäger and C. Thöne, *Eur. J. Inorg. Chem.*, 2000, 1983.
188. L. Christiaens, J. L. Piette, L. Laitem, M. Baiwir, J. Denoel and G. Llabres, *Org. Magn. Reson.*, 1976, **8**, 354.
189. H. Kageyama, K. Tani, S. Kato and T. Kanda, *Heteroatom Chem.*, 2001, **12**, 250.
190. M. Koketsu, S. Hiramatsu and H. Ishihara, *Chem. Lett.*, 1999, 485.
191. Y. Kawahara, S. Kato, T. Kanda and T. Murai, *Bull. Chem. Soc. Jap.*, 1994, **67**, 1881.
192. H. Poleschner, R. Radeglia and J. Fuchs, *J. Organomet. Chem.*, 1992, **427**, 213.
193. M. A. Lucas and C. H. Schiesser, *J. Org. Chem.*, 1996, **61**, 5754.
194. C. H. Schiesser and M. A. Skidmore, *J. Org. Chem.*, 1998, **63**, 5713.
195. M. Koketsu, M. Ishida, N. Takamura and H. Ishihara, *J. Org. Chem.*, 2002, **67**, 486.
196. S. Kato, T. Kawachi, K. Ibi, S. Nakaiida, K. Kawai, T. Kanda, T. Murai and H. Ishihara, *Heteroatom Chem.*, 1995, **6**, 215.
197. (a) R. Okazaki, N. Tokitoh, A. Ishii, N. Ishii, Y. Matsuhashi, T. Matsumoto and H. Suzuki, *Phosphorus Sulfur Silicon Relat. Elem.*, 1992, **67**, 49; (b) N. Takeda, N. Tokitoh and R. Okazaki, *Tetrahedron*, 1997, **53**, 12167.
198. T. Murai, K. Kakami, A. Hayashi, T. Komuro, H. Takada, M. Fujii, T. Kanda and S. Kato, *J. Am. Chem. Soc.*, 1997, **119**, 8592.
199. W. Gombler, *Z. Naturforsch.*, 1981, **36B**, 1561.
200. T. C. Wong, F. S. Guziec and C. A. Moustakis, *J. Chem. Soc., Perkin Trans. 2*, 1983, 1471.

201. A. Haas and M. Spehr, *Chimia*, 1988, **42**, 265. see also: J. Grobe, D. L. Van and J. Welzel, *J. Organomet. Chem*., 1990, **386**, 321.
202. K. Kobayashi, H. Tukada, K. Kikuchi and I. Ikemoto, *Bull. Chem. Soc. Jap*., 1986, **59**, 1741.
203. E. R. Cullen, F. S. Guziec, C. J. Murphy, T. C. Wong and K. K. Andersen, *J. Am. Chem. Soc*., 1981, **103**, 7055.
204. E. R. Cullen, F. S. Guziec, Jr., C. J. Murphy, T. C. Wong and K. K. Andersen, *J. Chem. Soc., Perkin Trans. 2*, 1982, 473.
205. D. E. J. Arnold, S. Cradock, E. A. V. Ebsworth, J. D. Murdoch, D. W. H. Rankin, R. K. Harris and B. J. Kimber, *J. Chem. Soc., Dalton Trans*., 1981, 1349.
206. K. Tani, T. Murai and S. Kato, *J. Am. Chem. Soc*., 2002, **124**, 5960.
207. J. Nakayama, T. Kitahara, Y. Sugihara, A. Sakamoto and A. Ishii, *J. Am. Chem. Soc*., 2000, **122**, 9120.
208. T. Murai, H. Ende, M. Ozaki and S. Kato, *J. Org. Chem*., **64**, 2130.
209. T. Murai, K. Kakami, A. Hayashi, T. Komuro, H. Takada, M. Fujii, T. Kanda and S. Kato, *J. Am. Chem. Soc*., 1997, **119**, 8592.
210. D. H. R. Barton and G. Fontana, *Tetrahedron*, 1996, **52**, 11163.
211. H. Blau, J. Grobe, D. Le Ven, B. Krebs and M. Läge, *Chem. Ber*., 1997, **130**, 913.
212. G. M. Li and R. A. Zingaro, *J. Chem. Soc., Perkin Trans. 1*, 1998, 647.
213. R. Kaminski, R. S. Glass and A. Skowronska, *Synthesis*, 2001, 1308.
214. M. Koketsu, M. Kanoh, E. Itoh and H. Ishihara, *J. Org. Chem*., 2001, **66**, 4099.
215. T. Murai, Y. Mutoh and S. Kato, *Org. Lett*., 2001, **3**, 1993.
216. T. Murai, H. Aso and S. Kato, *Org. Lett*., 2002, 1407.
217. W. Manz and G. Gattow, *Z. Anorg. Allg. Chem*., 1994, **620**, 151.
218. T. Murai, T. Mori and S. Kato, *Synlett*, 1998, 619.
219. M. J. Milewska and T. Połoński, *Tetrahedron: Asymm*., 1999, **10**, 4123.
220. S. Gronowitz, I. Johnson and A. B. Hörnfeldt, *Chem. Scr*., 1973, **3**, 94.
221. S. Gronowitz, I. Johnson and A. B. Hörnfeldt, *Chem. Scr*., 1975, **8**, 8.
222. M. Baiwir, G. Llabres, L. Christiaens and J. L. Piette, *Org. Magn. Reson*., 1981, **16**, 14.
223. M. Baiwir, G. Llabres, L. Christiaens, M. Evers and J. L. Piette, *Magn. Reson. Chem*., 1987, **25**, 129.
224. M. Baiwir, G. Llabres, L. Christiaens and J. L. Piette, *Org. Magn. Reson*., 1982, **18**, 33.
225. J. E. Lyons, C. H. Schiesser and K. Sutej, *J. Org. Chem*., 1993, **58**, 5632.
226. T. Kataoka, E. Honda, T. Iwamura, T. Iwama and S.-i. Watanabe, *J. Chem. Soc., Perkin Trans. 1*, 1999, 1155.
227. E. Honda, T. Iwamura, S.-i. Watanabe, T. Kataoka, O. Muraoka and G. Tanabe, *J. Chem. Soc., Perkin Trans. 1*, 2001, 529.
228. A. Levy, U. Biedermann, S. Cohen and I. Agranat, *Phosphorus Sulfur and Silicon*, 1998, **136–138**, 139.
229. A. Levy, U. Biedermann, S. Cohen and I. Agranat, *J. Chem. Soc., Perkin Trans. 2*, 2000, 725.
230. A. Levy and I. Agranat, *Tetrahedron Lett*., 2000, **41**, 6157.
231. M. Koketsu, Y. Miyajima and H. Ishihara, *Chem. Lett*., 1998, 645.
232. E. Block, M. Birringer and C. He, *Angew. Chem., Int. Ed. Engl*., 1999, **38**, 1604.
233. E. Block, M. Birringer, R. DeOrazio, J. Fabian, R. S. Glass, C. Guo, C. He, E. Lorance, Q. Qian, T. B. Schroeder, Z. Shan, M. Thiruvazhi, G. S. Wilson and X. Zhang, *J. Am. Chem. Soc*., 2000, **122**, 5052.
234. K. B. Borisenko, M. Broschag, I. Hargittai, T. M. Klapötke, D. Schröder, A. Schulz, H. Schwarz, I. C. Tornieporth-Oetting and P. S. White, *J. Chem. Soc., Dalton Trans*., 1994, 2705.
235. K. Okuma and T. Kubota, *Tetrahedron Lett*., 2001, **42**, 3881.
236. N. V. Onyamboko, M. Renson, S. Chapelle and P. Granger, *Org. Magn. Reson*., 1982, **19**, 74.

237. K. Geisler, A. Jacobs, A. Künzler, M. Mathes, I. Girrleit, B. Zimmermann, E. Bulka, W.-D. Pfeiffer and P. Langer, *Synlett*, 2002, 1983.
238. H. Duddeck, R. Bradenahl, L. Stefaniak, J. Jazwinski and B. Kamienski, *Magn. Reson. Chem*., 2001, **39**, 709.
239. H. Duddeck and P.W. Tjondropurnomo, unpublished results.
240. (a) H. Duddeck, P. Wagner, D. Müller and J. Cz. Jászbérenyi, *Magn. Reson. Chem*., 1999, **28**, 549; (b) H. Duddeck and T. Hotopp, *Magn. Reson. Chem*., 1995, **33**, 490.
241. S. Grivas, *Curr. Org. Chem*., 2000, **4**, 707.
242. M. Edin and S. Grivas, *ARKIVOC*, 2001, **2**, 1036.
243. A. Ishii, C. Tsuchiya, T. Shimada, K. Furusawa, T. Omata and J. Nakayama, *J. Org. Chem*., 2000, **65**, 1799.
244. W. Levason, S. D. Orchard and G. Reid, *Coord. Chem. Rev*., 2002, **225**, 159.
245. W. Levason, J. J. Quirk, G. Reid and C. S. Frampton, *Inorg. Chem*., 1994, **33**, 6120.
246. R. Champness, P. F. Kelly, W. Levason, G. Reid, A. M. Z. Slawin and D. J. Williams, *Inorg. Chem*., 1995, **34**, 651.
247. R. Champness, W. Levason, J. J. Quirk, G. Reid and C. S. Frampton, *Polyhedron*, 1995, **14**, 2753.
248. W. Levason, J. J. Quirk and G. Reid, *J. Chem. Soc., Dalton Trans*., 1996, 3713.
249. W. Levason, J. J. Quirk, G. Reid and S. M. Smith, *J. Chem. Soc., Dalton Trans*., 1997, 3719.
250. G. Booth, W. Levason, J. J. Quirk, G. Reid and S. M. Smith, *J. Chem. Soc., Dalton Trans*., 1997, 3493.
251. K. Davies, M. C. Durrant, W. Levason, G. Reid and R. L. Richards, *J. Chem. Soc., Dalton Trans*., 1999, 1077.
252. I. Cordova-Reyes, E. VandenHoven, A. Mohamed and B. M. Pinto, *Can. J. Chem*., 1995, **73**, 113.
253. M. Pinto, R. J. Batchelor, B. D. Johnston, F. W. B. Einstein and I. D. Gay, *J. Am. Chem. Soc*., 1988, **110**, 2990.
254. R. J. Batchelor, F. W. B. Einstein, I. D. Gay, J. H. Gu, B. D. Johnston and B. M. Pinto, *J. Am. Chem. Soc*., 1989, **111**, 6582.
255. B. M. Pinto, B. D. Johnston, R. J. Batchelor, F. W. B. Einstein and I. D. Gay, *Can. J. Chem*., 1988, **66**, 2956.
256. R. J. Batchelor, F. W. B. Einstein, I. D. Gay, J. H. Gu and B. M. Pinto, *J. Organomet. Chem*., 1991, **411**, 147.
257. R. J. Batchelor, F. W. B. Einstein, I. D. Gay, J.-H. Gu, S. Mehta, B. M. Pinto and X.-M. Zhou, *Inorg. Chem*., 2000, **39**, 2558.
258. R. J. Batchelor, F. W. B. Einstein, I. D. Gay, J.-H. Gu, B. M. Pinto and X.-M. Zhou, *Can. J. Chem*., 2000, **78**, 598.
259. R. D. Adams, K. T. McBride and R. D. Rogers, *Organometallics*, 1995, **16**, 3895.
260. C. Bornet, R. Amardeil, R. Meunier and J. C. Daran, *J. Chem. Soc., Dalton Trans*., 1999, 1039.
261. A. Mazouz, P. Meunier, M. M. Kubicki, B. Hanquet, R. Amardeil, C. Bournet and A. Zahidi, *J. Chem. Soc., Dalton Trans*., 1997, 1043.
262. H. Fujihara, M. Yabe, M. Ikemori and N. Furukawa, *J. Chem. Soc., Perkin Trans. 1*, 1993, 2145.
263. H. Fujihara, M. Yabe and N. Furukawa, *J. Chem. Soc., Perkin Trans. 1*, 1996, 1783.
264. H. Fujihara, T. Nishioka, H. Mima and N. Furukawa, *Heterocycles*, 1995, **41**, 2647.
265. (a) H. Fujihara, Y. Ueno, J. J. Chiu and N. Furukawa, *J. Chem. Soc., Chem. Commun*., 1991, 1052; (b) H. Fujihara, Y. Ueno, J. J. Chiu and N. Furukawa, *Chem. Lett*., 1991, 1649.
266. H. Fujihara, H. Mima, T. Erata and N. Furukawa, *J. Am. Chem. Soc*., 1992, **114**, 3117.
267. Y. Takaguchi, H. Fujihara and N. Furukawa, *Organometallics*, 1995, **15**, 1913.
268. H. Fujihara, H. Mima, T. Erata and N. Furukawa, *J. Chem. Soc., Chem. Commun*., 1991, 98.

269. H. Fujihara, H. Mima, M. Ikemori and N. Furukawa, *J. Am. Chem. Soc*., 1991, **113**, 6337.
270. H. Fujihara, H. Mima and N. Furukawa, *Phosphorus Sulfur Silicon Relat. Elem*., 1992, **67**, 141.
271. H. Fujihara, Y. Ueno, J.-J. Chiu and N. Furukawa, *J. Chem. Soc., Perkin Trans. 1*, 1992, 2247.
272. H. Mima, H. Fujihara and N. Furukawa, *Tetrahedron*, 1998, **54**, 743.
273. H. Fujihara, H. Mima and N. Furukawa, *Tetrahedron*, 1996, **52**, 13951.
274. H. Fujihara, Y. Takaguchi and N. Furukawa, *Heterocycles*, 1994, **39**, 431.
275. N. Furukawa, *Bull. Chem. Soc. Jpn*., 1997, **70**, 2571.
276. E. Vogel, C. Fröde, A. Beihan, H. Schmickler and J. Lex, *Angew. Chem., Int. Ed. Engl*., 1997, **36**, 2609.
277. M. A. El Amiri, P. Meunier, R. Louis, N. Pirio and H. Ossor, *Phosphorus Sulfur and Silicon*, 2000, **156**, 1.
278. J. D. Odom, W. H. Dawson and P. D. Ellis, *J. Am. Chem. Soc*., 1979, **101**, 5815.
279. K. Laali, H. Y. Chen and R. J. Gerzina, *J. Org. Chem*., 1987, **52**, 4126.
280. K. Laali, H. Y. Chen and R. J. Gerzina, *J. Organomet. Chem*., 1988, **348**, 199.
281. H. Poleschner, M. Heydenreich and R. Radeglia, *Magn. Reson. Chem*., 1999, **37**, 333.
282. S. Ogawa, S. Sato, T. Erata and N. Furukawa, *Tetrahedron Lett*., 1991, **32**, 3179.
283. E. Honda, T. Iwamura, S.-I. Watanabe and T. Kataoka, *Heterocycles*, 2000, **53**, 1997.
284. T. Kataoka, S.-i. Watanabe, K. Yamamoto, M. Yoshimatsu, G. Tanabe and O. Muraoka, *J. Org. Chem*., 1998, **63**, 6382.
285. S.-i. Watanabe, E. Mori, H. Nagai, T. Iwamura, T. Iwama and T. Kataoka, *J. Org. Chem*., 2000, **65**, 8893.
286. T. W.-M. Fan, A. N. Lane, D. Martens and R. M. Higashi, *Analyst*, 1998, **123**, 875.
287. H. Fujihara, T. Nakahodo, H. Mima and N. Furukawa, *Heterocycles*, 1995, **41**, 1127.
288. S. Ogawa, S. Sato, Y. Masutomi and N. Furukawa, *Phosphorus Sulfur and Silicon*, 1992, **67**, 99.
289. S. Sato and N. Furukawa, *Chem. Lett*., 1994, 889.
290. S. Sato and N. Furukawa, *Tetrahedron Lett*., 1995, **36**, 2803.
291. S. Sato, O. Takahashi and N. Furukawa, *Coord. Chem. Rev*., 1998, **176**, 483.
292. S. Sato, H. Arakawa, E. Horn and N. Furukawa, *Chem. Lett*., 1998, 213.
293. F. Ohno, T. Kawashima and R. Okazaki, *J. Chem. Soc., Chem. Commun*., 1997, 1671.
294. F. Ohno, T. Kawashima, and R. Okazaki, *J. Chem. Soc., Chem. Commun*., 2001, 463.
295. T. Takahashi, N. Kurose, S. Kawanami, Y. Arai and T. Koizumi, *J. Org. Chem*., 1994, **59**, 3262.
296. N. Kurose, T. Takahashi and T. Koizumi, *Tetrahedron*, 1997, **53**, 12115.
297. D. B. Denney, D. Z. Denney, P. J. Hammond and Y. F. Hsu, *J. Am. Chem. Soc*., 1981, **103**, 2340.
298. H. Fujihara, H. Mima and N. Kurukawa, *Tetrahedron*, 1996, **52**, 10375.
299. H. Fujihara, Y. Ueno, J.-J. Chiu and N. Furukawa, *J. Chem. Soc., Perkin Trans. 1*, 1992, 2247.
300. H. Mima, H. Fujihara and N. Kurukawa, *Tetrahedron*, 1998, **54**, 743.
301. H. Fujihara, T. Nakahodo and N. Furukawa, *Chem. Commun*., 1996, 311.
302. B. A. Fir, H. P. A. Mercier, J. C. P. Sanders, D. A. Dixon and G. J. Schrobilgen, *J. Fluorine Chem*., 2001, **110**, 89.
303. H. Poleschner, M. Heydenreich and R. Radeglia, *Magn. Reson. Chem*., 1999, **37**, 333.
304. H. Poleschner and K. Seppelt, *Magn. Reson. Chem*., 2002, **40**, 777.
305. M. Jansen and M. Tellenbach, *Z. Anorg. Allg. Chem*., 1998, **624**, 1267.
306. M. R. Rudd, S. V. Lindeman and S. Husebye, *Acta Chem. Scand*., 1997, **51**, 689.
307. E. Seppälä, F. Ruthe, J. Jeske, W.-W. du Mont and P. G. Jones, *Chem. Commun*., 1999, 1471.
308. E. Krawczyk, A. Skowronska and J. Michalski, *J. Chem. Soc., Dalton Trans*., 2002, 4471.

309. M. Yoshifuji, S. Sangu, M. Hirano and K. Toyota, *Chem. Lett*., 1993, 1715.
310. P. Bernatowicz, O. Bjorlo, E. H. Morkved and S. Szymanski, *J. Magn. Reson*., 2000, **145**, 152.
311. P. Bernatowicz, L. Stefaniak, M. Giurg, L. Syper and G. A. Webb, *Pol. J. Chem*., 1997, **71**, 441.
312. U. Herzog and G. Rheinwald, *J. Organomet. Chem*., 2002, **648**, 220.
313. C. M. Bates and C. P. Morley, *J. Organomet. Chem*., 1997, **533**, 193.
314. G. Jochem, K. Karaghiosoff, S. Plank, S. Dick and A. Schmidpeter, *Chem. Ber*., 1995, **128**, 1207.
315. P. Bhattacharyya, A. M. Z. Slawin and J. D. Woollins, *Chem. Eur. J*., 2002, **8**, 2705.
316. N. Tonkikh, H. Duddeck, M. Petrova, O. Neilands and A. Strakovs, *Eur. J. Org. Chem*., 1999, 1585.
317. P. Michelsen, U. Annby and S. Gronowitz, *Chem. Scr*., 1984, **24**, 251.
318. L. A. Silks, III, R. B. Dunlap and J. D. Odom, *J. Am. Chem. Soc*., 1990, **112**, 4979.
319. L. A. Silks, III, J. Peng, J. D. Odom and R. B. Dunlap, *J. Chem. Soc., Perkin Trans. 1*, 1991, 2495.
320. L. A. Silks, III, J. Peng, J. D. Odom and R. B. Dunlap, *J. Org. Chem*., 1991, **56**, 6733.
321. J. Peng, M. E. Barr, D. A. Ashburn, J. D. Odom, R. B. Dunlap and L. A. Silks, III, *J. Org. Chem*., 1994, **59**, 4977.
322. J. Peng, M. E. Barr, D. A. Ashburn, L. Lebioda, A. R. Garber, R. A. Martinez, J. D. Odom, R. B. Dunlap and L. A. Silks, III, *J. Org. Chem*., 1995, **60**, 5540.
323. R. Wu, J. D. Odom, R. B. Dunlap and L. A. Silks, III, *Tetrahedron: Asymm*., 1995, **6**, 833.
324. R. Wu, G. Hernández, J. D. Odom, R. B. Dunlap and L. A. Silks, *J. Chem. Soc., Chem. Commun*., 1996, 1125.
325. L. A. Silks, R. Wu, R. B. Dunlap and J. D. Odom, *Phosphorus Sulfur and Silicon*, 1998, **136–138**, 209.
326. R. Wu, L. A. Silks, J. D. Odom and R. B. Dunlap, *Spectroscopy*, 1996, **11**, 37. (Review)
327. R. Wu, J. D. Odom, R. B. Dunlap and L. A. Silks, III, *Tetrahedron: Asymm*., 1999, **10**, 1465.
328. R. W. Hoffmann, W. Klute, R. K. Dress and A. Wenzel, *J. Chem. Soc., Perkin Trans. 2*, 1995, 1721.
329. T. Takahashi, N. Kurose, S. Kawanami, Y. Arai and T. Koizumi, *J. Org. Chem*., 1994, **59**, 3262.
330. T. G. Back and Z. Moussa, *Org. Lett*., 2000, **2**, 3007.
331. T. C. Back, Z. Moussa and M. Parvez, *J. Org. Chem*., 2002, **67**, 499.
332. M. Tiecco, L. Testaferri, C. Santi, C. Tomassini, F. Marini, L. Bagnoli and A. Temperini, *Tetrahedron: Asymm*., 2000, **11**, 4645.
333. T. Wirth, *Angew. Chem. Int. Ed. Engl*., 1995, **34**, 1726.
334. T. Wirth and G. Fragale, *Chem. Eur. J*., 1997, **3**, 1894.
335. G. Fragale, M. Neuburger and T. Wirth, *J. Chem. Soc., Chem. Commun*., 1998, 1867.
336. G. Fragale and T. Wirth, *Eur. J. Org. Chem*., 1998, 1361.
337. C. Santi, G. Fragale and T. Wirth, *Tetrahedron: Asymm*., 1998, **9**, 3625.
338. T. Wirth, K. J. Kulicke and G. Fragale, *J. Org. Chem*., 1996, **61**, 2686.
339. T. Wirth, *Liebigs Ann./Recueil*, 1997, 1155.
340. T. Wirth, K. J. Kulicke and G. Fragale, *Helv. Chim. Acta*, 1996, **79**, 1957.
341. H. A. Stefani, I. M. Costa, D. De O Silva and P. H. Menezes, *Phosphorus Sulfur Silicon Rel. Elem*., 2001, **172**, 159.
342. G. R. Weisman, *Asymmetric Synthesis Vol. 1*, J. D. Morrison, ed. Academic Press, New York, London, 1983, p. 153.
343. H. Duddeck and D. Müller, unpublished results.
344. S. Hameed, R. Ahmad and H. Duddeck, *Magn. Reson. Chem*., 1998, **36**, S47.
345. S. Malik, H. Duddeck, J. Omelanczuk and M. I. Choudhary, *Chirality*, 2002, **14**, 407.
346. W. Amaratunga, O. Chaudry and J. Milne, *Can. J. Chem*., 1994, **72**, 1165.
347. W. Amaratunga and J. Milne, *Can. J. Chem*., 1994, **72**, 2506.

348. S. Ball and J. Milne, *Can. J. Chem*., 1995, **73**, 716.
349. T. M. Nguyen and D. Lee, *Org. Lett*., 2001, 3161.
350. J. Drabowicz, J. Luczak and M. Mikolajczyk, *J. Org. Chem*., 1998, **63**, 9565.
351. D.-L. An, K. Toyota, M. Yasunami and M. Yoshifuji, *Chem. Lett*., 1995, 199.
352. D. Crich, X.-Y. Jiao, Q. Yao and J. S. Harwood, *J. Org. Chem*., 1996, **61**, 2368.
353. D. H. R. Barton, G. Lalic and J. A. Smith, *Tetrahedron*, 1998, **54**, 1725.
354. D. H. R. Barton, M. Jacob and E. Peralez, *Tetrahedron Lett*., 1999, **40**, 9201.
355. T. Kanda, T. Ezaka, T. Murai and S. Kato, *Tetrahedron Lett*., 1995, **36**, 2807.
356. T. Murai, K. Kakami, N. Itoh, T. Kanda and S. Kato, *Tetrahedron*, 1996, **52**, 2839.
357. M. Iwaoka and S. Tomoda, *J. Am. Chem. Soc*., 1994, **116**, 2557.
358. G. Mugesh, A. Panda, H. B. Singh, N. S. Punekar and R. J. Butcher, *J. Am. Chem. Soc*., 2001, **123**, 839.
359. (a) J. E. Oldfield, *J. Nutr*., **117**, 1987, 2002; (b) D. L. Klayman and W. H. H. Günther, eds., *Organic Selenium Compounds: Their Chemistry and Biology*, Wiley, New York, 1973; (c) J. T. Rotruck, A. L. Pope, H.C. Gauther, A. B. Swanson, D.G. Hafeman, and W. G. Hoekstra, *Science*, 1973, **179**, 588; (d) A. Passwater, *Selenium as Food and Medicine*, Keats Publ., New Canaan, Conn., 1980; (e) G.-Q. Yang, in: *Selenium in Biology and Medicine* Vol. A, p. 9, G. F. Combs, Jr., J. E. Spallholz, O. A. Levander, and J. E. Oldfield, eds., Van Nostrand Reinhold, New York, 1987.
360. G. Mugesh, W.-W. du Mont and H. Sies, *Chem. Rev*., 2001, **101**, 2125.
361. A. D'Ulivo, L. Lampugnani, I. Sfetsios, R. Zamboni and C. Forte, *Analyst*, 1994, **119**, 633.
362. L. A. Silks, *Phosphorus Sulfur and Silicon*, 1998, **136–138**, 611.
363. M. Salzmann, E. M. Stocking, L. A. Silks, III and H. Senn, *Magn. Reson. Chem*., 1999, **37**, 672.
364. (a) M. Zhang and H. J. Vogel, *J. Mol. Biol*., 1994, **239**, 545; (b) M. Zhang, T. Yuan, J. M. Aramini and H. J. Vogel, *J. Mol. Biol*., 1995, **270**, 20901.
365. D. Besse, F. Siedler, T. Diercks, H. Kessler and L. Moroder, *Angew. Chem., Int. Ed. Engl*., 2001, **36**, 883.
366. M. A. Lucas, O. T. K. Nguyen, C. H. Schiesser and S. L. Zheng, *Tetrahedron*, 2000, **56**, 3995.
367. J. Stawinski and M. Thelin, *J. Org. Chem*., 1994, **59**, 130.
368. M. Bollmark and J. Stawinski, *Chem. Commun*., 2001, 771.
369. M. Bollmark, M. Kullberg and J. Stawinski, *Tetrahedron Lett*., 2002, **43**, 515.
370. G. A. Brown, K. M. Anderson, M. Murray, T. Gallagher and H. J. Hales, *Tetrahedron*, 2000, **56**, 5579.
371. M. W. Carland, R. L. Martin and C. H. Schiesser, *Tetrahedron Lett*., 2001, **42**, 4737.
372. A. E. Jakobs, L. E. Christiaens and M. J. Renson, *Tetrahedron*, 1994, **50**, 9315.
373. A. Mohsine and L. Christiaens, *Heterocycles*, 1996, **43**, 2567.
374. M. Iwaoka and S. Tomoda, *J. Am. Chem. Soc*., 1994, **116**, 4463.
375. R. Michalczyk, J. G. Schmidt, E. Moody, Z. Li, R. Wu, R. B. Dunlap, J. R. Odom and L. A. Silks, III, *Angew. Chem. Int. ed., Engl*., 2000, **39**, 3067.
376. K.-I. Fujita, M. Iwaoka and S. Tomoda, *Chem. Lett*., 1994, 923.
377. M. Iwaoka and S. Tomoda, *J. Am. Chem. Soc*., 1996, **118**, 8077.
378. R. Kaur, H. B. Singh and R. P. Patel, *J. Chem. Soc., Dalton Trans*., 2000, 2719.
379. G. Mugesh, H. B. Singh and R. J. Butcher, *Tetrahedron: Asymm*., 1999, **10**, 237.
380. G. Mugesh, A. Panda, H. B. Singh and R. J. Butcher, *Chem. Eur. J*., 1999, **5**, 1411.
381. A. Panda, G. Mugesh, H. B. Singh and R. J. Butcher, *Organometallics*, 1999, **18**, 1986.
382. D. H. R. Barton, M. B. Hall, Z. Lin, S. L. Parekh and J. Reibenspies, *J. Am. Chem. Soc*., 1993, **115**, 5056.
383. H. Komatsu, M. Iwaoka and S. Tomoda, *Chem. Commun*., 1999, 205.
384. H. Komatsu, M. Iwaoka and S. Tomoda, *Chem. Lett*., 1998, 969.
385. M. Iwaoka, H. Komatsu, T. Katsuda and S. Tomoda, *J. Am. Chem. Soc*., 2002, **124**, 1902.

386. M. Iwaoka, T. Katsuda, S. Tomoda, J. Harada and K. Ogawa, *Chem. Lett*., 2002, 518.
387. W. Nakanishi, S. Hayashi, A. Sakaue, G. Ono and Y. Kawada, *J. Am. Chem. Soc*., 1998, **120**, 3635.
388. W. Nakanishi, S. Hayashi and H. Yamaguchi, *Chem. Lett*., 1996, 947.
389. S. Hayashi and W. Nakanishi, *J. Org. Chem*., 1999, **64**, 6688.
390. N. Furukawa and K. Kobayashi, *J. Synth. Org. Chem. Jap*., 1997, **55**, 1006.

Structural Studies of Polymer Blends by Solid-State NMR

HIROMICHI KUROSU[1] AND QUN CHEN[2]

[1]*Department of Human Life and Environment, Nara Women's University, Kitauoya-Nishimachi, Nara 630-8506, Japan*
[2]*Analytical Center and The Key Laboratory of Education Ministry for Optical and Magnetic Resonance Spectroscopy, East China Normal University, Shanghai 200062, P. R. China*

In this review, we introduce recent research works on polymer blends as studied by solid state NMR and focus on the miscibility and phase separation of polymer blends that are responsible for the improvement in their physical properties.

1. INTRODUCTION

It is well-known that most polymer blends are immiscible since the combinatorial entropy of mixing is small and the free volume contribution increases the free energy of mixing. Therefore, it is necessary to have specific intermolecular interactions which are responsible for miscibility, such as hydrogen bonding, dipole–dipole interaction, ion interactions etc. Since the physical properties of polymer blends are strongly influenced by the miscibility, there is much interest in studying miscibility and phase behaviour. A better understanding of miscibility and phase behaviour of polymer blends are essential for the development of blend materials. Polymer blends are of particular interest because of the practical motivation for producing new materials. The use of polymer blends to obtain materials with specific performance is widespread in manufacturing.

ANNUAL REPORTS ON NMR SPECTROSCOPY
VOLUME 52 ISSN 0066 4103
DOI 10.1016/S0066-4103(04)52004-5

Solid state NMR offers powerful tools for probing miscibility, phase separated structure and molecular motion in polymer blends and which may be beyond the resolution limits of conventional microscopic or thermal analysis. A large number of NMR works have been published and some of them were reviewed.[1,2] In this review, therefore, we introduce recent research works on polymer blends by solid state NMR and focus on the miscibility and phase separation of polymer blends that are responsible for the improvement in their physical properties.

2. MISCIBILITY

2.1. Relaxation measurements

In polymer blends, the ^{1}H spin-lattice relaxation times in the rotating ($T_{1\rho}{}^{H}$) and laboratory frames ($T_{1}{}^{H}$) obtained from high-resolution solid-state ^{13}C CP/MAS NMR are sensitive to the domain size of polymer blends through the process of proton spin diffusion. Proton spin diffusion is not a physical movement of protons, but is the equilibration process of non-equilibrium polarizations of spins at different local sites which occur through the mutual exchange of magnetization. The $T_{1\rho}{}^{H}$ is measured by employing a CP pulse sequence modified by adding a variable spin-locking pulse immediately after the ^{1}H $\pi/2$ pulse. The $T_{1}{}^{H}$ is measured from CP/MAS ^{13}C NMR using an inversion-recovery pulse sequence.

Chang *et al*. reported the miscibility of poly(vinylphenol) (PVPh) with poly(methyl methacrylate) (PMMA).[3] Figure 1 shows the ^{13}C CP/MAS spectra of pure PVPh, PMMA, PVPh-co-PMMA, PEG, and PVPh-*co*-PMMA/ poly(ethylene oxide) (PEO) blends of various compositions with peak assignments. VPh contents of PVPh-*co*-PMMA is 51 mol% and Mn of PEO is 20,000. The spin lattice relaxation time in the rotating frame ($T_{1\rho}{}^{H}$) was measured to examine the homogeneity of PVPh-*co*-PMMA/PEO blends on the molecular scale.

Table 1 summarizes those $T_{1\rho}{}^{H}$ values derived from the binary exponential analysis, indicating that the blend with high PVPh-*co*-PMMA content exhibits a single exponential. However, the biexponential decay gradually appears at higher PEO contents at 70 ppm. A semicrystalline polymer will have two proton spin lattice relaxations; the crystalline phase and the amorphous phase, attributed to the long and short relaxation components, respectively. According to Table 1, the amorphous $T_{1\rho}{}^{H}$ decreases with increasing PEO content in the blend. Meanwhile, a high $T_{1\rho}{}^{H}$ value for PVPh-*co*-PMMA/PEO = 80/20 blend, implies that the polymer mobility is retarded reflecting the more rigid character of the PVPh-*co*-PMMA. On the contrary, a decrease of the $T_{1\rho}{}^{H}$ value in the PEO rich region is associated with increased mobility of the amorphous PEO, related to the reduction of the intermolecular

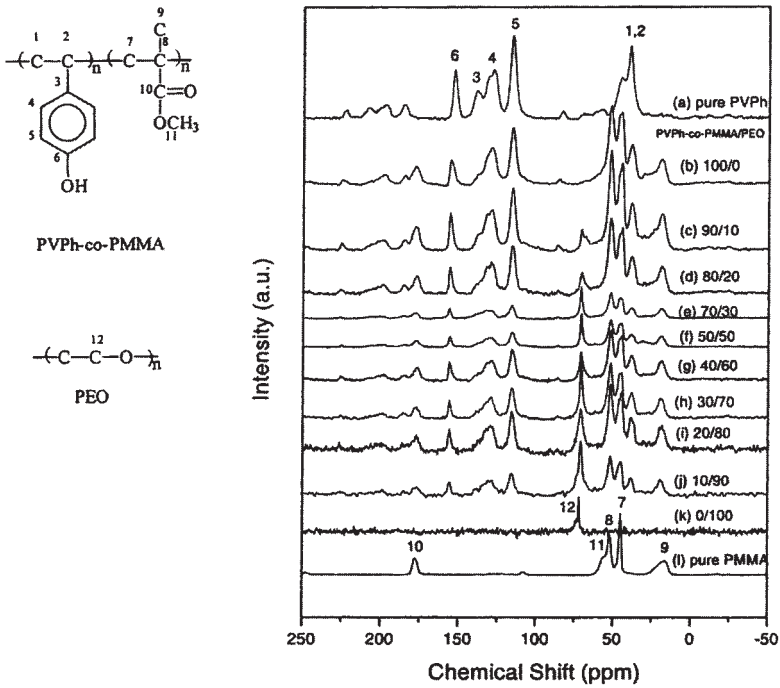

Fig. 1. ^{13}C CPMAS spectra at room temperature for pure PVPh, pure PMMA and various PVPh-*co*-PMMA/PEO blends: (a) pure PVPh; (b) 100/0; (c) 90/10; (d) 80/20; (e) 70/30; (f) 50/50; (g) 40/60; (h) 30/70; (i) 20/50; (j) 10/90; (k) 0/100; (l) pure PMMA. (Figures 1 and 9 in the original literature: S. W. Kuo and F. C. Chang, *Macromolecules*, 2001, **34**, 4089.)

Table 1. $T_{1\rho}{}^{H}$ (ms) values of pure PVPh and various PVPh-*co*-PMMA/PEO blend compositions

Blend composition	115 ppm	70 ppm	
Pure PVPh	7.24		
PVPh-*co*-PMMA/PEO			
100/0	12.08		
80/20	5.21	1.48	
40/60	4.30	1.38	
20/80	4.77	0.95	3.93
0/100		0.08	7.84

hydrogen bonding strength. An increasing amount of the long relaxation component with increasing PEO suggests the existence of a more crystalline PEO phase in the blend.

Table 1 also shows that both pure PVP and PVPh-*co*-PMMA/PEO blends exhibit only single-exponential relaxation through out all of the blends at

115 ppm, indicating good miscibility and dynamic homogeneity in the PVPh-co-PMMA phase. The maximum diffusive path length L can be estimated using the approximate Eq. (1).[4–6]

$$L = (6DT)^{1/2} \tag{1}$$

A typical value of D is 10^{-16} m^2 s^{-1}. For $T_{1\rho}{}^{H}$ of 5 ms, the dimensions of these PVPh-*co*-PMMA/PEO blends are below 2–3 nm in the amorphous phase. Interestingly, the $T_{1\rho}{}^{H}$ has a minimum value for the PVPh-*co*-PMMA = 40/60 blend showing that the overall chain mobility is maximal at this composition. This observation agrees with the earlier result concerning hydroxyl group association obtained by FTIR and solid-state NMR. In addition, all of the blends show a shorter $T_{1\rho}{}^{H}$ than that of the pure PVPh-*co*-PMMA implying that the PVPh-*co*-PMMA mobility also increases with the increase of PEO content.

The miscibility of poly(methyl acrylate) (PMAA, Mw = 150,000)/PVAc (Mw = 167,000) blends at various mixing ratios was investigated by both $T_1{}^{H}$ and $T_{1\rho}{}^{H}$ measurements.[7] ^{13}C CP/MAS NMR spectra of PMAA, PVAc and the PMAA/PVAc blends are shown in Fig. 2. Figure 3 shows the plots of the ^{1}H spin-lattice relaxation times in the laboratory ($T_1{}^{H}$, A) and in the rotating ($T_{1\rho}{}^{H}$, B) frames against the molar ratio of PMAA (χ_{PMAA}). The ^{1}H relaxation times from the CH_2 (○) and OCH (▲) carbons for PMAA and PVAc, respectively, can be observed because these two carbons are observed separately even in the blends (Fig. 2), so that it is possible to obtain each ^{1}H relaxation time for PMAA or PVAc in the blends independently.

Figure 3A shows that both the original $T_1{}^{H}$ values of pure PMAA and pure PVAc alter in the blends and the obtained $T_1{}^{H}$ values of PMAA are in excellent agreement with those of PVAc. This indicates that the complete averaging of the $T_1{}^{H}$ rates by ^{1}H spin diffusion, suggesting that PMAA and PVAc are in close proximity with each other and the PMAA/PVAc blends are homogeneous on a scale of 20–50 nm for all compositions. Similarly, Fig. 3B shows that the $T_{1\rho}{}^{H}$ values of PMAA in the PMAA-rich/PVAc blends, which are the PMAA/PVAc = 3/1, 2/1, and 1/1 blends, are fully consistent with those of PVAc. For the PMAA/PVAc-rich blends, which are the PMAA/PVAc = 1/2 and 1/3 blends, however, the $T_{1\rho}{}^{H}$ values of PMAA are different from those of PVAc, although the values of PMAA or PVAc alter toward each other and become close from those of pure ones. This exhibits that the partially averaging of $T_{1\rho}{}^{H}$ rates by ^{1}H spin diffusion occurs in the PMAA/PVAc-rich blends. These results show that the PMAA-rich/PVAc blends are homogeneous on a scale of 2–5 nm as well as 20–50 nm, but the PMAA/PVAc-rich blends are inhomogeneous on the scale.

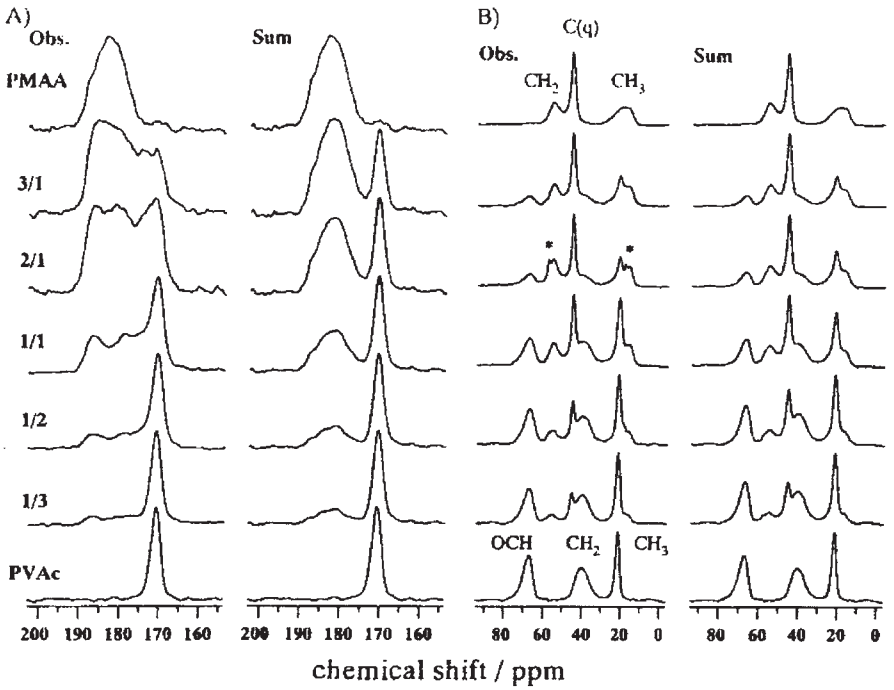

Fig. 2. Observed CP/MAS ^{13}C NMR spectra of PMAA, PVAc, and the PMAA/PVAc blends: (A) carboxyl regions of PMAA and carbonyl regions of PVAc. (B) Aliphatic region. The sum of the ^{13}C NMR spectra of pure PMAA and pure PVAc at the respective molar unit ratio is also depicted on the right of the observed spectra. (Figure 1 in the original literature: A. Asano, M. Eguchi, M. Shimizu and T. Kurotsu, *Macromolecules*, 2003, **25**, 8819.)

If the ^{1}H spin diffusion occurs entirely during a period less than the shortest ^{1}H relaxation time among the mixed polymers, the ^{1}H relaxation rate is averaged by ^{1}H mole fraction as follows:

$$1/T_1{}^{Ave} = f_{PMAA} \times 1/T_1{}^{PMAA} + (1 - f_{PMAA}) \times 1/T_1{}^{PVAc} \qquad (2)$$

where $T_1{}^{Ave}$ is the averaged ^{1}H relaxation time and f_{PMAA} the ^{1}H mole fraction of PMAA in the respective blend. $T_1{}^{PMAA}$ and $T_1{}^{PVAc}$ are the ^{1}H relaxation times for pure PMAA and PVAc, respectively. In a case of no significant change of molecular motion between the pure and the mixed states, the observed ^{1}H relaxation times for the blends are equal to the calculated values obtained from Eq. (2).

The solid lines in Fig. 4A and B represent the calculated values from Eq. (2). The observed $T_1{}^{H}$ values are in good agreement with the estimated values. The observed $T_{1\rho}{}^{H}$ values for PMAA-rich blends are also in good agreement with the calculated ones. These agreements indicate that the molecular motions

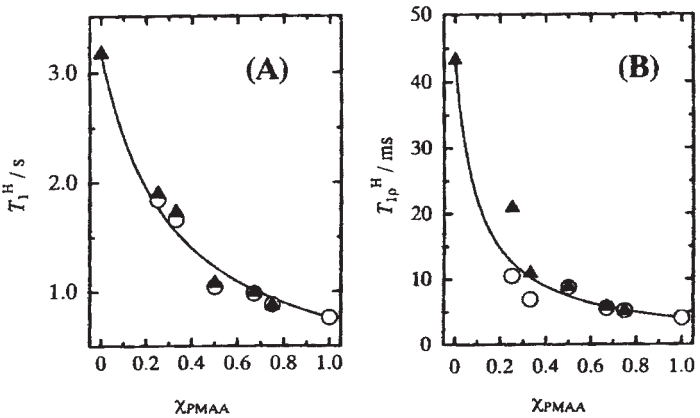

Fig. 3. Observed ^{1}H spin-lattice relaxation times in the laboratory (T_1^H, A) and in the rotating ($T_{1\rho}^H$, B) frames against the molar unit ratio of PMAA/PVAc blends (χ_{PMAA}): O, CH_2 carbon of PMAA; ▲, OCH carbon of PVAc. Each solid line represents the calculated curve from Eq. (2). (Figure 3 in the original literature: A. Asano, M. Eguchi, M. Shimizu and T. Kurotsu, *Macromolecules*, 2003, **25**, 8819.)

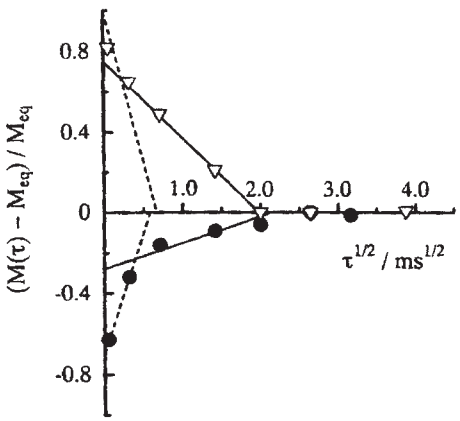

Fig. 4. Plots of ^{1}H normalized magnetization change (●, C(q) signal of PMAA; ▽, CH_3 signal of PVAc) vs. square root of ^{1}H spin-diffusion time $\tau^{1/2}$ for the PMAA/PVAc = 1/1 blend. Solid straight lines are drawn without the initial point to determine the intercept time te. Broken lines are drawn through the initial and the second data points. Meq represents the quasi-equilibrium magnetization after long mixing period but much shorter than T_1^H. (Figure 4 in the original literature: A. Asano, M. Eguchi, M. Shimizu and T. Kurotsu, *Macromolecules*, 2003, **25**, 8819.)

of both polymers in the blends are not changed drastically with each other compared with those found before mixing, and the fast ^{1}H spin diffusion is not hindered by the molecular motions. These results are reasonable by taking account of the high Tg for these blends.

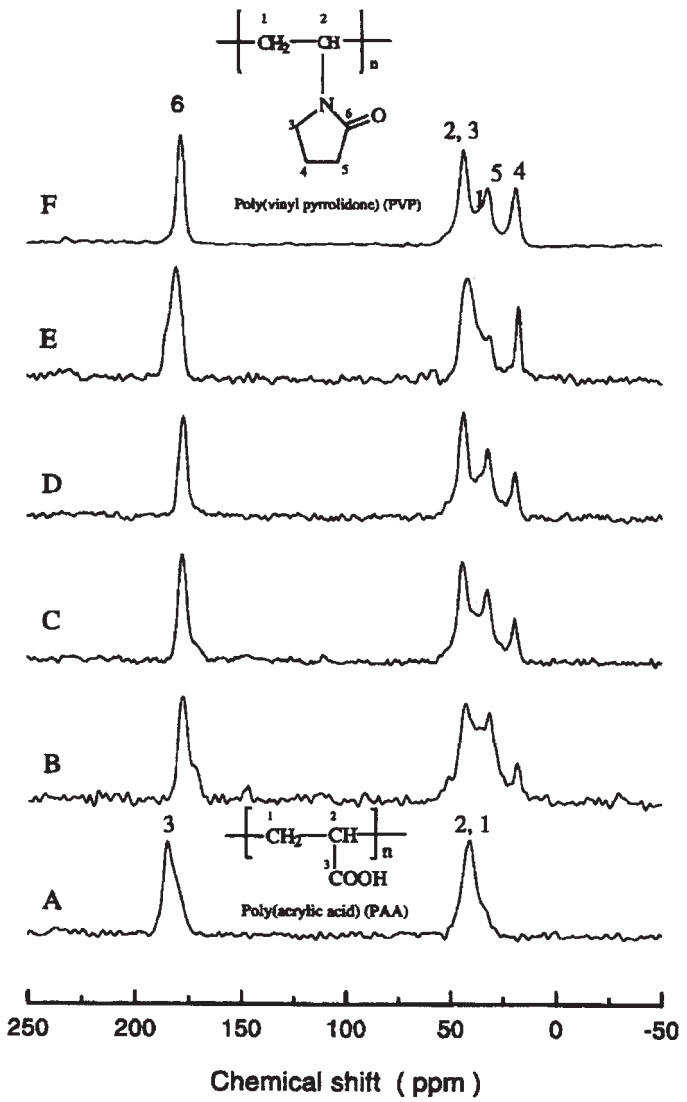

Fig. 5. ^{13}C CP/MAS spectra of the PAA/PVP blends: (A) 100/0; (B) 60/40; (C) 40/60, (D) 22/78; (E) complex (1/1); (F) 0/100. (Figure 6 in the original literature: C. Lau and Y. Mi, *Polymer*, 2002, **43**, 823.)

The miscibility of poly(acrylic acid) (PAA) and poly(vinyl pyrrolidone) (PVP) blends and complex was investigated by relaxation measurements.[8] Figure 5 shows ^{13}C CP/MAS spectra of the PAA/PVP blends, PAA, PVP and complex. In the $T_1{}^H$ experiment, the resonance intensities of all the samples were obtained with a series of different delay times based on the inversion

Table 2. The mean value of T_1^H and $T_{1\rho}^H$ for PAA/PVP system and their standard deviation

	Sample	wt/wt	mol/mol	T_1^H (s)	$\sigma\ T_1^H$	$T_{1\rho}^H$ (ms)	$\sigma\ T_{1\rho}^H$
	PAA	100/0		2.59	0.01	6.36	0.01
PAA/PVP	Blend	60/40	2/1	1.77	0.07	9.34	0.28
PAA/PVP	Blend	40/60	1/1	1.79	0.07	9.06	0.23
PAA/PVP	Blend	22/78	1/2	2.01	0.12	9.45	0.52
	PVA	0/100		1.83	0.03	15.21	0.43
PAA/PVP	Complex	49/51	1.48/1	2.36	0.15	5.46	0.22

recovery mode. The intensity of the resonance carbons can be described by the following exponential model,

$$\ln\left[\frac{M_e - M_\tau}{2M_e}\right] = \frac{-\tau}{T_1^H} \tag{3}$$

The mean value of the T_1^Hs for each sample was calculated. The calculated mean values of T_1^Hs and the standard deviations are presented in Table 2. It is seen, from Table 2, that the standard deviation in both blends and complex is negligibly small. This indicates that the spin-diffusion among all protons in the blends and the complex can average out the whole relaxation process and hence the domain size of these samples is smaller than the spin-diffusion path length within the time frame of T_1^H. From the obtained value of T_1^H and using the Eq. (1) with 10^{-16} m^2 s^{-1}, it is believed that the PAA/PVP blends are intimately mixed on the T_1^H measurement scale of 32–39 nm.

The miscibility of the blends and complex can be probed at even smaller scale by carrying out the $T_{1\rho}^H$ measurement, in which the relaxation time, $T_{1\rho}^H$, was determined by monitoring the decay in carbon signal intensities as a function of delay time. All the resonance peaks show a single-exponential decay and the logarithmic plot of ^{13}C resonance intensity M_τ vs. delay time τ for the selected carbon (33 ppm) of pure PVP, PAA/PVP blend (1/1), and complex. Furthermore, it can be seen from Table 2 that the standard deviation can be ignored and the $T_{1\rho}^H$ values obtained for each sample can be considered to be the same. All these imply that all of the blends and the complex are intimately mixed on the $T_{1\rho}^H$ measurement scale. The homogeneity data are accurate down to the scale of 2 nm for the blends and 1.5 nm for the complex.

Miscibility of amorphous poly(benzyl methacrylate) (PBzMA) and semicrystalline poly(ethylene oxide) (PEO) blends were investigated by solid state ^{13}C NMR.[9] Figure 6 shows the ^{13}C CP/MAS NMR spectrum of the PBzMA/PEO blend in 80/20 composition and the ^{13}C CP/MAS NMR spectra of various compositions are shown in Fig. 7. The logarithmic plots of ^{13}C

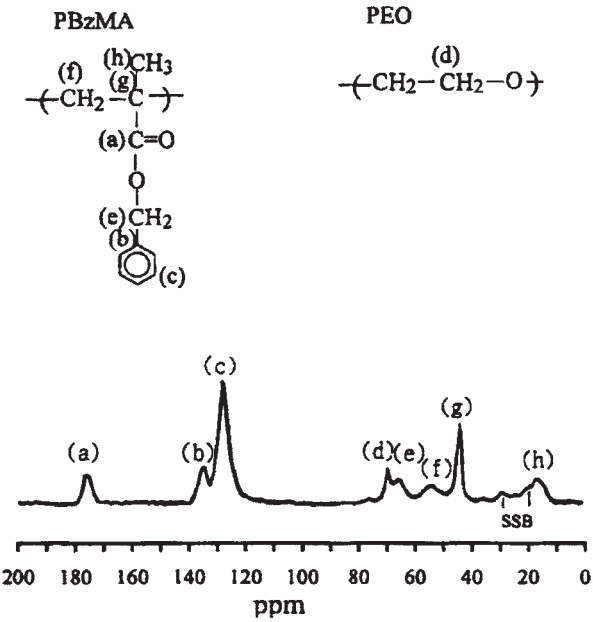

Fig. 6. ^{13}C CP/MAS NMR spectrum of the PBzMA/PEO blend in 80/20 composition. SSB denotes spinning side-band. (Figure 1 in the original literature: R.-H. Lin, E. M. Woo and J. C. Chiang, 2001, *Polymer*, **42**, 4289.)

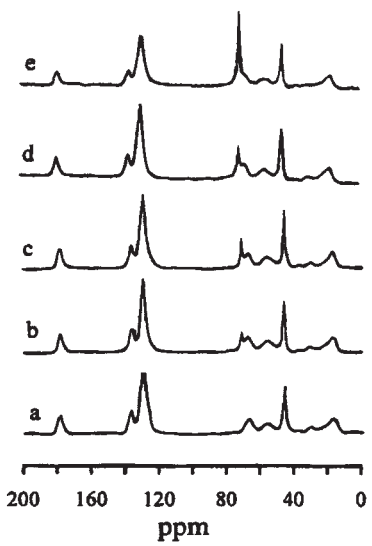

Fig. 7. ^{13}C CP/MAS NMR spectra of the PBzMA/PEO blends in various compositions: (a) 100/0, (b) 90/10, (c) 80/20, (d) 50/50 and (e) 30/70. (Figure 2 in the original literature: R.-H. Lin, E. M. Woo and J. C. Chiang, *Polymer*, 2001, **42**, 4289.)

magnetization intensity versus spin-lock time using a 1 ms contact time for neat samples of PBzMA and PEO. Neat PBzMA is characterized by single-exponential $T_{1\rho}^{H}$ relaxation behaviour, consistent with results usually observed on the amorphous polymer. Neat PEO also exhibits a single-exponential $T_{1\rho}^{H}$ relaxation behaviour using a 1 ms contact time. However, it displays double-exponential $T_{1\rho}^{H}$ relaxation behaviour if we use a 0.1 ms contact time, indicating that PEO contains dual morphologies. Essentially, PEO is a well-known semicrystalline polymer containing an amorphous phase and a crystalline phase. It should be noted that crystalline PEO, which has a very short $T_{1\rho}^{H}$, cannot be detected using a 1 ms contact time. The fitted values of $T_{1\rho}^{H}$ are 7.74 ms for neat PBzMA, and 2.72 and 0.2 ms for neat PEO, as listed in Table 3. The short $T_{1\rho}^{H}$ (0.2 ms) can be associated with the protons of the crystalline parts of PEO, and long $T_{1\rho}^{H}$ (2.72 ms) is contributed by the amorphous phase of PEO.[10] $T_{1\rho}^{H}$ for the PBzMA, PEO and PBzMA/PEO blends are listed in Table 3. PBzMA components in the blends were observed to exhibit single-exponential $T_{1\rho}^{H}$ relaxation behaviour through all the cases of different compositions, indicating that the PBzMA component always exhibits a homogenous phase within the blends at various compositions. This homogenous phase is not pure PBzMA, because the values of $T_{1\rho}^{H}$ for the PBzMA component are not identical to that in the neat PBzMA system (7.74 ms). In spite of the PEO content in the blend, the PBzMA component always predominates in the miscible amorphous phase because the $T_{1\rho}^{H}$ values in this phase are always closer to that of the neat PBzMA component (7.74 ms) and far way from that of the neat amorphous PEO component (2.72 ms). That indicates a miscible homogenous PBzMA-rich phase at a nanoscale level in the blends. Besides, those values of $T_{1\rho}^{H}$ for the PBzMA component slightly decrease (approaching the value of neat PEO) as the PEO component in the blend increases, suggesting that the PEO component in this miscible homogenous phase is presumably enhanced in a gradual way. For each blend the $T_{1\rho}^{H}$ values for PBzMA (6.27, 6.03, 5.72, and 5.34 ms) are eventually identical to the long $T_{1\rho}^{H}$ of the PEO component. This indicates

Table 3. $T_{1\rho}^{H}$ for the PBzMA, PEO and PBzMA/PEO blends (contact time: 1 ms)

PBzMA/PEO Blend (wt/wt)	PBzMA component $T_{1\rho}^{H}$ (ms)	PEO component $T_{1\rho}^{H}$ (ms)		
100/0	7.74	–		
90/10	6.27	6.33	–	
80/20	6.03	6.02	2.76	
50/50	5.72	5.70	2.77	
30/70	5.34	5.40	2.73	
0/100	–		2.72	0.2[a]

[a]Obtained using a contact time of 0.1 ms.

those miscible homogenous phases with PBzMA and PEO chains mixed at the molecular level.

However, double-exponential $T_{1\rho}^{H}$ relaxation behaviour of the PEO component in various compositions of blends except 90/10 (PBzMA/PEO) were observed and the long $T_{1\rho}^{H}$ of the PEO component was virtually the same as the $T_{1\rho}^{H}$ of PBzMA in the PBzMA-rich domain for each composition of blend, whereas all the short $T_{1\rho}^{H}$ of the PEO component in each blend were of the same value (about 2.75 ms) and identical with that of the amorphous phase of neat PEO. This suggests that the amorphous PEO component in each blend is distributed unevenly into two separated phase domains on a $T_{1\rho}^{H}$ relaxation scale. The PEO component in the blend of 90/10 (PBzMA/PEO) composition still exhibits a single-exponential $T_{1\rho}^{H}$ relaxation behaviour (6.33 ms). This single value of $T_{1\rho}^{H}$ for the PEO component is virtually the same as that of the PBzMA component, indicating that this blend is completely homogenous PBzMA-rich phase without constrained PEO and crystalline PEO. Thus, the non-crystallizable portion is referred to the 'constrained PEO' region. This inference illustrates that only one phase is present for this blend (90/10), which will be verified later in more detail.

The miscibility of poly(ethyl oxazoline) (PEOx)/poly(4-vinylphenol) (PVPh) blends were investigated by the solid state NMR.[11] Figure 8 shows the ^{13}C CP/MAS spectra of the PEOx/PVPh blends. To obtain information about the scale of miscibility and phase structure of the PEOx/PVPh blends, dynamic relaxation experiments were conducted, which include the measurements of the T_1^{H}, and $T_{1\rho}^{H}$. In T_1^{H} experiment, peak intensities of PEOx, PVPh and their blends change exponentially as a function of delay time (τ). From the slopes of the plots, T_1^{H}s were obtained, and the results of T_1^{H} for PEOx, PVPh and their blends are summarized in Table 4. Intermediate values of T_1^{H} were obtained for the blends compared to those of the two pure components. These results indicate that fast spin diffusion occurrs among all of the protons in these blends, which averages out the entire relaxation process. Therefore, the blends are homogenous on the scale where the spin diffusion occurs within the time-frame of T_1^{H}, and the mixing scale can be estimated using the one-dimensional diffusion equation for the average diffusive path length as shown in Eq. (1).

$T_{1\rho}^{H}$ was measured to examine homogeneity of the PEOx/PVPh blends at the molecular level. In this measurement, the intensities of carbon peaks of PEOx, PVPh and their blends display single exponential decays as a function of delay time. Values of calculated $T_{1\rho}^{H}$ are summarized in Table 4. A single $T_{1\rho}^{H}$ value was obtained for both pure components and blends and the values of the blends were larger than those of the two pure components, indicating strong hydrogen bonding between the two components, that restricts the segmental motion of the polymer chains and cause the relaxation times of the blends to be longer than those of the pure components. Thus, the

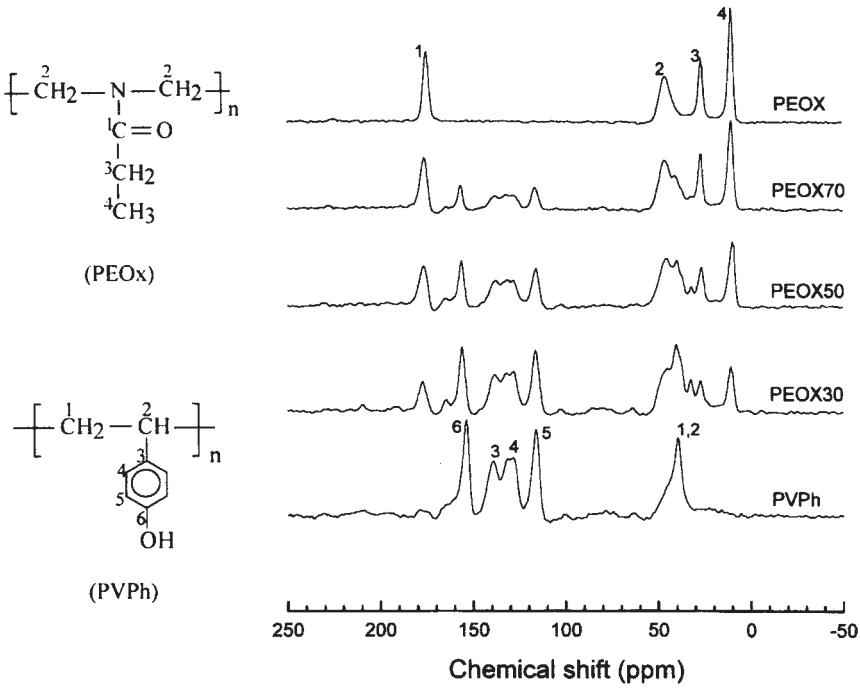

Fig. 8. ^{13}C CP/MAS NMR spectra of the PEOx/PVPh blends in various compositions. (Figure 4 in the original literature: J. Wang, M. K. Cheung and Y. Mi, *Polymer*, 2002, **42**, 2077.)

Table 4. $T_1{}^H$ and $T_{1\rho}{}^H$ values for PEOx, PVPh and their blends (the accuracy of the measurements is $\pm 15\%$)

	$T_1{}^H$ (s)		$T_{1\rho}{}^H$ (ms)	
PEOx/PVPh	PEOx C-3	PVPh C-5	PEOx C-3	PVPh C-5
100/0	2.76	–	7.16	–
70/30	2.62	2.65	8.57	8.06
50/50	2.39	2.35	8.74	8.90
30/70	2.04	2.27	8.59	8.10
0/100	–	1.32	–	6.79

blends are homogeneous on the $T_{1\rho}{}^H$ sensitive scale of 2–3 nm according to Eq. (1).

Miscibility of poly(4-vinylpyridibe) (P4VP) and PVPh is investigated by solid state NMR.[12] ^{13}C CP/MAS NMR spectra of P4VP/PVPh blends in various composition are shown in Fig. 9. To obtain information about the

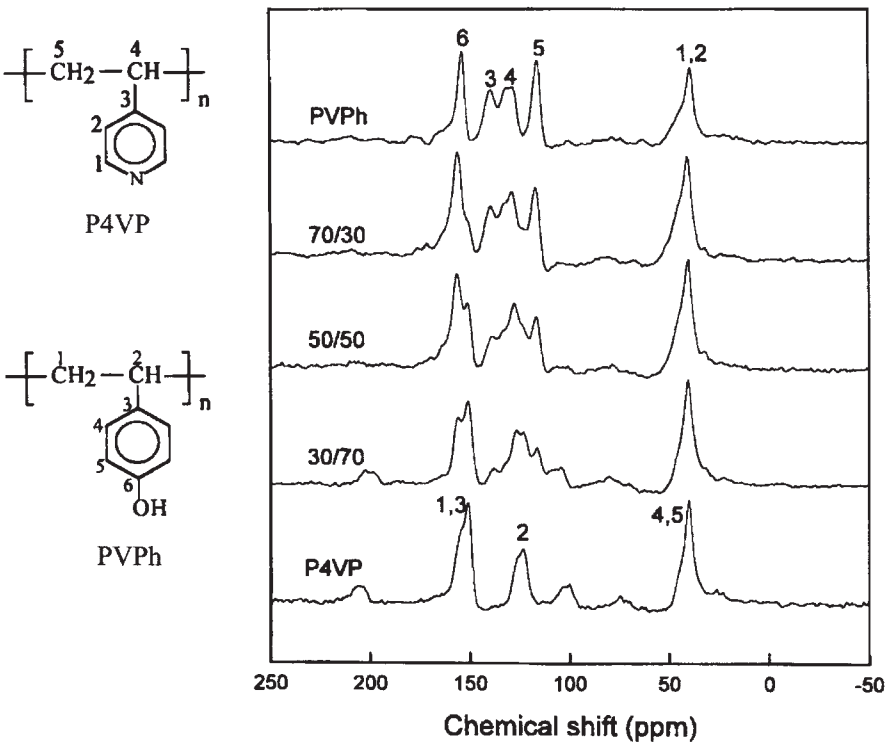

Fig. 9. ^{13}C CP/MAS NMR spectra of the P4VP/PVPh blends in various composition. (Figure 4 in the original literature: J. Wang, M. K. Cheung and Y. Mi, *Polymer*, 2001, **42**, 3087.)

scale of miscibility and phase structure of the P4VP/PVPh blends, relaxation time measurements were performed, which include the measurements of T_1^H, and $T_{1\rho}^H$. The experimental data can be fitted to a single exponential decay function, and from the slopes of the plots, T_1^H values can be obtained. It is found that single T_1^H decays are obtained for all blends, which indicates that fast spin diffusion occurred among all protons in these blends in the entire relaxation process. In addition, it is also found that the T_1^H values of the blends are shorter than those of the pure components, which indicates that the intermolecular interactions are stronger than the intra-molecular self-associations. This specific interaction is analysed to be hydrogen bonding between the nitrogen in the pyridine ring of P4VP and the hydroxyl groups in PVPh. The mixing scale can be estimated using Eq. (1). On the basis of T_1^H, it is believed that the two polymers are intimately mixed on a scale of less than 60–80 nm. Since such mixing level reflects the sum of domain A plus domain B of the blends, the domain size of a constituent domain is less than 40 nm.

Table 5. T_1^H (s) and $T_{1\rho}^H$ (ms) values of P4VP/PVPh blends at 300 K

P4VP/PVPh	T_1^H (s)		$T_{1\rho}^H$ (ms)	
	P4VP C-4,5	PVPh C-5	P4VP C-4,5	PVPh C-5
100/0	1.55	–	6.79	–
70/30	1.20	0.93	7.80	10.71
50/50	1.10	0.97	8.40	9.40
30/70	1.08	0.94	8.69	9.10
0/100	–	1.32	–	6.80

The spin-lattice relaxation time in the rotating frame $T_{1\rho}^H$ was measured to examine homogeneity of the P4VP/PVPh blends at the molecular level. It is found that the experimental data can be fitted to a single exponential decay function, and the slope gives the $T_{1\rho}^H$ value. The $T_{1\rho}^H$ values of the P4VP/PVPh blends (30/70, 50/50, 70/30) are longer than those of the two pure components as listed in Table 5. The likely molecular motions in this frequency range are those due to the pendent groups of P4VP and PVPh. Since strong inter-molecular hydrogen bonding hinders the motion of the pendent groups, the $T_{1\rho}^H$ is longer for the blends.[13–15] These imply that all the blends are homogeneous on the $T_{1\rho}^H$ sensitive scale.

By measuring $T_{1\rho}^H$, Chu *et al.*[16] studied the morphology and molecular dynamics of poly(amide-6) (PA6)/poly(2,6-dimethyl-1,4-phenylene oxide) (PPO) blends compatiblized with styrene maleic anhydride (SMA). SEM photomicrograph measurements demonstrate that the domain size of PA6/PPO blend (30/70 by weight) is reduced greatly with increasing SMA content. PA6, which remains semicrystalline in the blend samples, exhibits biexponential $T_{1\rho}^H$ relaxation behaviour. The long $T_{1\rho}^H$ value is attributed to the crystalline component, while the short one to the amorphous component. PPO, on the other hand, shows only a single $T_{1\rho}^H$ value. For all of the samples studied in the work, the $T_{1\rho}^H$s of the different components are not averaged by spin-diffusion to a common value, indicating the samples are phase separated at the length scale of several tens of Å. It is demonstrated that with increasing SMA content, the crystalline fraction of PA6 decreases steadily, due to the formation of SMA-g-PA6 segments. The mobility of amorphous PA and PPO is found to be enhanced with an increase of SMA. Mechanical properties, including tensile strength, tensile elongation and impact strength of the blends before and after annealing are correlated with $T_{1\rho}^H$ values. It is demonstrated that mechanical properties are sensitive to the molecular structures and dynamics take place within the range of several tens of Å.

Blends of polycaprolactone (PCL) with polyvinylalcohol (PVA) were studied by De Kesel *et al.*[17] Both constituent polymers are semicrystalline at the studying temperature. T_1^H is directly and indirectly measured by using

^{1}H wide-line and ^{13}C CP/MAS NMR techniques respectively. Both constituent polymers are found to exhibit same $T_1{}^H$ value, which is dependent on the blend composition. Such a result indicates the blends are compatible at the T_1 scale, namely 60–90 nm in this case.

Nakano *et al.*[18] reported a ^{13}C CP/MAS NMR study on poly(L-Alanine) (PLA)/Polyglycine (PG) blends. The comparison between the ^{13}C CP/MAS spectra of the blends and those of the parent polymers discloses that upon blending, new conformations of PLA and PG are formed, which is closely related to the presence of intermolecular hydrogen-bonding interactions. $T_{1\rho}{}^H$ measurements demonstrate that the major parts of PG and PLA in the blends, which are in 3_1-helix and α-helix conformation forms respectively, are phase separated. On the other hand, the β-sheet forms of PG and PLA, which are newly formed upon blending, exhibit similar $T_{1\rho}{}^H$ values, demonstrating that these two parts are miscible at the scale of 3–4 nm.

A solid-state ^{13}C NMR study of the intermolecular hydrogen bonding formation in a blend of phenolic resin and poly(hydroxyl ether) of bisphenol A was reported by Wu *et al.*[19] The presence of a single glass transition temperature for all of the blend samples with different composition as disclosed by the DSC measurements demonstrates that the blends are thermodynamically miscible. The solid state NMR parameters, including chemical shift, efficiency of cross-polarization and $T_{1\rho}{}^H$, confirm the presence of more free OH groups when one of the polymers is the minor component.

Hill *et al.*[20] studied the miscibility and hydrogen-bonding interactions in blends of poly(4-vinylphenol) (PVPh) and Poly(2-ethoxyethyl methacrylate) (PEEMA) by employing DSC, infrared spectroscopy (IR) and solid state NMR techniques. Figure 10 shows the ^{13}C CP/MAS signal of the carbonyl group of PEEMA as a function of blend composition. The signal of the blend samples apparently consists of two peaks, comparing with that of the neat PEEMA sample. The peak at the high frequency side is attributed to the hydrogen-bonded carbonyl groups, while the low frequency peak to the free carbonyl groups. The enhancement ratios of cross-polarization and the $T_{1\rho}{}^H$s for these two carbonyl peaks are almost equal to each other. This means that the relative peak intensities shown in Fig. 11 are quantitative. By analyzing the carbonyl signal, it is found that the fraction of hydrogen-bonded carbonyl groups decreases steadily with increasing the weight content of PEEMA, agreeing well with those obtained from the IR analyses. Similar results are also observed for the signal of phenolic carbon of PVPh, indicating that both the signals of carbonyl carbons and the phenolic carbons can be employed in quantitative determination of the fraction of intermolecular hydrogen-bonding. $T_{1\rho}{}^H$s of the blends are measured by ^{1}H wide-line NMR as well as ^{13}C CP/MAS NMR techniques. It is found that both components exhibit the same $T_{1\rho}{}^H$, the value of which depends on the blend composition. This result agrees well with those of DSC measurements,

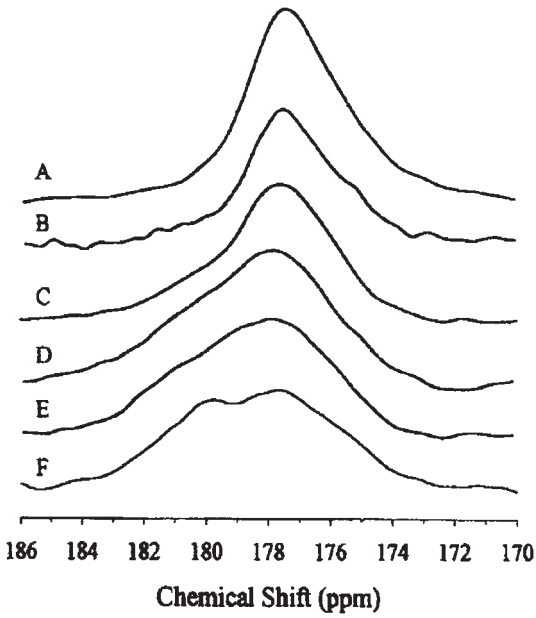

Fig. 10. ^{13}C CP/MAS spectra for the C=O resonance in the blends: (A) 100% PEEMA, (B) 85% PEEMA, (C) 75% PEEMA, (D) 55% PEEMA, (E) 45% PEEMA, (F) 30% PEEMA. (Figure 8 in original literature: D. J. T. Hill, A. K. Whittaker and K. W. Wong, *Macromolecules*, 1999, **32**, 5285.)

demonstrating that the blends are homogeneous. The scale of homogeneity is estimated to be about 2 nm from the value of $T_{1\rho}{}^{H}$.

Wang *et al.* studied the structure and dynamics of poly(aspartic acid) sodium (PAANa)/poly(vinyl alcohol) (PVA) blends by ^{13}C CP/MAS and ^{23}Na NMR spectrsocpy.[21,22] By comparing the ^{13}C CP/MAS spectra of the blends and the neat polymers, it is found that upon blending a new carbonyl peak appears at the high frequency side of the original carbonyl signal. This new peak is assigned to the carboxyl groups of the side chain of PAANa forming intermolecular hydrogen-bonds with the hydroxyl groups of PVA. The formation of intermolecular hydrogen-bonds is also evidenced by the intensity changes of the CH carbon of PVA upon blending. $T_1{}^{H}$ and $T_{1\rho}{}^{H}$ measurements via ^{13}C detection show that the miscibility of the blends is highly composition dependent, although certain amount of inter-polymer hydrogen-bonds exists. The miscibility of PAANa/PVA blend with a molar ratio of 1/1 is turned out to be the highest. This conclusion is supported by the results of the ^{23}Na MAS NMR spectra shown in Fig. 11. There are two peaks in ^{23}Na MAS spectrum of neat PAANa, which are corresponding to the isolated ^{23}Na (7 ppm) and associated ^{23}Na (−16 ppm), respectively. It is evident that in the spectrum of 1/1 blend, the peak of isolated ^{23}Na

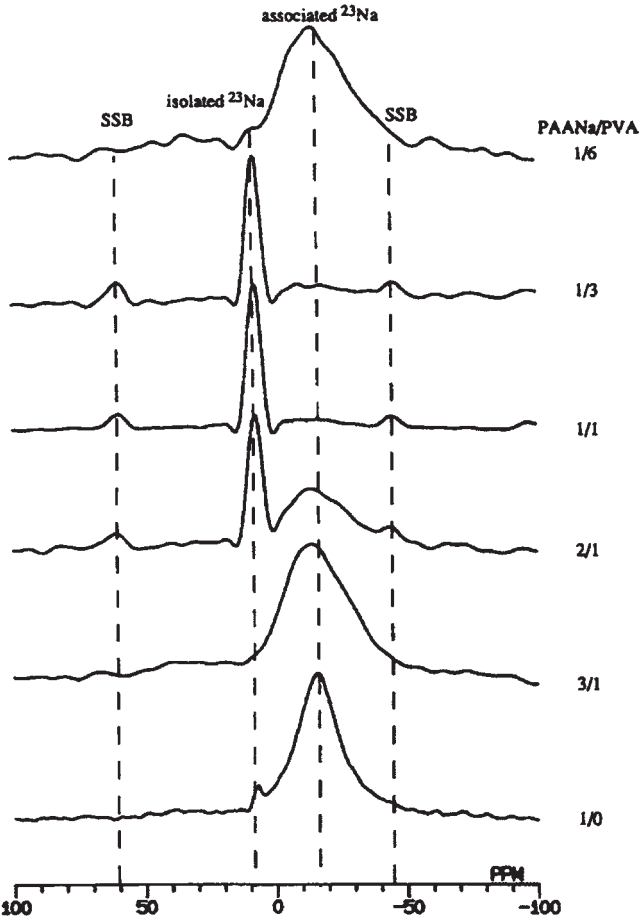

Fig. 11. ^{23}Na MAS NMR spectra of PAANa/PVA blends with various compositions at 25°C. (Figure 4 in original literature: P. Wang and I. J. Ando, *Mol. Struct*., 1999, **508**, 97.)

exhibits highest relative intensity, indicating enrichment of the inter-polymer hydrogen-bonding interaction which leads to a reduction of the possibility of COO^- and Na^+ association.

A series of polymer blends with inter-polymer specific interactions were studied by Mi *et al.* by using DSC, IR, and ^{13}C CP/MAS NMR techniques.[13,23–25] $T_1{}^H$, $T_{1\rho}{}^H$ and the cross-polarization transfer constant (T_{CH}) measurements as well as the spectral feature analyses were carried out to investigate the miscibility and inter-polymer interactions of the blends. The common feature of these works is there are chemical shift changes and/or signal broadening of the functional groups in the ^{13}C CP/MAS spectra upon blending, which are caused by the inter-polymer hydrogen-bonding

or dipolar–dipolar interactions. Such changes in spectral feature are direct evidence of intimate mixing. Measurement of T_{CH} is demonstrated to be a useful way of probing the inter-polymer interactions. In studying of poly(epichlorohydrin) (PECH)/poly(*N*-vinyl-2pyrrolidone) (PVP) blends,[23] the T_{CH} of the carbonyl carbon of PVP decreases from 0.99 ms to 0.28 ms upon blending, when the blend contains 30 wt% of PECH. This dramatic change is attributed to the inter-polymer hydrogen-bonds formed between the carbonyl groups of PVP and the α-protons of PECH, because the protons engaged in hydrogen bonds can serve as additional source of the ^{1}H–^{13}C magnetization transfer for the carbonyl carbons. Similar results are also observed in the blends of poly(hydroxyl ether of bisphenol A) (Phenoxy) with poly(ethyl oxazoline) (PEOx).[13] In the ^{13}C CP/MAS spectra of the blends, the relative intensity of the carbonyl peak of PEOx with respect to those of the other peaks of PEOx increases with increasing the content of Phenoxy, indicating the decrease of T_{CH} of the carbonyl carbon upon blending. This is also ascribed to the inter-polymer hydrogen-bonds formed between the carbonyl groups of PEOx and the hydroxyl groups of Phenoxy. For novolac/poly(ε-caprolactone)[24] and poly(vinyl chloride)/poly(*N*-vinyl pyrrolidone)[25] blends, it is interesting to find that poly(ε-caprolactone) and poly(vinyl chloride), which are semicrystalline before blending, remain to be partially crystallized, while the amorphous parts of these two polymers are intimately mixed with their counterparts.

2.2. Elongation induced phase separation

Inter-polymer hydrogen-bonding interaction is one of the driving forces that can make dissimilar polymer pair become miscible. Poly(vinyl alcohol) (PVA)/poly(acrylic-acid) (PAA) is a typical system of such kind of blends. Previous solid-sate NMR study has revealed that due to the strong inter-polymer hydrogen-bonding interaction between the hydroxyl group of PVA and the carboxyl group of PAA, molecular level miscibility of the blend is achieved. The crystalline phase of PVA can even be destroyed completely, when the molar ratio of vinyl alcohol is equal to or less than that of acrylic-acid in the blend. Recently, by employing both solid-state ^{13}C CP/MAS NMR and wide-angle X-ray diffraction, a new experimental phenomenon, which can be termed as elongation induced phase separation, was observed in the blends of PVA/PAA.[26]

Figure 12 shows the ^{13}C CP/MAS spectra of PVA, sample I and sample II, where sample I and sample II are corresponding to PVA/PAA blends with PAA contents in monomer molar of 0.27 and 0.53, respectively. Three overlapped peaks ranged from 65 ppm to 77 ppm are attributed to methine carbon of PVA and are designated to peaks 1, 2 and 3, respectively (Fig. 13). The assignment of these three methine peaks, which had been an attractive

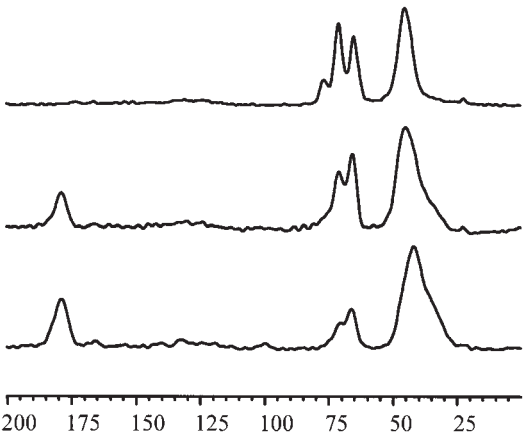

Fig. 12. ^{13}C CP/MAS spectra at room temperature: (a) PVA membrane sample; (b) sample I; (c) sample II. (Figure 1 in the original literature: Q. Chen, H. Kurosu, L. Ma and M. Matsuo, *Polymer*, 2002, **43**, 1203.)

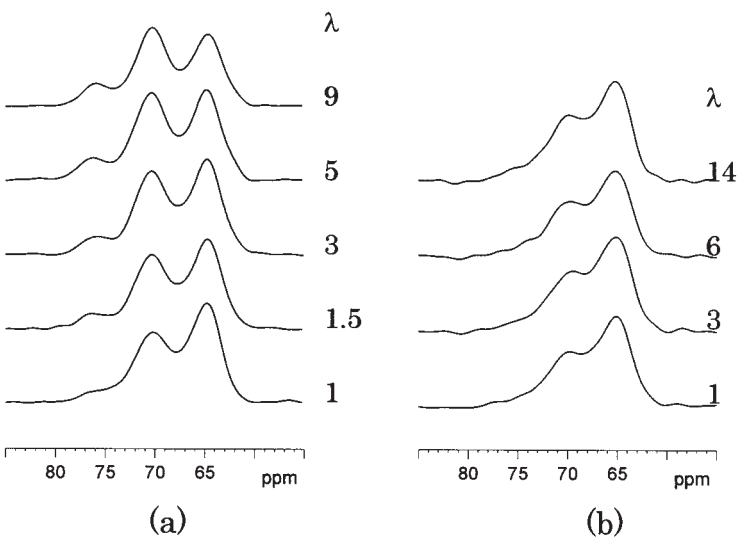

Fig. 13. ^{13}C CP/MAS spectra of the methine carbon of PVA: (a) sample I; (b) sample II with different draw ratios (λ). (Figure 2 in the original literature: Q. Chen, H. Kurosu, L. Ma and M. Matsuo, *Polymer*, 2002, **43**, 1203.)

research topic,[27,28] can be simply described as follows: Peaks 1, 2 and 3 are due to central methine carbons in triad sequences forming two, one and no hydrogen-bonds between hydroxyl groups. As is shown in Fig. 12, the relative intensities of peak 1 and peak 2 decrease with increasing PAA content, indicating the increase of the number of inter-polymer hydrogen bonds formed

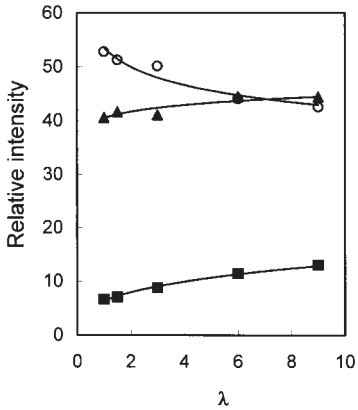

Fig. 14. Plots of the relative intensities of three methine peaks in the ^{13}C CP/MAS spectra of sample I against the draw ratio (λ), where (■), (▲) and (○) are corresponding to the data of peaks 1, 2 and 3, respectively. (Figure 3 in the original literature: Q. Chen, H. Kurosu, L. Ma and M. Matsuo, *Polymer*, 2002, **43**, 1203.)

between hydroxyl and carbonyl groups at the expense of intra-polymer hydrogen bonds formed between hydroxyl groups. This is a direct evidence of molecular level miscibility of the blends. Figure 14 shows the methine carbon signals of sample I and sample II with different draw ratios. Relative intensities of these three peaks as a function of the draw ratio are plotted in Fig. 15. From these two figures, it is evident that for sample I the relative intensity of peak 3 decreases with increasing of the draw ratio, while the relative intensities of peak 2 and peak 3 increase steadily. At the maximum draw ratio ($\lambda = 9$), the relative intensities of these three methine peaks are very close to those of the PVA membrane sample. Such a result suggests that phase separation has occurred during the elongation process. Because of the phase separation, the hydroxyl groups of PVA are able to form more intra-polymer hydrogen-bonds, as in the case of neat PVA. What is interesting is that no noticeable changes in the relative intensities of the three methine peaks with the variation of draw ratio are observed in the spectra of sample II, suggesting that the elongation induced phase separation phenomenon of PVA/PAA blends is composition dependent. Figure 4 depicts the X-ray diffraction intensity curves of sample I and sample II. The difference between the results of these two samples is obvious. The appearance of more diffraction peaks with the increase of draw ratio for sample I indicates that the degree of crystallinity increases upon elongation. This, in turn, provides further evidence for elongation induced phase separation in the sample. On the other hand, no apparent changes can be observed in the X-ray diffraction curves of sample II with increasing of draw ratio, demonstrating that PVA in the blend remains to be amorphous even at the maximum draw ratio.

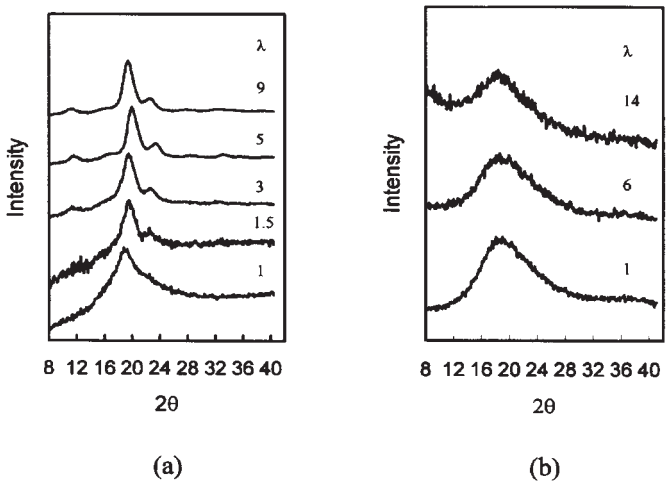

Fig. 15. X-ray diffraction intensity curves normalized to the same total intensity: (a) sample I; (b) sample II with different draw ratios (λ). (Figure 4 in the original literature: Q. Chen, H. Kurosu, L. Ma and M. Matsuo, *Polymer*, 2002, **43**, 1203.)

It is apparent that the results of X-ray diffraction agree with those obtained from NMR study.

In order to further testify the aforementioned conclusions, $T_{1\rho}{}^{H}$s of the drawn and undrawn blend samples were measured by employing ^{13}C CP/MAS method. It is found that for samples I and II before elongation, $T_{1\rho}{}^{H}$s of PVA and PAA are very close to each other, demonstrating both of them are miscible blends. However, upon elongation, the behaviour of these two samples becomes different. For sample II, the difference between the $T_{1\rho}{}^{H}$s of PVA and PAA is still within experimental error; while for sample I, marked difference can be observed. This means that for sample I upon elongation, PVA and PAA are no longer miscible on a scale of 2–3 nm. The results of $T_{1\rho}{}^{H}$ measurements, on the other hand, provide direct support to the conclusion that phase separation does happen in PVA/PAA blends with certain composition upon elongation.

2.3. Spin diffusion

Direct ^{1}H spin-diffusion measurements have been demonstrated to be a powerful tool for probing the domain size and the structural heterogeneity of multiphase polymers, including polymer blends.[29,30] These experiments normally consist of three steps: the first step is a selection period for generating an initial polarization gradient between different phase components. The second step is corresponding to a mixing time, τ_m, during which

diffusion of magnetization through dipolar interactions equilibrates the distribution of polarization. In the third step, the distribution state of polarization after τ_m is read out. By analyzing the evolution of polarization distribution with τ_m, quantitative determination of the domain size and evaluation of the degree of heterogeneity can be made.

The initial polarization gradient between different phase components can be generated by utilizing either the difference in mobility or the difference in structures of individual phase components. The mobility difference at experimental temperature can lead to difference in relaxation times like ^1H T_2, $T_{1\rho}{}^H$ etc. The differences in relaxation times can then be employed to selectively suppress the magnetization of the phase component with shorter relaxation time, while retaining the magnetization of the component with longer one. The selection of magnetization by traditional Goldman-Shen and 'dipolar filter' pulse sequences,[31,32] which are most commonly used in spin-diffusion experiments, are all based on differences in ^1H T_2 of the components. On the other hand, in ^1H solid-state high-resolution spectrum acquired by techniques like CRAMPS, signals due to different structures can be selectively suppressed or inverted.[33,34] Then the initial polarization gradient between different phase components can also be created. The read-out step of the spin-diffusion experiments can be fulfilled by directly analyzing the ^1H lineshape[35] or by indirectly monitoring the ^{13}C signal intensity changes via cross-polarization.[36]

As reviewed in the previous section, measurements of $T_1{}^H$ and $T_{1\rho}$ can provide an estimation of the length scale of miscibility of polymer blends. Compared with such kinds of experiments, the results of the spin-diffusion experiments are more quantitative and straightforward. The accuracy of the results of spin-diffusion experiments relies, to a large extent, on the values of spin-diffusion coefficients (D) employed in calculation of the constituent phase components. Despite efforts that have been made,[37] there still lacks a suitably applicable method of directly measuring the spin-diffusion coefficients, at least for polymers. For rigid polymer below T_g, 0.8 nm^2/ms has been turned out to be a reliable value of spin-diffusion coefficient.[38] The difficulty left then concerns how to determine the coefficient of the mobile phase, which is very sample dependent. Recently, through studies on diblock copolymers and blend samples with known domain sizes, Mellinger *et al.*[39] established empirical relations between the ^1H T_2 and D as follows:

$$D = (8.2 \times 10^{-6}\, T_2^{-1.5} + 0.007)\ \mathrm{nm^2/s} \quad \text{for } 0 < T_2^{-1} < 1000\ \mathrm{Hz}$$

and

$$D = (4.4 \times 10^{-4}\ T_2^{-1} + 0.26)\ \mathrm{nm^2/s} \quad \text{for } 1000 < T_2^{-1} < 3500\ \mathrm{Hz} \qquad (3.1)$$

The ^{1}H T_2 of the mobile phase is determined by a Carr-Purcell-Meiboom-Gill (CPMG) pulse sequence in that work. Based on an easily accessible NMR parameter, i.e., ^{1}H T_2, the above empirical correlation, which is claimed by the authors to be sample independent, gives a practical way to estimate the ^{1}H spin-diffusion coefficient of the mobile phase of a multiphase system and should be applicable to future studies on polymer blends either by relaxation times or direct ^{1}H spin-diffusion measurements.

In recent years, the investigation of the miscibility and heterogeneity of polymer blends by ^{1}H spin-diffusion continues to be a field of active research. Jack *et al.*[40] measured the domain sizes of compatibilized Polystyrene-(Ethylene-Propylene Rubber) blends by experiments of ^{1}H spin-diffusion. What is worth while to mention is that the domain sizes of the blend samples studied in the work are about one order of magnitude larger than those which are thought to be suitable for ^{1}H spin-diffusion measurement. This is evident by the fact that T_1^H relaxation times of polystyrene (PS) and Ethylene-Propylene Rubber (EPR), which are inherently quite different from each other, are not significantly altered upon blending. Therefore, one purpose of the work is to investigate the applicability of ^{1}H spin-diffusion measurement for studying the domain structure of immiscible blends. The selection step of the ^{1}H spin-diffusion experiments is fulfilled by employing the dipolar filter pulse sequences and the spin-diffusion process is monitored indirectly by observing the ^{13}C signals. Due to the large domain size of EPR, only a very limited amount of inter-domain spin-diffusion is observed during a mixing time of 300 ms. However, by using the 'initial rate approximation',[29] the average sizes of the dispersed EPR particles in blends can still be estimated. Because the agreement between the average domain sizes measured by NMR and SEM is poor, the authors concluded that quantitatively the NMR method employed in the work is not suitable to determine the average sizes of domains that are great than a few hundreds of nanometers. On the other hand, because the reduction tendency in the average EPR particle size upon addition of compatibilizer is reflected by the results of NMR, it is suggested that ^{1}H spin-diffusion method is qualitatively applicable for studying the domain structures of immiscible blends.

Study on the blends of ethylene-propylene-diene terpolymer (EPDM) and atactic polypropylene (aPP) reported by Silva *et al.*,[41] is another case of immiscible blends investigated by ^{1}H spin-diffusion. For a 50/50 blend, T_1^Hs of EPDM and aPP are found to be 300 and 700 ms, respectively, indicating the blends are clearly a phase-separated system. The WISE pulse sequence,[29] which is usually employed to monitor the ^{1}H spin-diffusion process in a 2D manner, is used in an alternative way: After the first $\pi/2$ pulse, the magnetization is allowed to dephase for 40 μs. During this period, the polarization of aPP is destroyed, while most of the EPDM polarization is still remained. The second $\pi/2$ pulse flips the remaining magnetization back to z direction to allow T_1^H relaxation to occur in a period of τ_m. It is apparent

that the starting points of T_1^H relaxation for EPDM and aPP are quite different from each other. The recovered polarization is finally read out via the ^{13}C signal. By doing so, the T_1^H relaxation curves of both polymers are obtained. It is found that the relaxation curve of aPP consists of two relaxation components. One is related to the original T_1^H relaxation. The additional relaxation which corresponds to a time constant of about 170 ms, is attributed to inter-domain spin-diffusion. The domain size of aPP is then estimated to be 13 nm. The above work demonstrates that for immiscible blends, the impact of inter-domain spin-diffusion, which is not observable in standard T_1^H relaxation measurement, can possibly be revealed by employing the WISE pulse sequence with suitable initial conditions. A similar idea is used by Ricardo *et al.*[42] in the study of Blends of natural rubber (NR) and polyurethane (PU). Because the constituent polymers exhibit different values of T_1^H, the blends are immiscible from point of view of NMR. By employing the standard Goldman-Shen pulse sequence to detect T_1^H relaxation of the blend, a small degree of spin-diffusion between NR and the hard segment of PU is observed.

For polymer blends constituted by a semicrystalline polymer, the miscibility study often becomes even complicated, due to the existence of one or two additional crystalline domains. Harris *et al.*[43] reported a NMR investigation on sodium poly(α-L-glutamate)/Poly(ethylene oxide) blend. The blends consist of one crystalline poly(ethylene oxide) (PEO) domain, one amorphous PEO domain, which is rather mobile, and one rigid sodium poly(α-L-glutamate) (PGNa) domain. The comparative study between PEO/PGNa blends and neat PEO by ^{13}C CP/MAS NMR and double quantum NMR spectroscopy indicates that the PEO crystallites are undisturbed upon blending. ^1H spin-diffusion measurement by a standard Goldman-Shen pulse sequence with ^{13}C detection demonstrates proximity of amorphous PEO and PGNa on a 10 nm scale.

Brus *et al.*[44] reported a solid-state NMR study on the blends of polycarbonate (PC) and PEO. Because both constituent polymers are semicrystalline, complicated domain models need to be considered. Figure 16 shows the 2D exchange ^1H NMR spectra of the 1:1 PC-PEO blend measured at different mixing times. The pulse sequence used is proposed by Caravatti *et al.*[45] and based on the CRAMPS (combination of rotation and multiple-pulse spectroscopy) technique. The diagonal peaks are, from left to right, corresponding to aromatic protons of PC, methylene protons of PEO and methyl protons of PC, respectively. As is evident by the figure, the cross-peaks indicating spin-diffusion between methylene proton of PEO and both type protons of PC become perceptible in the spectrum of 300 μs mixing time. This indicates the smallest distance between amorphous PC and amorphous PEO is about 0.5–0.6 nm. In order to evaluating the domain sizes quantitatively, WISE experiments are carried out. The spin-diffusion curves indicate that for 1:1 and 1:4 PC-PEO blends, there exist two spin-diffusion

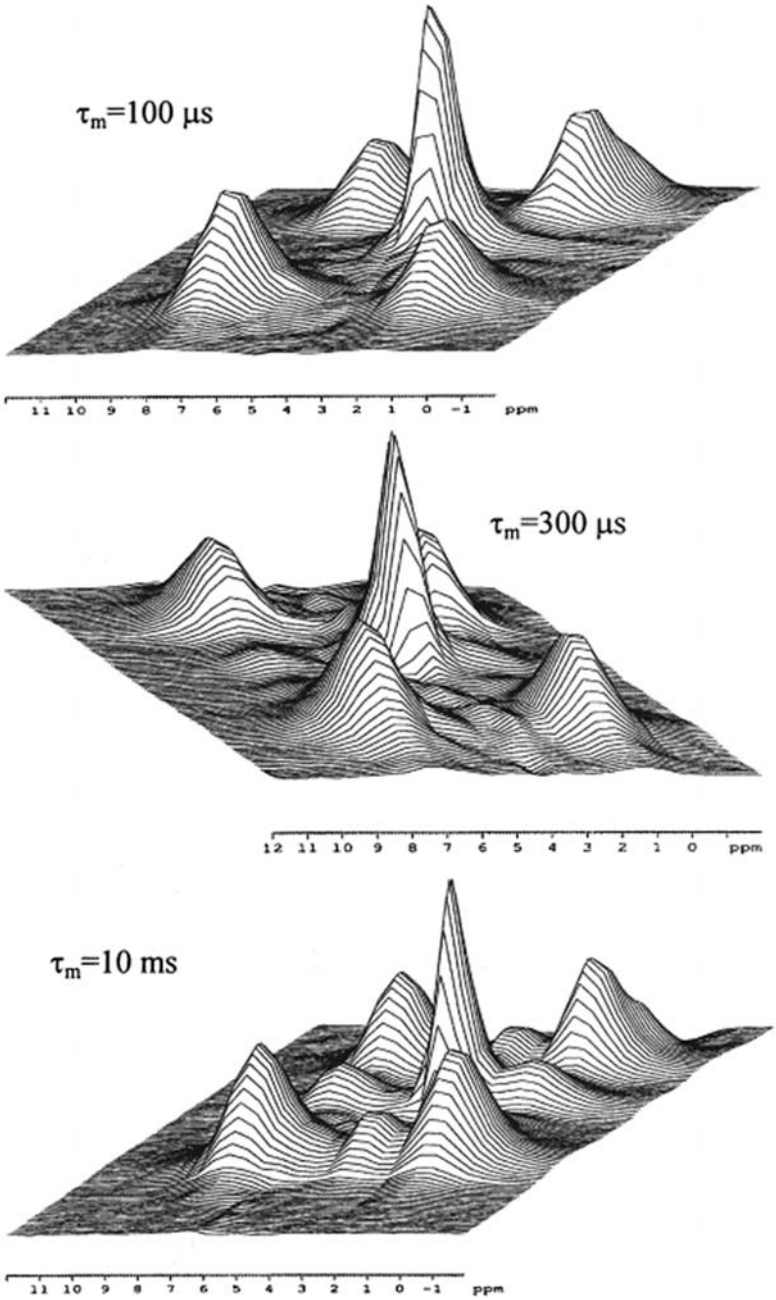

Fig. 16. 2D ^{1}H exchange NMR spectra (CRAMPS, BR24) of the 1:1 PC-PEO blend measured at different mixing times τ_m. (Figure 11 in the original literature: F. M. Mulder, W. Heinen, M. van Duin, J. Lugtenburg and H. J. M. de Groot, *Macromolecules*, 2000, **33**, 5544.)

processes. The first process corresponds to a fast magnetization transfer form mobile amorphous PEO to adjacent PC. The second slow process is due to the spin-diffusion started from amorphous PEO to crystalline PEO domain and finally to a part of PC which is assumed to be located in the inter-lamellar region of PEO. The domain model is therefore rather complicated. Numeric simulation is carried out to evaluate the spin-diffusion curves. The domain sizes and the morphology are then determined.

Mulder *et al.*[46] have studied the microscopic dynamic properties of the blends of Poly(methyl methacrylate) (PMMA) and a rubbery epoxy resin (PPO) with poly(propylene oxide) backbone. The NMR techniques involved are the standard Goldman-Shen experiment with ^{13}C detection and the WISE experiment. For the blend containing 50% PPO, the mobile domain size determined by ^{1}H spin-diffusion experiment is found to be larger than the PPO domain sizes determined by TEM. Such a result suggests that a part of PMMA is mobile in the material. As is expected, in the 2D WISE spectrum with zero spin-diffusion time, the ^{13}C signals of PPO are correlated with narrow ^{1}H lines and a very little amount ($< 5\%$) of a broader signal. This result indicates that at least 95% of the PPO polymer chains are mobile. The ^{13}C signals of PMMA, on the other hand, correlate with both broad and narrow ^{1}H lines, demonstrating further that a part of PMMA is mobile. In the 2D wise spectrum with a spin-diffusion time of 50 ms, the lineshape of PPO signals are hardly changed. This shows that during the spin-diffusion time of 50 ms, the polarization transfer between the rigid PMMA phase and the mobile PPO phase is very small. However, the lineshape of PMMA signals changed greatly. The ^{13}C signals of PMMA are now correlated with a strong narrow ^{1}H line, while the contribution of the broad component is greatly reduced. This suggests that ^{1}H spin-diffusion has equilibrated the polarization of the mobile and rigid PMMA within 50 ms, which suggests that the mobile part and the rigid part of PMMA are intimately associated. The mobile part of PMMA is estimated to be at least 40%. From the above experimental results, one interesting conclusion is drawn that the mobility of PMMA is largely enhanced at the low-frequency region by the microscopic morphology of the blend. The authors pointed out that such kind of mobility enhancement is in line with the depression of glass temperature in thin polymer films, which is a hot topic in the field of polymer physics in recent years.

By employing solid-state ^{1}H NMR techniques with fast magic-angle spinning, Mirau and Yang[47] studied the structure and dynamics of block and random ethylene oxide/propylene oxide copolymers and their composites with poly(methyl silsesquioxane). It is demonstrated that for the block copolymer embedded in the matrix of poly(methyl silsesquioxane), the segment of ethylene oxide becomes amorphous and mobile, although it is highly crystallized before blending. ^{1}H spin-diffusion measurement with a dipolar-filter pulse sequence is then carried out to determine the domain size

of copolymers in the composites. The domain sizes of block and random copolymers embedded in the composites are 4.8 nm and 7.3 nm, respectively. The NMR results, thereofore, show that the composites are very promising as ultralow-k dielectric materials. It is worth while to note that in order to avoid the possible influence of magic-angle spinning on the spin-diffusion coefficients, the ^{1}H spin-diffusion experiments are carried out in the static state.

A common feature of the above spin-diffusion experiments is to use the difference in relaxation times of the constituent polymers to create polarization gradient as the starting point of spin-diffusion. To do so, it is necessary that the constituent polymers have distinct difference in their mobility at the experimental temperatures. Mulder *et al.*[48] reported a ^{1}H spin-diffusion study on the cross-linking induced phase separation in SAN/SMA semi-interpenetrating networks, where SAN is a copolymer of styrene and acrylonitrile and SMA is a copolymer of styrene and maleic anhydride. Both copolymers are rigid at room temperature. It is therefore not possible to create a polarization gradient by utilizing the difference in ^{1}H relaxation times of the constituents. Instead of using ^{1}H CRAMPS spectroscopy, the authors employed the CP^{3} NMR spin-diffusion technique.[49] For this purpose, SAN is ^{13}C-enriched to 98% at the CN position and SMA is enriched to 98% at the CO and CH_2 positions. Figure 17 illustrates the 2D version and the 1D versions of CP3 pulse sequence. Both pulse sequences consist of three stages of CP. After the first polarization transfer from ^{1}H, ^{13}C magnetization is allowed to evolution in the period of t_1. Following a second CP transfer, the chemical shift modulated ^{13}C magnetization is transferred back to ^{1}H, and equilibration of magnetization proceeds via ^{1}H spin-diffusion. Finally, after a third CP transfer, the encoded information is detected with ^{13}C MAS NMR. As is stated by the authors, the method combines the high resolution nature of ^{13}C MAS for selection and detection with the efficient spin-diffusion via strong ^{1}H dipolar interactions. For the 1D version of the pulse sequences, a rotor synchronized DANTE pulse sequence is used to reverse the ^{13}C signal of the CN group, to create a large polarization gradient between the components. The variation of the normalized intensity of ^{13}CN signal of SAN with the spin-diffusion time t_m, is monitored, which describes the ^{1}H spin-diffusion process between components. Figure 18 shows the 2D ^{13}C–^{13}C NMR correlation spectra of the phase separated semi-interpenetrating network of SAN and SMA (50/50%; w/w) with 35% cross-linker (4,4′-methylenedianiline). For Fig. 18a, where a zero spin-diffusion time is used, strong intramolecular cross-peaks between the CO and CH_2 groups of SMA are observed, indicating that the last two CP's (totally 2 ms) are long enough for intramolecular spin-diffusion to occur. Figure 18b with a spin-diffusion time of 40 ms, shows clear intermolecular cross-peaks, demonstrating that there is a substantial inter-domain spin-diffusion. In Fig. 19, the normalized intensities of the ^{13}CN signal, acquired with the 1D version of

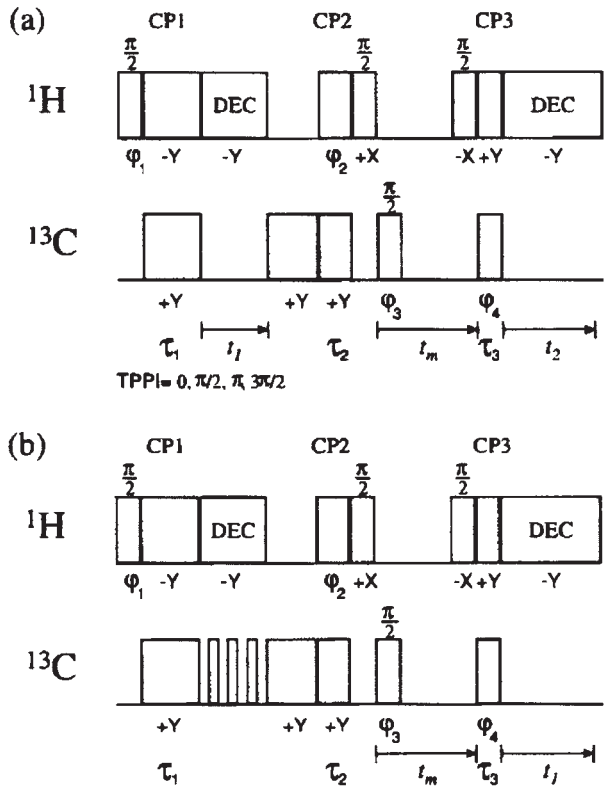

Fig. 17. CP[3] NMR pulse sequences for probing ^{1}H spin-diffusion with ^{13}C selection and detection, using 2D ^{13}C–^{13}C correlation spectroscopy (a) and using 1D inversion recovery experiment including a selective rotor-synchronized DANTE inverse period (b). (Figure 2 in the original literature: F. M. Mulder, W. Heinen, M. van Duin, J. Lugtenburg and H. J. M. de Groot, *Macromolecules*, 2000, **33**, 5544.)

the pulse sequences, are plotted against the square root of the spin-diffusion time t_m. The domain-sizes are estimated by using the standard procedures.[1] It is demonstrated that there exists a linear correlation between the domain sizes and the amount of cross-linker in SAN/SMA semi-interpenetrating network.

2.4. WISE experiments

It is known that information about the domain size, morphology and local dynamics of the blends can be obtained by 2D WISE measurements.[2950–54] The pulse sequence for the 2D WISE experiment (Fig. 20a) consists of three 90° pulses applied in the proton channel followed by a CP transfer to the

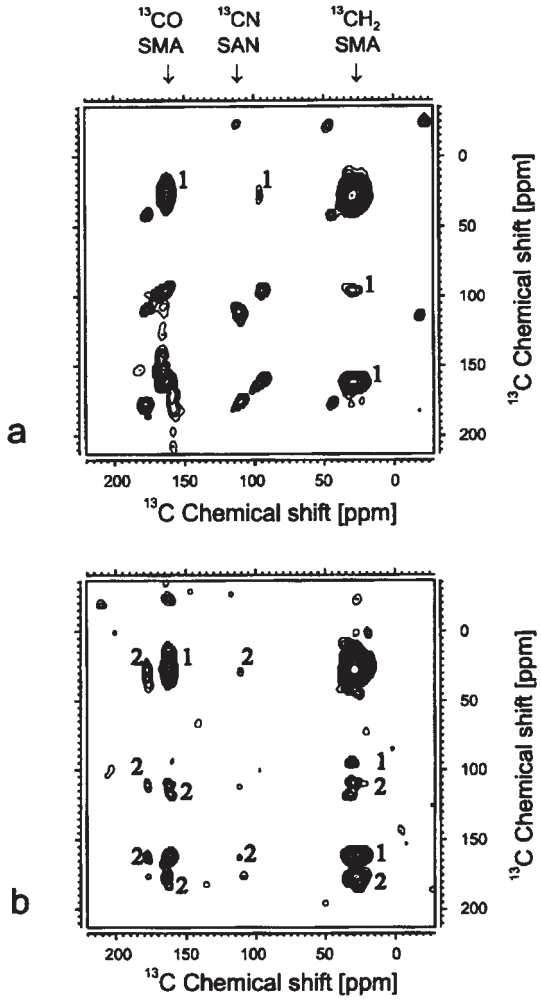

Fig. 18. 2D ^{13}C–^{13}C NMR correlation spectra of the phase separated semi-interpenetrating network of selectively ^{13}C labelled SAN and SMA (50/50; w/w) with 35% cross-linker. The measurements used duration τ_1, τ_2 and τ_3 of 2, 1, and 1 ms, respectively. The spin-lock time following t_1 was 400 μs, and the spinning speed was $\omega_r/2\pi = 6550 \pm 3$ Hz. (a) Data set collected with a mixing time $t_m = 0$ ms. The ^{13}CO and ^{13}CH$_2$ of SMA resonate at 196 and 20 ppm, respectively. The correlations resulting from intramolecular magnetization exchange in SMA is indicated with **1**. (b) $t_m = 40$ ms. The ^{13}CN peak in SAN has an isotropic chemical shift of 114 ppm, with a strong sideband at 180.5 ppm that yields the more intense inter-domain correlations. They are indicated with a **2**. (Figure 3 in the original literature: F. M. Mulder, W. Heinen, M. van Duin, J. Lugtenburg and H. J. M. de Groot, *Macromolecules*, 2000, **33**, 5544.)

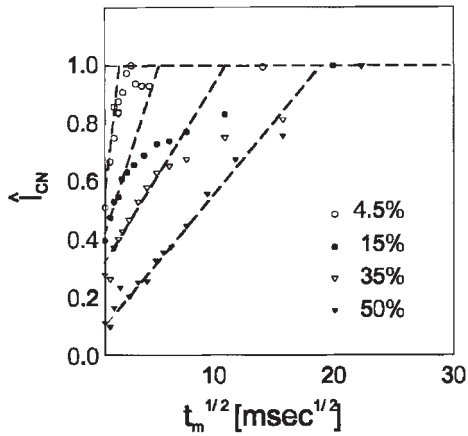

Fig. 19. Intensity $\hat{I}_{CN}$ of the CN sideband pattern of ^{13}C labelled SAN versus the square root of the mixing time t_m. The numbers indicate the amount of 4,4′-methylenedianiline cross-linker added as a percentage of the amount of MA monomers in the blend. (Figure 4 in the original literature: F. M. Mulder, W. Heinen, M. van Duin, J. Lugtenburg and H. J. M. de Groot, *Macromolecules*, 2000, **33**, 5544.)

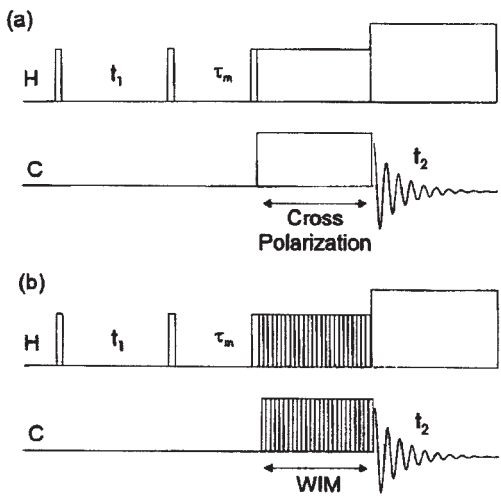

Fig. 20. The pulse sequence for 2D (a) WISE and (b) WIM/WISE NMR. t_1: ^1H evolution time, t_m: ^1H spin diffusion (mixing) time, t_2: detection time. (Figure 1 in the original literature: X. Qiu and P. A. Mirau, *J. Magn. Reson.*, 2000, **142**, 183.)

carbon system. Two-dimensional Fourier transformation yields a data matrix with the carbon frequency along one axis and the proton frequency along the other. It is typically most informative to view the data as cross sections through the 2D matrix. Since the chemical shift range for protons (5 kHz) is

much smaller than the linewidths (ca. 50 kHz), wideline spectra are observed in the t_1 dimension. Mirau *et al.* applied a modified version of 2D WISE experiment with windowless isotropic mixing (WIM) instead of CP to polystyrene (PS)/poly(vinyl methyl ether) (PVME) blend sample.[55] The pulse sequence for 2D WIM/WISE experiment is shown in Fig. 20b. The 2D WIM/WISE experiment provides an unambiguous measure of the proton dynamics because the lineshapes are not averaged by spin diffusion during the windowless isotropic mixing. The rate of spin diffusion is a factor of two less than that for the exchange of z magnetization,[29] but significant spin-diffusion can occur during the cross polarization contract times (1–2 ms) that are typically used in the solid state NMR analysis of polymers. Therefore, protons appear with a motionally narrowed lineshape in the WISE spectrum, not from molecular motion, but from spin diffusion. By using WIM instead of simple cross polarization, it can be correlated the carbon chemical shifts with the proton linewidths without the effect of spin diffusion, and the lineshapes can be related to the dynamics of individual groups in polymer chains. Figure 21 shows a contour plot of the WIM/WISE spectrum of the 50/50 molar PS/PVME blend at 27°C. The contour plot shows that very different proton linewidths are observed for the polystyrene and PVME chains, and Fig. 22 compares cross sections through the WIM/WISE spectra for the aromatic peak of polystyrene and the main chain methine peak of PVME. The aromatic protons in pure polystyrene have a full width at

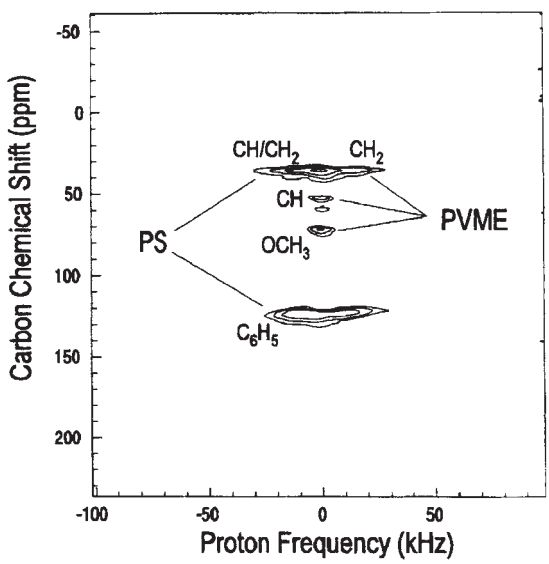

Fig. 21. A contour plot for the WIM/WISE spectrum of the polystyrene/poly(vinyl methyl ether) blend. (Figure 5 in the original literature: X. Qiu and P. A. Mirau, *J. Magn. Reson.*, 2000, **142**, 183.)

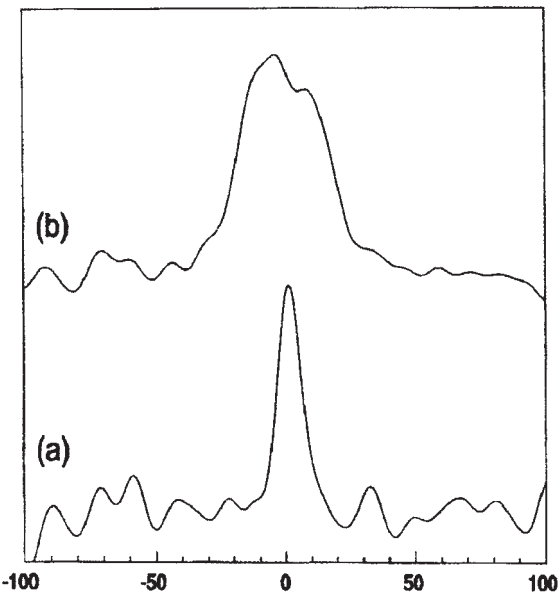

Fig. 22. Cross sections through the WIM/WISE spectrum of the polystyrene/poly(vinyl methyl ether) blend at the frequency of the (a) poly(vinyl methyl ether) methine carbon and the (b) polystyrene aromatic carbon resonance. (Figure 6 in the original literature: X. Qiu and P. A. Mirau, *J. Magn. Reson.*, 2000, **142**, 183.)

Table 6. WIM/WISE linewidths for the polystyrene aromatic protons and the poly(vinyl methyl ether) main chain methine protons as a function of temperature

Temperature (°C)	Linewidth (kHz)	
	PS C_6H_5	PVME CH
27	35.7	12.4
50	29.5	11.0
80	9.0	11.1

half maximum of 40 kHz while the same peak in the blend has a width of 36 kHz. This demonstrates that the aromatic rings are more mobile in the blend, and that they feel the effect of being dissolved in a matrix with the lower Tg PVME. The opposite effect is observed for PVME. PVME has a Tg of 31°C and chain motion at ambient temperature averages the proton lineshape to 6 kHz, WIM/WISE NMR shows that the methine motion is restricted relative to the pure PVME in the blend with polystyrene, where a 12 kHz linewidth is observed. WIM/WISE NMR has also been used to study the

effect of temperature on the chain dynamics for the PS/PVME blend, and some of the results are shown in Table 6. The polystyrene aromatic proton linewidth is reduced from 36 kHz at 27°C to 30 kHz at 50°C to 9 kHz at 80°C. By contrast, the already averaged lineshape of PVME changes to a much smaller degree over this temperature range.

REFERENCES

1. K. Takegoshi, *Annu. Rep. NMR Spectrosc.*, 1995, **30**, 97.
2. A. Asano and K. Takegoshi, *Solid State NMR of Polymers*, Chapter 10, I. Ando and T. Asakura, eds., Elsevier, Netherlands, 1998, 351.
3. S. W. Kuo and F. C. Chang, *Macromolecules*, 2001, **34**, 4089.
4. V. J. McBrierty and D. C. Douglass, *Polym. Sci., Macromol. Rev.*, 1981, **16**, 295.
5. D. E. Demco, A. Johansson and J. Tegenfeldt, *Solid State Nucl. Magn. Reson.*, 1995, **4**, 13.
6. J. Clauss and K. Schmidt-Rohr, *Acta Polym.*, 1993, **44**, 1.
7. A. Asano, M. Eguchi, M. Shimizu and T. Kurotsu, *Macromolecules*, 2003, **25**, 8819.
8. C. Lau and Y. Mi, *Polymer*, 2002, **43**, 823.
9. R.-H. Lin, E. M. Woo and J. C. Chiang, *Polymer*, 2001, **42**, 4289.
10. J. J. Dechter, *J. Polym. Sci., Polym. Lett. Ed.*, 1985, **23**, 261.
11. J. Wang, M. K. Cheung and Y. Mi, *Polymer*, 2001, **42**, 2077.
12. J. Wang, M. K. Cheung and Y. Mi, *Polymer*, 2001, **42**, 3087.
13. C. Lau, S. Zheng and Y. Mi, *Macromolecules*, 1998, **31**, 7291.
14. K. S. Jack and A. K. Whittaker, *Macromolecules*, 1997, **30**, 3560.
15. D. L. VanderHart and A. N. Garroway, *J. Chem. Phys.*, 1979, **71**, 2773.
16. P. P. Chu, J. M. Huang, H. D. Wu, C. R. Chiang and F. C. Chiang, *J. Polym. Sci. Polym. Phys. Ed.*, 1999, **37**, 1155.
17. C. De Kesel, C. Lefàvre, J. B. Nagy and C. David, *Polymer*, 1999, **40**, 1969.
18. J. Nakano, S. Kuroki, I. Ando, T. Kameda, H. Kurosu, T. Ozaki and A. Shoji, *Biopolymer*, 2000, **54**, 81.
19. H. D. Wu, C. C. Ma and F. C. Chang, *Macromol. Chem. Phys.*, 2000, **201**, 1121.
20. D. J. T. Hill, A. K. Whittaker and K. W. Wong, *Macromolecules*, 1999, **32**, 5285.
21. P. Wang and I. Ando, *J. Mol. Struct.*, 1999, **508**, 103.
22. P. Wang and I. Ando, *J. Mol. Struct.*, 1999, **508**, 97.
23. M. K. Cheung, S. X. Zheng, Y. L. Mi and Q. P. Guo, *Polymer*, 1998, **39**, 6289.
24. Z. K. Zhong, Q. P. Guo and Y. L. Mi, *Polymer*, 1998, **40**, 27.
25. S. X. Zheng, Q. P. Guo and Y. L. Mi, *J. Polym. Sci. Polym. Phys. Ed.*, 1999, **37**, 2412.
26. Q. Chen, H. Kurosu, L. Ma and M. Matsuo, *Polymer*, 2002, **43**, 1203.
27. T. Terao, S. Maeda and A. Saika, *Macromolecules*, 1983, **16**, 1535.
28. M. Kobayashi, I. Ando, T. Ishii and S. Amiya, *Macromolecules*, 1995, **28**, 6677.
29. K. Schmidt-Rohr and H. W. Spiess, *Multidimensional Solid State NMR and Polymers*, Academic Press, London, 1994 and references therein.
30. I. Ando and T. Asakura, eds., *Solid-State NMR of Polymers*, Elsevier Science, Tokyo, 1998, 351–414 and references therein.
31. M. Goldman and L. Shen, *Phys. Rev.*, 1966, **144**, 321.
32. N. Egger, K. Schmidt-Rohr, B. Blumich, W. D. Domker and B. Stapp, *J. Appl. Polym. Sci.*, 1992, **44**, 289.
33. P. Caravatti, P. Neuenschwander and R. R. Ernst, *Macromolecules*, 1986, **19**, 1889.
34. D. L. VanderHart, Y. Feng, C. C. Han and R. A. Weiss, *Macromolecules*, 2000, **33**, 2206.
35. R. A. Assink, *Macromolecules*, 1978, **11**, 1233.

36. K. Schmidt-Rohr, J. Clauss, B. Blumich and H. W. Spiess, *Magn. Reson. Chem.*, 1990, **28**, 3.
37. W. Zhang and D. G. Cory, *Phys. Rev. Lett.*, 1998, **80**, 1325.
38. J. Clauss, K. Schmidt-Rohr and H. W. Spiess, *Acta Polym.*, 1993, **44**, 1.
39. F. Mellinger, M. Wilhelm and H. W. Spiess, *Macromolecules*, 1999, **32**, 4686.
40. K. S. Jack, A. Natansohn, J. Wang, B. D. Favis and P. Cigana, *Chem. Mater.*, 1998, **10**, 1301.
41. N. M. Silva, M. I. B. Tavares and E. O. Stejskal, *Macromolecules*, 2000, **33**, 115.
42. N. M. Ricardo, M. Lahtinen, Colin Price and F. Heatley, *Polym. Int.*, 2002, **51**, 627.
43. D. J. Harris, T. J. Bonagamba and K. Schmidt-Rohr, *Macromolecules*, 2002, **35**, 5724.
44. J. Brus, J. D. Schmidt, J. Kratochvil and J. Baldrian, *Macromolecules*, 2000, **33**, 6448.
45. P. Caravatti, P. Neuenschwander and R. R. Ernst, *Macromolecules*, 1985, **18**, 119.
46. F. M. Mulder, B. J. P. Jansen, P. J. Lemstra, H. E. H. Meijer and H. J. M. de Groot, *Macromolecules*, 2000, **33**, 457.
47. P. A. Mirau and S. Yang, *Chem. Mater.*, 2002, **14**, 249.
48. F. M. Mulder, W. Heinen, M. van Duin, J. Lugtenburg and H. J. M. de Groot, *Macromolecules*, 2000, **33**, 5544.
49. F. M. Mulder, W. Heinen, M. van Duin, J. Lugtenburg and H. J. M. de Groot, *J. Am. Chem. Soc.*, 1998, **120**, 12891.
50. K. Schmidt-Rohr, J. Clauss and H. W. Spiess, *Macromolecules*, 1992, **25**, 3237.
51. N. M. da Silva, M. I. B. Tavares and E. O. Stejskal, *Macromolecules*, 2000, **33**, 115.
52. I. Quijada-Garrido, M. Wilhelm, H. W. Spiess and J. M. Barrales-Rienda, *Macromol. Chem. Phys.*, 1998, **199**, 985.
53. J. Brus, J. Dybal, P. Schmidt, J. Kratochvil and J. Baldrian, *Macromolecules*, 2000, **33**, 6448.
54. D. J. Harris, T. J. Bonagamba and J. Schmidt-Rohr, *Macromolecules*, 2002, **35**, 5724.
55. X. Qiu and P. A. Mirau, *J. Magn. Reson.*, 2000, **142**, 183.

Structural Characterization of Si-based Polymer Materials by Solid-State NMR Spectroscopy

SHIGEKI KUROKI, HIDEAKI KIMURA AND ISAO ANDO

Department of Chemistry and Materials Science, International Research Center of Macromolecular Science, Tokyo Institute of Technology, Ookayama, Meguro-ku, Tokyo, Japan

Structural characterization of silicon-based polymers, with the properties of both organic materials such as light weight, high flexibility and modability and inorganic materials such as high thermal stability and high strength, by means of solid-state ^{1}H, ^{13}C, ^{29}Si, and ^{11}B NMR methods have been reviewed. These studies lead to the development of new molecular designs which improve upon the already excellent material properties.

ANNUAL REPORTS ON NMR SPECTROSCOPY
VOLUME 52 ISSN 0066 4103
DOI 10.1016/S0066-4103(04)52005-7

1. INTRODUCTION

Silicon (Si)-based polymers with the properties both of organic materials such as light weight, high flexibility, and modability and inorganic materials such as high thermal stability and high strength have been extensively studied over more than 30 years.[1–4] These polymer materials have been developed for use in various fields. For example, poly(silylenemethylene)s with the repeating Si–C backbone units, Si-based interpenetrating polymer networks with the Si–C and Si–O backbone units and silicon-based polymer networks with the C≡C–Si(CH_2–)–Ph, C≡C–Si(Ph)–C=C–, C–Si(CH_3)$_2$–C–$B_{10}H_{10}$C, and C–Si(CH_3)$_2$–OCH_3 units as considered in this review article have been widely studied in order to improve the already excellent material properties.

In order to develop new polymer materials, the design has been performed on the basis of advanced polymer science and technology. The properties of polymer materials are closely related to their structures and dynamics. From such situations, the establishment of methods for elucidating the structures and dynamics is important for making reliable polymer materials and developing new advanced polymer gels. In Si-based polymer materials, although the mobility of network polymer chains is much higher than in rigid solids, it is much lower than in linear organic polymer materials. Thus, by taking into account such a difference in molecular motion between the mobile and immobile regions, solid-state high-resolution NMR proves to be a useful tool to characterize such systems.

From such a background, the structure and dynamics of Si-based polymer materials by solid-state NMR[5–11] have been widely used in order to make reliable polymer designs and to develop new advanced polymer materials. Details of the most recent work on structural and dynamic characterization of Si-based polymer materials by solid-state NMR will be reviewed, in addition mention is made of a review on inorganic polymer materials by Takayama.[52]

2. EXPERIMENTAL

2.1. Materials

2.1.1. *Si-based silyleneethynylene polymers and silylenemethylene polymers*

2.1.1.1. Poly[(phenylsilylene)ethynylene-1,3-phenyleneethynylene], [–Si(Ph)H–C≡C–Ph–C≡C–]$_n$

Si-based polymers composed of [–SiR_1R_2–C≡C–](R_1, R_2=alkyl, phenyl, or H) units have been prepared because of their potential applications in areas such as ceramic precursors and conducting materials.[12–16] Poly(phenylsilyleneethynylene-1,3-phenyleneethynylene), [–Si(Ph)H–C≡C–Ph–C≡C–]$_n$ (MSP)

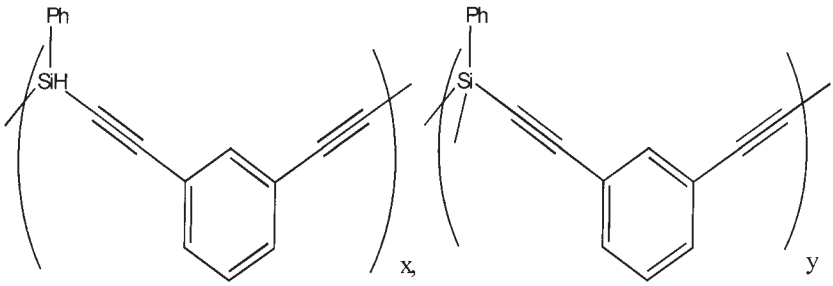

Fig. 1. Chemical structure of MSP.

(Fig. 1), is prepared by a dehydrogenative coupling polymerization reaction between phenylsilane and *m*-diethynylbenzene in the presence of magnesium oxide, which has an extremely high thermal stability by curation.[12,13]

The thermosetting reaction of MSP occurs above 150°C, and an exothermic peak at 210°C is observed in the DSC curve.[12,13] From the TGA–DTA curves of MSP, there is no weight loss during curation under argon below 400°C, and the TG–MS results[21] show that there is no evolution of a cracking product below 400°C. It is found that the infrared absorption bands of the Si–H and C≡C bonds of MSP are gradually reduced by curation.[13] The elemental composition obtained by elemental analysis[22] is not changed by curation. From these results, it is assumed that an additional cross-linking reaction involving the Si–H and C≡C bonds might have occurred to form a highly thermally stable structure.

2.1.1.2. Poly(diphenylsilmethylene) and poly(methylphenylsilmethylene)
Poly(silylenemethylene)s (PSM) with the repeating Si–C backbone units are one of the most well examined carbosilane polymers, and a number of research activities can be found in the literature.[17–21] The largest interest in the study of PSMs seems to be the pyrolytic profiles of these polymers to SiC ceramics. Despite the above situation, there is little research work on the thermal or mechanical properties rather than on the pyrolytic properties of PSMs. Several works on the synthesis and the pyrolytic behaviour of PSMs, and on the basic physical properties and the thermal and mechanical properties of poly(diphenylsilmethylene) (PDPhSM), and poly(methylphenylsilmethylene) (PMPhSM) have appeared (Fig. 2). The melting temperature of PDPhSM is about 350°C, and the glass transition temperature (T_g) is ca. 140°C. On the other hand, the T_g of PMPhSM is around 20°C. The thermal and mechanical properties of these two polymers are very different. The difference of these properties seems to come from the structures and dynamics of the Si–C backbone and side-chains.

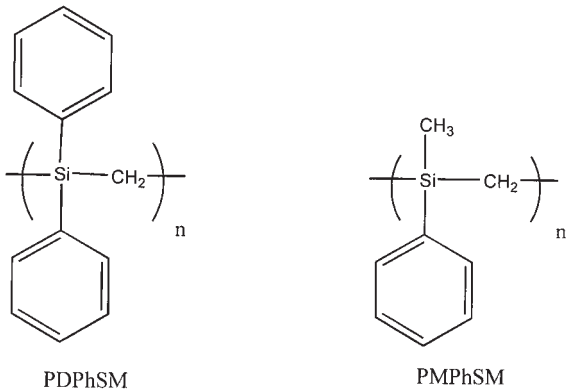

PDPhSM PMPhSM

Fig. 2. Chemical structures of PDPhSM and PMPhSM.

2.1.2. *Si-based interpenetrating polymer networks*

Recently, Si-based organic–inorganic composites have been prepared and studied by many groups.[1–4,22–24] The hybrid materials have been expected to have both the properties of organic materials such as light, flexible, moldability, etc., and inorganic materials such as thermally stable, high strength, etc. These materials are expected to be used in a wide variety of applications. Similarly, other approaches to improve the thermal and mechanical properties of polymer materials, interpenetrating polymer networks (IPN) are widely studied with much interest.[22–24] Many carbon-based IPN materials have been synthesized and the thermal and mechanical properties of IPN materials are improved compared with each of the components or their mechanical blends.[24] Tsumura, *et al.* have reported that the synthesis of silicon-based IPNs consisting of the stable Si–O and Si–C linkages,[25] and have used a ladder silsesquioxane oligomer (LDS) and a polycarbosilane (PCS) as the two components for the IPN. It is shown that the thermal and mechanical properties of cured LDS/PCS (8/2) are better than those of each of the components. The structural characterization by solid-state NMR of the phase structure and miscibility of silicon-based IPN systems, that is five LDS/PCS curing systems (LDS/PCS=10/0, 8/2, 5/5, 2/8, and 0/10 [wt/wt]) as obtained by condensation reaction and hydrosilylation reaction for ladder silsesquioxane oligomer (commercial name is Glass Resin GR100) (LDS) and polycarbosilane (PCS), respectively, is described. The chemical structures of LDS and PCS are shown in Fig. 3.

2.1.3. *Silyl-carborane hybrid Si-based polymer networks*

The chemical structure of the silyl-carborane hybrid Si-based polymer discussed in this review is shown in Fig. 4.[26,27] The polymer contains the 1,7-dicarba-*closo*-dodecarborane (*m*-carborane) group in the side chains as well as

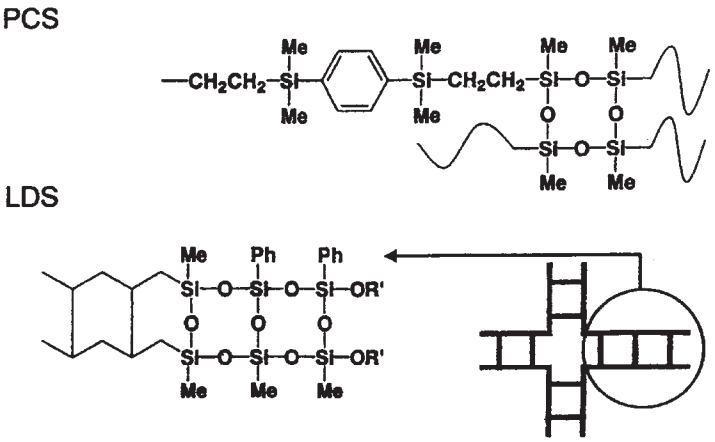

Fig. 3. Chemical structures of LDS and PCS.

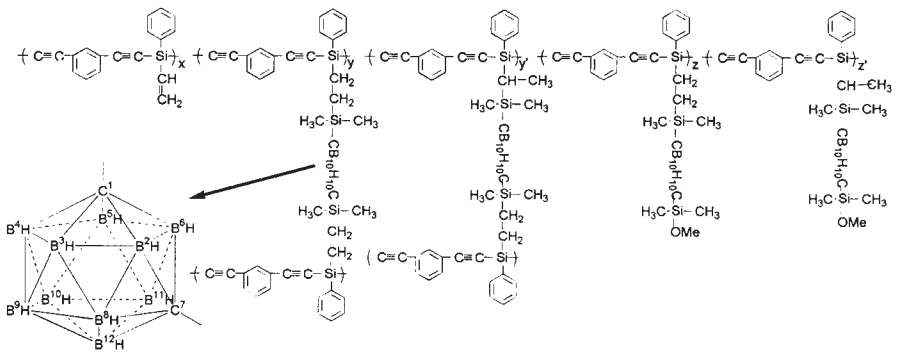

Fig. 4. Chemical structure of the silyl-carborane hybrid diethynylbenzene–silylene polymer.

the Si and the C≡C group in the main chain. The *m*-carborane group also has a remarkable thermal stability.[28–38] The silyl-carborane hybrid Si-based polymer exceeds other polymers in heat resistance in air.[26] The 5% weight loss temperature (T_{d5}) of the polymer cured at 350°C under air is over 1000°C as shown by thermogravimetric analysis (TGA). The oxygen concentration to burn the polymer cured at 350°C (the oxygen index) is over 40%.

The silyl-carborane hybrid diethynylbenzene-silylene polymer is prepared by a hydrosilylation reaction between diethynylbenzene-silylene polymer with the reactive vinyl side group and the 1,7-bis(dimethylsilyl)carborane group in toluene as solvent.[26] The weight-average molecular weight of the polymer is determined to be 22,400 by using JASCO 802-SC gel permeation chromatography (GPC). The samples cured at 350 and 500°C are molded at 250°C for 6 min and pressed at 1795 kg/cm^2 under vacuum for 30 s.

Table 1. Characteristics of silyl-carborane hybrid diethynybenzene–silylene polymers

Sample	Curing condition	OI[a]	HDT (°C)[b]	FM (GPa)[c]
A-1	as received	–	–	–
A-2	A-1 was molded and pressed at 250°C[d]	34	132	2.28
A-4	A-2 was thermally cured at 350°C[e]	40	> 380[f]	2.66
A-500	A-2 was thermally cured at 500°C[g]	> 50	> 380[f]	–[h]

[a]The oxygen index.
[b]Heat deflection temperature.
[c]Flexural modulus.
[d]Molded for 6min and pressed at 1795 kg/cm^2 under vacuity for 30 s.
[e]Cured for 1 h.
[f]More than 380°C.
[g]Cured for 30 min.
[h]Too brittle.

The curing condition and mechanical characteristics of these samples are summarized in Table 1, for which the flexural modulus is determined by a Shimazu Autograph AG-5000B.

2.2. NMR measurements

2.2.1. *One-dimensional solid-state NMR*

At first, we introduce 1D solid-state NMR methods such as cross polarization/magic angle spinning (CP/MAS) and dipolar decoupling/magic angle spinning (DD/MAS).[8–11] Thus, we explain two types of CP/MAS variations. One is the CP + dipolar dephasing (DDph) method (Fig. 5(a)) and another is the $T_{1\rho}{}^{H}$ measurment (Fig. 5(b)).

The CP+dipolar dephasing (CP/DDph) method (Fig. 5(a)) is a spectrum-editing technique used to suppress rate spins such as ^{13}C strongly coupled to the abundant spin such as the ^{1}H system (CH_2 and CH signals) because they decay rapidly during the time decoupling. Other signals from the carbons which couple weakly with protons (quaternary C and CH_3) survive since their decay is slow during the τ_{dd} period.

$T_{1\rho}{}^{H}$ can be measured by changing the spin-locking time for ^{1}H after the ^{1}H 90 degree pulse for the CP method shown as Fig. 5(b), and then can be determined from the plots of the peak intensity against the spin-locking time.

In an abundant ^{1}H spin system, ^{1}H–^{1}H homonuclear dipolar coupling in solids is very large and the ^{1}H signal is broadened to about 50 kHz. Since this large ^{1}H linewidth is sufficiently larger than the typical MAS rate of several kHz, we cannot observe the ^{1}H high resolution NMR spectrum in solids by only using the MAS method. Under these situations, it is very useful to use multiple

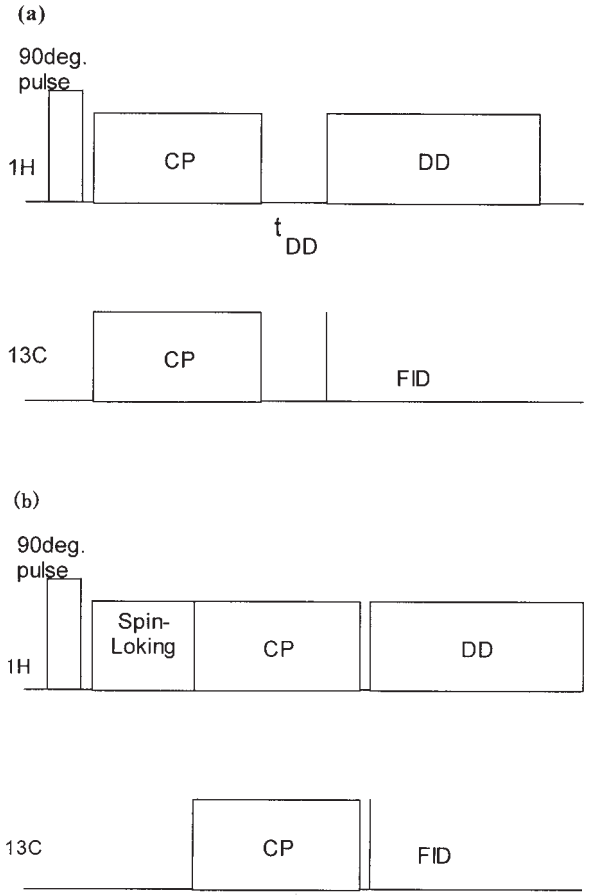

Fig. 5. Pulse sequence of the CP+DDph method (a) and $T_{1\rho}{}^{H}$ measurement using the CP method (b).

pulse techniques such as WAHUHA, MREV8, BR24, etc., to reduce dipolar broadening in conjunction with MAS.[39] This method is the so-called CRAMPS (combined rotation and multiple-pulse spectroscopy).

2.2.2. *Two-dimensional solid-state NMR*

Two-dimensional (2D) NMR method is very useful to get information about interatomic interactions as a function of interatomic distance.[8–11] Thus, this method is sometimes used to discover whether two different kinds of polymer chains in blend are miscible with each other or not. For example, the ^{13}C–^{13}C 2D exchange NMR spectrum gives information on whether two kinds of ^{13}C nuclei are close to each other, which may belong to a polymer chain or to each of two different polymer chains. If cross peaks exist in a 2D ^{13}C–^{13}C exchange spectrum, two ^{13}C nuclei are very close to each other in

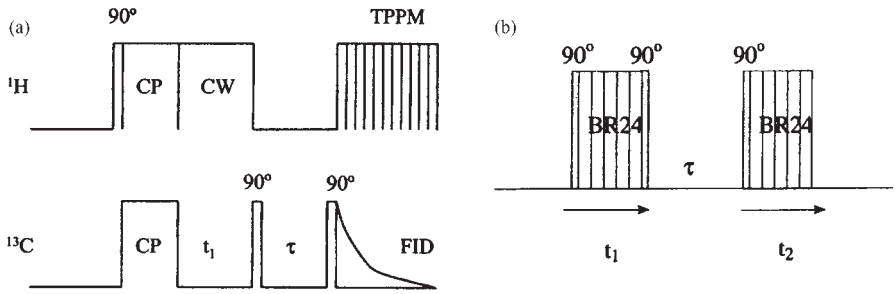

Fig. 6. The pulse sequences for measuring the ^{13}C–^{13}C 2D exchange NMR spectrum (a) and for measuring the ^{1}H–^{1}H 2D exchange NMR spectrum (b).

distance. The pulse sequence as shown in Fig. 6(a) is used with the mixing time of 0.5 s and the acquisition number was 80×128. Also, ^{1}H–^{1}H 2D NOESY NMR with the BR24 ^{1}H homonuclear decoupling pulse is very useful to get information about interatomic interactions as a function of proton–proton distance like ^{13}C–^{13}C 2D exchange NMR. The ^{1}H 90° pulse length is 1.5 μs and the mixing time is 100 μs. The acquisition number is 16. The pulse sequence for the ^{1}H–^{1}H 2D NOESY NMR spectrum is shown in Fig. 6(b).

2.2.3. *MQ/MAS NMR*

The multiple-quantum (MQ)/MAS NMR[40–44] is one of the 2D NMR methods, which is capable of averaging out the second-order quadrupolar interaction in nuclei with spin $>1/2$ such as ^{2}H, ^{11}B, ^{17}O, etc. The ^{11}B MQ/MAS NMR measurements on boron as contained in silyl-carborane hybrid Si-based polymer networks considered here. The molded samples are cut into small pieces to insert them into a 4-mm NMR rotor and spun at 12 kHz in a MAS probe. The observation frequency of the ^{11}B nucleus (spin number $I = 3/2$ and isotope natural abundance = 80.42%) is 96.3 MHz. Excitation of both the echo (−3Q) and anti echo (+3Q) coherences is achieved by using a three-pulse sequence with a zero quantum filter (*z*-filter). The widths of the first, second, and third pulses are 3.0–4.1 μs, 1.1–1.6 μs, and 19–28 μs, respectively. The *z*-filter is 20 μs. The recycle delay time is 6–15 s and the data point of F1 (vertical) axis is 64 and for each the number of scans is 144. Then, the total measurement time is 15–38 h. The phase cycling used in this experiment consists of 12 phases. Boron phosphate (BPO_4; $\delta = 0$ ppm) is used as an external standard for ^{11}B. The chemical shift value of BPO_4 is −3.60 ppm from $BF_3{\cdot}O(C_2H_5)_2$ which is used as a standard reference in ^{11}B NMR in the liquid state. The transmitter frequency of ^{11}B is set on peak of BPO_4 for a trustworthy chemical shift after Fourier transform.[45,46]

3. STRUCTURAL CHARACTERIZATION OF Si-BASED SILYLENEETHYNYLENE POLYMERS AND SILYLENEMETHYLENE POLYMERS MATERIALS

3.1. Thermosetting structural characterization of MSP

3.1.1. *Structural characterization by ^{13}C solid-state NMR*

Figure 7 shows ^{13}C CP/MAS spectra of MSP samples cured at various temperatures.[47] Peaks at 87.1 and 107.6 ppm in the spectrum of the MSP sample before curing are assigned to the C≡C carbons. These peaks decrease in intensity and are broadened with an increase in curing temperature and vanish by curation at 400°C. The peak at 122.3 ppm as assigned to the

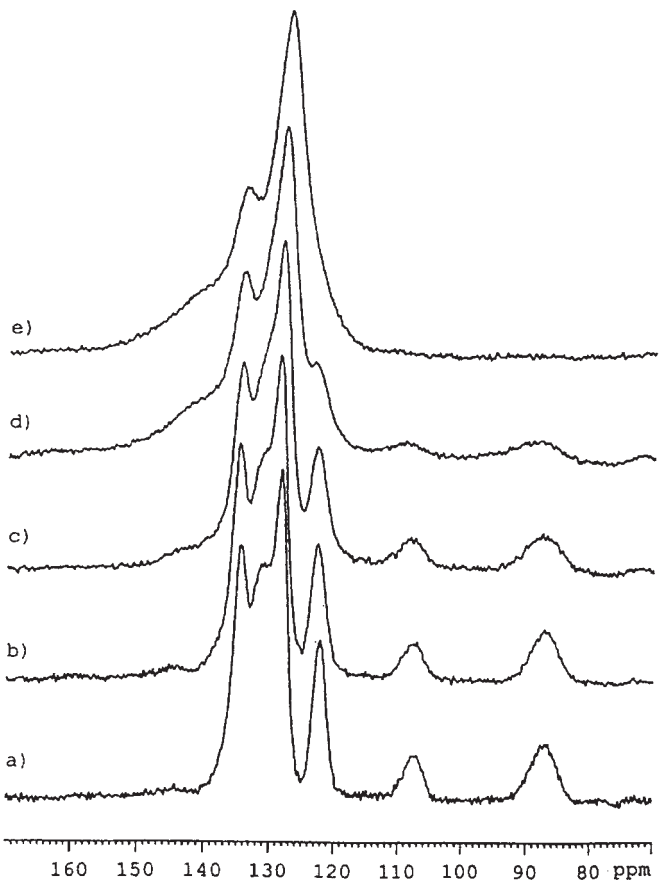

Fig. 7. ^{13}C CP/MAS NMR spectra of MSP cured at various temperatures: (a) before curing, (b) at 150°C, (c) at 200°C, (d) at 300°C, and (e) at 400°C.

phenylene carbons bonded to the C≡C decreases in intensity and is broadened with an increase in curing temperature, and disappears by curation at 400°C in the same way. Every peak is broadened with an increase in curing temperature. The broadening of peaks may come from the conformational distribution of the products by a cross-coupling reaction. Peaks which appear at 0–100 ppm as assigned to sp^3 carbons these do not appear on curing. The cured MSP samples have a new peak at 144 ppm, which increased in intensity and are broadened with an increase in curing temperature. This peak can be assigned to the C=C carbons and the phenyl carbons bonded to the C=C bond.

Figure 8 shows ^{13}C CP+DDph (dipolar dephasing)/MAS spectra of the MSP samples cured at various temperatures. The peaks appearing in the spectrum come from the carbons which are weakly coupled with protons. On the other hand, the peaks which come from the carbons strongly coupled with protons disappear in the spectra. Peaks at 87.1 and 107.6 ppm in the spectrum of the non-cured MSP sample are assigned to the C≡C carbons, the peak at 122.3 ppm to the phenylene carbon bonded to the C≡C carbons, and the peak at 136.3 ppm to the side-chain phenyl carbon bonded to Si. These carbons do not have directly-bonded protons. In addition, two peaks at 128.6 and 134.9 ppm which are assigned to the side-chain phenyl carbons, appear. These carbons have directly-bonded protons. However, dipole–dipole interactions with protons vanish due to the flip-flop motion of the phenyl ring, so that these peaks can be observed.

The MSP sample cured at 150°C shows two new peaks at 131.8 ppm and 144 ppm. The peaks come from the carbons without directly-bonded protons. Although there is no change in the intensity of the peak at 131.8 ppm, that at 144 ppm increases in intensity and is broadened with an increase in curing temperature. The peak at 131.8 ppm corresponds to the 4a and 8a position carbons of the naphthalene ring and that at 144 ppm corresponds to the C=C carbons and the phenyl carbons bonded to the C=C bond, and the biphenyl bonds carbons.

From the ^{13}C solid-state NMR results, it is suggested that naphthalene rings may be formed and that the C≡C bonds change into C=C bonds by curation. The naphthalene rings may be produced by the coupling reaction between two C≡C bonds, and the C=C bonds may be caused by the hydrosilylation reaction between the Si–H and C≡C over a wide range of temperatures from 150 to 400°C.

3.1.2. *Structural characterization by ^{29}Si solid-state NMR*

^{29}Si CP/MAS spectra of the MSP sample before curing and cured at 400°C are shown in Fig. 9.[47] These indicate that the MSP sample before curing has three peaks at −70.3, −65.0, and −60.8 ppm as assigned to the branched Si without directly-bonded protons, SiH and SiH_2 in the end-group. The MSP sample cured at 400°C shows a very broad peak with a half width of 2969 Hz

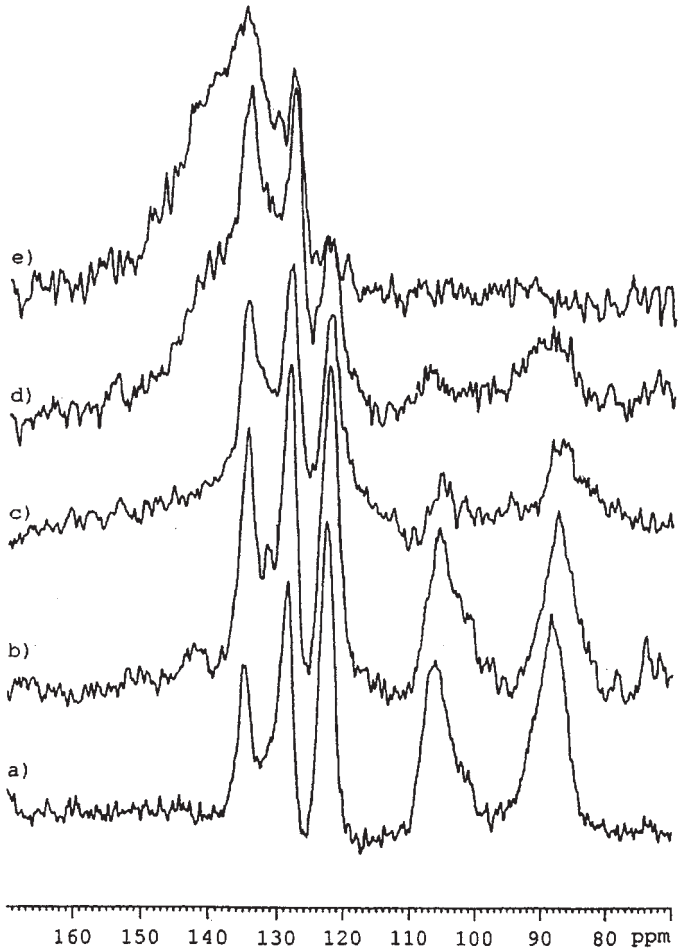

Fig. 8. ^{13}C CP/MAS+DDph NMR spectra of MSP cured at various temperatures: (a) before curing, (b) at 150°C, (c) at 200°C, (d) at 300°C, and (e) at 400°C.

at −11.9 ppm. Figure 10 shows the dipolar dephasing decays of the peaks for the branched ^{29}Si without directly-bonded protons which appears at −70.3 ppm and the ^{29}Si with directly-bonded protons which appears at −65.0 ppm in the spectrum of the MSP sample before curing, and for the ^{29}Si signal which appears at −11.9 ppm in the spectrum of the MSP sample cured at 400°C. The dipolar-dephasing relaxation time (T_{dd}) of the Si with directly-bonded protons in the MSP sample before curing is 0.437 ms, and that of the branched Si is 1.776 ms. The T_{dd} of the Si in the MSP sample cured at 400°C is 1.298 ms. This value is close to that of the branched Si without directly-bonded protons in the MSP sample before curing.

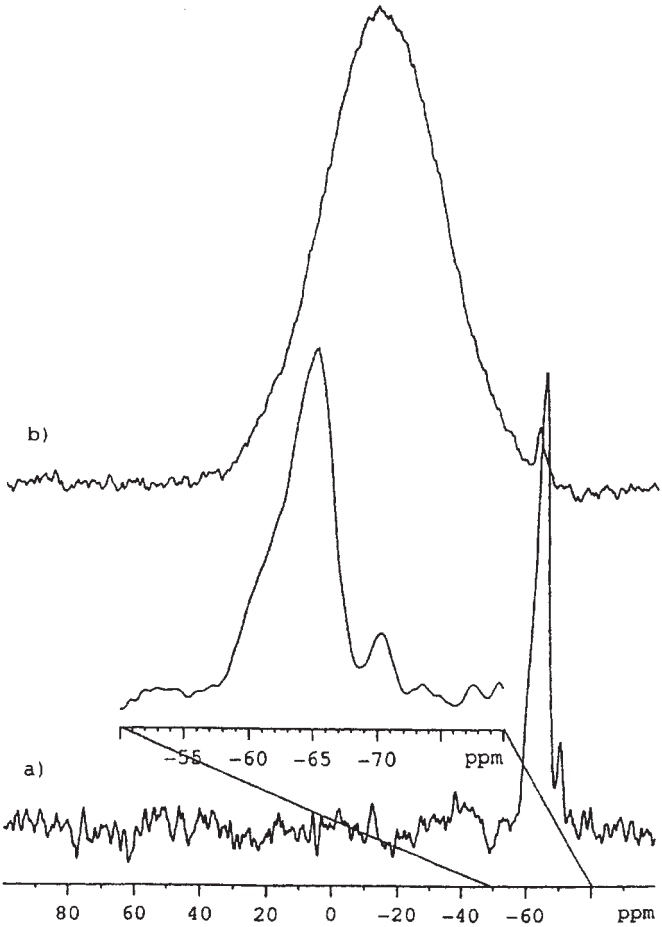

Fig. 9. ^{29}Si CP/MAS NMR spectra of MSP: (a) before curing and (b) after curing at 400°C.

This indicates that most of the Si atoms of cured MSP do not have directly-bonded protons.

Figure 11 shows the ^{29}Si CP/MAS spectra of the MSP sample cured at various temperatures. The MSP sample cured at 150°C has a new peak at −37 ppm. The T_{dd} of this peak is 0.685 ms, so that it comes from a Si with directly-bonded protons. From the ^{13}C NMR results, it is apparent that the peak comes from the Si–H caused by the coupling reaction between two C≡C bonds. The MSP sample cured at 200°C has two new peaks at −50 and −17 ppm, respectively. From the T_{dd} measurements of poly(methylsilyleneethynylene-1,3-phenyleneethynylene),[47] the peak at −50 ppm comes from the Si with directly-bonded protons and the peak at −17 ppm comes from the Si without directly-bonded protons. By considering the ^{13}C NMR results,

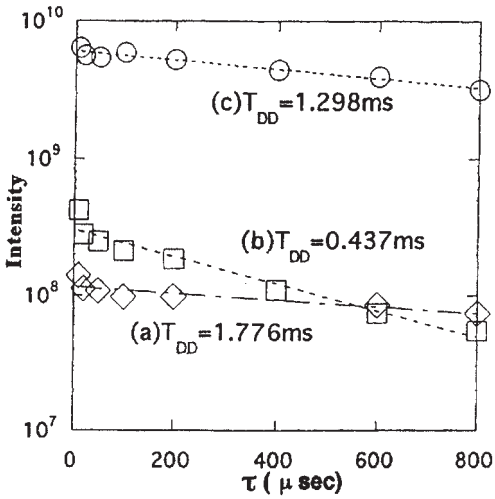

Fig. 10. Dipolar dephasing decays of the branched ^{29}Si without directly-bonded protons (a) and the ^{29}Si with directly-bonded protons (b) of MSP before curing, and ^{29}Si signal of MSP cured at 400°C (c), respectively.

it seems that the peak at −50 ppm comes from Si–H and that at −17 ppm comes from a Si without directly-bonded protons formed by the hydrosilylation reaction. In the spectrum of the MSP sample cured at 300°C, especially the intensity of the peak at −17 ppm, which comes from a Si without directly-bonded protons, is increased. In the MSP sample cured at 400°C a very broad signal appears at −11.9 ppm.

From the solid-state ^{13}C and ^{29}Si NMR results, it can be said that the thermosetting reaction of MSP is due to: (1) the Diels-Alder reaction between the Ph–C≡C and the C≡C and (2) the hydrosilylation reaction between the Si–H and the C≡C (Fig. 12).

It seems that a new signal at −37 ppm of the MSP sample cured at 150°C can be assigned to a Si–H formed by the Diels-Alder reaction. Finally, every Si of MSP cured at 400°C changes into Si atoms that do not have directly-bonded protons by the hydrosilylation reaction.

3.2. Structural characterization of PDPhSM and PMPhSM

3.2.1. *Structural characterization at room temperature*

Figure 13(a) shows the ^{29}Si and ^{13}C CP/MAS NMR spectra of PDPhSM at room temperature.[48] The ^{29}Si CP/MAS NMR spectrum has two sharp peaks at −7.6 and −9.3 ppm and in the intensity ratio is about 1:1. The T_1 value of the peak at −7.6 ppm is 273 s, and that of the peak at −9.3 ppm is 306 s. Thus,

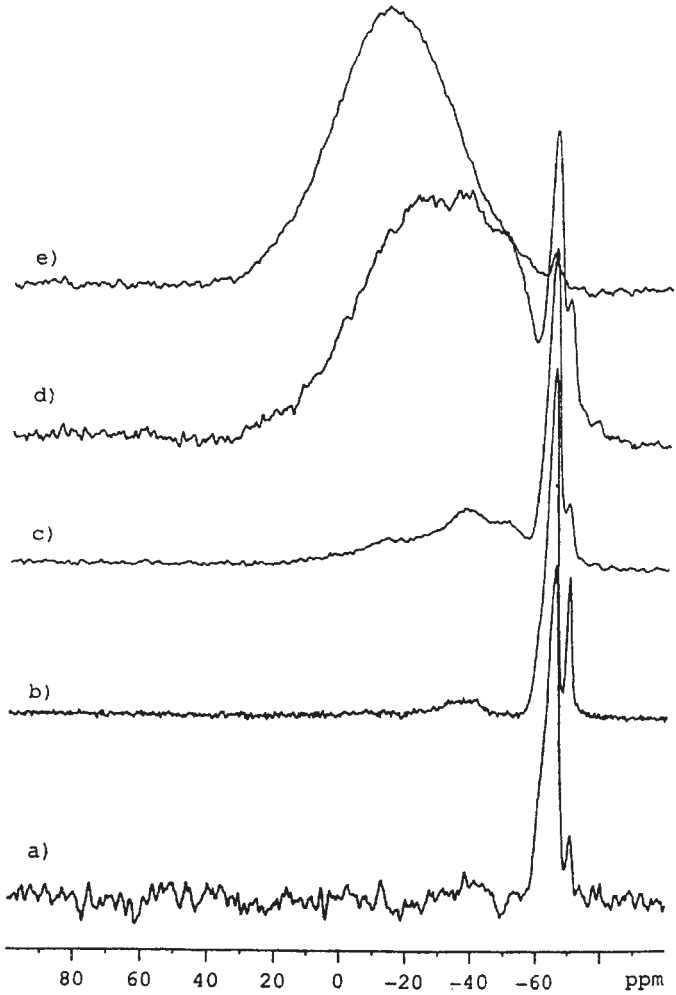

Fig. 11. ^{29}Si CP/MAS NMR spectra of MSP cured at various temperatures: (a) before curing, (b) 150°C, (c) 200°C, (d) 300°C, and (e) 400°C.

it can be said that these signals observed in the ^{29}Si CP/MAS experiments come from the crystalline region of PDPhSM. Figure 13(b) shows the ^{29}Si DD/MAS NMR spectrum of PDPhSM at room temperature. As compared with the ^{29}Si CP/MAS NMR spectrum, the shoulder peak at −8.5 ppm observed in ^{29}Si DD/MAS NMR spectrum is assigned to the non-crystalline region of PDPhSM. From these results, we see that there exists two conformational isomers in the crystalline region of PDPhSM the signals at −7.6 ppm and −9.3 ppm are assigned to these two conformational isomers in the crystalline region. The phenyl region from 120 to 150 ppm in the

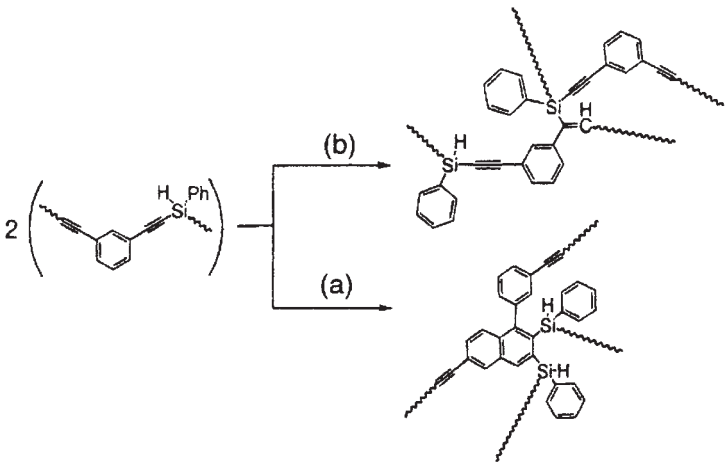

Fig. 12. Thermosetting mechanism of MSP based on solid-state NMR results. (a) Diels-Alder reaction between the Ph–C≡C and the C≡C and (b) the hydrosilylation reaction between the Si–H and the C≡C.

^{13}C CP/MAS NMR spectrum of PDPhSM, shown in Fig. 14, is very complicated and contains some peaks which arise because the molecular motion of the phenyl rings of PDPhSM is restricted at room temperature. There are two signals at 0.0 and −3.1 ppm which are assigned to the main chain methylene group in a similar manner to the ^{29}Si NMR result. Thus, there exists two conformational isomers in the crystalline region of PDPhSM.

Figure 15 shows the ^{29}Si and ^{13}C CP/MAS NMR spectra of PMPhSM at room temperature. From the ^{29}Si CP/MAS NMR spectrum, only one broad line is observed at −4.5 ppm. This polymer is an amorphous polymer so that this broad signal means a conformational distribution along the Si–C backbone. Peaks at 141.7 ppm (the C1), 134.0 ppm (the C2), 128.5 ppm (the C3 and C4), 7.0 ppm (the methylene carbon) and 0.5 ppm (the methyl carbon) are observed in the ^{13}C CP/MAS NMR spectrum. The broad signal is assigned to the methylene carbons of the main-chain implies conformational distribution along the Si–C backbone in a similar manner to the ^{29}Si NMR results.

3.2.2. *Molecular motion of the phenyl ring of PDPhSM and PMPhSM*

Figure 16 shows ^{13}C CP+DDph NMR spectra in the phenyl region for PMPhSM at room temperature, and for PDPhSM at room temperature, 113°C and 226°C, respectively.[48] The DDph spectra are obtained by inserting a dephasing period between the CP and detection periods. During the dephasing period, the carbons with directly-bonded protons undergo rapid dephasing (on a time scale of tens of μs), and

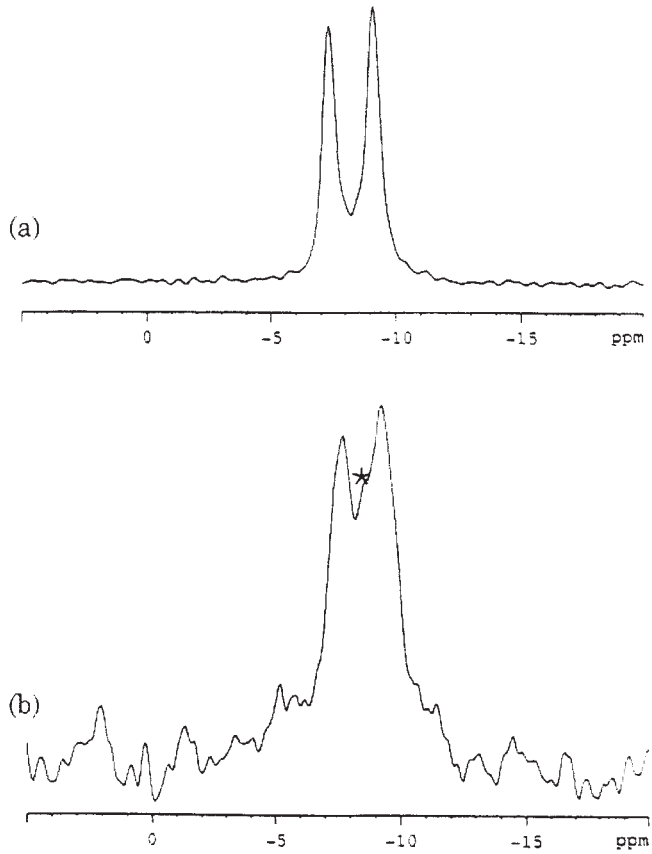

Fig. 13. ^{29}Si CP/MAS (a) and ^{29}Si DD/MAS NMR (b) spectra of PDPhSM at room temperature. The signal corresponding to the non-crystalline region is indicated by an asterisk.

hence their ^{13}C magnetizations are dramatically depressed before ^{13}C detection. Since, sometimes, the rapid rotation of the phenyl group dramatically attenuates the ^{1}H–^{13}C dipolar interactions, dipolar-dephasing spectra of the phenyl region are very useful to evaluate the molecular motion of the phenyl group.

Three signals at 141.7, 134.0, and 128.5 ppm as observed in the ^{13}C CP+DDPh NMR spectrum of PMPhSM (Fig. 16(a)) are assigned to the C1, C2, and C3 carbons, respectively. This shows that dipolar interactions with protons vanish due to the flip-flop motion of the phenyl ring of PMPhSM at room temperature.

Three or more sharp peaks assigned to the C1 carbons without directly-bonded protons, and very small peaks assigned to the C2 and C3

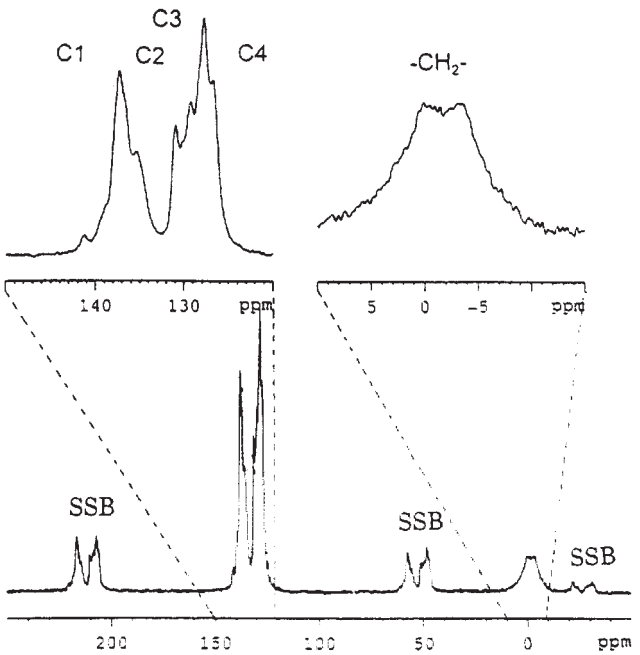

Fig. 14. ^{13}C CP/MAS spectrum of PDPhSM at room temperature. SSB means a spinning sideband.

are observed in the spectrum of PDPhSM at room temperature (Fig. 16(b)). This indicates that the flip-flop motion of the phenyl rings is restricted and more than three magnetically non-equivalent phenyl rings exist at room temperature. In the ^{13}C CP/DDph NMR spectrum of PDPhSM at 113°C, peaks corresponding to C2 and C3 can be observed, but the peak intensities are smaller than those at 226°C. It is suggested that the flip-flop motion of the phenyl rings starts but is not rapid enough to remove the ^{1}H–^{13}C dipolar interactions completely at 113°C. Peaks corresponding to C2 and C3 are obviously observed at 226°C. Thus, it can be said that the molecular motion of the phenyl rings is fast enough to remove ^{1}H–^{13}C dipolar interactions.

3.2.3. *Structural characterization of PDPhSM and PMPhSM by ^{29}Si variable temperature CP/MAS NMR*

Figure 17 shows the change of the ^{29}Si chemical shift values of PDPhSM at various temperatures from 27 to 226°C.[48] The plots of the ^{29}Si chemical shifts and relative intensities of the PDPhSM signals are presented in Fig. 18. The lower frequency peak at −9.3 ppm at room temperature moves to high frequency by 1.2 ppm with an increase in temperature below 130°C. Above

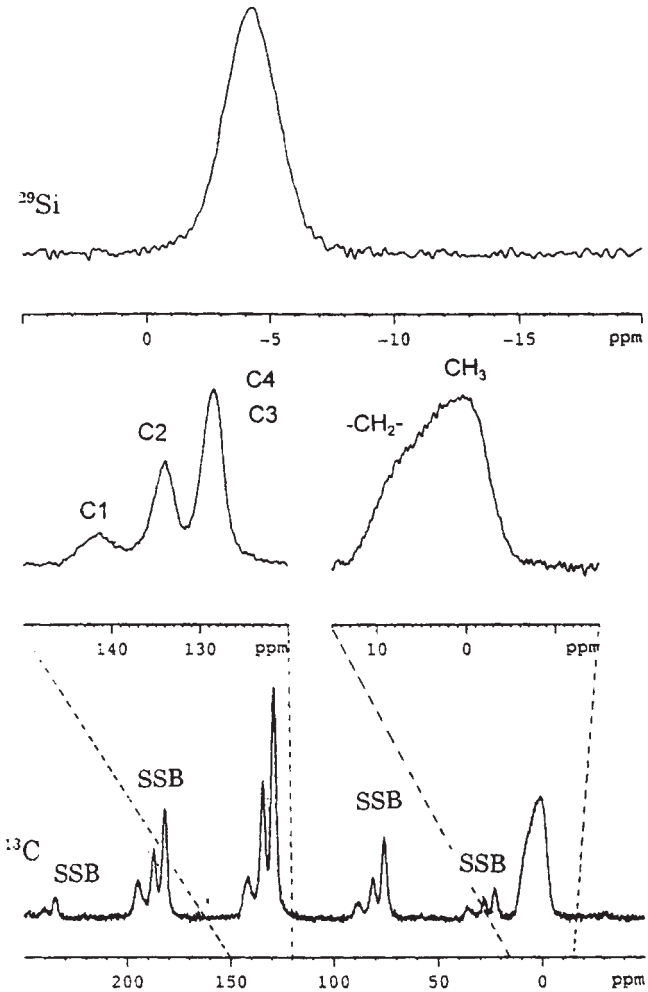

Fig. 15. ^{29}Si and ^{13}C CP/MAS NMR spectra of PMPhSM at room temperature. SSB means a spinning sideband.

130°C the chemical shifts are unchanged. The higher frequency peaks at −7.6 ppm at room temperature moves to high frequency by 0.6 ppm with an increase in temperature below 130°C and above 130°C the chemical shifts are also unchanged. Both the peaks have intensity minima at about 130°C, so the polymer has a motion of the order of several tens of kHz, which dramatically attenuates the ^{1}H dipolar interaction at 130°C. Above the T_g at 140°C, obtained by storage moduli and loss moduli, there are still two signals assigned to the two conformational isomers.

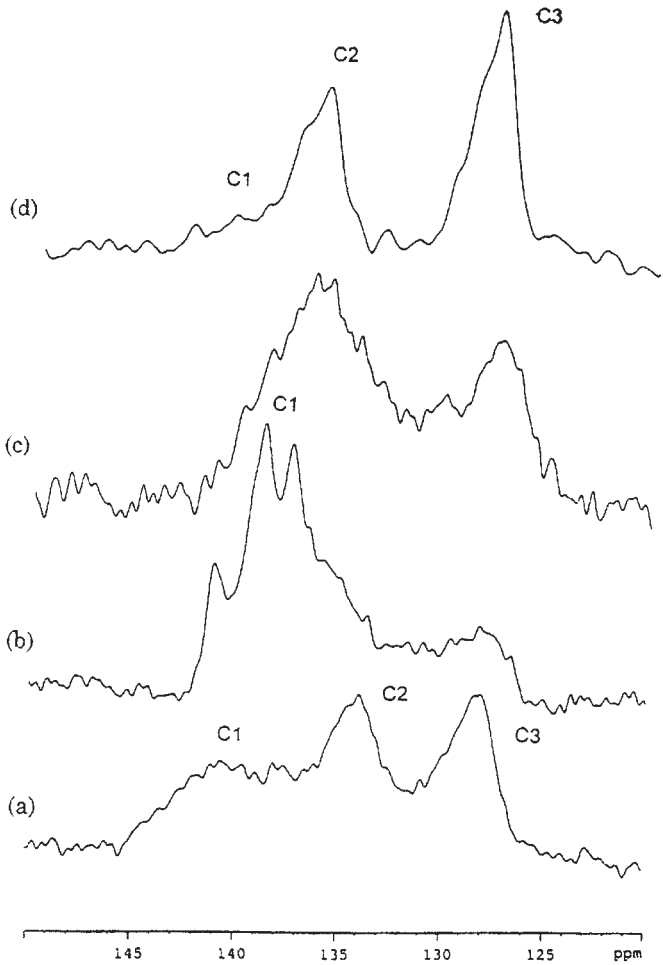

Fig. 16. ^{13}C CP+DDph NMR spectra in the phenyl region of PMPhSM (a) at room temperature and PDPhSM at room temperature, (b) at 113°C, and (c) at 226°C.

This shows that this polymer has no micro-Brownian motion of the Si–C backbone.

Figure 19 shows plots of the ^{29}Si chemical shifts and half width of the ^{29}Si NMR signals of PMPhSM at −37 to 65°C. The T_g of this polymer is about 20°C obtained by storage moduli and loss moduli. The broad signal below the T_g implies conformational distribution along the Si–C backbone and a micro-Brownian motion of the Si–C backbone occurs above T_g. This motion leads to a decrease in the half width of the signal.

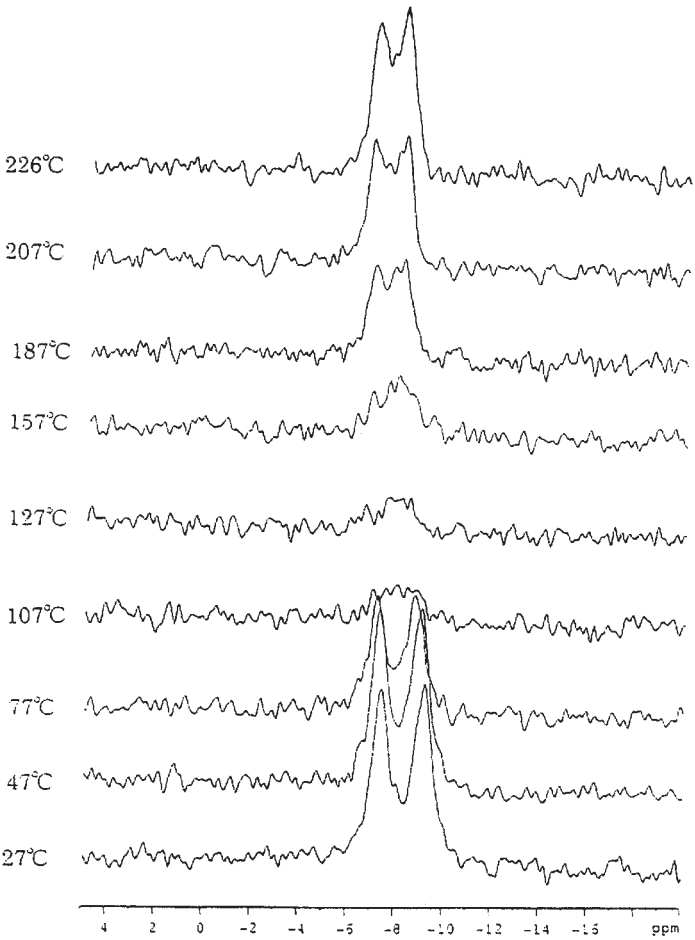

Fig. 17. ^{29}Si CP/MAS NMR spectra of PDPhSM at various temperatures. Each spectrum was recorded for 56 scans and a repetition time of 20 s.

4. STRUCTURAL CHARACTERIZATION OF SILICON-BASED INTERPENETRATING POLYMER NETWORK MATERIALS

4.1. Structural and dynamic elucidation by ^{13}C CP/MAS NMR

The observed ^{13}C CP/MAS TOSS NMR spectra of five kinds of cured LDS/PCS IPN samples with mixture weight ratios (LDS/PCS=10/0, 8/2, 5/5, 2/8, and 0/10) are shown in Fig. 20.[49] ^{13}C CP/MAS spectrum of unblended LDS is shown at the bottom of these spectra in Fig. 20. LDS has phenyl carbons and methylene carbons as seen from Fig. 3. Signals appearing

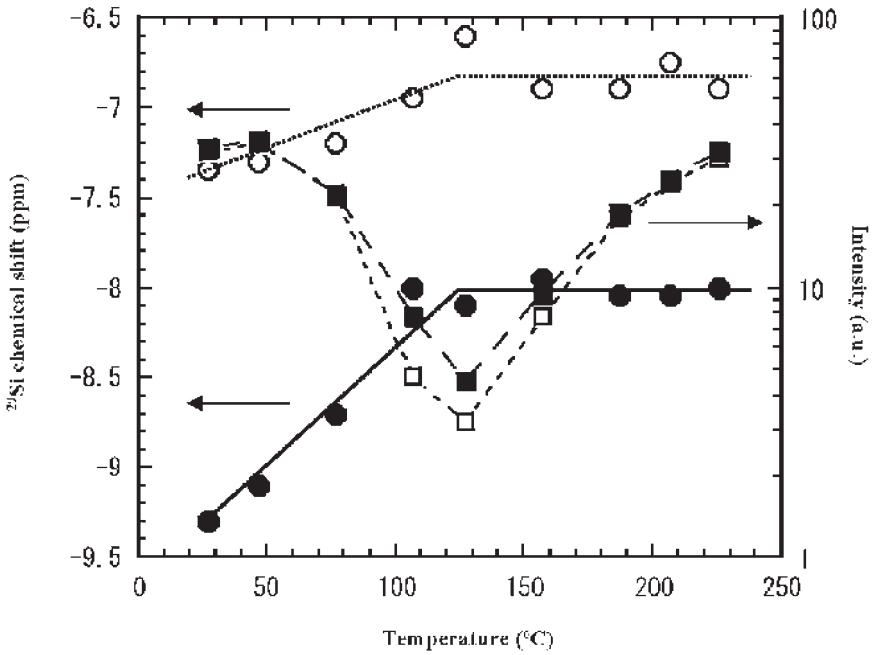

Fig. 18. The plots of ^{29}Si chemical shifts and relative intensities for two signals of PDPhSM against temperature in a wide range of temperatures from 27°C to 226°C. (○: low frequency peak, ○: high frequency peak, □: intensity of low frequency peak and ■: intensity of high frequency peak)

at about 17 ppm and 125–135 ppm are assigned to the methyl and phenyl carbons, respectively. In the phenyl signal region, the peaks at 135, 130, and 126 ppm are assigned to the C_1 and C_2 carbons, the C_4 carbon and the C_3 carbons. On the other hand, the ^{13}C CP/MAS spectrum of an unblended PCS sample is shown at the top in Fig. 20. PCS has phenyl carbons, two types of methylene carbons and three types of methyl carbons as seen from Fig. 3. Peaks appearing at about −5 ppm and 10 ppm can be assigned to the methylene and methyl carbons, respectively. In the phenyl signal region, the high frequency signal at 140 ppm is assigned to the C_1 carbon, and the lower frequency signal at 126 ppm to the other C_2 carbons. These assignments are based on an other Si-based polymer.[47] The ^{13}C chemical shift values of the individual carbons in unblended LDS and PCS are useful for the signal assignments of cured blend LDS/PCS samples.

The observed ^{13}C CP/MAS spectra of cured LDS/PCS systems with three kinds of mixture ratios are shown in Fig. 20. The methyl and phenyl carbon signals from the LDS and PCS portions in the cured blend sample overlap with each other. Therefore, these signals are decomposed by

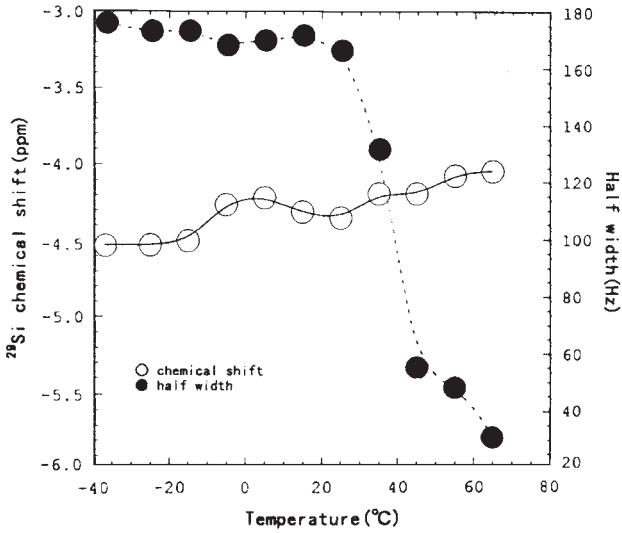

Fig. 19. The plots of ^{29}Si chemical shifts and half widths for a signal of PMPhSM against temperature in a wide range of temperatures from −37 to 65°C.

computer-fitting as shown in Fig. 21. The ^{13}C CP/MAS spectrum of cured LDS/PCS (5/5) is decomposed by Gaussian functions. As expected, the intensities of individual peaks are corresponding to the mixture composition in LDS/PCS samples. The ^{13}C chemical shift values of the decomposed peaks are almost the same as those of LDS and PCS. This shows that there are no new signals with significant intensity formed by curing the LDS/PCS (5/5) sample. The peak intensities determined by such a decomposition are used in the $T_{1\rho}{}^{H}$ analysis, in order to elucidate the miscibility of blended LDS/PCS samples.

Figure 22 shows the partially-relaxed ^{13}C spectra of cured LDS/PCS (5/5) (a) and cured LDS/PCS (2/8) (b) as a function of spin locking time τ by the pulse sequence for the $T_{1\rho}{}^{H}$ measurement (Fig. 5(b)), where the asterisks indicate spinning sidebands. It is seen that the intensities of the individual peaks $M(\tau)$ decay with an increase in τ. These decays follow the equation $M(\tau) = M(0)\ \exp(-\tau/T_{1\rho}{}^{H})$, where $M(0)$ is the peak intensity at $\tau = 0$. The plots of ln $M(\tau)$ for the methyl, methylene, and phenyl carbons as obtained from the decomposition of the overlapping peaks by computer-fitting as above-mentioned against τ are shown in Fig. 23 then the $T_{1\rho}{}^{H}$ values of the corresponding carbons are determined from its slope. From these $T_{1\rho}{}^{H}$ curves, it is found that the relaxation behaviour for the methyl, methylene, and phenyl carbons is a single exponential decay. This means that molecular motions of these carbons are one component. The determined $T_{1\rho}{}^{H}$ values of cured LDS/PCS samples are summarized in Table 2. The $T_{1\rho}{}^{H}$ values for the

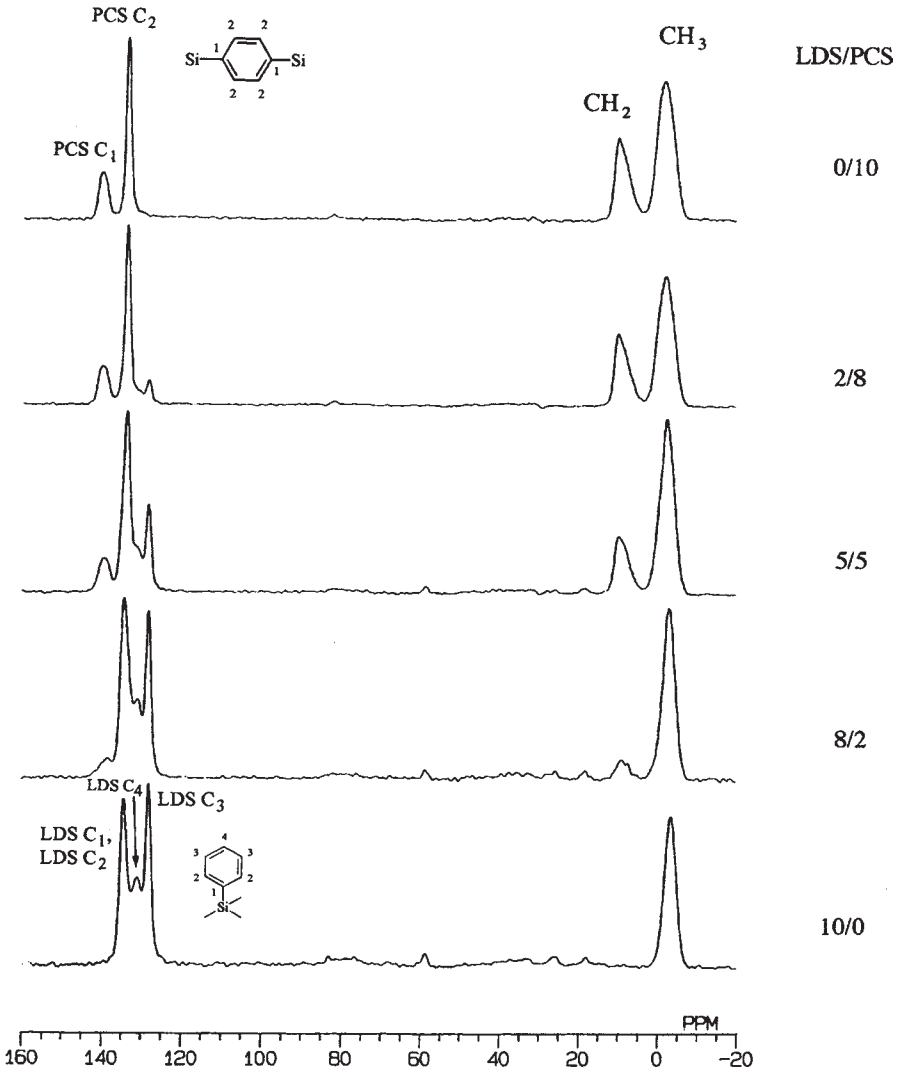

Fig. 20. ^{13}C CP/MAS (TOSS) NMR spectra of five kinds of cured LDS/PCS systems (LDS/PCS = 10/0, 8/2, 5/5, 2/8, and 0/10 [wt/wt]).

methyl, methylene, and phenyl carbons of each sample are 34 ms for LDS/PCS(8/2), 40 ms for LDS/PCS(5/5) and 47 ms for LDS/PCS(2/8). These values for the three functional groups are close to each other for the samples studied. This means that intramolecular ^1H spin diffusion occurs in cured LDS/PCS samples. However, the $T_{1\rho}{}^H$ values in unblended LDS are 39 and 38 ms for the methyl and phenyl carbons, respectively, and in

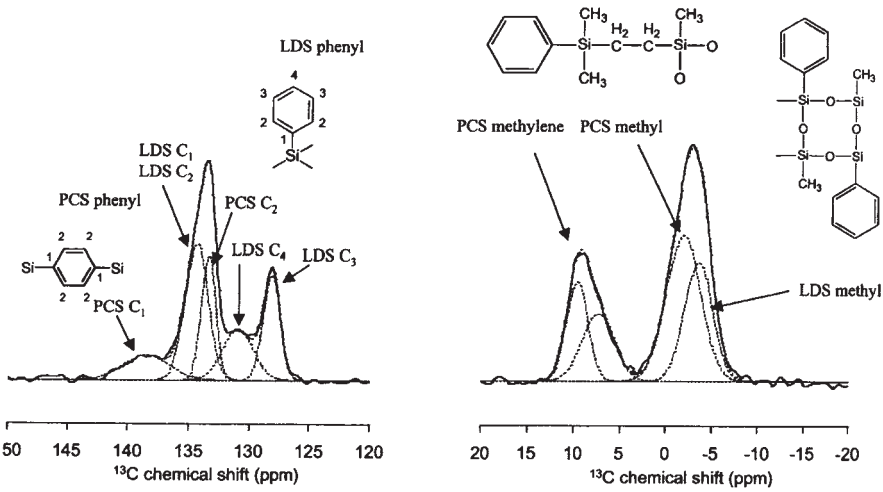

Fig. 21. ^{13}C CP/MAS spectrum of cured LDS/PCS (5/5) decomposed by computer-fitting with Gaussian functions.

unblended PCS 38, 38, and 37 ms for the methyl, methylene, and phenyl carbons, respectively. It is found that the $T_{1\rho}{}^{H}$ values of LDS/PCS (8/2) are smaller than that of unblended LDS and PCS. On the other hand, the ^1H $T_{1\rho}$ values of LDS/PCS (5/5) are almost the same as for unblended LDS and PCS, and those of LDS/PCS (2/8) are much larger. Dipole–dipole interactions between the nuclear spins predominantly govern the relaxation mechanisms in polymer systems. The dipole–dipole interaction H_d is expressed by

$$H_d = \sum (h^2/8\pi^2)\,\gamma_i\gamma_j\,(3\cos^2\theta - 1)(I_iI_j - 3I_{iz}I_{jz})/r_{ij}^3 \qquad (1)$$

where h is the Planck constant, r_{ij} is the internuclear distance between nuclei i and j, θ is the angle between the vector i–j and the magnetic field, γ_i and γ_j are the magnetogyric ratios of nuclei i and j, respectively, and I is the nuclear spin operator.[8–11]

In general, ^1H NMR relaxation is mainly induced by dipole–dipole interaction and is greatly affected by the internuclear distance of the nuclear spins fluctuating in the magnetic field. However, an interatomic distance of more than ca. 5 Å does has almost no effect on the ^1H NMR relaxation as seen from Eq. (1) since H_d is proportional to r^{-3}. Thus, the NMR relaxation times, in principle, provide information about the interatomic distance r, if r is less than ca. 5 Å. From such a background, we are concerned with the miscibility between the LDS and PCS portions in blended LDS/PCS samples. The intermolecular distance between the LDS and PCS portions in blended

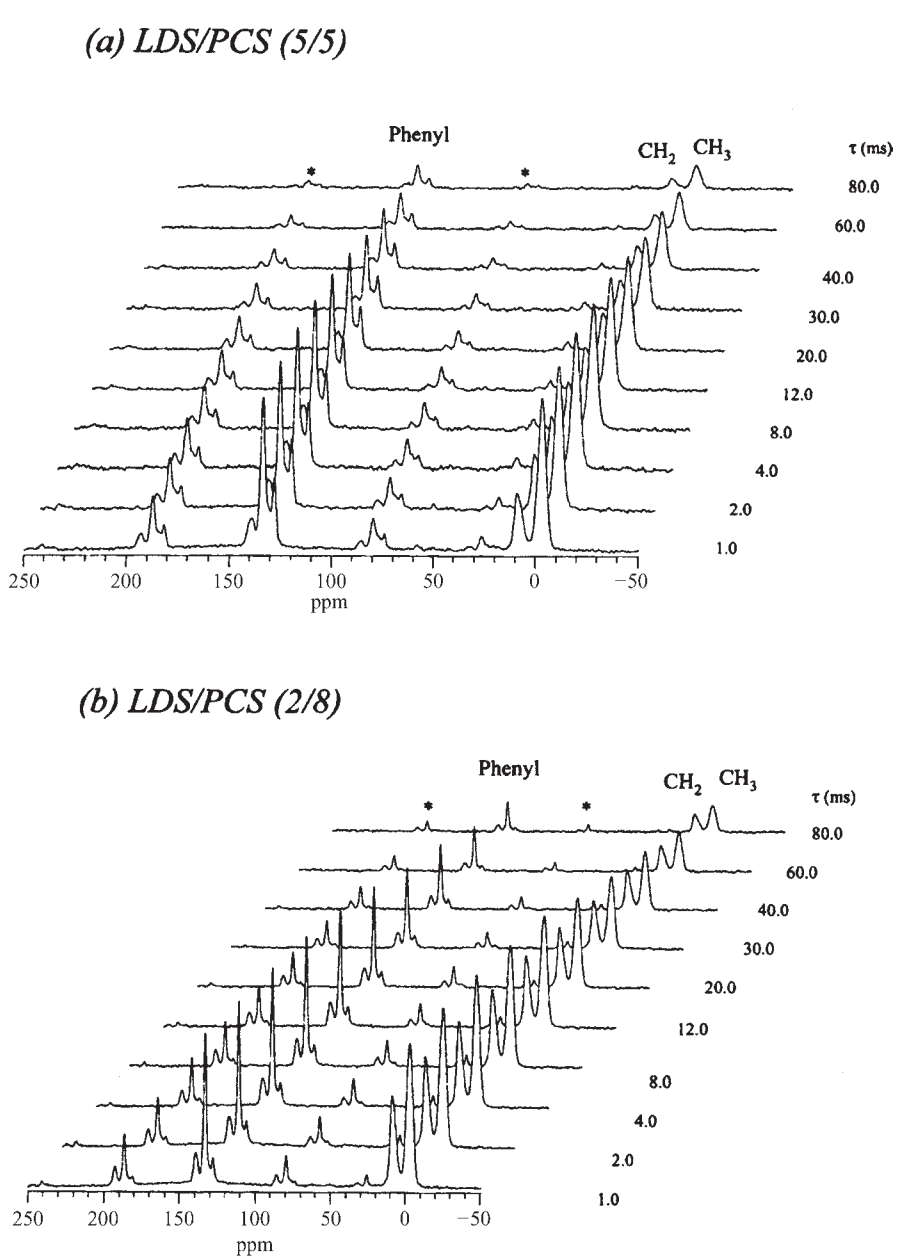

Fig. 22. Partially-relaxed ^{13}C spectra of cured LDS/PCS (5/5) (a) and cured LDS/PCS (2/8) sample (b) by the pulse sequence for $T_{1\rho}{}^{H}$ measurement.

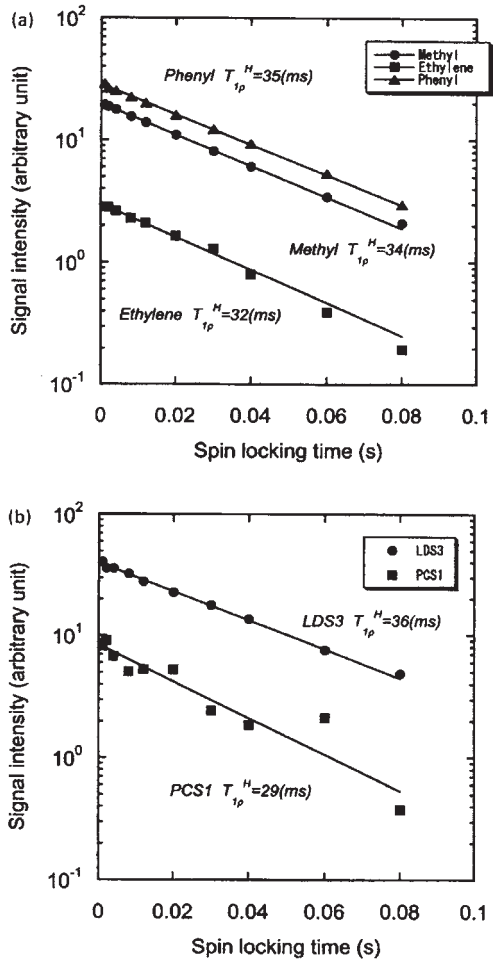

Fig. 23. $T_{1\rho}{}^{H}$ decay curves for cured LDS/PCS (8/2). (a) peak intensity for the methyl, ethylene, and phenyl carbons, and (b) decomposed peak intensity for LDS-C_3 and PCS-C_1 carbons in the phenyl region.

LDS/PCS IPN systems predominantly affects the $^{1}HT_{1\rho}$ values considered here, which are closely related to the miscibility. This may be supported by the experimental results on the density of the blended LDS/PCS samples as summarized in Table 3. The density of LDS/PCS (8/2) is the largest for the three kinds of blended LDS/PCS samples studied. Therefore, it can be said that the intermolecular distance between LDS and PCS in LDS/PCS (8/2) may be the shortest in the three kinds of blended LDS/PCS IPN samples. This result suggests that intermolecular dipole–dipole interactions affect the $^{1}HT_{1\rho}$ values in LDS/PCS (8/2). From these experimental results,

Table 2. Determined $T_{1\rho}{}^{H}$ values[a] of cured LDS/PCS samples with various mixture ratios determined at 25°C

Samples	$T_{1\rho}{}^{H}$/ms				
	Methyl	Methylene	Phenyl (Total)	Phenyl (LDS)	Phenyl (PCS)
cured IPN LDS/PCS (8/2)	34	32	35	36	29[b]
cured IPN LDS/PCS (5/5)	40	42	39	36	38
cured IPN LDS/PCS (2/8)	46	49	47	43	46
cured LDS	39		38		
cured PCS	38	38	37		

[a]Experimental error is ±2 ms.
[b]Experimental error is larger than other values because of low signal–to–noise ratio.

Table 3. The density of cured LDS/PCS samples with various mixture ratios determined at 25°C

Samples	Density (g/cm^3)
cured LDS	1.258
cured IPN LDS/PCS (8/2)	1.258
cured IPN LDS/PCS (5/5)	1.216
cured IPN LDS/PCS (2/8)	1.161
cured PCS	1.019

the miscibility of LDS and PCS in LDS/PCS (8/2) can be predicted to be the highest.

4.2. Structural characterization by 2D ^{13}C–^{13}C and ^{1}H–^{1}H exchange NMR

In order to evaluate the intermolecular distance between LDS and PCS in blended LDS/PCS systems, ^{13}C–^{13}C and ^{1}H–^{1}H spin diffusion experiments are carried out. Figure 24(a) shows the ^{13}C–^{13}C 2D exchange NMR spectrum of LDS/PCS (5/5) with a mixing time of 500 ms. In order to recognize the cross peaks appearing due to intramolecular interaction and intermolecular interaction, the expanded spectra of the aliphatic and phenyl regions are shown in Fig. 24(b) and (c), respectively. As seen from these spectra, cross peaks are observed between the methyl carbon and methylene carbon in the aliphatic region, and between PCS-C_1 and PCS-C_2, PCS-C_1 and LDS-C_1, PCS-C_1 and LDS-C_2, LDS-C_3 and LDS-C_1, LDS-C_3 and LDS-C_2 , and LDS-C_3 and PCS-C_2 in the phenyl region. The peak assignments follow those made by computer-fitting as shown in Fig. 21. These cross peaks are

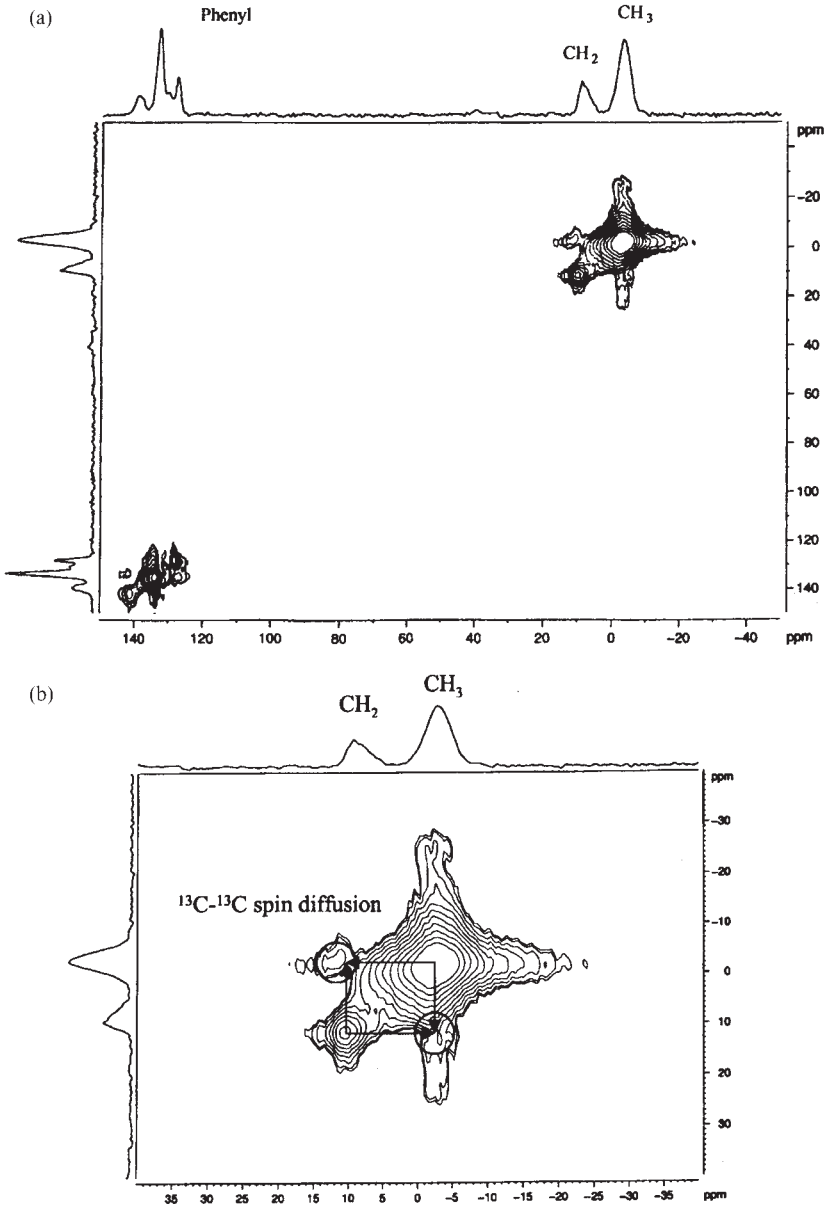

Fig. 24. (a) ^{13}C–^{13}C 2D exchange NMR spectrum of LDS/PCS (5/5) with mixing time 500 ms. Expanded spectra of the aliphatic region (b) and phenyl region (c).

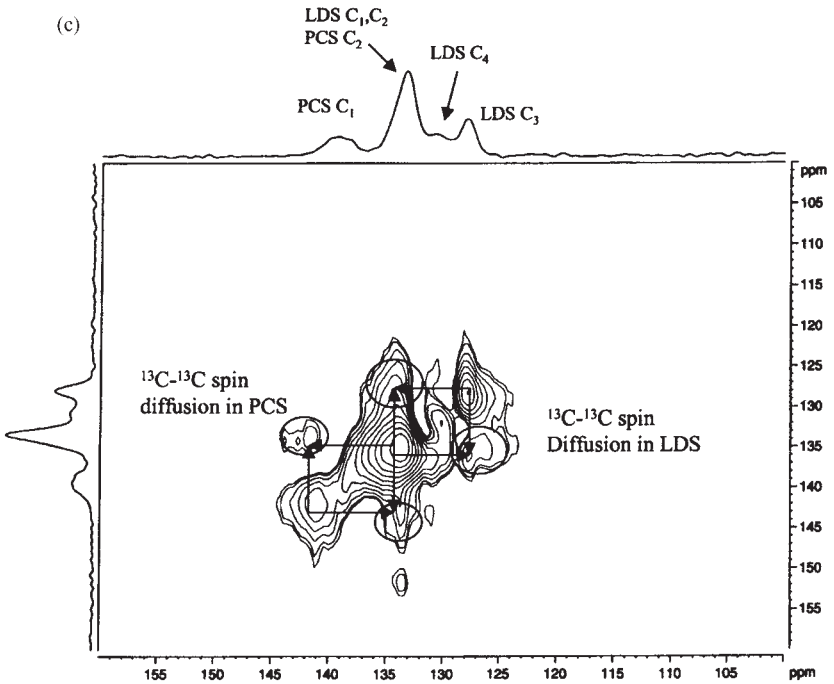

Fig. 24. Continued.

assigned to intramolecular ^{13}C–^{13}C spin diffusion in the LDS and the PCS portions. In ^{13}C–^{13}C 2D exchange NMR spectra of LDS/PCS (8/2) and LDS/PCS (2/8), intramolecular spin diffusion is clearly observed. On the other hand, no cross peak appears, due to intermolecular ^{13}C–^{13}C spin diffusion between the PCS-C_1 and LDS-C_3 carbons in LDS/PCS (8/2) since as expected the miscibility is much higher. Hence the intensity of the PCS-C_1 peak is much too weak.

Figure 25 shows ^{1}H CRAMPS NMR spectra of unblended LDS and PCS, and blended LDS/PCS (8/2). The aliphatic proton signal and phenyl proton signal are clearly observed, of which the ^{1}H chemical shift values are indicated on the peak top. As seen from these spectra of unblended LDS and PCS, the ^{1}H chemical shifts of the methyl and phenyl protons of LDS appear at low frequency to those of PCS. On the other hand, in LDS/PCS (8/2) the peaks of the methyl and phenyl protons in the LDS portion and the PCS portion overlap with each other. The apparent top position of the signal changes by changing the mixture ratio. The positions of the overlapping peaks in LDS/PCS (8/2) are in between those found in LDS and PCS. These ^{1}H chemical shift behaviours will be used for ^{1}H–^{1}H 2D exchange NMR spectral analysis.

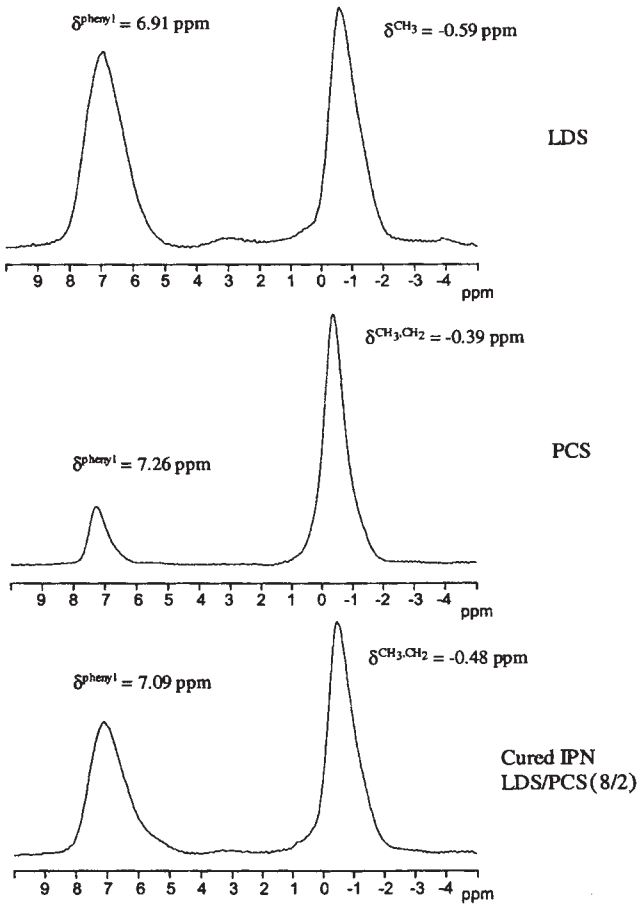

Fig. 25. ^{1}H CRAMPS NMR spectra of unblended LDS and PCS, and blended LDS/PCS (8/2).

Figure 26(a) shows the ^{1}H–^{1}H 2D exchange NMR spectrum of LDS/PCS(8/2) with a mixing time of 100 μs. The cross peaks, which come from the existence of ^{1}H–^{1}H spin diffusion between the phenyl protons and CH_3 protons, and the phenyl protons and the CH_2 protons appear clearly. For convenience, the expanded spectrum in the cross peak region is shown in Fig. 26(b). The dashed lines indicate the ^{1}H chemical shift positions of unblended LDS and PCS. These values become reference data for understanding the observed cross peaks due to ^{1}H–^{1}H spin diffusion. The peak top at around the ^{1}H chemical shift position (X1, X2) = (−0.8 ppm, 6.9 ppm) may be assigned to intramolecular spin diffusion between the CH_3 protons of LDS and the phenyl protons of LDS because of the most intense peak. The shoulder around the ^{1}H chemical shift position

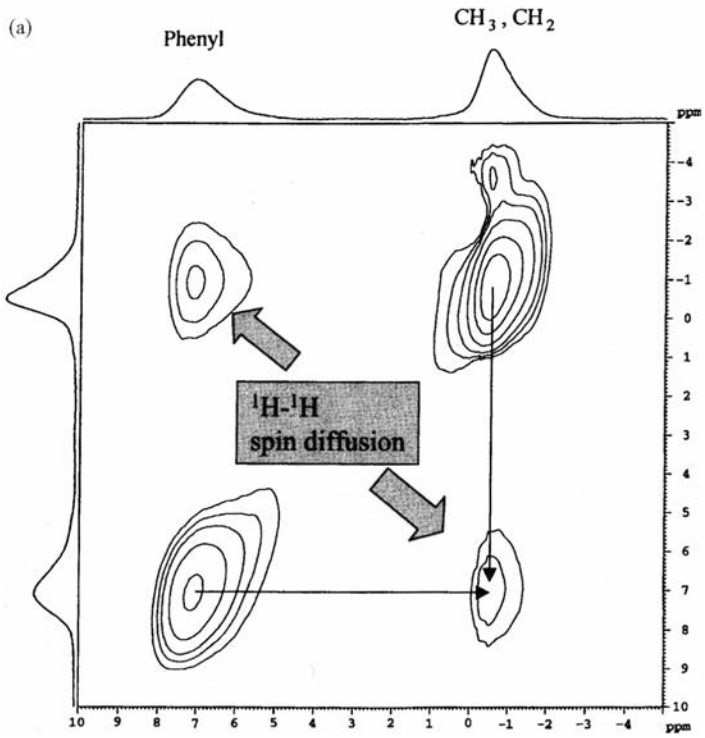

Fig. 26. ^{1}H–^{1}H 2D exchange NMR spectra of LDS/PCS (8/2) with mixing time 100 μs (a) and expanded spectra of the cross peak region (b).

(X1, X2) = (−0.4 ppm, 7.2 ppm) may be assigned to intramolecular spin diffusion between the CH_3 and CH_2 protons of PCS and the phenyl protons of PCS because of the next most intense peak. The remaining shoulder around the ^{1}H chemical shift position (X1, X2) = (−0.4 ppm, 6.9 ppm) may be assigned to intermolecular spin diffusion between the CH_3 and CH_2 protons of PCS and the phenyl protons of LDS because of a very weak peak. The two cross peaks at around (−0.4 ppm, 6.9 ppm) and (−0.4 ppm, 7.2 ppm) can be significantly recognized by making a careful spectral analysis of the region. In the other blend of LDS/PCS samples, a corresponding shoulder at around the ^{1}H chemical shift position (X1, X2) = (−0.4 ppm, 6.9 ppm) does not appear. From these experimental results, it appears that intermolecular ^{1}H–^{1}H spin diffusion occurs in LDS/PCS (8/2) only. This suggests that the interchain distance between the LDS and PCS portions is almost within the order of some tens of nm. Thus it appears that the phase structure and miscibility of silicon-based interpenetrating polymer networks composed of LDS and PCS portions are successfully elucidated by solid-state ^{13}C CP/MAS NMR, ^{1}H CRAMPS, and 2D ^{1}H–^{1}H exchange NMR. The ^{13}C

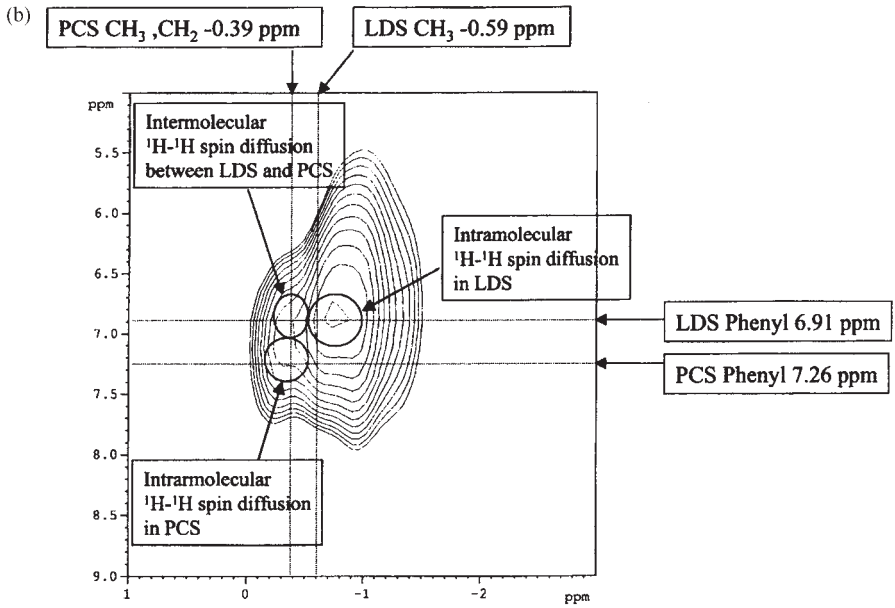

Fig. 26. Continued.

CP/MAS NMR experimental results suggest that intermolecular dipole–dipole interactions occur significantly in LDS/PCS (8/2) because of short intermolecular distances between the LDS and PCS portions. It is suggested from the observation of intermolecular spin diffusion in the 2D ^{1}H–^{1}H exchange NMR spectrum in LDS/PCS (8/2) that the interchain distance between the LDS and PCS portions is within a few tens of nm.

5. STRUCTURAL CHARACTERIZATION OF SILYL-CARBORANE HYBRID SI-BASED POLYMER NETWORK MATERIALS

5.1. ^{29}Si CP/MAS NMR spectral analysis and structural characterization

Figure 27 shows the 59.6 MHz ^{29}Si CP/MAS NMR spectra of silyl-carborane hybrid diethynylbenzene–silylene polymers ((a) polymer A-1 (before curing), (b) polymer A-2 (molded and pressed at 250°C), (c) polymer A-4 (cured at 350°C after molding and pressing at 250°C), and (d) polymer A-500 (cured at 500°C after molding and pressing at 250°C)).[27] The spectrum of polymer A-1 before curing has very resolved and narrow peaks, but the spectrum becomes very broad with an increase in curing temperature. From these experimental results, it is found that thermal curing leads to

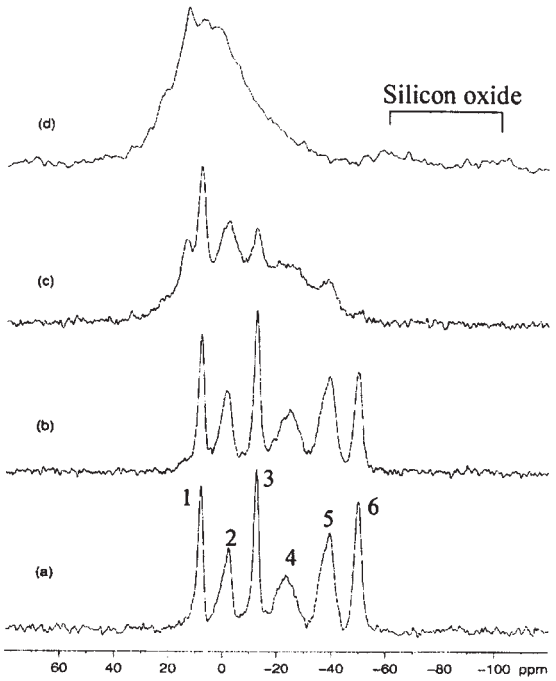

Fig. 27. 59.6 MHz ^{29}Si CP/MAS NMR spectra of silyl-carborane hybrid diethynylbenzene–silylene polymers; (a) A-1 (before curing), (b) A-2 (molded and pressed at 250°C), (c) A-4 (cured at 350°C after molding and pressing at 250°C), and (d) A-500 (cured at 500°C after molding and pressing at 250°C). Peak assignments: 1: –$CB_{10}H_{10}C$–$Si(CH_3)_2$–$CH(CH_3)$, 2: $CB_{10}H_{10}C$–$Si(CH_3)_2$–CH_2, 3: –$CB_{10}H_{10}C$–$Si(CH_3)_2$–OMe, 4: –$Si(Ph)(CH(CH_3)$–)–, 5: –$Si(Ph)(CH_2$–)–, and 6: –$Si(Ph)(CH{=}CH_2)$–.

a structural change of the hybrid polymer. In the ^{29}Si CP/MAS NMR spectrum (a) of polymer A-1, six peaks with different chemical shifts appear. The six peaks are numbered from high frequency by 1, 2, 3, 4, 5, and 6, respectively. The widths of peaks the 1, 2, 3, and 6 are relatively narrow, and those of peaks 4 and 5, are broad. The peak assignment is made as follows. Peak 6 at −49.8 ppm in spectrum (a) can be assigned to the main chain –$Si(Ph)(CH{=}CH_2)$– silicon,[47] and peaks 4 and 5 at −23.2 and −39.2 ppm are assigned to the –$Si(Ph)(CH(CH_3)$–)– and –$Si(Ph)(CH_2$–)–silicons of the main chain, respectively. Peaks 3, 2, and 1 at −12.5, −2.2, and 8.1 ppm can be assigned to the –$CB_{10}H_{10}C$–$Si(CH_3)_2$–OMe, $CB_{10}H_{10}C$–$Si(CH_3)_2$–CH_2 and the –$CB_{10}H_{10}C$–$Si(CH_3)_2$–$CH(CH_3)$– silicons of the side chains, respectively. There exists a large number of vinyl groups in the hybrid polymer before thermal curing because peak 6, assigned to the main chain –$Si(Ph)(CH{=}CH_2)$– silicon, is relatively intense in spectrum (a).

Next, we are concerned with the ^{29}Si CP/MAS NMR spectra of thermally cured polymers. Spectrum (b) of the cured polymer after molding and pressing

at 250°C is very similar to spectrum (a) of the uncured polymer. In comparison with spectrum (a) of the uncured polymer, the intensity of peak 6 at −49.8 ppm is slightly decreased in spectrum (b) of the cured polymer after molding and pressing at 250°C. As the curing temperature is further increased, peak 6 almost disappears at 350°C as shown in spectrum (c). This shows that a thermal hardening reaction of the vinyl group occurs at curing temperatures from 250 to 350°C. The intensities of peaks 4 and 5 at −23.2 and −39.2 ppm are largely decreased at a curing temperature of 350°C, and almost disappear at 500°C. ^{29}Si CP/MAS NMR spectra of cured poly(phenylvinylsilylene-ethynylene-1,3-phenylene-ethynylene), (–C≡C–Ph–C≡C–Si(Ph)(CH=CH$_2$)–)$_n$, in the curing temperature range of 250–450°C are very broad in the range from 10 to −40 ppm.[47] This spectral pattern is very similar to the patterns of the spectra (c) and (d). We can look at some broad peaks ranging from 10 to −40 ppm as shown in spectrum(c), and three or four peaks centered at about 0 ppm in spectrum (d). The broad spectrum comes from the appearance of a variety of chemical structures in the thermally cured *m*-carborane hybrid silicon-based polymer. Further, it is shown that a structural change from the –C≡C–Si–C≡C– group to the –C=C–Si–C≡C– and –C=C–Si–C=C– groups leads to the appearance of peaks centered at about 0 ppm. If we look at the low frequency region of spectrum (d) carefully, we find small and broad peaks at about −100 and −60 ppm. This suggests that a small amount of silicon oxides are produced at a curing temperature of 500°C.

From the ^{29}Si NMR experimental results, it is found that (1) the thermal curing at temperatures from 250 to 500°C leads to changes in structure of the silyl-carborane hybrid diethynylbenzene–silylene polymer, (2) the thermal hardening reaction of the vinyl group occurs at curing temperatures from 250 to 350°C, (3) the C≡C group changes into the C=C group by thermal hardening, and (4) a small amount of silicon oxides form at a curing temperature of 500°C.

5.2. Structural characterization by ^{13}C CP/MAS NMR

In order to confirm that the acetylene group in the main chain and the vinyl groups in the side chains play an important role in thermosetting reactions of the silyl-carborane hybrid diethynylbenzene–silylene polymers, the structure of the polymers are characterized by ^{13}C CP/MAS NMR as mentioned below.[27] Figures 28 and 29 show 75.6 MHz ^{13}C CP/MAS NMR spectra and 75.6 MHz ^{13}C dipolar dephased CP/MAS NMR spectra of the polymers [(a) A-1, (b) A-2, (c) A-4 and (d) A-500] used in Section 3.1, where in the ^{13}C dipolar dephased CP/MAS NMR spectrum, the ^{13}C magnetization of a carbon bonded to a proton is dephased by their dipolar couplings and then the ^{13}C signal disappears. The dipolar dephased CP MAS NMR spectrum naturally depends on the dipolar dephasing delay time. The dipolar dephasing delay

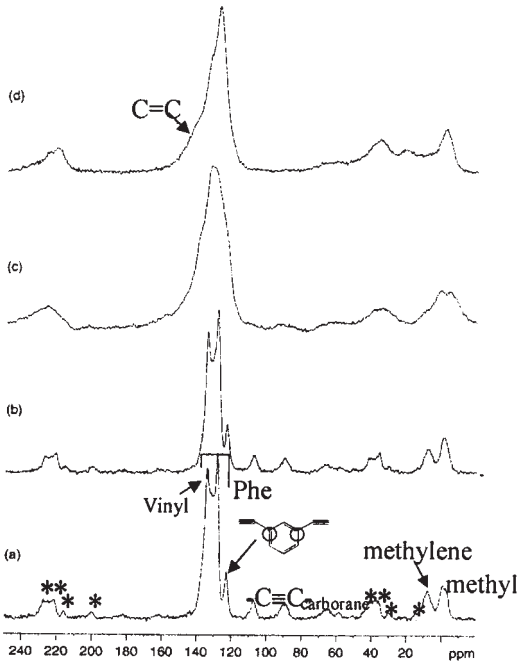

Fig. 28. 75.6 MHz ^{13}C CP/MAS NMR spectra of silyl-carborane hybrid diethynyl-benzene-silylene polymers; (a) A-1, (b) A-2, (c) A-4, and (d) A-500. The peaks marked with an asterisk are 350°C spinning sidebands of the phenyl carbons and the C≡C carbons.

time dependent experiments are carried out in the range of 10–200 μs. As a result, signals of the phenyl carbons bonded to protons do not vanish even at a dipolar dephasing delay time of 200 μs. Then, the dipolar dephasing delay time of 60 μs is adopted.

At first, we are concerned with polymer A-1 before curing. The ^{13}C CP/MAS spectrum (Fig. 28(a)) has relatively resolved and narrow peaks. The peak at 134.8 ppm and peaks at 108.0 and 90.0 ppm can be assigned to the vinyl group and the C≡C group according to our previous study of the ^{13}C CP/MAS NMR spectrum.[40,47,50,51] Peaks at 106.8 and 88.3 ppm can be assigned to the Si–C≡C–Ph carbons, and peaks at 122.8 and 134.1 ppm to the phenyl carbons in an *ipso* position bonded to the C≡C group and the phenyl carbons in an *ipso* position bonded to silicon, respectively, because these carbons do not bond to protons, the corresponding carbons appear in the ^{13}C dipolar dephased CP/MAS NMR spectra. The peak at 128.3 ppm can be assigned to the phenyl carbons bonded to protons because their dipolar interactions are greatly reduced due to the fast flip-flop motion of the phenyl ring. Two peaks at ca. 10 and 15 ppm can be straightforwardly assigned to the methyl and methylene carbons,

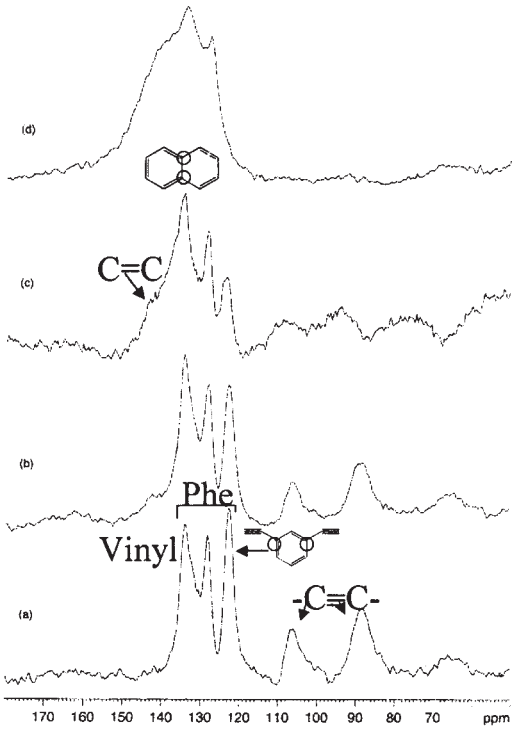

Fig. 29. 75.6 MHz ^{13}C CP/MAS+DDph NMR spectra of silyl-carborane hybrid diethynylbenzene–silylene polymers; (a) A-1, (b) A-2, (c) A-4, and (d) A-500. The dipolar dephasing delay time is 60 μs.

respectively, in the ^{13}C CP/MAS NMR spectra. Further, it can be said that two weak peaks in the 60–70 ppm range can be assigned to the carbonane carbons.

The structure of the polymer is significantly changed by thermal curing as mentioned in Section 6.1. The ^{13}C CP-MAS NMR spectrum of polymer A-2 cured at 250°C is very similar to that of the uncured polymer. On the other hand, as shown in the ^{13}C dipolar dephased CP MAS NMR spectra (Figs. 29(a) and (b)), the intensity of the peak at 122.8 ppm, assigned to the phenyl carbons in an *ipso* position bonded to the C=C group, is somewhat decreased by thermal curing at 250°C. This spectral change agrees with the ^{29}Si NMR results. It can be said that the structural change is very small at curing temperatures below 250°C. As the curing temperature is further increased, the intensity of the peak largely decreases. At a curing temperature of 500°C, the corresponding peak completely disappears. In cooperation with this, the peak intensity of the methylene carbons at ca. −10 ppm increases with an increase in curing temperature. This result

suggests that the vinyl group converts to the methylene group by thermal hardening reactions. The intensities of the corresponding peaks for the vinyl group gradually decrease with an increase in curing temperature, and then should completely disappear by curing at 500°C according to the ^{29}Si NMR results. A broad peak at 140 ppm in spectrum (Fig. 28(c)) appears and its intensity increases with an increase in curing temperature. This peak can be assigned to the C=C group and the phenyl carbons bonded to protons based on the ^{13}C dipolar dephased CP MAS NMR method that the ^{13}C magnetization of a carbon with directly-bonded protons is dephased by their dipolar couplings and thus the ^{13}C signal does not appear.

The intensities of the signals from the C≡C carbons and the phenyl carbons bonded to the C≡C group decrease with an increase in curing temperature, and then the peaks disappear by curing at 500°C. A broad shoulder which comes from the C=C carbons appears at about 140 ppm in the ^{13}C dipolar dephased CP spectrum (Fig. 29(b)) and its intensity increases with an increase in curing temperature. Therefore, it can be said that the C≡C bond changes to the C=C bond by thermal curing at temperatures from 250 to 500°C. The intensity of the peak at 134.1 ppm in the ^{13}C dipolar dephased CP spectrum (Fig. 29(a)) increases with an increase in curing temperature, and, on the other hand, that at 134.8 ppm in the ^{13}C CP/MAS spectrum (Fig. 28(a) decreases with an increase in curing temperature. As described on the Section 4, the peak at 134.1 ppm (Fig. 29(a)) corresponds to the 4a and 8a position carbons of the naphthalene ring.[40,47,50,51] Therefore, it can be said that thermal curing of the silyl-carborane hybrid diethynylbenzene–silylene polymer leads to formation of the naphthalene rings by a Diels-Alder reaction (Fig. 30). From these solid-state ^{13}C NMR results, it is found that (1) the naphthalene rings form by diene reaction between the Ph–C≡C group and the C≡C group at temperatures from 250 to 500°C, (2) the −C≡C− group changes to the >C=C< group by another addition reaction, and (3) the vinyl group converts to the alkyl group by thermal hardening reactions at temperatures from 250 to 350°C. Further, it is supposed that the vinyl group adds to the C≡C bond. The three-dimensional network may be formed by addition reactions between the vinyl group and the C≡C group as shown in Fig. 31. Besides the main chain C≡C group, the vinyl group may add to the *m*-carborane group in the side chains.

5.3. Structural characterization by ^{11}B MQ-MAS NMR

Figure 32 shows the 96.3 MHz 2D ^{11}B MQ/MAS NMR spectrum of the silyl-carborane hybrid diethynylbenzene–silylene polymer A-1 in the solid state. The F1 axis (the vertical axis) shows the high-resolution ^{11}B NMR spectrum, and the F2 axis (the horizontal axis) is the ^{11}B MAS NMR spectrum. Analysis and interpretation of this sheared spectrum are

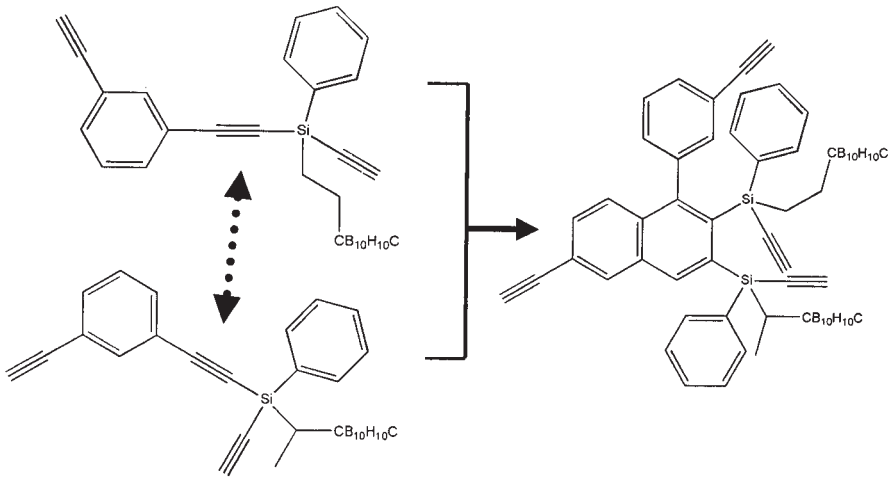

Fig. 30. A scheme for thermosetting mechanism of silyl-carborane hybrid diethynylbenzene–silylene polymer by diene reaction between theC≡C group and Ph–C≡C group.

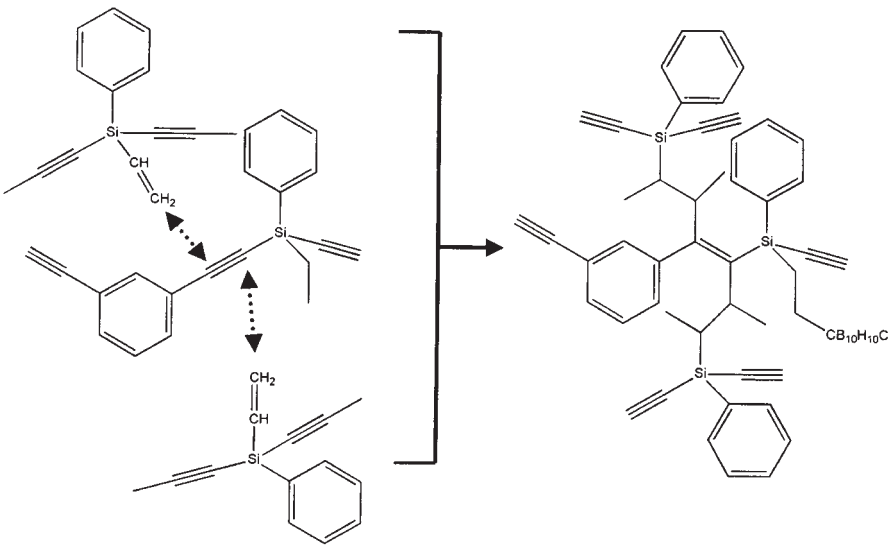

Fig. 31. A scheme for thermosetting mechanism of silyl-carborane hybrid diethynylbenzene–silylene polymer by addition reaction between the C≡C group and the vinyl group.

facilitated by introducing the chemical shift (CS) axis and the quadrupolar induced shift (QIS) axis because a shearing transformation places the anisotropic axis parallel to the F2 axis.[51] The QIS direction in the sheared spectrum has a constant slope of −10/17 and the CS axis has a

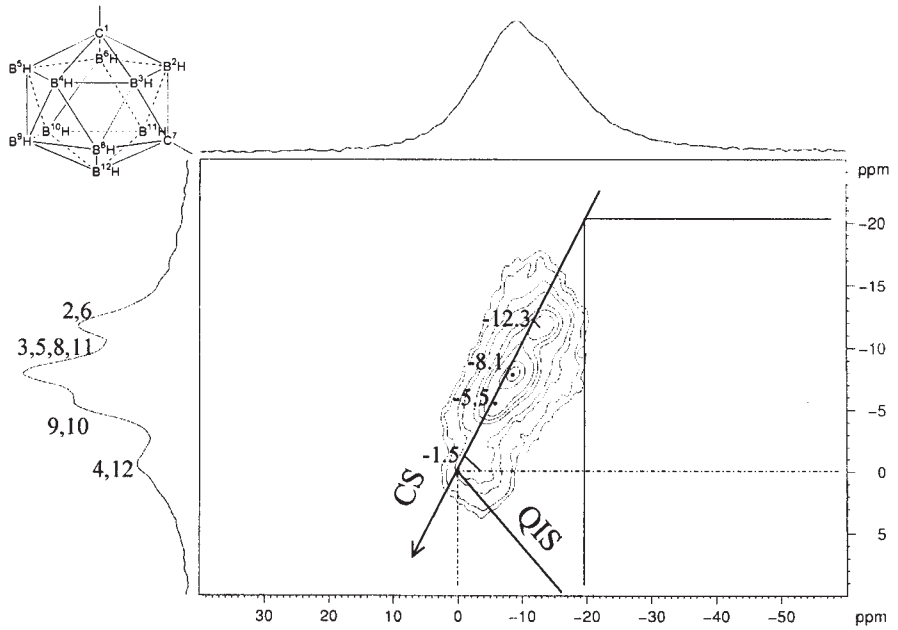

Fig. 32. 96.3 MHz ^{11}B MQ/MAS NMR spectrum of silyl-carborane hybrid diethynybenzene–silylene polymer (A-1) in the solid state. The chemical shift (CS) axis and the quadrupolar induced shift (QIS) axis are drawn as described in the text.

constant slope of 1.[41] The resonance position differs from the frequencies observed in the spectrum due to the presence of the QIS. The isotropic chemical shifts are obtained as shown Fig. 32. In the high-resolution ^{11}B NMR spectrum, there are four signals in the −10–0 ppm range. Each of the four peaks for the *m*-carborane group of the polymer can be easily assigned as shown in Fig. 32 on the basis of the ^{11}B NMR of pure *m*-carborane in the liquid state.[42] The ^{11}B NMR spectrum of the polymer in the solid state is very close to that in the liquid state. Peak assignments of the high-resolution ^{11}B NMR spectrum of the hybrid polymer are made as follows: $\delta = -12.3$ ppm, $B_{2,6}$; $\delta = -8.1$ ppm, $B_{3,5,8,11}$; $\delta = -5.5$ ppm, $B_{9,10}$; and $\delta = -1.5$ ppm, $B_{4,12}$.

Figure 33 shows isotropic projections of the ^{11}B MQ-MAS NMR spectra of silyl-carborane hybrid diethynybenzene–silylene polymers [(a) A-1, (b) A-2, (c) A-4, and (d) A-500]. These spectra are from the F1 axis in the ^{11}B MQ NMR. Spectrum [Fig. 33(a)] before curing is almost the same as spectrum [Fig. 33(b)] after molding and pressing at 250°C. This shows that the structure of the carborane group is not affected by the molding and pressing at 250°C. Structural changes of the carborane group occur at curing temperatures of 350 and 500°C. In the spectrum of the carborane

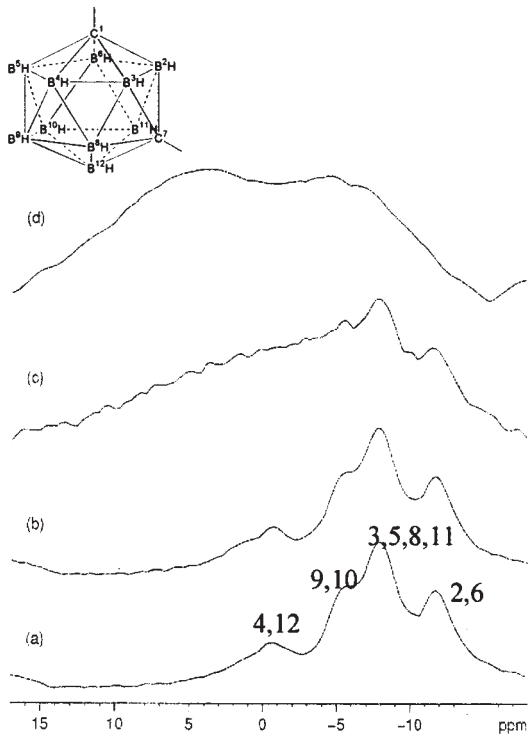

Fig. 33. Isotropic projections of ^{11}B MQ/MAS NMR spectra of silyl-carborane hybrid diethynybenzene–silylene polymers; (a) A-1, (b) A-2, (c) A-4, and (d) A-500.

group at 350°C, a large proportion of the original carborane groups remain. On the other hand, the structural change of the carborane group at 500°C is remarkable as seen from spectrum [Fig. 33(d)]. The original carborane group does not remain. Such a structural change comes from oxidation of the carborane group as clarified by X-ray photoelectron spectroscopy (XPS) under air atmosphere.

Figure 34 shows the B1s core level spectra of silyl-carborane hybrid diethynybenzene–silylene polymers cured at various temperatures. The X-ray photoelectron spectra are obtained on a Kratos AXIS-165 equipped with a Mg anode X-ray source, hermi-spherical analyzer, and a multi-channel detector. The operating pressure is about 1.6×10^{-10} Torr. The binding energy of the B 1s core level for the polymer cured at 500°C increases from 187 to 192 eV. Such a shift in the binding energy suggests a large change in the chemical bond of boron after 500°C thermal curing. Peaks at 187 and 192 eV can be assigned to B–H and B–O, respectively. Therefore, it can be said that oxidation of the carborane group occurs by 500°C thermal curing. There are a large number of unreacted *m*-carborane

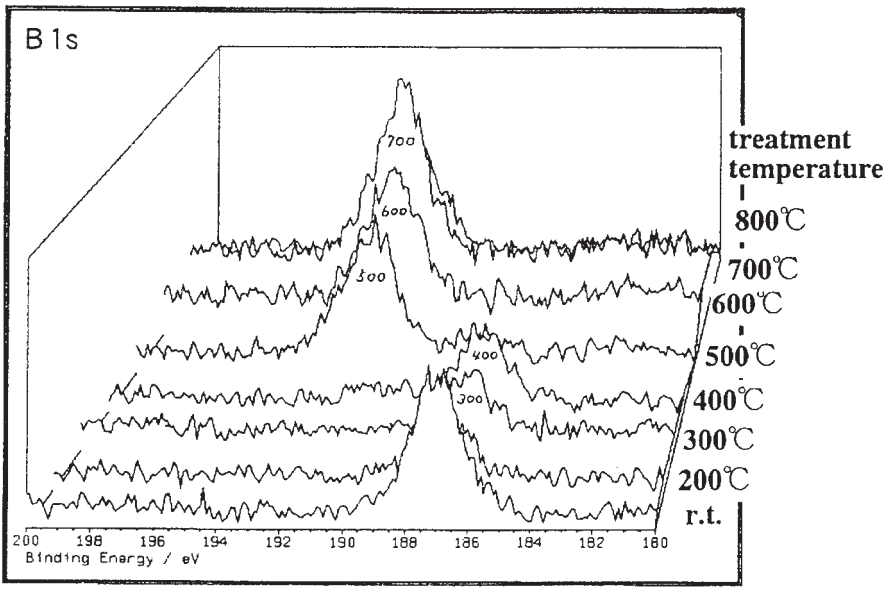

Fig. 34. Boron 1s core level X-ray photoelectron spectra of silyl-carborane hybrid diethynybenzene–silylene polymers cured at various temperatures.

groups in the polymer A-4 (350°C thermal curing). These unreacted carborane groups are completely oxidized by 500°C thermal curing. It can also be said that structural changes of the carborane group at 350°C do not occur by oxidation. It is supposed that structural changes of the *m*-carborane group at 350°C occur by crosslinking reactions. From the ^{13}C and ^{29}Si NMR results, the C≡C group and the vinyl group are crosslinked by 350°C thermal curing. Then, the *m*-carborane can be crosslinked to the C≡C group and the vinyl group.

5.4. Relationship between thermosetting structure and characteristics of a silyl-carborane hybrid Si-containing polymer network

Structural changes of the *m*-carborane hybrid polymer seem to be related to the characteristics of the polymer as shown in Table 3. The thermal durability of the hybrid polymer such as the oxygen index and heat deflection temperature is modified by thermal curing at temperatures from 350 to 500°C. The oxygen index of polymer A-4 increases from 34 to 40. The increase of the flexural modulus of the polymer leads to an increase of the temperature that is too high to measure. The modification of the thermal durability must be followed by the formation of a thermal hardening structure. As the binding energy of the polymer is increased by a crosslinking

reaction, structural change of the *m*-carborane group in the polymer and the formation of crosslinking structure lead to desirable thermal durability of the hybrid polymer.

The oxygen index of polymer A-500 is more than 50. This suggests that oxidation of the *m*-carborane group improves the desirable thermal durability of the hybrid polymer. The flexural modulus of polymer A-4 is higher than that of polymer A-2. The mechanical strength of polymer A-4 must be followed by a crosslinking reaction between the polymers. However, when the *m*-carborane hybrid silicon-based polymer is oxidized and decomposed by 500°C thermal curing, the characteristic strength of the polymer is lost.

6. CONCLUSIONS

Most recent works on the structural characterization of silicon-based organic–inorganic composites which are expected to have both the properties of an organic material such as light, flexible, moldability, etc., and an inorganic materials such as thermally stable, high strength, etc., by solid-state NMR are reviewed. NMR methodology is playing an important role for the development of new molecular design.

REFERENCES

1. R. G. Jones, W. Ando and J. Chojnowski, *Silicon-Containing Polymers*, Kluwer Academic Publishers, Dordrecht, 2000.
2. M. A. Brook, *Silicon in Organic, Organometallic, and Polymer Chemistry*, Wiley-Interscience Publication, New York, 2000.
3. M. Zeldin, K.J. Wynne, and H.R. Allcock, eds., *Inorganic and Organometallic Polymers*, ACS Symp. Ser. 360, American Chemical Society, Washington, DC, 1998.
4. J.M. Zeigler and F.W.G. Fearon, eds., *Silicon-based Polymer Science*, ACS Symp. Ser. 224, American Chemical Society, Washington, DC, 1990.
5. R.A. Komoroski, ed., *High Resolution NMR Spectroscopy of Synthetic Polymers in Bulk*, VCH Publishers, Deerfield Bleach, FL, 1986.
6. I. Ando, T. Yamanobe and T. Asakura, *Prog. NMR Spectrosc.*, 1990, **22**, 349.
7. K. Kurosu, S. Ando, H. Yoshimizu and I. Ando, *Ann. Rept. NMR Spectrosc.*, 1994, **28**, 189.
8. I. Ando and T. Asakura, eds., *Solid State NMR of Polymers*. Elsevier Science, Amsterdam, 1998.
9. D.M. Grant and R.K. Harris, eds., *Encyclopedia of NMR*, Vol. 1–8, John Wiley & Sons, New York, 1995.
10. D.M. Grant and R.K. Harris, eds., *Encyclopedia of NMR Supplements (Advances in NMR)*, Vol. 9, John Wiley & Sons, New York, 2002.
11. K. Schmidt-Rohr and H.W. Spiess, *Multidimensional Solid-State NMR and Polymers*, Academic Press, London, 1994.
12. M. Itoh, M. Mitsuzuka, K. Iwata and K. Inoue, *Macromolecules*, 1994, **27**, 7917.
13. M. Itoh, K. Inoue, K. Iwata, M. Mitsuzuka and T. Kakigano, *Macromolecules*, 1997, **30**, 694.
14. H. Q. Liu and J. F. Harrod, *Can. J. Chem*, 1990, **68**, 1100.

15. J. L. Brefort, R. J. P. Corriu, P. Gerbier, C. Guerin, B. J. L. Henner, A. Jean, T. Kuhlmann, F. Garnier and A. Yassar, *Organometallics*, 1992, **11**, 2500.
16. K. Nate, T. Inoue, H. Sugiyama and M. Ishikawa, *J. Appl. Polym. Sci.*, 1987, **34**, 2445.
17. D. R. Weyenberg and L. E. Nelson, *J. Org. Chem*, 1965, **30**, 2618.
18. W. A. Kriner, *J. Org. Chem*, 1964, **29**, 1601.
19. W. A. Kriner, *J. Polym. Sci., Part A-1*, 1966, **4**, 444.
20. H.-J. Wu and L. V. Interrante, *Macromolecules*, 1992, **25**, 1840.
21. I. L. Rushkin and L. V. Interrante, *Macromolecules*, 1995, **28**, 5160.
22. Y. Chujo and T. Saegusa, *Adv. Polym. Sci.*, 1992, **100**, 11.
23. D. Klempner, L.H. Sperling, and L.A. Utracki, *Interpenetrating Polymer Networks*, ACS Symp. Ser. 239, American Chemical Society, Washington, DC, 1994.
24. L. H. Sperling, *Interpenetrating Polymer Networks and Related Materials*, Plenum, New York, 1981.
25. M. Tsumura, K. Ando, J. Kotani, M. Hiraishi and T. Iwahara, *Macromolecules*, 1998, **31**, 2716.
26. M. Ichitani, K. Yonezawa, K. Okada and T. Sugimoto, *Polym. J.*, 1999, **31**, 908.
27. H. Kimura, K. Okita, M. Ichitani, T. Sugimoto, S. Kuroki and I. Ando, *Chem. Mater.*, 2003, **15**, 355.
28. M.F. Hawthorne, *Advances in Boron Chemistry*, The Royal Society of Chemistry, Cornwall, U.K., 1997, p. 261.
29. M. F. Hawthorne, *Current Topics in the Chemistry of Boron*, G. M. Kabalka, ed., The Royal Society of Chemistry, Tennessee, 1994, p.207.
30. R. N. Grimes, *Carboranes*, Academic Press, New York, 1970.
31. W. Clegg, H. M. Colquhoun, R. Coult, M. A. Fox, W. R. Gill, P. L. Herbertson, J. A. H. MacBride and K. Wade, *Current Topics in the Chemisty of Boron*, G. W. Kabalka ed., The Royal Society of Chemistry, Tennessee, 1994, p.232.
32. S. Papetti, B. B. Schaeffer, A. P. Gray and T. L. Heying, *J. Polym. Sci. Part A-1*, 1966, **4**, 1623.
33. D. D. Stewart, E. N. Peters, C. D. Beard, G. B. Dunks, E. Hadaya, G. T. Kwiatkowski, R. B. Moffitt and J. J. Bohan, *Macromolecules*, 1973, **12**, 373.
34. T.K. Dougherty, *United States Patent*, 23, 5,264,285, 1993.
35. P. E. Pehrsson, L. J. Henderson and T. M. Keller, *Surf. Interface Anal.*, 1996, **24**, 145.
36. L. J. Henderson and T. M. Keller, *Macromolecules*, 1994, **27**, 1660.
37. R. A. Sundar and T. M. Keller, *J. Polym. Sci. Part A*, 1997, **35**, 2387.
38. E. J. Houser and T. M. Keller, *J. Polym. Sci. Part A*, 1982, **36**, 1969.
39. B. C. Gerstein, R. G. Pembleton, R. C. Wilson and L. M. Ryan, *J. Chem. Phys*, 1977, **66**, 361.
40. L. Frydman and J. S. Harwood, *J. Am. Chem. Soc.*, 1995, **117**, 5367.
41. P. P. Man, *Phys. Rev. B*, 1998, **58**, 2764.
42. C. Fernandez, L. Delevoye, J.-P. Amoureux, D. P. Lang and M. Pruski, *J. Am. Chem. Soc.*, 1997, **119**, 6858.
43. C. Fernandez, D. P. Lang, J.-P. Amoureux and M. Pruski, *J. Am. Chem. Soc.*, 1998, **120**, 2672.
44. S. H. Wang, S. M. De Paul and L. M. Bull, *J. Magn. Reson.*, 1997, **125**, 364.
45. M. Hanaya and R. K. Harris, *J. Phys. Chem. A*, 1997, **101**, 6903.
46. J.-P. Amoureux and C. Fernandez, *Solid State NMR*, 1998, **10**, 211.
47. S. Kuroki, K. Okita, T. Kakigano, J. Ishikawa and M. Itoh, *Macromolecules*, 1998, **31**, 2804.
48. S. Kuroki, J. Nanba, I. Ando, T. Ogawa and M. Murakami, *Polym. J.*, 1999, **31**, 369.
49. M. Konayashi, S. Kuroki, I. Ando, K. Yamauchi, H. Kimura, K. Okita, M. Tsumura and K. Sogabe, *J. Mol. Structure*, 2002, **602/603**, 321.
50. H. Kimura, K. Okita, M. Ichitani, K. Okada and T. Sugimoto, *Kobunshi Ronbunshu*, 2000, **57**, 23.
51. S. Kuroki, T. Kakigano, J. Ishikawa, M. Itoh and K. Okita, *Kobunshi Ronbunshu*, 1997, **54**, 229.
52. T. Takayama, has reviewed research works on polysilanes and copolymers of silanes and siloxanes. T. Takayama, *Solid State NMR of Polymers*, I. Ando and T. Asakura eds., Elsevier Science, Amsterdam, 1998, p. 613.

Index